Tidal Effects in Pre-merger Neutron Stars and Dynamics of Scalarized Compact Objects

Dissertation
der Mathematisch-Naturwissenschaftlichen Fakultät
der Eberhard Karls Universität Tübingen
zur Erlangung des Grades eines
Doktors der Naturwissenschaften
(Dr. rer. nat.)

vorgelegt von
Hao-Jui Kuan
aus Hsinchu/Taiwan

Tübingen
2022

Gedruckt mit Genehmigung der Mathematisch-Naturwissenschaftlichen Fakultät der Eberhard Karls Universität Tübingen.

Tag der mündlichen Qualifikation:	16.12.2022
Dekan:	Prof. Dr. Thilo Stehle
1. Berichterstatter:	Prof. Dr. Kostas D. Kokkotas
2. Berichterstatter:	Prof. Dr. Andrea Santangelo
3. Berichterstatter:	Prof. Dr. José A. Font

Zusammenfassung

Im ersten Teil dieser Doktorarbeit untersuchen wir Gezeitenphänomene in der Premergerphase von sich verschmelzenden Binärsystemen, in denen mindestens ein Neutronenstern (NS) involviert ist. Insbesondere während der letzten paar Minuten der Annäherung kann das Gezeitenfeld des Begleitsterns im Primärstern gewisse Quasinormalmoden stark anregen, welche zu beobachtbaren Effekten führen. Unter anderem kann Resonanz von Niedrigfrequenzmoden (z.B. g- und i-Moden) das Brechen der Kruste verursachen, wodurch die Energie freigesetzt wird, die dort gespeichert war; dies kann zu einer Vorläuferemission von einem sogenannten Short Gamma Ray Burst (SGRB) führen, wenn der NS stark magnetisiert ist. Insbesondere halten wir es für möglich zwei Vorläuferemissionen von SGRB 090510 mit den durch Resonanz angeregten g_1- und g_2-Moden zu assoziieren. Zusätzlich präsentieren wir, dass die beobachteten Frequenzen dieser zwei $g-$Moden einen neuartigen Pfad eröffnen um die Rotationsrate des NS zu bestimmen, welche auf jeden SGRB angewendet werden kann, der zwei oder mehr Vorläufersignale hat. Dieses wahrscheinlich g-Moden-verwandte Phänomen kann also das Eingrenzen der nuklearen Zustandsgleichung begünstigen, da die Kandidaten hierfür anhand der g-Modenfrequenz gruppiert werden können. Andererseits beschleunigt die Erregung der f-Mode die Verschmelzung und führt zu einer "Gezeitensturzphase"; dadurch bildet sich in der Gravitationswellenform eine Phasenverschiebung aus, welche den evolutionären Pfad des Binärsystems bestimmt. Auch wenn die adiabatischen Gezeiten viel stärker zur Phasenverschiebung beitragen als die dynamischen wenn der NS langsam rotiert, ist die Situation eine andere für schnell rotierende Sterne: Eine Phasenverschiebung von mehreren Hundert Radiant könnte das Ergebnis sein.

Der zweite Teil der Arbeit ist der Dynamik von kompakten Objekten, d.h. von NS und schwarzen Löchern, beschrieben in alternativen Theorien der Gravitation im Regime von starker Gravitation, gewidmet. Insbesondere untersuchen wir einige Theorien, welche Skalarfelder beinhalten, wie z.B. die (Multi-)Skalar-Tensor-Theorien oder die Skalar-Gauß-Bonnet Theorie. In der Theorie mit drei Skalarfeldern fällt das Skalarfeld von statischen Sternen quadratisch mit der Distanz ab und ist deshalb nicht von Beobachtungen von Pulsaren eingeschränkt und sie haben diskrete Arten von Topologien, welche durch eine topologische Ladung beschrieben werden. Wir zeigen für die Konfigurationen ohne Ladung, dass bis zu drei verschiedene Gleichgewichtskonfigurationen von Sternen für gewisse Intervalle von

zentralen Energiedichten existieren können und dass deren Stabilität verloren geht, sobald der massereichste Stern (entweder skalarisiert oder nicht-skalarisiert) erreicht wird. Akkretion kann daher einen stabilen, skalarisierten NS in einen instabilen Zustand überführen, welche allerdings keine Deskalarisierung in Gang setzt und stattdessen einen gravitativen Phasenübergang auslöst. Dieser neuartige Phasenübergang führt zu einer plötzlichen Verringerung der Größe des Sterns, welche einen gewöhnlichen materiellen Phasenübergang mimt. Allerdings wird der erstere Phasenübergang von eine Skalarfeld-induzierten Gravitationswelle begleitet, welche bei materiellen Phasenübergängen nicht präsent sind. Zusätzlich zum Akkretionsprozess untersuchen wir den kugelsymmetrischen Kernkollaps eines Sterns in Skalar-Tensor und Skalar-Gauß-Bonnet Theorien. Obwohl ein skalarisiertes schwarzes Loch in erstgenannter Theorie auf Grund des sogenannten No-Hair-Theorems nicht existiert, können wir ein solches in zweitgenannter Theorie konstruieren. Insbesondere demonstrieren wir numerisch die Skalarisierung in einem schwarzen Loch, welches nach einem Sternkollaps übrig bleibt, um ein erstes Beispiel eines Produktionskanals für skalarisierte schwarze Löcher in Skalar-Gauß-Bonnet Theorie zu geben. Die Skalarfeld-induzierten Gravitationswellen, welche zusammen mit der (De-)Skalarisation in beiden Theorien gebildet werden, werden auch diskutiert.

Abstract

In the first part of this thesis, we investigate some tidal phenomena in the pre-merger stage of coalescing binaries with at least one neutron star (NS) involved. In particular, during the last few minutes of coalescences, the tidal field exerted by the companion can force the primary strongly to excite certain quasi-normal modes thus resulting in various observable effects. Among other things, resonance of low frequency modes (e.g., g- and i-modes) may result in crustal fracture, whereby unleash the energy used to be stored in the cracked area, possibly constituting a pre-emission of short gamma-ray burst (SGRB) if the NS is highly magnetised. In particular, we find it possible to associate two pre-emissions of SGRB 090510 with the resonantly excited g_1- and g_2-modes. We present, in addition, that the inferred frequencies of these two g-modes provide a novel avenue to estimate the spin of the NS, which can be applied to any SGRB preceded by two or more precursors. This presumably, g-mode-related phenomenon can also benefit in constraining the equation of state (EOS) since the EOS candidates can be grouped in terms of g-mode frequency. On the other hand, f-mode excitation accelerates the merger course, leading to a "tidal plunge" phase; thereby, a phase shift is rendered in the associated gravitational waveform, which dictates the evolutionary track of the binary. Although the adiabatic tide attributes much more to the phase shift than the dynamical ones if the NS rotates slowly, the situation for fast spinning stars is different: a few hundred radiants of shift may be rendered.

The second part of this thesis is dedicated to the study of the dynamics of compact objects, viz. NSs and black holes (BHs), in alternative gravity theories in the strong gravity regime. In particular, we consider some theories involving scalar field(s) as additional mediator(s) of gravitational interaction such as the (multi-)scalar-tensor theory and scalar-Gauss-Bonnet theory. In the former theory, it can happen that the scalar field of static stars dies out in the power of -2 of the distance, suppressing the scalar dipole radiation thus not constrained by pulsar experiments. In addition, these solutions are of discrete topological types, characterised by topological charge. For the zero charge configurations, we show that up to three stable stars exist for a certain range of central energy density, and the stability is lost right at the occurrence of the most massive (either scalarized or non-scalarized) star. Accretions may therefore bring a stable scalarized NS into an unstable state, where a descalarization would be triggered, generating the gravitational phase transition (PT). This novel kind of PT leads

to a sudden shrink in size of the star, mimicking well the traditional, material PT. However, the former transition will be accompanied by scalar-induced gravitational waves that are absent in material PT. In addition to the accreting process, we consider the spherically-symmetric core collapse for the scalar-tensor and the scalar-Gauss-Bonnet theories. Although a scalarized BH is absent in the former theory due to no-hair reason, we can construct one in the latter theory. In particular, we numerically demonstrate scalarization in a remnant BH behind stellar collapse, giving a first example on the production channel for scalarized BHs in the scalar-Guass-Bonnet theory. The scalar-induced gravitational waves generated along with (de)scalarization in both theories are also discussed.

Acknowledgements

Five full years of me after my Bachelor degree have been devoted to pursue a joint PhD degree between National Tsing Hua University and University of Tübingen. During this period, I am heartly grateful to both of my supervisors, Kostas Kokkotas and Chao-Qiang Geng. Without their invaluable guidance and support of all its forms, I would have not fulfilled my thesis. A specific gratitude to Kostas Kokkotas is felt during my stay in Tübingen, when the whole world had experienced shutdown for more than one year due to an extremely infective coronavirus. I truly appreciate his mentoring and guidance through a plenty of online meetings of ours.

I am indebted to all my collaborators whom I always have fruitful discussions with, and learn a lot from; they are Daniela Doneva, Da Huang, Christian Krüger, Ling-Wei Luo, Arthur Suvorov, and Stoytcho Yazadjiev. I want to thank especially my office mate Arthur Suvorov, who sharpens my scientific writing, enriches my physics thinking, and improves my presentation skill. His help in this thesis is technically comprehensive.

I have my gratitude to my family, especially my mom and dad, who always support my decision, and give me an ample room to chase whatever I want to do. During the last few years of my PhD, my daily life were continuously affected by country-wise lockdown. Without their mental support, I would have undergone a much more difficult time during this worldwide pandemic while studying abroad.

My particular appreciation is due to my fiancé, Ting Cheng, for her pouring many physics insights to me when we pondering the universe together, and for those discussions concerning both works and life with her. Although her company is of a broad sense thus impossible to grasp in a few words, one concrete example is that my pursue of this joint degree program would not have realised without her encouragement.

I am grateful to the travel support from the COST Action CA16214 "PHAROS" for attending a winter school in Poland. In addition, as the principal investigator, I acknowledge an one-year Sandwich Grant (JYP No. 109-2927-I-007-503) awarded by Taiwanese Min-

istry of Science and Technology (MOST) and Deutscher Akademischer Austauschdienst e.V. (DAAD).

A special recognition of mine goes to Daniela Doneva and Christian Krüger for their useful feedback on the manuscript of the Abstract and Introduction. A particularly kind support from Christian Krüger for the German translation of abstract is also highly appreciated.

Contents

Preface

I claim that most results included in this thesis have been carried out by myself partially at the National Tsing Hua University and partially at the University of Tübingen, while contributions of my collaborators will be mentioned at the beginning of each Chapter. The numerical simulations are carried out in the workstations "snowman" and "zwicky" that belong to my host workgroup at the University of Tübingen.

Results that are not original of me or my collaborative efforts with co-authors are cited where appropriate. A list of the articles upon which this thesis based, are detailed below:

- Chapter 1 is written by me and does not appear elsewhere.
- Chapter 2 is written by me, while following very closely to the several papers that are cited at appropriate places.
- Chapter 3 is based on the publication: "*Constraining equation of state groups from g-mode asteroseismology*" in Mon. Not. Roy. Astron. Soc., 513(3):4045-4056[1] [1] by H.-J. Kuan, C. J. Krüger, A. G. Suvorov, and K. D. Kokkotas.
- Chapter 4 is based on the two publications: "*General-relativistic treatment of tidal g-mode resonances in coalescing binaries of neutron stars – I. Theoretical framework and crust breaking.*" in Mon. Not. Roy. Astron. Soc., 506(2):2985–2998[2] [2], and "*General-relativistic treatment of tidal g-mode resonances in coalescing binaries of neutron stars – II. As triggers for precursor flares of short gamma-ray bursts.*" in Mon. Not. Roy. Astron. Soc., 508(2):1732-1744[3] [3] both by H.-J. Kuan, A. G. Suvorov, and K. D. Kokkotas.
- Chapter 5 is based on the preprint submitted to Mon. Not. Roy. Astron. Soc.: "*Measuring spin in coalescing binaries of neutron stars showing double precursors*" by H.-J. Kuan, A. G. Suvorov, and K. D. Kokkotas.

[1] Published by Oxford University Press.
[2] Published by Oxford University Press.
[3] Published by Oxford University Press.

- Chapter 6 is based on the publication: "*f-mode Imprints in Gravitational Waves from Coalescing Binaries involving Spinning Neutron Stars*" in Phys. Rev. D, 106:064052 [4] by H.-J. Kuan, and K. D. Kokkotas.

- Chapter 7 is based on the publication: "*Nonlinear evolution and nonuniqueness of scalarized neutron stars.*" in Phys. Rev. D, 104:124013 [5] by H.-J. Kuan, J. Singh, D. D. Doneva, S. S. Yazadjiev, and K. D. Kokkotas.

- Chapter 8 is based on the publication: "*Gravitational waves from accretion-induced descalarization in massive scalar-tensor theory.*" in Phys.Rev.Lett. 129(12):121104 [6] by H.-J. Kuan, A. G. Suvorov, D. D. Doneva, and S. S. Yazadjiev.

- Chapter 9 is based on the three publication: "*Viable Constraint on Scalar Field in Scalar-Tensor Theory.*" in Class. Quant. Grav., 37:115001[4] [7] by C.-Q. Geng, H.-J. Kuan, and L.-W. Luo, "*Inverse-chirp imprint of gravitational wave signals in scalar tensor theory.*" in Eur. Phys. J. C, 80:780 [5] [8] by C.-Q. Geng, H.-J. Kuan, and L.-W. Luo, and "*Scalar gravitational wave signals from core collapse in massive scalar-tensor gravity with triple-scalar interactions.*" in Class. Quant. Grav., 38:245006[6] [9] by D. Huang, C.-Q. Geng, and H.-J. Kuan.

- Chapter 10 is based on the publications: "*Dynamical Formation of Scalarized Black Holes and Neutron Stars through Stellar Core Collapse.*" in Phys. Rev. Lett., 127:161103 [10] by H.-J. Kuan, D. D. Doneva, and S. S. Yazadjiev.

- Appendix A is based on the appendix of the publication: "*Constraining equation of state groups from g-mode asteroseismology*" in Mon. Not. Roy. Astron. Soc., 513(3):4045-4056[7] [1] by H.-J. Kuan, C. J. Krüger, A. G. Suvorov, and K. D. Kokkotas.

- Appendix B is based on parts of the publication: "*Viable Constraint on Scalar Field in Scalar-Tensor Theory.*" in Class. Quant. Grav., 37:115001[8] [7] by C.-Q. Geng, H.-J. Kuan, and L.-W. Luo,.

- Appendix C is in collaboration with A. G. Suvorov, D. D. Doneva, and S. S. Yazadjiev, and does not appear elsewhere.

[4] © IOP Publishing. Reproduced with permission. All rights reserved.
[5] With kind permission of The European Physical Journal (EPJ).
[6] © IOP Publishing. Reproduced with permission. All rights reserved.
[7] Published by Oxford University Press.
[8] © IOP Publishing. Reproduced with permission. All rights reserved.

"Gravity is the tendency of matter to go where time is slower."

– Kip Thorne

Acronyms

NS	Neutron star
BH	Black hole
SGRB	Short gamma ray burst
GW	Gravitational wave
QNM	Quasi-normal mode
EOS	Equation of state
GR	General relativity
DEF	Damour-Esposito-Farese scalar tensor theory
TMST	Tensor-multiscalar theory
SGB	Scalar-Gauss-Bonnet theory
PN	post-Newtonian
aLIGO	(advanced) Laser Interferometer Gravitational-Wave Observatory
ET	Einstein Telescope

Chapter 1

Introduction

Contents

The geocentric model once ruled our knowledge of the universe, when the whole visual scenery was meant by the term "universe". Limited to the intuition of humankind, heliocentrism had been greatly underestimated when it first burst onto the scientific horizon led by Nicolaus Copernicus in the late 15th century, while Galileo's observations and the modification introduced by Kepler during the cross of the late 16th and the early 17th century started to shed some light on this revolutionary model that had sat in the dark corner for a while. Before too long after Kepler elucidated the fundamental role of elliptical orbits, Isaac Newton came up with three laws that satisfy, again, the whole visual scenery at that time. Only this time, people had gained more knowledge about the "universe". History then brings Maxwell's equations to our understanding of nature, which translate, though highly non-trivially, into special relativity in a young man's mental universe at the beginning of 20th century. As of the fifteenth year since the idea of special relativity had been contemplated, the same gentleman, Albert Einstein, managed to lead our knowledge of nature to an even further place: time has become a parameter, which functions in much the same way as other long-known spatial coordinates. The theory remains effective today even though scientists have tested it with ever more precise measurements, with most wild speculative experiments, and with phenomena at an ever wider scale range. Fortunate enough, the astrophysics community is now ushering in a novel era heralded by the ever first witnessing of gravitational waves (GWs) emanating from a black hole binary, coded by GW150914 [11], which coincidentally celebrated the centennial of Einstein's theory. As the later wave will always push the former one, novel observation will always push forward our sight about the whole visual scenery.

Despite the fact that the first detection of GW150914 [11] suffices to prove the GW prediction of Einstein's theory, an event that opens a new direction to investigate equation of state (EOS) at supranuclear density only came in two years later, when the very first detected binary neutron star (NS) was observed via the gravitational wave event GW170817 [12]. Since then GW physics has attracted enormous attention as this kind of weakly-interacting-with-matter radiations delivers undistorted information of the source, therefore providing an invaluable avenue to acquire the yet-to-be-understood particulars of the interior of NSs, viz. EOS, and to test gravity theories. I aim to touch on these two perspectives in this dissertation, which is accordingly divided into two parts with each devoted to one of the subjects.

1.1 Evolutionary Study of Binary Neutron Stars

One of the most promising source for GWs is thought to be coalescing binaries consisting of compact objects, viz. NSs and/or black holes (BHs). Without delicate internal structures, gravitational waveforms emanating from binary BHs are easier to model; for those, the analytic wave form has been derived up to 3.5 PN order [13], while the step towards 4 PN and even 4.5 PN order effects has been attempted recently [14–16]. In contrast, those launched by binaries with at least one NS involved channel the information of interior particulars of NSs thus the tidal effects have to be considered as well, and the analytic study has been carried out up to 7.5 PN order recently [17, 18]. Owing to its extreme gravitational strength, supra-nuclear regime can be realised in NS which lies in the otherwise inaccessible QCD phase diagram, and thus provides a unique avenue to probe the supra-nuclear EOS, a pursue towards which is a "holy-grail" of nuclear physics and relativistic astrophysics.

From the detailed analysis of gravitational waveforms, the chirp mass of the binary can be measured to a great accuracy, and the symmetric mass ratio can also be determined though with a marginally less precision [19–21]. These two parameters suffice to make an estimate of the individual masses of the two constituents. On top of these are point-like properties, finite-size effects gradually become measurable; for instance, in the milestone observation of GW170817 [12], the (mutual) tidal deformability of the binary has been estimated, while at this stage the waveform template including spin-effects is not well understood yet so that the spins of the progenitors can only be treated as a free parameter [22]. For this particular event, we turned out to be incredibly fortunate in the sense that the associated multi-messenger phenomena have been observed, viz. the follow-up launch of SGRB, the afterglow, and an late-time optical-infrared transient (kilonova) caused by r-process nucleosynthesis [23–29]. The second binary NS merger observed by the LIGO-Virgo collaboration is GW190925 [30] for which no EM counterparts came into sight, while its total mass ($\sim 3.4 M_\odot$) exceeds any of the known galactic binary NSs [31, 32], thus hinting that at least one of the progenitors

may be a fast-spinning NS. In addition, in the witnessed events, NS is a sight for sore eyes; other than the aforementioned two binary NSs, there are only two more events with a NS involved, and both are black hole-NS binaries, viz. GW200105 and GW200115 [33].

Electromagnetic (EM) counterparts throughout the coalescing course, in general, include precursor flares, short gamma-ray bursts (SGRBs), and multi-band afterglows. Each of those helps us acquire source properties when we deepen our knowledge of their central engines. As perfect systems to examine EOS in either GR framework or modified gravity theories, each of the aforementioned EM phenomena warrant further investigation. In particular, pre-emissions have been detected for a few SGRBs [34–38], and are hypothesised to be associated with tidal resonances of quasi-normal modes (QNMs) during the inspiral [39–41] or interacting magnetospheres [42–44]. In any case, there is observational evidence that those systems which produce precursors may be strongly magnetised ($\gtrsim 10^{15}$ G; see, e.g., [41]). We will adhere our attention to the resonant shattering scenario in Chap. 4 which is to explore this mechanism. By virtue of the timing of the observed precursors, any mode with frequency of ~ 100 Hz may be a candidate responsible for precursors in this context, such as interface- and g-modes for slow-rotating NSs, and f- and r-modes for fast-rotating stars. Although the logic behind this scenario is simple, the physics is rather involved: Not only depend mode frequencies on several physical aspects, e.g., the EOS, the spin rate, the structure and the strength of the inhabited magnetic field, and the degree of stratification, but also the maximal sustainable strain the crust can bear is uncertain [45–49]. Keeping this latter uncertainty in mind, however, we adopt a specific value of the maximal bearable strain to examine the mechanism with a particular emphasis on g-modes.

Unlike the pressure restored modes (e.g., f- and p-modes), g-modes manifest from either thermal and/or compositional gradients [50–52], or discontinuities [53, 54] in NSs; therefore, this class of modes encodes the particulars of the interior of NSs. In addition, the g-mode spectrum may discern the nature of the inner core of NSs since certain imprints will be caused by a superfluid core [55–57] or phase transitions either to free quark or hyperon condensation [58, 59]. Asteroseismology of stellar oscillations has proven useful in astrophysics when (i) inferring properties of protoneutron stars left behind after core collapses [60–63], and coalescing binary NSs before [64] and after [65, 66] merger, and (ii) connecting stellar parameters of pre- and post-merger stars [67]. Here we list just a few examples, and the mentioned applications are absolutely far from complete; however, the importance of asteroseismology is obvious. Among other modes, the asteroseismology of g-modes may particularly help probe the fabric constituting NSs, thus limiting EOS in an aspect other than acoustic modes. In Chap. 3, we aim at making the first step towards this direction by establishing several universal relations for g-modes, which can be quite useful, from experience, in determining source properties thus leading to certain conditions for EOS candidate to satisfy.

Adopting a piecewise-polytropic approximation for several equations of state [68, 69] –

by which we are effectively considering barotropic EOS without compositional particulars, we show in Chap. 3 that there exist three groups of equations of state regarding g-mode frequencies. The grouping originates from the physics involved in certain equations of state. Those belonging to groups I and II assume that neutron stars are made from neutrons, protons, electrons and muons. Although having the same constituents, some of them can support stars with more than 2 solar mass, while others cannot. Those able to realise heavy stars are members in group I, and those not belong to group II. It is a fresh view connecting the maximal mass of an EOS, which is a bulk property of stars, to the g-mode spectrum, which is determined by microscopic physics. There still is group III, whose members assume phase transitions either to free quarks or hyperon condensation inside stars. Putting group III aside, the other two groups admit universal relations with other parameters such as tidal deformability. At our proposal, two-fold benefits can be extracted out from g-mode-related phenomena to narrow down candidates of equations of state: (i) the source can be mapped onto the established g-space, whereby it is possible to set constraints on g-mode branches, and (ii) certain parameters can be derived through universal relations to help limit EOS, e.g., the derived f-mode frequency and the g-mode frequency can be incorporated to constrain the mass-radius curves.

To employ the g-mode asteroseismology, observations related to g-mode have to be studied. The candidate phenomena that may be caused by g-modes include precursors [34, 36–38], and quasi-periodic oscillations in X-ray tails [70–72]. We pay especially attention to the precursors, and show that the two early emissions of GRB090510 may be attributed to g_1- and g_2-modes. In general, for systems exhibiting double precursors, additional information on spin priors of pre-merger neutron stars can be obtained if we attribute the two pre-emissions to two resonantly excited modes of one of the constituents: the almost constant ratio between their free frequencies together with the rotation-modified frequencies indicated by the precursor timing admit an algebraic relation for the star's spin (detailed in Chap. 5). The increased knowledge about the spin helps reduce systematic errors in some parameters of pre-merger stars, such as mutual tidal deformability. Since some remnants' properties correlate strongly to those of progenitors, including this spin-extracting scheme in the analysis of future gravitational waves from systems showing two precursors will therefore ameliorate measurements of stellar parameters in both pre- and post-merger stages, thus may place stricter constraint on the EOS.

In addition, f-modes contribute to setting constraints on EOS in another aspect. Although other modes are rather "invisible" in GW data stream, f-mode effects have a good chance to be seen in future observations (e.g., [73, 74]) owing to their marginally strong coupling with tidal field exerted by the companion. The tidal effect produced by f-modes is dubbed as dynamical tidal effect, while that caused by the deformation of the star is called equilibrium tidal effect. The imprint in gravitational waveform left by the latter tides is well described

by the Love number of stars [21, 75–77], while the influence in GW of the dynamical ones are still under research [73, 78–80]. Although the adiabatic tide attributes much more to the phase shift than the dynamical ones if the neutron star rotates slowly, the dynamical tides would impact the gravitational waveform more significantly for increasing spin of NSs in the pre-merger stage. Mode excitations will be enhanced for increasing stellar spin since mode frequencies will be reduced by spin (at least for the most relevant oscillation modes) thus expediting the onset of excitation for each mode, where the most dominant excitation contributing to dephasing is f-mode. Especially, there are astrophysical processes that may lead to fast rotating NSs in coalescing binaries, such as dynamical encounters in a star cluster [81, 82], hierarchical triple system [83], and tidal capture of a natal NS kicked off from its born site by a compaction object [84, 85]. We examine the tidal dephasing for binaries embracing one rapidly spinning neutron star in Chap. 6, where a phase shift of up to a few hundred radians is found to be possible. Our results thus explain themselves as an imperative concern in the GW analysis.

1.2 Testing Gravities beyond General Relativity

Theories of gravity other than general relativity are motivated by certain theoretical concerns such as renormalisability when catering gravity to a quantum context [86, 87] (see also [88] for a review). Balancing the simplicity of an alternative theory so that it is manageable and the ability to alleviate the tension with aforementioned concerns, the most popular way is to introduce scalar field(s) to the theory. Owing to the additional degree(s) of freedom introduced in alternative theories, configurations and dynamical behaviours of compact objects, viz. NSs and BHs, will deviate from that in GR. In particular, the phenomenon of scalarization may happen in a variety of theories, e.g., [89–95]. Measuring the extent of such deviation will provide tests upon the nature of gravity (see [96] for a detailed review). In addition to the modifications in the physics present in GR, certain novel physics will be introduced. Among others, we will specialise ourselves to the (multi-)scalar-tensor theories and the scalar-Gauss-Bonnet theories. Several free parameters are introduced accordingly with the coupling function as proxy. To constrain these parameters, we have to connect them with some observables. For instance, scalarization in these theories can only occur for a certain range of parameters, thus a detection of scalarized object then serves as evidence to rule out regions in the parameter space. A timely relevant observation to test theory parameters is GWs. Although the waveform of gravitational radiation in general relativity has been understood to a great accuracy after 40 years of effort of the community, gravitational waveforms of alternative gravities are still at the stage as 1990's general relativity. The beyond 2.5 post-Newtonian order waveforms for some theories are just developed in these two years (2021 and 2022; e.g., [97–100]). In particular, scalarization and descalarization enrich

by much the waveform modelling. We here make one of the early steps towards modelling such scalar-radiations in the considered theories.

Focusing on spherically symmetric spacetime, we first examine the stability of scalarized NSs in Chap. 7 for multi-scalar-tensor theories, where we show that the conventional criterion for the stability of neutron stars in the general relativity still holds: *Models with the central energy density less than that of the configuration having the maximal mass are stable.* In this class of theories, this criterion indicates that there can be up to three stable stars for a certain range of central energy densities. On the other hand, similar to single scalar-tensor theories, there exists no stable solution (neither scalarized nor GR-like one) for a range of central energy densities. For unstable solutions, they will migrate to a scalarized star having the same baryonic mass as the initial state; if the initial star is scalarized then it will undergo a reconfiguration of scalar field, while an initially non-scalarized star will undergo a scalarization.

According to the above observation, a scalarized solution having the mass close to the maximal mass will become unstable and activate some non-linear dynamics if certain amount of accretion has fallen onto the star. Although the over-accreted, scalarized star in the multi-scalar-field theories considered in Chap. 7 will collapse to a black hole, a different scenario can occur if the maximal mass of the scalarized solution is less than the maximal mass of the unscalarized ones. We examine this latter scenario in scalar-tensor theories in Chap. 8 by over-accreting a star, where a descalarization of a NS will lead it to another stable state instead of collapsing to a BH. The migration triggers a *gravitational phase transition*, bearing a striking similarity with the matter phase transition in general relativity, thus indicating a degeneracy in phenomena adding to the already known 'EOS vs non-Einstein gravity' one (e.g., [101]). In addition, this phenomenon will be accompanied by scalar gravitational emission, thereby alter the evolution track of the star. Some imprints may also be left in the electromagnetic outburst; the rapid reduction of radius followed the descalarization may generate a 'dent' in the X-ray flux, manifesting a 'broken plateaus' of afterglow light-curves. The sudden compactification caused by a *gravitational* transition may trigger a nuclear phase transition, leading to successive transitions. If double transitions occur in massive scalar-tensor theories, the scalar-radiation by the first transition will arrive at the detector *later* than the tensorial gravitational wave caused by the second transition. This double transition scenario, as well as the direction of considering stars with differential rotation, and relatively high temperature, may be worth of further investigation. Apart from completing more the scenario, an extension to the multi-scalar-tensor theories is also considered, and is now in preparation.

We then go on to consider realistic core collapse in massive scalar-tensor theories with or without a self-interaction of scalar field in Chap. 9. The chirp pattern of scalar-gravitational-waves dictated in the massive theories is observed. While we choose to formalise the theory

in the Einstein frame for numerical simulation, we cannot be confident *a prior* if the chosen frame is suitable for the physical process in study or not [102–104]; that said, we do not know if this reformulation of the theory would introduce frame-dependent singularities or not. To justify that the introduced auxiliary scalar field in the Einstein frame can actually be smoothly converted back to the scalar field in the physical frame, i.e., the Jordan frame, we derive a condition for the scalar field in the Einstein frame. We specifically identify the region on the parameter space over which the simulated results obey the above condition, so that the scalar field in the Einstein frame is legitimate for expressing the scalar-gravitational-waves in the Jordan frame.

In Chap. 10, we study the core collapse in the context of the scalar-Gauss-Bonnet theory, where spontaneous scalarization is induced by curvature. Here we do not introduce an auxiliary frame to carry out numerical evolution, and all fields are evolved in the Jordan frame. Although there is the no-hair theorem for (multi-)scalar-tensor theories, black holes in scalar-Gauss-Bonnet can be scalarized [105,106], which has been examined by constructing such scalarized configuration. However, there has been proposed no realistic physical mechanism for the formation of isolated scalarized black holes and neutron stars in Gauss-Bonnet theories of gravity. We demonstrate for the very first time that scalarized black holes can be produced in a dynamical process. In particular, we show a scenario where the non-scalarized protoneutron star generated by a core collapse undergoes a scalarization as of the formation of a black hole remnant, though such scalarized black holes exist only for a certain range of parameters. On top of this specific outcome, we also demonstrate all possible paths to the final scalarized state. The richness of the evolution tracks is suggestive of interesting possibilities for observational manifestations; any observation of such kind can therefore pose constraints on the theory parameters.

Part I

Tidal Effects in Pre-merger Neutron Stars

Chapter 2

Stellar Oscillation

Contents

Overview

In this Chapter, we lay out the equations and the numerical scheme for resolving stellar quasi-normal modes, aiming to pave the way for the later applications of, in particular, fundamental (f-) and gravity (g-) modes. We will not go into the detail of the restoring forces for different kinds of modes here, but rather to introduce the method for finding modes in general. Some information about the origin of the aforementioned modes will be provided where appropriate in the later Chapters.

2.1 Stellar structure

We consider a static, spherically symmetric line element

$$ds^2 = -e^{2\Phi(r)}dt^2 + e^{2\lambda(r)}dr^2 + r^2(d\theta^2 + \sin^2\theta^2 d\phi^2), \tag{2.1}$$

where (t, r, θ, ϕ) are the usual Schwarzschild coordinates, and Φ and λ are functions of r only. The Einstein equations

$$G_{\mu\nu} = 8\pi T_{\mu\nu}, \tag{2.2}$$

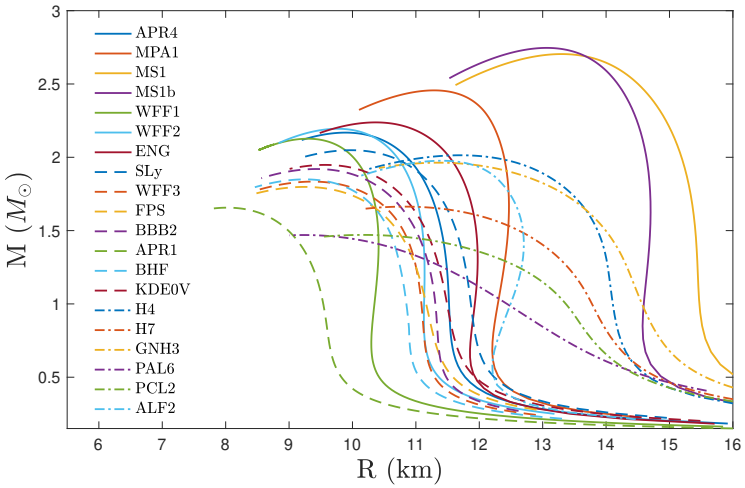

Figure 2.1: Mass-radius diagrams for the EOS considered here (see plot legends).

for the stress-energy tensor associated with a single, perfect fluid,

$$T^{\mu\nu} = (\rho + p)\, u^\mu u^\nu + p g^{\mu\nu}, \tag{2.3}$$

describe the structure of a static, non-rotating star. Here ρ is the energy-density, p is the stellar pressure, $g_{\mu\nu}$ is the metric tensor defined in (2.1), and $u^\mu = e^{-\Phi}\partial_t$ is the 4-velocity of a generic fluid element (rotational corrections to the stellar structure are considered in Sec. 4.4.3). The metric function λ is related to the mass distribution function $m(r)$, which yields the mass inside the circumferential radius r, through

$$e^{-2\lambda} = 1 - \frac{2m(r)}{r}. \tag{2.4}$$

The conservation law,

$$0 = \nabla^\mu T_{\mu\nu}, \tag{2.5}$$

relates the functions $\rho(r)$, and $p(r)$ to the metric variables, and forms the following system

$$\frac{d\Phi}{dr} = \frac{1}{p(r) + \rho(r)} \frac{dp}{dr}, \tag{2.6a}$$

$$\frac{dm}{dr} = 4\pi r^2 \rho(r), \tag{2.6b}$$

and

$$\frac{dp}{dr} = -\frac{[\rho(r)+p(r)]\,[m(r)+4\pi r^3 p(r)]}{r^2\left[1-\frac{2m(r)}{r}\right]}. \tag{2.6c}$$

Non-rotating, spherically symmetric equilibrium stellar models are then obtained as solutions to the above, so-called, Tolman-Oppenheimer-Volkoff equations [107, 108], and the star's radius $R_\star$ and mass $M_\star$ are defined by the boundary conditions $p(R) = 0$ and $m(R_\star) = M_\star$, respectively. Outside of the star, where $p = \rho = 0$, the metric (2.1) reduces to the Schwarzschild metric of mass $M_\star$. The aforementioned equations should be completed by an EOS, for which we adopt the piece-wise polytropic approximation to several [68, 69]; see Fig. 2.1 for the EOS list and their mass-to-radius relations. The EOS are chosen to cover a wide range, from those obtained for NSs with purely $nep\mu$ matters, to those influenced by the hypothetically existing hyperons (e.g., GNH3, H4) possibly even displaying phase transition to free quarks (i.e., hybrid stars; e.g., ALF2). Although some of the considered EOS cannot support the heaviest pulsar observed to-date, namely PSR J0740+6620 [109] with the mass of $\sim 2.14 M_\odot$, they are included for the sake of demonstrating the generality of the trifurcation of EOS space, while we note that only EOS in Group I support the mass of PSR J0740+6620.

2.2 Perturbation Equations

Oscillatory patterns of motion in a star can be resolved into QNMs with complex eigenfrequency $\varpi = \omega_\alpha + i/\tau_\alpha$, where α denotes the ensemble of quantum numbers $\alpha = (nlm)$ for overtone number n, and spherical harmonic indices l and m. The oscillating frequency is the real part of the eigenfrequency ω_α, while the reciprocal of the imaginary part defines the damping rate τ_α due to radiation-reaction.

The perturbed metric tensor with even parity of a general relativistic stellar model reads [110]

$$\begin{aligned} ds^2 =& -e^{2\Phi}(1+r^l H_0 Y_{lm} e^{i\varpi t})dt^2 - 2i\varpi r^{l+1} H_1 Y_{lm} e^{i\omega t} dt dr \\ &+ e^{2\lambda}(1-r^l H_0 Y_{lm} e^{i\varpi t})dr^2 + r^2(1-r^l K Y_{lm} e^{i\varpi t})d\Omega^2, \end{aligned} \tag{2.7}$$

and the associated (Lagrangian) displacement vector $\boldsymbol{\xi}$ can be expressed by

$$(\xi^r, \xi^\theta, \xi^\phi) = \left(r^{l-1} e^{-\lambda} W Y_{lm} e^{i\varpi t}, -r^{l-2} V \partial_\theta Y_{lm} e^{i\varpi t}, -\frac{r^{l-2} V}{\sin^2\theta}\partial_\phi Y_{lm} e^{i\varpi t}\right). \tag{2.8}$$

Here H_0, H_1, K, W, V are functions of r only, reflecting the spherical symmetry assumed for the equilibrium. Linearising the Einstein's equations renders a coupled, differential equation set for these five functions, which constitutes an eigenproblem if being augmented with some

boundary conditions. As relevant to the stellar pulsations, we consider three conditions at the centre, stellar surface, and spatial infinity. In particular, we require eigenfunctions to be regular at $r = 0$, the perturbation of pressure

$$\Delta p = -r^l e^{-\Phi} X Y_{ln} \tag{2.9}$$

to vanish at the surface, and, lastly, eigenfunctions to be purely out-going at infinity (see below). In the above definition, X is defined as

$$X = \varpi^2(\rho + p)e^{-\Phi}V - r^{-1}p'e^{\Phi-\lambda}W + \frac{1}{2}(\rho + p)e^{\Phi}H_0, \tag{2.10}$$

which is connected to H_0, H_1, and K through the equality

$$\begin{aligned}[3M + \frac{1}{2}(l+2)(l-1) + 4\pi r^3 p]H_0 = 8\pi r^3 e^{-\Phi}X - \left[\frac{1}{2}l(l+1)(M + 4\pi r^3 p) - \varpi^2 r^3 e^{-2\Phi-2\lambda}\right] H_1 \\ + \left[\frac{1}{2}(l+2)(l-1)r - \varpi^2 r^3 e^{-2\Phi} - r^{-1}e^{2\lambda}(M + 4\pi r^3 p)(3M - r + 4\pi r^3 p)\right] K.\end{aligned} \tag{2.11}$$

We can see that the coefficients of Eq. (2.10) are non-zero inside the star, which admits that rephrase the differential equation set for $\{H_0, H_1, K, W, V\}$ to one for $\{H_0, H_1, K, W, X\}$. On the other hand, the coefficient of H_1 in Eq. (2.11) is not vanishing in general; in fact, it will be zero wherever the relation

$$\varpi^2 = \frac{1}{4}l(l+1)\frac{1}{r}\frac{d}{dr}(e^{\Phi}), \tag{2.12}$$

holds. Despite that H_1 is not be derivable from H_0, K, and X (or V) for stars that the aforementioned equality is met somewhere inside, H_0 is always solvable if other functions are provided. This indicates that we can reduce the degrees of freedom by one, resulting in a four dimensional perturbation equation set [111], given by

$$H_1' = -\frac{1}{r}\left[l + 1 + \frac{2m}{r}e^{2\lambda} + 4\pi r^2(p - \rho)e^{2\lambda}\right] H_1 + \frac{1}{r}e^{2\lambda}\left[H_0 + K - 16\pi(\rho + p)V\right], \tag{2.13}$$

$$K' = \frac{l(l+1)}{2r}H_1 + \frac{H_0}{r} + \left[\Phi' - \frac{l+1}{r}\right] K - \frac{8\pi}{r}(\rho + p)e^{\lambda}W, \tag{2.14}$$

$$\begin{aligned}W' &= -\frac{l+1}{r}W + re^{\lambda}\left[\frac{1}{\Gamma p}e^{-\Phi}X - \frac{l(l+1)}{r^2}V + \frac{H_0}{2} + K\right] \\ &= -\left(\frac{l+1}{r} + \frac{p'}{\Gamma p}\right)W + re^{\lambda}\left[\frac{H_0}{2} + K - \frac{l(l+1)}{r^2}V + \frac{\rho + p}{\Gamma p}\left(e^{-2\Phi}\varpi^2 V + \frac{H_0}{2}\right)\right],\end{aligned} \tag{2.15}$$

and

$$X' = -\frac{l}{r}X + (\rho+p)e^{\Phi}\left\{\frac{1}{2}\left(\frac{1}{r}-\Phi'\right)H_0 + \frac{1}{2}\left(\varpi^2 re^{-2\Phi} + \frac{l(l+1)}{2r}\right)H_1 + \left(\frac{3}{2}\Phi' - \frac{1}{2r}\right)K \right.$$
$$\left. - \frac{l(l+1)}{r^2}\Phi' V - \frac{1}{r}\left[\varpi^2 e^{-2\Phi+\lambda} + 4\pi(\rho+p)e^{\lambda} - r^2\frac{d}{dr}\left(\frac{1}{r^2}e^{-\lambda}\Phi'\right)\right]W\right\},. \tag{2.16}$$

The latter equation (2.16) can be replaced by

$$V' = \frac{1}{2\varpi^2}e^{2\Phi}\left(\frac{p'}{\Gamma p} - \frac{\rho'}{\rho+p}\right)\left(H_0 + \frac{2}{r}e^{-\lambda}\Phi' W\right) + rH_1 + \left(\frac{p'}{\Gamma p} - \frac{\rho'}{\rho+p} + 2\Phi' - \frac{l}{r}\right)V - \frac{1}{r}e^{\lambda}W. \tag{2.17}$$

Here the prime denotes the derivative with respect to r, γ stands for the radially-dependent adiabatic index for the background stellar model, defined by

$$\gamma = \frac{\rho+p}{p}\frac{dp}{d\rho}, \tag{2.18}$$

while Γ represents the adiabatic index for perturbations in the star, which does not necessarily equal to γ (see Chap. 3 for more detail).

The linearised Einstein equations summarised above, together with proper boundary conditions, are then solved numerically. Eigenvalues of the perturbation equations determine the quasi-normal mode spectrum. We will address these boundary conditions and the procedure of solving the eigenproblem in the next subsection.

2.3 Numerical Scheme

As addressed in [112], in order to resolve eigenfrequencies down to a few tens of Hz (typical for $g-$modes), the appropriate set of functions to be solved near the centre is $\{H_1, K, W, V\}$. Since the perturbation equations are singular at the origin, it is beneficial to have the Taylor expansion of the solutions about $r = 0$ being of the form

$$\Upsilon(r) = \Upsilon_0 + \frac{1}{2}r^2\Upsilon''(0) + O(r^4), \tag{2.19}$$

where $\Upsilon \in \{H_1, K, W, V\}$ to extract the physical nonsingular solutions from these equations. We note that the field equations imply that the linear coefficients vanish. Expand the fluid profiles (λ, Φ, p, and ρ) of the equilibrium in the same manner, one can show that the second order coefficients are related to the central values of pressure p_c, density ρ_c, and adiabatic

index γ_c through

$$\lambda'' = \frac{8\pi\rho_c}{3}, \qquad \Phi'' = \frac{4\pi}{3}(\rho_c + 3p_c), \qquad p'' = -\Phi''(\rho_c + p_c), \qquad \text{and} \qquad \rho'' = \frac{p''(\rho_c + p_c)}{\gamma_c p_c} \tag{2.20}$$

Similar to the above expression, the relations of Υ'' are expressed by the central values of relevant functions, which are given by

$$-\Gamma p\left[(n+1)V'' + \frac{l+3}{2}W''\right] = -\frac{1}{2}(3\Gamma p + \rho + p)K(0) + [(n+1)\lambda''\Gamma p - lp'' - e^{-2\Phi}\omega^2(\rho+p)]V(0), \tag{2.21}$$

$$\begin{aligned}(l+2)V'' + W'' = {} & 2H_1(0) - \frac{e^{2\Phi}}{\omega^2}\left(\frac{\rho''}{\rho+p} - \frac{p''}{\Gamma p}\right)K(0) \\ & + \left\{l\lambda'' + 4\Phi'' + 2(1 - l\omega^{-2}e^{2\Phi}\Phi'')\left[\frac{p''}{\Gamma p} - \frac{\rho''}{\rho+p}\right]\right\}V(0),\end{aligned} \tag{2.22}$$

$$-\frac{n(l+3)}{2}H_1'' + nK'' - 8\pi n(\rho+p)V'' = n(\Phi'' - \lambda'')H_1(0) - n\lambda''K(0) + 2Q_aV(0) + Q_b, \tag{2.23}$$

$$\frac{n(n+1)}{2}H_1'' - \frac{n}{2}(l+2)K'' - 4\pi(\rho+p)nW'' = Q_aW(0) - n\Phi''K(0) + Q_b, \tag{2.24}$$

where

$$Q_a = 4\pi n[(\rho'' + p'') + \lambda''(\rho+p)], \tag{2.25}$$

$$\begin{aligned}Q_b = {} & [(n+1)\Phi'' - \omega^2 e^{-2\Phi}]H_1(0) + (\omega^2 e^{-2\Phi} - \Phi'')K(0) \\ & - [8\pi\omega^2 e^{-2\Phi}(\rho+p)V(0) - p''W(0)],\end{aligned} \tag{2.26}$$

$n = (l+2)(l-1)/2$, and Γ_c is the central value of Γ. Here we drop the subscript of c for the ease of presentation, which should not raise a risk of confusion.

In addition, the first-order constraints imposed on these functions by the perturbation equations are

$$H_1(0) = \frac{2lK(0) + 16\pi(\rho_c + p_c)W(0)}{l(l+1)}, \qquad V(0) = -\frac{W(0)}{l}, \qquad H_0(0) = K(0), \tag{2.27}$$

indicating there are only two free parameters K_0 and W_0 to specify a solution. Following [111], we fix $W(0) = 1$ and solve the equation set twice with $K_0 = \pm(\rho_c + p_c)$. On the other hand, the vanishing pressure perturbation at the surface leads to the boundary condition $X(R) = 0$ from (2.9).

For a given trial frequency, we solve the equations (2.13)-(2.17) from the centre and surface towards a matching point at r_m. For the region of $0 \le r \le r_m$, there are two linearly

independent solutions from the initial values we feed in, while there are three for the other region. We linearly superpose the solutions in each region such that the values match at r_m. In practice, we compute the equilibrium adiabatic index self-consistently from the pressure and density profile, then we use 4-th order Runge-Kutta (RK4) method to integrate Eqs. (2.13)-(2.17). Since RK4 algorithm needs to evaluate functions between two grids, namely $f(r_i+h/2)$ where f is the function appearing as a coefficient in Eqs. (2.13)-(2.17) and $h = r_{i+1} - r_i$ is the grid size, we extrapolate linearly the functions at points between two grids.

In general, eigenfunctions of the perturbation equations consist of outgoing and incoming components at spatial infinity, whereas those identified as a stellar quasi-normal mode should possess no incoming component. The ratio between incoming and outgoing waves can be determined by the values of Zerilli functions at the surface as explained in the following. In the exterior of the star, material perturbations (W, V and/or X) are absent, while two metric perturbations H_1 and K remain relevant. Instead of solving the asymptotic values of metric perturbations directly, we introduce the Zerilli function $Z(r)$, and consider also its derivative with respect to the tortoise coordinate, defined by

$$\frac{d}{dr_*} = \left(1 - \frac{2M_\star}{r}\right)\frac{d}{dr}, \tag{2.28}$$

where $M_\star$ is the stellar mass. Both Z and dZ/dr_* are a linear combination of H_1 and K (see, e.g., Eq. (A27) of [110]), and the equations for H_1 and K can be translated to a simple function for $Z(r)$, given by

$$\left[\frac{d^2}{dr_*^2} + [\varpi^2 - V(r)]\right] Z = 0, \quad \text{for} \quad V(r) = 2\left(1 - \frac{2M_\star}{r}\right)\frac{n^2(n+1)r^3 + 3n^2M_\star r^2 + 9nM_\star^2 r + 9M_\star^3}{r^3(nr+3M_\star)^2}. \tag{2.29}$$

In order to match to the interior solution, we rephrase the above equation so as to get rid of the derivative with respect to the tortoise coordinate. In particular, we consider an auxiliary function Ψ, defined through

$$\Psi = \left(1 - \frac{2M_\star}{r}\right)^{1/2} Z, \tag{2.30}$$

which recast Eq. (2.29) to

$$\left(\frac{d^2}{dr^2} + U(r)\right)\Psi = 0, \quad \text{with} \quad U(r) = \left(1 - \frac{2M_\star}{r}\right)^{-2}\left[\omega^2 - V(r) + \frac{2M_\star}{r^3} - \frac{3M_\star^2}{r^4}\right]. \tag{2.31}$$

The Wronskian of any two linearly independent solutions to Eq. (2.31) can be shown to

be a constant, which allows for expressing them as [113, 114]

$$\psi^{\pm} = q^{-1/2} \exp\left[\pm i \int q dr\right] \tag{2.32}$$

for some function $q(r)$ satisfying (see Eq. (18) of [114])

$$\frac{1}{2q}\frac{d^2q}{dr^2} - \frac{3}{4q^2}\left(\frac{dq}{dr}\right)^2 + q^2 - U = 0. \tag{2.33}$$

The general solution to Eq. (2.31) is therefore

$$\Psi = A_{\rm in}\psi^{+} + A_{\rm out}\psi^{-}. \tag{2.34}$$

Without lost of generality we can set the lower bound of the phase integral in Eq. (2.32) to be the stellar radius $R_\star$, thus $\Psi(R_\star) = (A_{\rm in} + A_{\rm out})q^{-1/2}(R_\star)$. The ratio between $A_{\rm in}$ and $A_{\rm out}$ is [114]

$$\frac{A_{\rm out}}{A_{\rm in}} = \frac{Z_s(1-2M_\star/R_\star)[iq - (1/2q)(dq/dr)] - M_\star/R_\star^2 - Z_s'}{Z_s(1-2M_\star/R_\star)[iq + (1/2q)(dq/dr)] + M_\star/R_\star^2 + Z_s'} \tag{2.35}$$

for $Z_s = Z(R_\star)$ and $Z_s^{'} = (dZ/dr_*)(R_\star)$. The poles of this ratio are then related to quasi-normal modes.

Chapter 3

g-mode asteroseismology

Contents

Breakdown of Contributions

The computations are derived by me, and the figures are produced by me. The code for computing g-mode frequencies are modified from a previous code of Kostas D. Kokkotas. Christian J. Krüger helps generate the g-mode spectra for thermalised neutron stars to help justify the parameter we introduced to capture the thermally-supported g-modes. My contribution in paper-writing is to pen the manuscript, based on which Arthur G. Suvorov helps polish. At each stage of this work, Kostas D. Kokkotas assists with discussion and provides critical comments on the manuscript.

Overview

Buoyancy-restored modes inside neutron stars depend sensitively on both the microphysical (e.g., composition and entropy gradients) and macrophysical (e.g., stellar mass and radius) properties of the star. Asteroseismology efforts for g-modes are therefore particularly promising avenues for recovering information concerning the nuclear equation of state. In this work it is shown that the overall low-temperature g-space consists of multiple groups corresponding to different classes of equation of state (e.g., hadronic vs. hybrid). This is in contrast to the case of pressure-driven modes, for example, which tend to follow a universal relation

regardless of microphysical considerations. Using a wide library of currently-viable equations of state, perturbations of static, stratified stars are calculated in general relativity to demonstrate in particular how g-space groupings can be classified according to the mean mass density, temperature, central speed of sound, and tidal deformability. Considering present and future observations regarding gravitational waves, accretion outbursts, quasi-periodic oscillations, and precursor flashes from gamma-ray bursts, it is shown how one might determine which group the g-modes belong to.

3.1 Introduction

Neutron stars (NSs), with their extremely high core densities, reside in an otherwise hard-to-realise region of the QCD phase diagram. The details of the (supra-)nuclear equation of state (EOS) can only be accessed by connecting their observed outbursts or manifestations with, for example, theoretical predictions of the quasi-normal mode (QNM) spectrum, the maximal supportable mass, and gravitational radiation. Although substantial progress regarding constraints on the EOS from, e.g., the tidal deformability measured by the phase shift in the gravitational waveform for merging binaries [22, 115, 116] and observations of the moments of inertia [117], have been made in the literature, uncertainties remain and a wide pool of possibilities remain viable. Universal relations between certain stellar properties, however, offer additional avenues that are EOS-independent to infer inaccessible unknowns, and thus can indirectly narrow the space of valid candidate descriptions for the stellar interior.

In particular, the QNM spectrum of a NS is strongly associated with the global properties of the star, in the sense that several universal expressions relating mode frequencies and/or damping times to the bulk quantities of the star, like average density, moment of inertia, and tidal Love number, have been established for the f-, p-, and w-modes [118–123]. This EOS-insensitive information provides hope for independent constraints by offering a critical tool in rephrasing the detected quantities in terms of others. For example, the mutual tidal deformability of a not-too-massive NSNS binary equates, in a roughly one-to-one fashion, into a compactness of the long-lived remnant because the f-mode properties of both the pre-merging and post-merger stars follow the same universal relation [67]. To account for the compositional structure, universal relations for g-modes, which distinguish one chemical configuration from another, need to be established.

In this article, we aim to introduce some global formulae for g-modes of NSs in various configurations and at various stages of their lives, either isolated or in binaries. The frequencies of this class of oscillatory modes are encoded in the Brunt-Väisälä frequency, which measures the mismatch in the adiabatic index between the equilibrium and the mode-driven motions (see, e.g., [124]). Using the (non-isentropic) general-relativistic pulsation equations, one of our main results is that we can encapsulate the Brunt-Väisälä frequency into *the*

temperature-modified mean density of the star, and draw a relation to the g-mode frequency, viz.

$$f_g \propto \rho_{\text{mean}}^{(1-\varsigma)/2} T, \tag{3.1}$$

for some EOS- and mode-number-dependent constant $-0.7 \lesssim \varsigma \lesssim 0.5$ (see Sec. II). We also obtain two invertible mappings for the g-mode frequencies in terms of the *central speed of sound*, v_s, and *tidal deformability*, Λ, expressed as

$$\log\left(\frac{f_{g_1}}{100\ \text{Hz}} M\right) = \sum_{i=0}^{3} a_i (\log \Lambda)^i, \tag{3.2}$$

$$\frac{f_{g_1}}{100\ \text{Hz}}\left(\frac{v_s}{R}\right) = \sum_{i=0}^{3} b_i (\rho_{\text{mean}})^{i/2}, \tag{3.3}$$

with certain coefficients $\{a_i\}$ and $\{b_i\}$, stellar mass M, and radius R. Importantly, the first relation (3.1) divides EOS into three quotient sets, and introduces the concept of *g-space*, which characterises a specific EOS in terms of the g-mode spectrum. This occurs essentially because ς takes values in different blocks for different EOS families in a sense that is made precise in the main text. By representing a (hypothetically) observed g-mode as a point in g-space, we can, in principle, place constraints on the associated EOS for a wide range of systems including pulsars, progenitors of binary mergers, and the remnants of mergers. On the other hand, the latter two relations (3.2) and (3.3) are common for the set of twenty EOS considered in this article (i.e., the a_i and b_i are roughly constant among EOS). Leveraging this universality, we can deduce certain otherwise inaccessible quantities from g-mode observables.

Although still a matter of debate, it has been suggested that various NS phenomena may be triggered by the excitation of g-modes. For instance, a small percentage of short gamma-ray bursts display precursor phenomena [38, 125], where energetic flashes are observed even many seconds prior to the main event in some cases. If the stellar oscillation modes briefly come into resonance with the orbital motion while the stars are inspiralling, significant amounts of tidal energy may be deposited into the mode(s), possibly to the point that the crust yields due to the exerted shear stresses exceeding the elastic maximum [39, 40]. g-modes in particular appear to lie in a sweet-spot, frequency wise, where the expected mode frequencies match the orbital frequency at the time of the precursor flashes (Chap. 4). Similarly, g-mode frequencies match those observed in quasi-periodic oscillations (QPOs) of X-ray light curve from several NS systems and thus provide another promising avenue for detecting g-modes (see, e.g., [70] for such speculation).

In addition, a new and quite important asteroseismological relation emerged through this

study connecting the f-mode frequency f_f, with the radius and tidal deformability of an oscillating neutron star

$$\log\left(\frac{f_f}{\text{kHz}}R\right) = \sum_{i=0}^{2} c_i (\log\Lambda)^i \,. \tag{3.4}$$

This relation can be considered as complementary to the one by [120].

This Chapter is organised as follows. We first introduce the stellar structure that will be relevant throughout the Part I of the present thesis in Sec. 2.1, and the existence of g-mode in the stellar QNM spectrum is justified in Sec. 3.2. The grouping of EOS in terms of the range of g-mode frequencies, and we discuss the tidal effects of g-modes in Section 3.1. We then turn to investigate the uniformity among the EOS set considered, producing some universal relations of g-modes in Section 3.3. We speculate some circumstances, where we may be able to detect g-mode frequencies in Section 3.4. A discussion on the possible application of the obtained results is offered in Section 3.5. Some EOS are found to allow for NSs with g-modes immune to external tidal field, which is discussed in Appendix A.

Except where stated otherwise, we adopt in this Chapter the normalisation of 10 km $=$ $1 = 1\ M_\odot$ for the mass and the radius of stars, and we reduce the dimension of velocity by unitising the speed of light, $c = 1$.

3.2 g-mode grouping

In general, QNMs are categorised according to the nature of the restoring force. For example, $p-$modes are supported by pressure, while g-modes are supported by buoyancy: Inhomogeneities in composition and/or temperature give rise to stellar stratification and buoyancy as gravity tends to smooth out these gradients [50, 53, 126, 127]. Explicitly, stratification prevents the Schwarzschild discriminant,

$$A := e^{-\lambda}\frac{dp}{dr}\frac{1}{p}\left(\frac{1}{\gamma} - \frac{1}{\Gamma}\right), \tag{3.5}$$

from vanishing. The parameter Γ represents the adiabatic index of the *perturbation*, which need not match that of the background for non-isentropic perturbations [128].

The polytropic (adiabatic) index of the star expresses the pressure exerted by a bulk of certain density, and depends on the detailed thermodynamic balance, chemical composition, and degeneracy status of the system [129]. However, weak interactions (e.g., Urca processes) and/or diffusive processes within the star modulate the relative particle abundances over time [130, 131], leading to entropy [50, 127] and/or compositional gradients [53]. These variations permit mobile fluid elements to experience buoyancy whenever perturbed away equilibrium, giving rise to the existence of g-modes. The frequencies of these modes therefore depend

strongly on the strength of the stratification. In principle, one could determine δ from first principles by calculating the sound speed and the determinant of the Brunt-Väisälä frequency from the nuclear Hamiltonian together with the Gibbs equation describing the evolution of the chemical composition [124, 127]. However, here we approximate the cold EOS as barotropic, i.e., $p = p(\rho)$, which erases the compositional information in practice. The composition and thermal gradients, which offers buoyancy for g-modes, is therefore, strictly speaking, absent. The artificial parameter Γ is used as a proxy for perturbation-induced changes in the chemical potentials and/or temperature resulting from a *non-adiabatic* perturbation. In addition, as shown by [132], NSs are in general stably stratified due to the interior equilibrium composition gradient, implying $A < 0$ inside the star (i.e. $\gamma < \Gamma$). We thus consider positive δ hereafter.

Aiming to provide a proof-of-principle framework in the present thesis, we assume that the adiabatic indices for the perturbation (Γ) and the equilibrium (γ) have a constant ratio $1 + \delta$, viz.

$$\Gamma = \gamma(1 + \delta), \tag{3.6}$$

which provides a simple parameterisation for the forces supporting g-modes; see Chap. 4 for a discussion on the validity of this approximation. We identify δ with the temperature T of isothermal stars in Sec. 3.2.1. Although we find that the correlation between δ and T holds only for $T \lesssim 10^{10}$ K, we show the validity of the justification for binaries undergoing the tidal heating of g-modes Sec. 3.2.2. Respect to the simple parametrisation of stratification, three divisions of EOS are illustrated in Sec. 3.2.3. Overtones are denoted by g_n-mode, for which the radial eigenfunction has n nodes.

The numerical calculation of the complex $g-$mode frequencies is known to be difficult because $|1/\tau_\alpha| \ll |\omega_\alpha|$, meaning that high precision is necessary to prevent errors in the real parts contaminating the imaginary parts, as discussed by [133]. Searching for low-frequency g-modes and their respective eigenfunctions entails a delicate separation of the ingoing- and outgoing-waves at spatial infinity, so that one can impose the purely outgoing boundary condition[1]. Techniques based on *phase integrals* have been proven to be adequate for this purpose [114]. On top of that, the minute displacements of $g-$modes, which is translated from eigenfunctions, make the differential system of the eigenproblem put forward by [110, 111] inappropriate for solving $g-$modes. The issue for these long-lived modes (due to their small imaginary components) has been addressed in [112] by solving a slightly different set of differential equations (see also [133]). In this work we adopt the combined algorithm of [114] and [112] to compute $g-$modes (see Appendix for details). Our code is capable of determining the real parts of mode frequencies to within a tolerance of ~ 10 Hz. Shown in Fig. 3.1 are the radial displacement ξ^r for the first five g-modes of a particular star.

[1] Solutions to the perturbation equations include those of purely ingoing- and outgoing-waves, and even the hybrid waves. However, only those pulsate energy outward, i.e., purely outgoing ones, are physically realised [134].

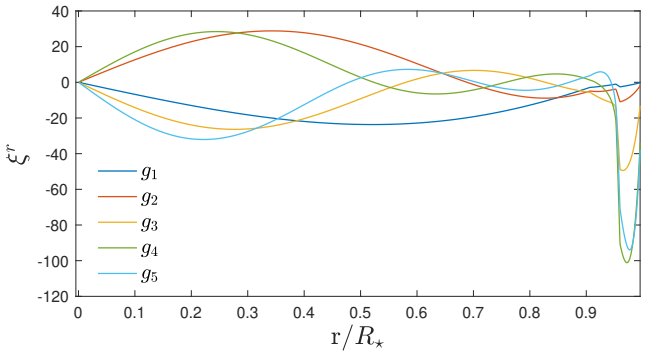

Figure 3.1: Normalized radial displacement ξ^r for the $n = 1 - 5$, $l = 2$, g-modes of the star with EOS SLy, $M_\star = 1.27 M_\odot$, and $\delta = 0.005$.

It has been shown that the f-mode frequency of a given star is largely determined by the square root of its mean density,

$$\rho_{\rm mean} = \frac{M}{\frac{4}{3}\pi R^3}, \tag{3.7}$$

over a plethora of EOS for non-rotating NSs [135] and for (rapidly-)rotating NSs [121]; therefore, the eigenfrequencies of $f-$modes can be inferred by the square root of the mean density of the background star and vice versa [119, 136, 137]. Similar relations have been found for other modes also [118, 138, 139]. In particular, though restricted to polytropic EOS, [140] found universal relations between the frequencies of $l = 2$, g_1-modes and the strength of stratification (i.e., δ in our notation). Similar to [140], we find a similar empirical relation but augmented with a dependence on stratification, given by

$$\omega_g/\sqrt{\delta} \propto \rho_{\rm mean}^{(1-\varsigma)/2}, \tag{3.8}$$

for quadrupolar (l=2) g_1-, g_2-, and g_3-modes in stars having mass larger than $1 M_\odot$ for a variety of EOS. Here ς is the fitting parameter[2] is collated in Table 3.1, which varies for different EOS, while the proportionality constant depends on the mode quantum numbers for fixed overtone numbers (g_1-, g_2-, ...) as well as the EOS. However, despite this dependence, we find that it behaves in a quantitatively similar manner between different EOS groups (see Sec. 3.2.3). Furthermore, the fact that g_1- to g_3-modes follow the same relation indicates that the ratio between their frequencies can be approximated by a constant, e.g., we find that (though in Chap. 5 we will have a more accurate treatment of the relations between the frequencies of g_1- and g_2-modes)

$$\omega_{g_2}/\omega_{g_1} \simeq 0.68 \tag{3.9}$$

[2]For the polytropic EOS studied in [140], the corresponding constant is $\varsigma = 0.5$ — it is lower for realistic EOS.

for every EOS considered.

3.2.1 Temperature dependence

We consider EOS to be barotropic at the background level as stated before, hence g-modes are supported by the entropy gradient. In general, the temperature profile of NSs in different systems can differ significantly. For instance, mature, isolated NSs are expected to be almost isothermal [112] (with the notable exception of magnetars, where the decaying magnetic field may provide an internal heat source [141]), while NSs in binaries [142], post-merger NS remnants [143, 144], and especially accreting pulsars [141, 145, 146] can have spatially-dependent temperature profiles that span several orders of magnitude. The resultant position-dependent thermal pressure makes the ratio between the effective adiabatic index of the equilibrium and that for the perturbation a function of position.

For mature NSs, the temperature is typically low enough to allow the appearance of solid crust, superfluid core, and superconductivity of protons. Taking the multilayer complexity in full, g-modes can be distinguished into two classes, viz. core and crust g-modes, depending on the configuration of the rendered motions [51, 52]. For instance, the radial motion caused by a crust g-mode will be viscously-quenched at the crust-core interface, leading to only slight perturbations in the crust. The mode frequencies for both classes will acquire some modifications by the inclusion of superfluidity, which tends to increase the frequencies of crust g-modes. Nonetheless, we do not take the multilayer influences on the spectrum into account as the first step to reveal the trifurcation of EOS in terms of g-modes.

Assuming single component fluid NSs, the justification for δ introduced above may then be obtained by separating the contribution of the thermal pressure,

$$p^x_{\rm th} = \frac{\pi^2}{6}\frac{n_x}{E^x_F}(kT)^2, \tag{3.10}$$

in the perturbation equations used to solve for QNMs, where $\mathrm{x} = \{\mathrm{n}, \mathrm{p}, ...\}$ runs over the different constituents of the fluid. Here $p^{\rm x}_{\rm th}$ represents the thermal pressure provided by the species x, whose Fermi energy is $E^{\rm x}_F$. In particular, the thermal pressure contributes to the linearised equations of the radial and the tangential displacements (cf. Eqs. (B3) and (B4) of [112]), which replace the term γp for NSs, where thermal gradients are absent, with (cf. Eq. (B5) of [112])

$$\Gamma p := \gamma p + \sum_{x=n,p} \frac{\partial p^x_{\rm th}}{\partial n_x} n_x = \gamma(1+\delta)p \tag{3.11}$$

where

$$\delta = \left[\frac{k^2\pi^2}{6}\sum_{x=n,p}(E_F^x)^{-1}\right]T^2 \tag{3.12}$$

is proportional to T^2. Although this implies that Eq. (3.8) can be translated to

$$\omega \propto \rho_{\rm mean}^{(1-\varsigma)/2}T \tag{3.13}$$

if the NS is isothermal, such a parameterisation needs to be justified for an inhomogeneous temperature profile. To evaluate the reliability of Eq. (3.13) for a NS with more general temperature distribution, we have compared the mode frequencies in isothermal stars with the cases of stars with radial temperature profiles that fall by one to two orders of magnitude from centre to the surface by using the code described in [112]. In particular, we solve for the frequencies of the g_1-mode for a particular stellar model with the following temperature profiles (in the unit of K):

1. isothermal with $\log T = \{10, 9.5, 9\}$;
2. falling temperature by an order of magnitude as approaching the surface from the temperature at the center being $\log T = \{11, 10\}$;
3. fixing surface temperature as $\log T = 9$, temperature falls by more than one order of magnitude from a central temperature of $\log T = \{11, 10.8, 10.6, 10.4, 10.2, 10\}$

where the falling temperatures profiles are such that the temperature decreases linearly with the radius on a logarithmic temperature scale. As such, those profiles are highly artificial and given the multitude of different cooling and heating mechanisms operating inside a neutron star it would be difficult, and beyond the scope of the present work, to reproduce a realistic temperature profile. However, as we argue below, the most important part of the temperature profile is only that close to the surface of the star and since we are mostly interested in a qualitative understanding of temperature-related effects, such a simply constructed temperature distribution suits our needs.

We found that the spectrum of NSs with the same surface temperature differs only slightly among the above three scenarios, indicating that, to leading order, the QNM spectrum is unaffected by the temperature gradient except in extreme circumstances (cf. the case of proto-neutron stars discussed by [61]; see also [63]). This finding makes sense as the thermal pressure $p_{\rm th}$ is a function quadratic in the temperature; being causal for the buoyancy, it can compete with the static pressure, which grows substantially toward the center of the star, only in the outer regions of the star and, hence, the surface temperature is the primary quantity to determine the g-mode spectrum of a star. This argument also tells us that the shell below the surface which impacts the g-mode spectrum grows in depth with increasing

surface temperature. We do observe this effect: Linearity between f and T was observed for $T \lesssim 10^{10}$ K, and a more complicated pattern arises only for $T > 10^{10}$ K.

3.2.2 Tidal Heating

For stars within compact binaries permitting "tidally-neutral g-modes" (see Appendix A for details), mode-related tidal effects are dominated by the non-resonant f-mode until merger. Resonant g-modes may contribute to the tidal effects comparable to f-mode for stars whose g-modes are tidally-susceptible, e.g., the produced stress may cause crust yielding (Sec. 4.5; see also [147]), and the heating via shear viscosity may be as important as that resulting from the f-mode [124]. For the latter heating process, we find that the energy absorbed into the star via g-modes up to g_{16}-mode[3] can amount to $E_{\rm kin} \sim 10^{43}$ erg for binaries consisting of identical components, where the kinetic energy of each mode acquired during the tidal excitation is consistent within a factor of ~ 5 with the stationary-phase-approximated formula (see Eq. (6.11) in [124]),

$$E_{nl} \simeq 9.70 \times 10^{42} \left(\frac{\rho_{\rm mean}}{0.49}\right)^{-1} \left(\frac{f_{nl}}{100\ {\rm Hz}}\right)^{1/3} \left(\frac{Q_{ln}}{10^{-5}}\right)^{2} {\rm erg}. \tag{3.14}$$

A portion of the mechanical energy will be converted into thermal energy via viscosity [124, 149] mainly provided by lepton shear viscosity when $T < 10^9$ K [cf. Fig. (1) of [150] and also [151]], and chemical reactions, such as direct or modified Urca processes [152]. To set an upper limit for the heating effect, we assume the whole energy budget deposited by the finite series of g-modes is converted into thermal energy through the aforementioned channels; consequently, NSs will be heated up to a temperature

$$T \simeq 4.7 \times 10^{6} \left(\frac{E_{\rm kin}}{10^{43}\ {\rm erg}}\right)^{1/2} {\rm K}, \tag{3.15}$$

by equating the dissipated energy to the heat content U of NSs [124, 152], which related to the averaged temperature over the core via (Eq. (8.28) in [124])

$$U \simeq 4.5 \times 10^{45} \left(\frac{T}{10^{8}\ {\rm K}}\right)^{2} {\rm erg}. \tag{3.16}$$

Although f-mode excitation may also extract orbital energy thus attributing to the tidal heating, the amount of the kinetic energy is estimated to be comparable to the gross value of g-modes [124]. The square root dependence of the temperature to the kinetic energy, as expressed in Eq. (3.15), therefore indicates the resultant temperature will be of the same

[3] We note that $\sim$ 80% of the energy budget is deposited by g_1-g_5 modes. In addition, there is a caveat that high order g-modes, whose oscillatory period are smaller than the timescale of the involved reaction rate, are likely swept off from the spectrum [148].

Table 3.1: Fitting index ς defined in Eq. (3.8) for a variety of EOS. Although there are a few outliers, we see that those listed in the first column have $\varsigma \gtrsim 0.2$, the second column features the range 0-0.2, and in the final column are $\varsigma \lesssim 0$.

Group I		Group II		Group III	
EOS	ς	EOS	ς	EOS	ς
APR4[a]	0.413	SLy[f]	0.158	H4[j]	-0.094
MPA1[b]	0.321	WFF3[d]	0.027	H7[j]	-0.221
MS1[c]	0.266	FPS[g]	0.011	GNH3[k]	-0.081
MS1b[c]	0.333	BBB2[h]	0.101	PAL6[l]	0.059
WFF1[d]	0.453	APR1[a]	0.128	PCL2[m]	-0.309
WFF2[d]	0.461	BHF[h]	0.143	ALF2[n]	-0.657
ENG[e]	0.179	KDE0V[i]	0.200		

[a] [155]. [b] [156]. [c] [157]. [d] [158]. [e] [159]. [f] [160]. [g] [161]. [h] [162]. [i] [163]. [j] [164]. [k] [165]. [l] [166]. [m] [167]. [n] [168].

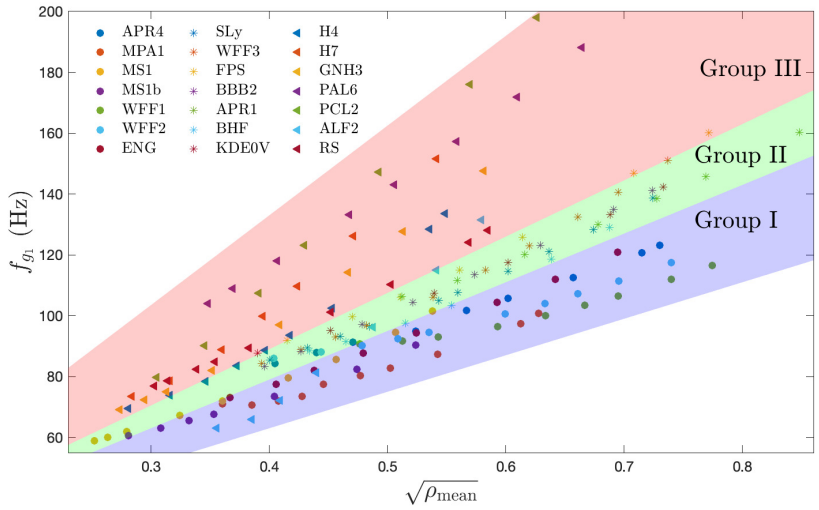

Figure 3.2: g-mode frequency for $\delta = 0.005$ as a function of the square root of the mean density, $\sqrt{\rho_{\rm mean}}$, for each of the EOS under study. The circles represent those models drawn with solid line in Fig. 2.1, the asterisks pair the dashed-line EOS, and the triangles correspond to the dash-dot EOS.

order, which is cold enough not only for the appropriateness of our implementation of cold EOS, but for the justification of $\delta \propto T^2$.

We note that the above temperature may be too cold to admit g_1-mode with frequency of $\gtrsim$ 100 Hz since we estimate the heating effect for non-spinning NSs. For the rotating stars, r-modes, even f-mode, may undergo a period of resonance [153,154] thus soaking more energy in expense of orbital one to heat further the star.

3.2.3 Three Groups

In Eq. (3.8), the exponent is determined as follows: for a certain value of ς, a least-squares fitting is applied to $f_g/\sqrt{\delta}$ and $\rho_{\rm mean}^{(1-\varsigma)/2}$, from which we calculate the correlation coefficient; we then define the parameter to be the value of ς that maximises the correlation coefficient. We collate the fitting parameters ς in Tab. 3.1. We see that ς can be divided into three ranges

(with a few outliers): $\gtrsim 0.2$ (*Group I*; first column), $\sim$ 0–0.2 (*Group II*; second column), and $\lesssim 0$ (*Group III*; final column). The width of the 95% confidence interval of ς for each EOS is $\lesssim 0.01$, indicating the grouping presented here is statistically sharp. The three divisions intriguingly correspond to EOS consisting of only hadronic matters that can support heavy stars of mass $\gtrsim 2.12M_\odot$ or more (Group I), those that cannot (Group II; $\lesssim 2.07M_\odot$ or less), and EOS involving phase transitions leading to either hyperon condensation or quark deconfinement (Group III). We note that the considered EOS of Group III cannot support stars much heavier than $\sim 2M_\odot$. The two peculiar EOS are ENG and PAL6; the first is an outlier of *Group I* with $\varsigma < 0.2$, while the latter EOS is an exception of *Group III* since it has a positive ς and the matter consists of hadrons. This slight mixing between Group III and the others is not entirely surprising, since first-order transitions in EOS that only support relatively light stars will not play a big role. In general, we see that the mass-radius relation is 'flattened' with decreasing ς, and becomes a one-to-one mapping when $\varsigma \lesssim 0.2$ except for the Group I EOS ENG and the Group III EOS ALF2. A natural question about this grouping is whether they are classified by "softness"? While this may be a general trend it is not absolute since, for example, the stiffest EOS are MS1 and MS1b, which are in Group I, while members in Group III tend to be stiffer than those in the other two groups.

We illustrate the nature of the groups by plotting the g-mode frequency for a fixed δ as a function of (the square root of) $\rho_{\rm mean}$ in Fig. 3.2, where the different markers are used to indicate the different correlations between the range of ς. For instance, EOS for which $\varsigma \gtrsim 0.2$ (group I) are represented by solid circles. One observes that the g-mode frequencies even of very stiff EOS like MS1 and MS1b align well [in the sense of Eq. (3.8)] with other EOS of Group I, especially when the difference in the radius for NSs with a fixed mass among these EOS can be as large as 1.5 times (between WFF1 and MS1). This observation is similar for respective members of the other two groups, clearly indicating that global parameters associated with the EOS are not the only factor in contributing to g-modes. On the other hand, it has been shown that g-modes in proto-NS following a core collapse, which may be detected in the near future by third generation detectors [62, 169], tend to obey a universal relation, and there is no obvious partition (see, e.g., Fig. (2) in [61]). The absence of grouping in proto-NSs may arise for two reasons: (i) they have very high temperature, likely indicating that they are thermally-stratified to the degree that $\delta \gtrsim 1$ (for which the correlation we find between T and δ may no longer hold), and thus the situation may be different from cold NSs (see Sec. 3.2.3 for the discussion on valid range of the introduced parameter δ); (ii) the EOS families that have been previously considered in this context may incidentally belong to the same branch. Although beyond the scope of this paper, it would be worth revisiting g-mode studies in proto-NS with a wider EOS library to investigate these points.

Cold NSs with similar bulk properties display universal relations between the f-, p- and w-modes, indicating the particulars of internal structure does not impact these modes much [118,

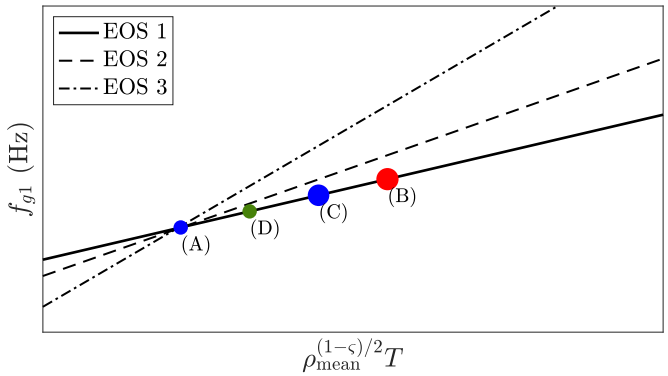

Figure 3.3: Symbolic *g-space* (see main text for the definition) for three EOS – one from each group, and four hypothetical observations. The chosen EOS trifurcates around a certain point in the space, so that all three branches can explain observation (A). However, suppose that, for demonstration purposes, Group I (EOS 1) governs NS from different systems (and thus passes through each observation). The member(s) in Group II (EOS 2) can fit the observation in system (A), and may be able to explain observation (D) depending on the error bars of the measurement, though are incapable of matching the data for (C) or (B). The group III case (EOS 3), by contrast, is unable to explain any observation except (A).

121–123]. However, the compositional content of NSs, which is to a large extent unknown, will substantially affect the g-mode spectrum. The uncertainty in the internal physics, on top of the various methods and/or assumptions adopted to model the nuclear interactions, leads to the richness in variations of EOS candidates; the grouping we observe therefore indicates that microphysical considerations can be broadly categorised into three channels, each leading to a family of g-modes in Fig. 3.2. For instance, the constituents in the core depend on their evolution track since certain cooling/reaction channels have density-dependent activation thresholds. In addition, atomic abundances in the crust may vary from system to system, depending on their birth site [170,171]. Crustal variations are unlikely to considerably modify the *core* g-mode spectrum however, and thus would not be responsible for the grouping.

Due to the limited precision of any given observation, it is likely that we can only distinguish one family of EOS from another rather than two EOS in the same family. If it happens that there are two phenomena caused by g-modes, and these are found to reside in different groups, it might imply that the NSs have followed a different evolutionary track as far as the EOS is concerned. Nonetheless, if we assume that a certain functional EOS applies to NSs in different systems, such as binaries and long-lived remnants of mergers, these compact objects will belong to the same line (solid line in Fig. 3.3) describing the g-mode frequency as a function of $\rho_{\rm mean}^{(1-\varsigma)/2}T$, just at different stages. Defining the g-space as the set consisting of the g_n-mode frequencies that can be possessed by at least one star with this EOS, we indicatively draw the g_1-space in Fig. 3.3 for EOS 1-3, each belongs to Group I-III, respectively. The observations of several events can therefore be incorporated to provide a mutual constraint on the EOS candidates (see below) but in a manner that is distinct from Bayesian analyses, where various observations shape the prior of the parameterization of EOS differently to

gradually reduce the viable region for EOS candidates (see, e.g., [172–174]). We note that in a formal, Bayesian analysis, this common EOS assumption will shape the (informative) prior of model parameters differently than the situation when the assumption is absent, thus affecting the statistical inference [144].

As an illustrative example, we consider the particular combination of systems; (A) represents a NS in a binary undergoing the inspiral, (B) stands for a newly-born NS from merger after the temperature has dropped sufficiently to validate Eq. (3.13) and differential rotation has largely stabilised[4], and (C) denotes an old, long-lived remnant from an NS merger, with finally a less-compact version in (D) (see also below). Each type of observation from different NSs is designated as a point in the space spanned by f_{g_1} and $\rho_{\rm mean}^{(1-\varsigma)/2}T$, and the solid line connecting these three points indicates a hypothetical case where one EOS "branch" satisfies (A)-(D). We see that the lines for different groups diverge, but with only one measurement point (A), one cannot tell which line it is unless some additional observations are available; branches can be ruled out by incorporating the multi-stage information across (A) to (C), depending on the relative error bars on the measurements. Nonetheless, we emphasise that the above analysis surrounding Fig. 3.3 does not necessarily reflect the reality. Instead, it is simply a demonstration of the idea.

In order to map a certain system onto the g-space, the mean density, which implies we are able to probe the mass and radius to certain extent, and volume-averaged temperature, must be known. Although certain constraints can already be set by the simultaneous determinations of the mass and the radius by, e.g., marking a valid region on the mass-radius diagram for EOS, there will still be a bunch of EOS surviving such restriction if the radius has even small error bars (e.g., [178,179]). Information from the g-mode frequency can, in such cases, provide additional constraints of a different flavour. Considering a NS with a canonical mass of $1.5M_\odot$ and a radius of $11-12$ km (corresponding to $\sqrt{\rho_{\rm mean}}=0.46-0.52$), for example, several members of Group I and II are adequate in terms of the mass and the radius observations, viz. APR4, MPA1, WFF2, SLy, WFF3, FPS, KDE0V, and BBB2 (though considering higher mass or more compact stars reduces the pool; [179]). Some of these EOS will be ruled out if f_{g_1} can be acquired; for instance, $f_{g_1}\lesssim 80$ Hz will exclude ones belonging to Group II thus making a 62.5% reduction in the aforementioned EOS candidates (see. Fig. 3.2).

To observe a given system on the g_1-space, there must be some phenomena attributed to its g_1-mode. The candidate systems allowing for g-mode measurement will be discussed in Sec. 3.4, where we consider electromagnetic precursor flares prior to merger (Sec. 3.4.1), and quasi-periodic oscillations (QPOs) in the X-ray light curves of accreting millisecond X-ray pulsars (AMXPs; Sec. 3.4.2).

[4] A NS remnant from a merger forms in a differentially-rotating state, and is likely to be highly magnetised due to the Kelvin-Helmholtz instability occurring at the shear boundary formed upon the contact of the two progenitors [175]. The non-uniform rotation will wind the field lines and is thought to produce a turbulent viscosity however, which diffuses the angular momentum from the fast to slow regions, thus unifying the rotation profile (or at least confining it to vary only along flux lines in accord with the axisymmetric Ferraro theorem) in just a few tens of milliseconds [176,177].

3.3 Universal relations

In addition to the EOS-dependent relation (3.8) [or Eq. (3.13)], we provide three EOS insensitive relations bearing g-mode frequencies to f-mode frequency, dimensionless tidal deformability Λ (Sec. 3.3.1), and the central speed of sound (Sec. 3.3.2), respectively. These relations offer extra means not only to distinguish EOS groups, but to extract information on the properties of NSs from gravitational- and/or electromagnetic-radiation observations. We consider hereafter only EOS of Group I and II, pondering that these are favoured by precursor events (see the discussion near the end of Sec. 3.4.1).

3.3.1 Gravitational Waves

In the analysis of GW waveform, the chirp mass,

$$\mathcal{M} = \frac{(M_1 M_2)^{3/5}}{(M_1 + M_2)^{1/5}} \tag{3.17}$$

of the system can be determined to a relatively high precision since it enters the phase evolution at the lowest post-Newtonian order [19, 180]. Although not with the same level of accuracy, the symmetric mass ratio,

$$\eta = \frac{M_1 M_2}{(M_1 + M_2)^2}, \tag{3.18}$$

can also be obtained by exploiting its post-Newtonian order contribution to the GW phase (see, e.g., Eq. (32) in [20]). Therefore, the individual masses M_1 and M_2 can be estimated from $\mathcal{M}$ and η. In addition, a detailed extraction of the phase shift $\delta\Psi = \delta\Psi_{\rm eq} + \delta\Psi_{\rm dyn}$ may shed light on both equilibrium and dynamical tidal effects [181], for which the mutual, dimensional tidal deformability [12, 77],

$$\tilde{\Lambda} = \frac{16}{13}\frac{(M_1 + 12M_2)M_1^4\Lambda_1 + (M_2 + 12M_1)M_2^4\Lambda_2}{(M_1 + M_2)^5}, \tag{3.19}$$

is the agency of the former, and the latter is mainly produced by the late stage growth of f-mode [78, 80, 182]. Here $\Lambda_{1(2)}$ is the tidal deformability of the primary (companion). With observables $\mathcal{M}$, η, and $\tilde{\Lambda}$, we get a relation for Λ_1 and Λ_2, and the masses M_1 and M_2 though with certain error. However, the uncertainty of EOS involved in such analysis has a ramification on measuring stellar properties, which can be mitigated by implementing EOS-insensitive relations.

Although there are several universal relations in hand, most of them pertain to properties of individual NSs, such as I-Love-Q relation [183], and can only become useful when the mass ratio between two components of a binary is provided. We, therefore, are seeking a scheme

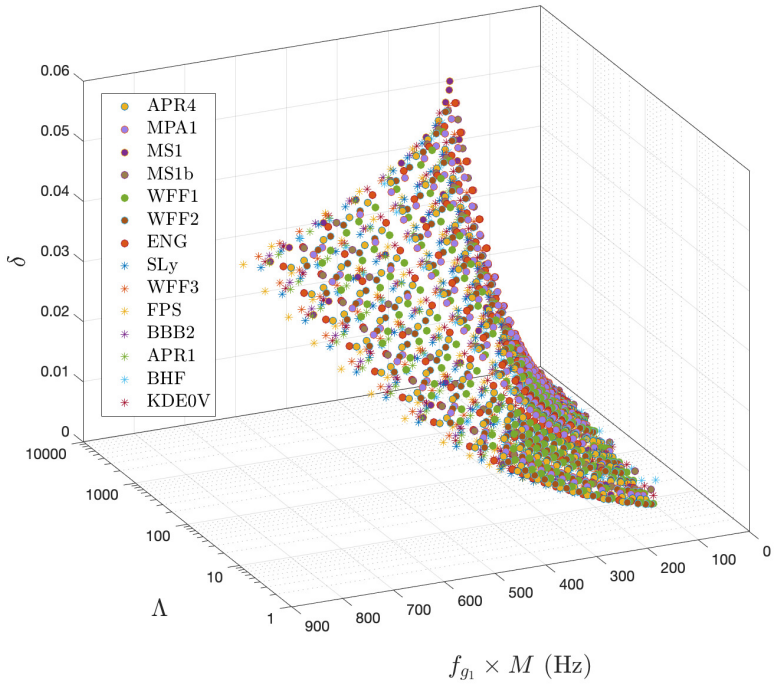

Figure 3.4: Three-dimensional universal relation among mass-scaled g_1-mode frequency, the tidal deformability, and the stratification for EOS in Group I and II.

to obtain the properties of individual star from the observables without the *a prior* input of the mass ratio. We illustrate that with g-mode frequency obtained from electromagnetic observations, e.g., the timing of precursors (Sec. 4.6.1), such methodology can be established.

In Fig. 3.4 we show a universal sheet associating the g_1-mode frequency, the tidal deformability, and the stratification. The caveat of this relation is that δ may be identified with different temperature for different EOS; therefore, it may not be useful even the temperature can be observed or estimated. To circumvent this dilemma, we can count on an additional information of g_2-mode, whose frequency is linearly correlated with that of g_1-mode through

$$f_{g_1} = a_0 + a_1 f_{g_2}, \tag{3.20}$$

where the coefficients a_0 and a_1 are found to be rather insensitive with δ, e.g., $a_0 = 4.3162$ and $a_1 = 0.620$ for $\delta = 0.005$, and $a_0 = 5.7221$ and $a_1 = 0.623$ for $\delta = 0.01$. Nonetheless, the difference $f_{g_1} - f_{g_2}$ depends strongly on δ thus limiting δ to a certain range if the frequencies of these two modes can be observed. One of the possible scenario, where such detection is plausible, is precursor flares of SGRBs, and we will give a concrete example in Sec. 3.4.1 of limiting the range of δ via the frequency difference.

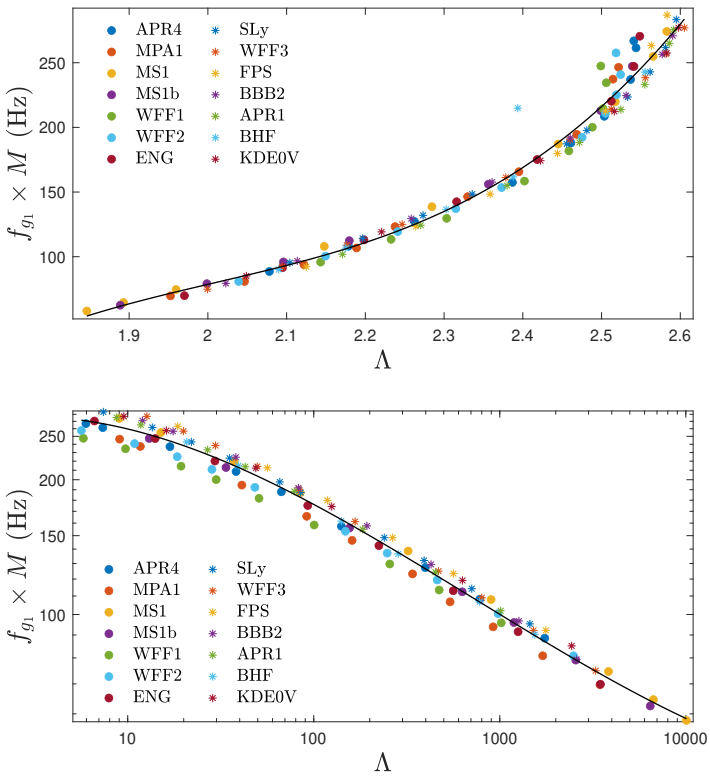

Figure 3.5: Universal relations for the EOS considered here: the mass-scaled g_1-mode frequency as a function of the radius-scaled f-mode frequency (top panel), and the compactness-scaled g_1-mode frequency as a function of Λ (bottom panel).

Denoting $\delta_5 = \delta/0.005$, we plot as the solid line the universal behaviour,

$$\frac{f_{g_1}}{100\ \text{Hz}}\frac{M}{\sqrt{\delta_5}} = -48.641 + 70.782\left(\frac{f_f}{1\ \text{kHz}}R\right) - 34.426\left(\frac{f_f}{1\ \text{kHz}}R\right)^2 + 5.695\left(\frac{f_f}{1\ \text{kHz}}R\right)^3, \tag{3.21}$$

relating the radius-scaled f-mode frequency and the mass-scaled g_1-mode frequency in the top panel of Fig. 3.5. The above equation suggests that the quantity of g_1-mode frequency divided by $\sqrt{\delta_5}$ depends on the global quantities of the star given f-mode frequencies strongly correlated to the mean density, which matches to the indication of Eq. (3.8). Although the relation is valid for, as far as we have checked, $0.001 \leq \delta \leq 0.05$, we present only the results for $\delta_5 = 1$ (coloured dots) in Fig. 3.5 for ease of presentation. In the bottom panel, we plot a certain section of the sheet in Fig. 3.4, which shows a bearing on dimensionless tidal deformability via the relation (solid line),

$$\log\left(\frac{f_{g_1}}{100\ \text{Hz}}\frac{M}{\sqrt{\delta_5}}\right) = 0.411 + 0.106\log\Lambda - 0.126(\log\Lambda)^2 + 0.015(\log\Lambda)^3. \tag{3.22}$$

Here the individual quantity Λ must not be confused with the observed mutual deformability $\tilde{\Lambda}$. Additionally, there has been a relation between the mass-scaled f-mode frequency and Λ proposed by [120], which reads

$$\log\left(\frac{f_f}{\text{kHz}}M\right) = 0.814 - 0.050(\log\Lambda) - 0.035(\log\Lambda)^2, \tag{3.23}$$

for the EOS considered here. We note that Eqs. (3.21) and (3.22) are invertible maps over the domains of interest, suggesting a one-to-one relation connecting $f_f \times R$ and $\log\Lambda$. Despite the fact that inverting these two equations and then using the common factor $f_{g_1} \times M$ to parametrically fit $f_f \times R$ and $\log\Lambda$ can establish such a relation, we instead directly establish a fitting formula between the data, given by

$$\log\left(\frac{f_f}{\text{kHz}}R\right) = 0.409 + 0.013(\log\Lambda) - 0.013(\log\Lambda)^2, \tag{3.24}$$

which can be viewed as an equivalent of Eq. (3.23), and both are shown in Fig. 3.6. Combining above relations (3.22) and (3.23), the ratio between the frequencies of f- and g_1-modes can be expressed as a function of Λ, given by

$$\log\left(\frac{f_{g_1}/\sqrt{\delta_5}}{f_f}\right) = -1.403 + 0.156(\log\Lambda) - 0.091(\log\Lambda)^2 + 0.015(\log\Lambda)^3. \tag{3.25}$$

The aforementioned relations are powerful in rephrasing observables in terms of unobservable but important quantities. Stipulating that we get individual masses from the mea-

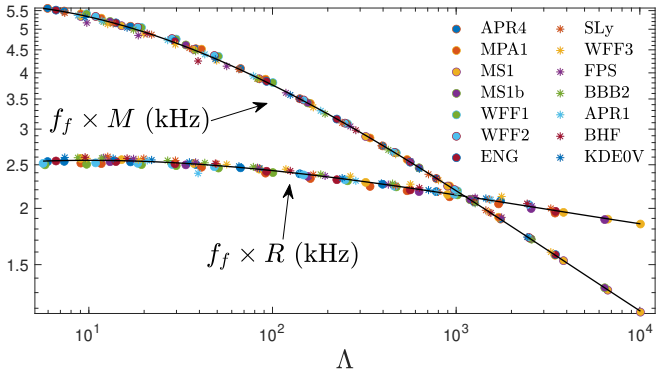

Figure 3.6: Universal relations established in [120] relating the mass-scaled f-mode frequency to Λ, and relation (3.24) associating the radius-scaled f-mode frequency to Λ, for the EOS considered here.

surements of the chirp mass and the symmetric mass ratio (see below), and the frequency of g_1-mode of the primary from, e.g., precursor observations, we can deduce the individual deformability Λ_1 from Eq. (3.22). Subsequently, Eq. (3.23) translates the mass into f_f of the primary, which then returns the radius R_1 via Eq. (3.21). If we also have knowledge of the mutual tidal deformability, the companion's individual deformability Λ_2 can be obtained which, together its mass, gives the secondary's f-mode frequency via Eq. (3.23). Accordingly, Eq. (3.25) provides an estimate on the g_1-mode frequency of the companion, which, combined with aforementioned companion properties, returns the radius through Eq. (3.21).

In reality, the measurements of η, $\tilde{\Lambda}$, and $\mathcal{M}$ all come with error, though the uncertainty on $\mathcal{M}$ is typically smaller than the others (see, e.g., [19,184]). On top of the above, an uncertainty of ~ 10 Hz in f_{g_1} could also be expected, which effectively translates into error bars for the temperature. All these errors will be reflected in the predictions of Eqs. (3.21)-(3.25). As a specific example, we assume $f_{g_1} = 100 \pm 10$ Hz, and adopt the chirp mass $\mathcal{M} = 1.167$ with $\eta = 0.242 - 0.25$ and the mutual tidal deformability $\tilde{\Lambda} = 200 - 800$ of a GW170817-like binary (e.g., [116,185]) in Fig. 3.7, where the derived tidal deformability of the primary (top panel) and the companion (bottom panel) are plotted for $0.005 \leq \delta \leq 0.01$. Here the blue lines represent the stratification $\delta = 0.005$, typical for mature NSs in coalescing binaries [e.g., [154]], while the red lines depict a relatively large $\delta = 0.01$, which may be realised in heated stars (achieved, e.g., through close, tidal interaction or accretion). The mid point, $\delta = 0.0075$, is plotted as orange lines. The region bounded by the lines encapsulates the possible range. We first look at the influence of δ by taking, for instance, $\eta = 0.25$, $\tilde{\Lambda} = 800$, and $f_{g_1} = 100$ Hz. We find for the primary $\Lambda_1 = 692.72^{+552.47}_{-389.44}$, $R_1 = 1.55^{+0.42}_{-0.44}$, and $f_f = 1829.31^{-256.62}_{+394.23}$ Hz, while $\Lambda_2 = 907.28^{-552.47}_{+389.44}$, $R_2 = 1.26^{-0.20}_{+0.09}$, and $f_f = 1708.63^{+454.48}_{-152.89}$ Hz for the companion, where the values correspond to $\delta = 0.0075$ with the superscript (subscript) associated to $\delta = 0.01$ ($\delta = 0.005$).

Among the uncertainties in $\mathcal{M}$, η, and $\tilde{\Lambda}$, the latter is the most significant since it is

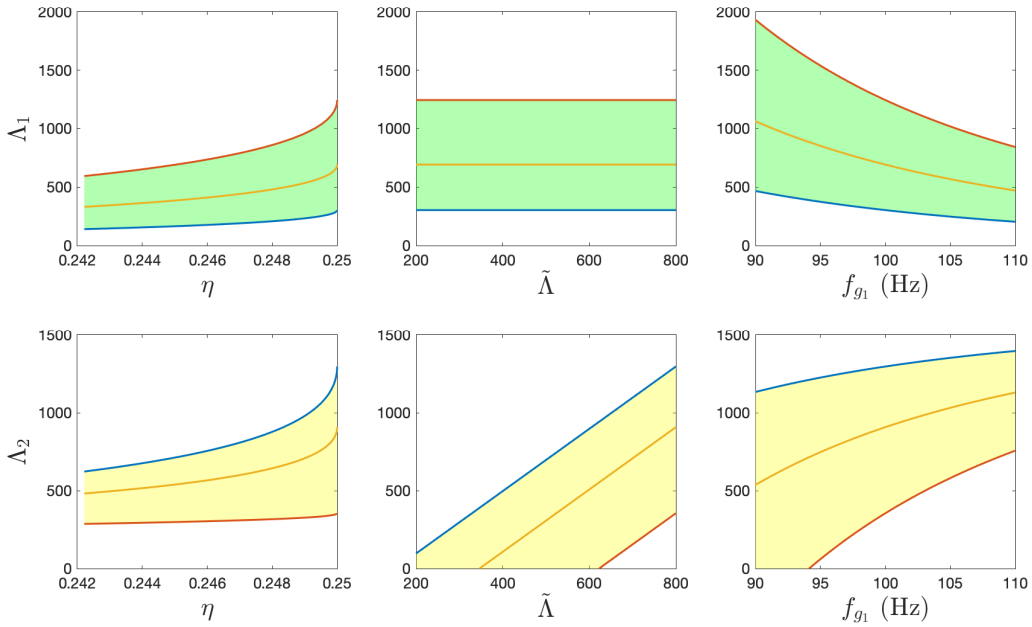

Figure 3.7: Inferred, individual tidal deformability of the primary (top panel) and the companion (bottom panel), determined via Eqs. (3.21)-(3.23), using a fixed value of $\mathcal{M} = 1.167$. The width of each band is due to an assumed uncertainty in the stratification δ. Three specific δ are plotted as solid lines on the shaded area: $\delta = 0.005$ (blue lines), typical for mature NSs, $\delta = 0.01$ (red lines), which may be relevant if the star is heated by some processes (see the main text), and a mid-point stratification $\delta = 0.0075$ (orange lines). In each cell, one of η, $\tilde{\Lambda}$, and f_{g_1} is varied (as per the horizontal axis) while the other two are fixed at $\eta = 0.25$, $\tilde{\Lambda} = 800$, and $f_{g_1} = 100$ Hz.

extracted from 5-th post-Newtonian (PN) order effects in the gravitational waveform [75,76], which leaves a smaller imprint than the Newtonian-order parameter $\mathcal{M}$ and 1PN parameter η. Although in our scheme, the large uncertainty in the mutual tidal deformability does not alter the inference of the parameters of the primary if the g_1-mode frequency and the masses of the NSs are well-constrained (see, e.g., the second column in the top panel of Fig. 3.7), the inferred properties of the companion are affected considerably. For example, $\Lambda_2 = 97$–1297 and $R_2 = 0.86$–1.36 correspond to this error given $\eta = 0.25$, $f_{g_1} = 100$ Hz, $\delta = 0.005$, and the above parameters of the primary. Physically speaking, this is because we attribute a g-mode to the primary and not the secondary, so that less information is obtained about the latter using the formulae derived here. In addition, the predictions are sensitive to η and f_{g_1} as illustrated in Fig. 3.7, where the inferred tidal deformability can drop by 50% from symmetric case ($\eta = 0.25$) to a mildly asymmetric case with $\eta = 0.242$. On the other hand, they can increase by a factor of two if the g_1-mode frequency of the primary is $f_{g_1} = 90$ Hz instead of 110 Hz.

Although the individual masses M_1 and M_2 can be determined by the chirp mass and the symmetric mass ratio measurements, with an error mainly due to the latter [see, e.g., Sec. 5 and 6 of [20] for a discussion], the radii of constituents can not be easily constrained. The g-mode methodology, however, can additionally determine the radii of binary members with high accuracy if the temperature is modest. As the radius of NSs with a mass of $1.4M_\odot$ still spans a range of 11–13 km for EOS candidates that pass the observations [e.g., [186–189]], such a novel way to measure the radius may therefore constitute a valuable tool in whittling down the pool of currently-viable EOS.

On top of this arguably already executable application of universal relations, we speculate on the possibility of detecting, though indirectly, the f-mode frequency from the accumulation of phase, $\delta\Phi_{\rm dyn}$. This is expected to be a plausible with detectors in the near future. In particular, f_f of the progenitors of GW 170817 may be determined to within tens of Hz with the Einstein Telescope [181].

The determination of f_f has a double-dose of implications. Firstly, incorporation of Eqs. (3.21)-(3.23) results in an "on-shell" (physically realisable) condition of $M(R)$ if f_f and f_{g_1} are provided. In Fig. 3.8, we overlap the "on-shell" $M(R)$ to the mass-to-radius diagram of the EOS considered here for the typical values of $f_f = 2 - 2.2$ kHz and $f_g = 80 - 120$ Hz. Here the solid line corresponding to $f_f = 2$ kHz and $f_{g_1} = 100$ Hz. Secondly, we can know simultaneously the mean density due to its universal relation with f-mode frequency [120,121]. According to the derived mean density and the g_1-mode frequency, we can represent the NS on Fig. 3.2, and thereby sift the branch of EOS for this system. We note that even for binaries without precursors, f_{g_1} can be determined through Eq. (3.22) if the tidal deformability Λ is measured.

Another scenario where these EOS-insensitive expressions are particularly helpful is black

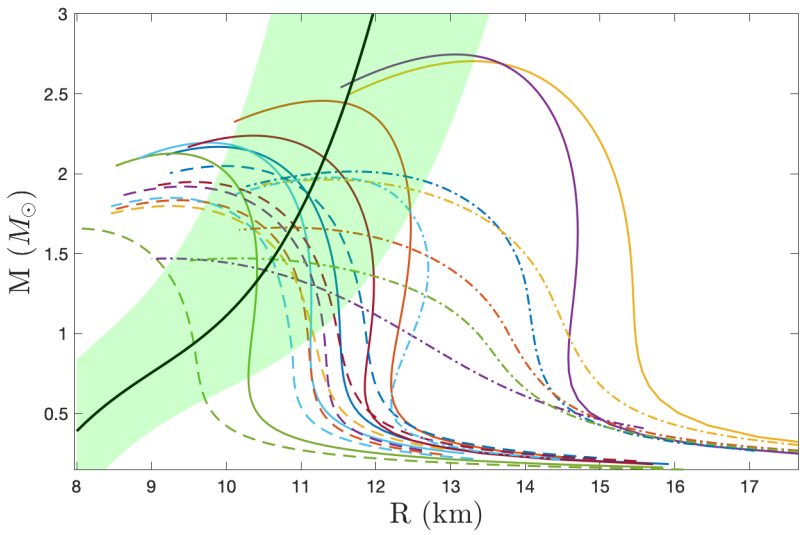

Figure 3.8: The curves same in Fig. 2.1 overlapped with Eq. (3.21). The solid line stands for the case with $f_f = 2.2$ kHz and $f_{g_1} = 100$ Hz, and the shaded area corresponds to the range of $f_f = 2 - 2.4$ kHz and $f_{g_1} = 80 - 120$ Hz.

hole-NS binaries since the individual tidal deformability equals to the mutual one, which is an observable, thus activating the Eqs. (3.22)-(3.25) without the additional processing translating observables to Λ.

3.3.2 Speed of sound

The measurement of g_1-mode can be translated into the central sound speed of the equilibrium via the strong correlation,

$$\frac{f_{g_1}/\sqrt{\delta_5}}{100\ \text{Hz}}\left(\frac{v_s}{R}\right) = 0.124 - 0.296\rho_{\text{mean}}^{0.5} + 1.685\rho_{\text{mean}} + 1.442\rho_{\text{mean}}^{1.5}, \tag{3.26}$$

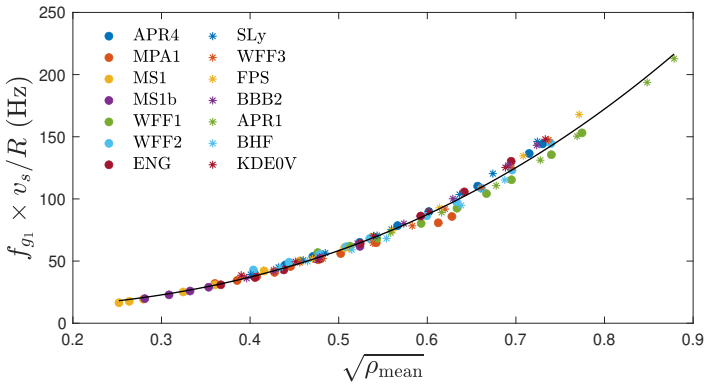

Figure 3.9: Rescaled g_1-mode frequency as a function of ρ_{mean} for the EOS considered here, with v_s being the central sound speed.

shown as the solid black line in Fig. 3.9. Given that the stiffness of a EOS can be characterised by the maximum sound speed [190], this central value may be informative enough for shedding light on the stiffness of the EOS since the sound speed culminates at the center. The stiffness of EOS affects the bulk properties of NSs, such as the maximum mass that is supportable with the EOS [191, 192], and the tidal deformability [190, 193]; therefore, the constraint on the stiffness may be translated to either the upper or the lower bound for the sound speed. For instance, the lower bound of sound speed should be larger than $\sqrt{6}$ if the secondary of the binary hosting GW 190814 is a NS [194]. In the light of the constraint set by GW 170817, the determination of the stiffness can augment the GW channel to limit viable EOS. Another aspect of utilising the speed of sound to benefit astrophysics can be found in, e.g., [195], where the authors build a family of nuclear interactions in terms of the behaviour of v_s, thus the inferred v_s from Eq. (3.25) limits the EOS model.

3.4 *g*-mode candidate systems

To better utilise the universal relations involving g-modes developed in the present article, we propose some candidate systems where g-mode detection may be plausible.

3.4.1 Precursor flares

For the NS progenitor of a merger, it has been proposed that mode resonance(s) may trigger precursor flashes of the SGRB following the merger, notably via interface- [39, 40] and g-modes (Chap. 4) for slow-rotating NSs, and f- and/or r-modes for fast-spinning NSs [41]. The uncertainties in both the spin rate of NS progenitors and the jet formation timescale of the main episode allow for candidates of several kinds of mode, where the former quantity shifts the mode frequency relative to the orbital frequency inferred from the occurrence of precursors, and the latter timescale blurs the amount of time prior to the merger[5].

Seeing that NSs in coalescing binaries are expected to be mature and thus slowly rotating, we shall examine in Chap. 5 in detail how two precursor flares (associated, for example, with GRB 090510 [34]) can be accommodated by the lowest two orders of either g-modes or interface-modes. In there, we find that the indicated spin rate of the host NS is $\lesssim 50$ Hz for the former modes (see also below), while $\ll 10$ Hz is suggested by the latter modes. Nevertheless, we emphasise here that we restrict ourselves to the g-mode resonance scenario (Chap. 4), but other (e.g., i-mode) possibilities exist [39, 40]. The timing of precursors thus allows one to infer the (inertial-frame) frequency of the relevant mode, given by

$$\omega \simeq \omega_0 - 0.89 m \Omega_{\rm s} \tag{3.27}$$

[5] Precursors can only be timed relative to the main burst by definition, which occurs only some time after the merger since jet formation is not instantaneous, but has a development timescale that depends on its formation mechanism (see Sec. II. A of [41] for a discussion).

when the stellar magnetic field strength is small ($B \lesssim 10^{14}$ G), where ω_0 is the free mode frequency (i.e., the frequency not accounting for tidal modulations to stellar structure), $\Omega_{\rm s}$ is the spin rate of the star, and m is the winding number of the mode [Eq. (4.61)]. The numerical factor 0.89 arises by considering leading-order corrections in the slow-rotation approximation, though is also, in principle, sensitive to the compactness of the star [Fig. 4.9].

For the specific case of SGRB 090510, the two precursors are detected when $\Omega_{\rm orb} \approx 160$ Hz and $\Omega_{\rm orb} \approx 510$ Hz, respectively. If they are attributed to $l = m = 2$ g_1- and g_2-modes of the star, we obtain the equalities

$$\omega_{g_1} - 1.78\Omega_{\rm s} = 510 \text{ Hz}, \quad \text{and} \quad \omega_{g_2} - 1.78\Omega_{\rm s} = 160 \text{ Hz}, \tag{3.28}$$

associating with the frequencies of the g_1- and g_2-modes of the primary. The notation $\omega = 2\pi f$ gives the angular frequency for linear frequency f. Exploiting the fact that the ratio between the frequencies of g_1- and g_2-modes is roughly a constant, viz. $\omega_{g_2}/\omega_{g_1} \simeq 0.68$ [Eq. (3.9)], regardless the EOS and δ, we deduce that $\omega_{g_1} = 174 \times 2\pi$ Hz, $\omega_{g_2} = 118 \times 2\pi$ Hz, and $\Omega_{\rm s} = 52.2 \times 2\pi$ Hz. The g_1-mode frequency can set a lower bound for δ since ω_1 is smaller for decreasing δ. In addition, although the ratio $\omega_{g_2}/\omega_{g_1}$ varies only slightly with respect to EOS and δ, the difference $\omega_{g_1} - \omega_{g_2}$ requires δ to fall in certain range resulted from its dependence on δ, as well as EOS. For instance, the difference of $\omega_{g_1} - \omega_{g_2} = 55.7 \times 2\pi$ Hz here restrains the stratification to be $0.008 \lesssim \delta \lesssim 0.2$ for EOS APR4, and $0.006 \lesssim \delta \lesssim 0.44$ for EOS ENG.

We should emphasise that aforementioned requirements for ω_{g_1}, ω_{g_2}, and δ are the necessary conditions for these two g-modes to be responsible for precursors; the sufficient condition is that the mode amplitude can be resonantly excited beyond certain threshold value. It turns out the necessary and sufficient requirements are stringent for stellar parameters, and the viable region on the parameter space is expected to be narrow [see Chap. 4 for a thorough discussion]. Nonetheless, we note that the EOS of Group I are favoured in igniting precursors with moderately massive or light stars. Although the g-mode resonance in the quite massive ($\gtrsim 2M_\odot$) or light ($\sim 1M_\odot$) stars for the EOS of Group II are possible to fuel these early flares, it is unlikely that stars with EOS of Group III can host such pre-emissions.

In addition, the inferred g_1-mode is close to 200 Hz, which is marginally high in terms of its typical value ~ 100 Hz. The tidal heating resulted from g- and f-modes investigated in Sec. 3.2.2 may pose a tension between the realisability of such frequency. Nonetheless, it is possible for a spinning NS to have low amplitude r-mode excitations, which may not slow down the star but still heat up the material to make the NS hot enough to admit such g-modes.

3.4.2 Quasi-periodic oscillations

Apart from the possibility of precursor flashes observed prior to merger events, there have not yet been direct g-mode observations in neutron stars, either of the nascent or mature variety. It has, however, been speculated by [70] that g-modes may be responsible for the QPOs observed in the X-ray light curves of accreting millisecond X-ray pulsars (AMXPs). While it is unclear which particular modes may be responsible in these cases (and indeed it is usually thought that *disk* g-modes may be responsible rather than *stellar* g-modes), it is necessary that their (inertial-frame) frequency matches that was observed, which is theoretically possible for the class of g-modes considered here.

We take XTE J1751-305 and XTE J1807-294 as examples since their QPO frequencies lie in the range of interest (i.e., $\lesssim$ 400 Hz). Although there are other possibilities, r- and g-modes are candidates for matching to these frequencies [70–72]. The excitation of the former modes would generally be expected to sap angular momentum from the star also, especially if they are driven CFS unstable. However, at least for the specific outburst observed in XTE J1751-305, it is likely that if r-modes were responsible, the spin-up behaviour of the star following the first X-ray pulse in 2002 (the small variation in the flux is only observed in this stage) would have been lower [71], which brings g-modes to our attention. Nevertheless, we emphasise that the trigger mechanism for QPOs is not well-established, and we consider g-modes in this context to demonstrate how one may phenomenologically pin the pulsar in the g_1-space given an observation. The above-described scenario is represented by point (D) in Fig. 3.3.

According to Eq. (3.13), the mass, the radius, and the temperature of stars must be known in order to mark them on the g-space. Although we can deduce the mean density of two AMXPs, viz. the range of 0.919-1.214 for[6] XTE J1751-305 [71], and the range of 0.499-1.425 for XTE J1807-294 [196], the lack of the knowledge of their temperature prevent us from locating them on *g-space*. To better utilise the tool of g-space, future measurement of the temperature is crucial.

3.5 Discussion

In this article we investigate the dependence of g-mode frequencies on both microscopic (e.g., local changes in the adiabatic index) and macroscopic (e.g., stellar compactness) physics, revealing three families of EOS which still somehow support a number of universal relations. In particular, we found that g-mode frequencies correlate to the temperature-modified mean density to the power of a parameter ς [Eq. (3.13)], where the range of ς divides EOS considered

[6] Note that this density is inferred from the calculations in [71], who operated under the assumption that an r-mode was responsible for the outburst event, and it is therefore, strictly speaking, inconsistent to use their values in a g-mode analysis here. We adopt these values however to offer a proof-of-principle.

here (Tab. 3.1). This empirical fitting formulae define the *g-space*, where a given point corresponds to a unique EOS, which is split into three bands depending on ς. Given some observations, from, e.g., precursors and QPOs, points can be pinned down in the *g-space* to scrutinise the EOS candidate (Fig. 3.3). Although joint constraints have been studied via Bayesian analysis in, e.g., [172–174], our approach here is not interlaced with uncertainties in the prior of the parameterisation of the EOS. In addition, the appliance of Eq. (3.13) to g_1- to g_3-modes implies that the ratios between any two of them are roughly constant. Furthermore, if we are able to measure both g_1- and g_2-modes in a NS, e.g., from two precursors in a SGRB (the double events in GRB090510 may serve as an example Sec. 4.6), we can measure the spin of the star within some tolerance by solving Eq. (3.28).

On top of the trifurcation, universal dependences of g-modes can be found in terms of certain quantities [Eqs. (3.21)-(3.23)]. These EOS insensitive information can aid in placing constraints on EOS without *a priori* knowledge of the EOS. We show the universal sheet among the g_1-mode frequency, the tidal deformability, the stratification, and the mass of NSs (Fig. 3.4). Although inferring δ in a certain system is non-trivial, some estimates will be possible if we can measure additionally ω_{g2}. For a particular value of δ, a specific section of the universal sheet will be picked up; assuming a typical value $\delta = 0.005$, we reduce the sheet to Eq. (3.21). For this δ, we also establish the relation between f_{g_1}, M, and Λ [Eq. (3.22)]. Three prospective applications of the above universal relations can be summarised as:

1. Assuming we can measure $\mathcal{M}$, η, $\tilde{\Lambda}$, and f_{g_1}: the mass M, the radius R, and the f-mode frequency f_f can be inferred from Eqs. (3.21)-(3.23). The particular case of GW 170817 is discussed in Sec. 3.3.1.

2. Assuming we can measure the f- and g_1-modes: a region of feasible models can be drawn on the mass-to-radius diagram (Fig. 3.8); such measurements are expected to be plausible with near-future detectors.

3. Given Λ and the f-mode frequency: the g_1-mode value f_{g_1} can be extracted via Eq. (3.25). In addition, the strong correlation between f_f and $\rho_{\rm mean}$ gives an estimate of the latter quantity, which delegates f_{g_1} on a certain region in Fig. 3.2, thus picking a certain group of EOS for the system.

Besides the global quantities, Eq. (3.26) sheds light on the central sound speed if the radius and the g_1-mode frequency are available. Seeing that the central sound speed of the NSs near the EOS-related maximal mass reflects the "stiffness" of EOS, this indicates another aspect to disfavour certain range of "stiffness" other than the analysis having been done to GW 170817, which is based on the measurement of $\tilde{\Lambda}$ [22].

In addition, universal relations may also be leveraged to pin down observations on g-space if we can maneuver out of the observables the mass, radius, and temperature of NSs. As a naïve example, we consider the remnant of merger. The transcendental information

associating the tidal deformability of the *progenitors* of mergers to the compactness of the long-lived *remnant* (cf. Eq. (4) and Fig. 9 of [67]) says that we can learn the compactness of the remnant $\mathcal{C}_{\rm rem}$ from the measurement of $\tilde{\Lambda}$. In addition, the f-mode frequency of the remnant, $f_{f,\rm rem}$, may be measured from its influence on SGRB photon counts following the merger since the jet opening angle may widen and shorten as the star oscillates [197]. Envisaging we have $f_{f,\rm rem}$ and $\mathcal{C}_{\rm rem}$, the five stellar parameters $f_{g_1,\rm rem}$, $f_{f,\rm rem}$, $M_{\rm rem}$, $R_{\rm rem}$, and $\Lambda_{\rm rem}$ of the remnant can be calculated by mutually solving Eqs. (3.21)-(3.23). This information suffices to pin the system down in g-space within some tolerance.

To make further use of g-mode asteroseismology via the universal relations, we point out two possible avenues for detecting g-modes via electromagnetic sector, viz. the pre-emissions of SGRBs (Sec. 3.4.1) and (more speculatively) the QPOs in the X-ray light curve of AMXPs (Sec. 3.4.2). If the temperature in these systems can be measured somehow with future observatories (e.g., phase-resolved hot spot tracking for the latter), including the merger remnants, the g-mode ansatz introduced in this work, as well as the universal relations provided here, can be readily applied to place constraints on the EOS by identifying observations on *g-space*, as demonstrated in Fig. 3.3.

Chapter 4

Tidally-driven Shattering Flares in Coalescing Binary Neutron Stars

Contents

Breakdown of Contributions

The code for solving stellar quasi-normal modes for (slow) rotating and/or magnetising, relativistic neutron stars is extended by me from the previous code of Kostas D. Kokkotas, which was designed for non-rotating and non-magnetising relativistic stars. The perturbing forces and the associated frequency shifts they caused are derived by me, while the dipolar magnetic field configuration is derived by Arthur G. Suvorov. All the plots are produced by me. I have penned the manuscript, upon which Arthur G. Suvorov helps polish and performs final edition. Kostas D. Kokkotas offers meticulous comments throughout every stages of this work.

Overview

During the final stages of a NS binary coalescence, stellar QNMs can become resonantly excited by tidal fields. If the strain exerted by the excited modes exceeds the extent to

which the crust can respond linearly, localised crustal failures may occur. In this Chapter, we re-examine resonant mode excitations of relativistic NSs in the last ~ 10 seconds of an inspiral with an emphasise placed on g-modes. We adopt realistic EOS that pass constraints from GW170817, include 3rd order post-Newtonian (PN) terms for the conservation orbital motion, and employ a 2.5 PN scheme for gravitational back-reaction. Frequency modulations of the modes due to tidal fields, Lorentz forces, and (slow) rotation are also considered to investigate the maximal strain achievable by resonantly-excited g-modes. Depending on the EOS, degree of stratification, and stellar magnetic field, we find that certain g-modes excitations may be able to break the crust some seconds prior to coalescence. The crust yielding releases the energy used to be stored in the cracking area, which may constitute flares in the inspiralling stage if the NS is highly magnetised, i.e., magnetar.

For few SGRBs, precursor flares occurring $\sim$ seconds prior to the main episode have been observed. These flares may then be associated with the last few cycles of the inspiral when the orbital frequency is a few hundred Hz. During these final cycles, tidally-driven QNM resonances in the inspiralling stars, leading to a rapid increase in their amplitude. It has been shown that these modes can exert sufficiently strong strains onto the NS crust to instigate yieldings. Due to the typical frequencies of g-modes being ~ 100 Hz, their resonances with the orbital frequency match the precursor timings and warrant further investigation. Solving the general-relativistic pulsation equations and the evolutionary equations for binaries, we study g-mode resonances in coalescing quasi-circular binaries. We show that the resonantly excited g_1- and g_2-modes may lead to crustal failure and trigger precursor flares for some combination of stellar parameters, viz. certain particulars of stellar rotation rates, degrees of stratification, and magnetic field structures. One indication on the stellar spin can be maneuvered out from systems exhibiting double precursors if we attribute these pre-emissions to g-mode excitations; this aspect will be elucidated in Chap. 5.

4.1 Introduction

Tidal effects in compact binary systems containing at least one NS may be studied by both electromagnetic and GW measurements [12, 23, 24]. Such studies allow one to probe the fundamental properties of the progenitor NSs, such as the EOS [22, 198]. In the final stages of a merger, orbital energy and stellar internal energy are redistributed efficiently by tidal force(s) and dissipation. The former excites stellar QNMs, leading to the transfer of orbital energy into excited modes, thus leaving certain imprints into the orbit evolution (e.g., accelerating coalescence and causing shifts in the GW phase by $f-$mode excitations [199, 200]). The latter, resulting from viscosity, damps the excited modes, turning kinetic energy into thermal energy, which can heat up the star to $\sim 10^8$ K before merger [124]. In particular, when the tidal-perturbing frequency matches the eigenfrequency of a particular QNM at some point

prior to merging, the mode becomes resonantly excited. The amplitudes of resonantly-excited modes increase rapidly as a consequence of their ability to efficiently absorb orbital energy over a resonance timescale. If a certain mode is driven so strongly that the resultant strain exceeds a critical value such that the crystalline structure of the crust can no longer respond linearly, a crustal failure may occur [45, 46, 49]. On the other hand, the external tidal field contributed by the companion star deforms the shape of the primary, inducing a quadrupole moment and certain crustal stress (see, e.g., Equations (64) and (65) of [201]). In the final stage of inspiralling, the tidal field becomes tremendous and distorts the star to an extent that may lead to crustal failure (e.g., [202]), though the yielding resulting from this process can occur only within $\lesssim 10^2$ ms prior to the merger [39, 203, 204].

Generally speaking, if the stress exerted on the stellar surface exceeds the maximum that the elastic crust can support, a yielding may be expected. The crust failure then liberates charged particles that are accelerated to form ejecta by induction-generated electric fields. The outflow interacts with the surrounding medium, eventually leading to the conversion of magnetic energy flux into radiation [205–207]. It has been suggested that localised failure events offer a possible mechanism [39, 41, 147] to trigger 'precursor' events of SGRBs [34], which are commonly defined as bursts having 90% of their photon count detected with $T_{90} \lesssim 2$ s [208], and are thought to result from compact object mergers involving at least one NS [209–212]. Since precursors are observed to have a non-thermal spectrum [34, 37] , (at least one of) the inspiralling stars should be highly magnetised ($B \gg 10^{13}$) so that the energy can be efficiently transported via Alfvén waves [39, 206]. Further credence is given to this scenario because magnetar birth rates [213] coincide with the recent estimates on the proportion of SGRBs preceded by at least one precursor flare [34, 36, 125]. Additionally, in light of the relative time difference of precursors to the main episodes, which ranges from a few hundred milliseconds to a few tens of seconds prior to the main episode (see Tab. 4.2), the aforementioned equilibrium tidal effects are seemingly not capable of accommodating the observed precursors. In view of these points, mode excitations in magnetars are worth exploring as they may be the central engine for these precursors [34, 39, 41].

At the non-rotating level[1], the QNMs of NSs can be generally resolved into p-, f-, w-, and g-modes. Since the (rotating-frame) frequencies of the stellar g-modes, which are QNMs restored by buoyancy, are typically in the hundreds of Hz [50, 53, 54, 140], these modes are generally thought to lie in the sweet spot of the precursor scenario (that is, they match well with the expected driving frequency at the time when precursors are observed relative to the main burst). Shifts in the spectra due to magnetic fields (Section 4.4.1), tidal fields (Section 4.4.2), and rotation (Section 4.4.3), are also considered. We note that interface

[1] Because mature NSs as part of binary systems are expected to be slowly rotating [203, 214], the inertial-frame and rotating-frame frequencies of the modes roughly coincide. For rapidly rotating stars however, r- and even f-mode frequencies can be comparable with the frequency of tidal driving $\sim$ seconds before merger [41, 215]; see Sec. 4.4.3 for a discussion on rotational corrections.

modes [51,52,216] and shear modes [217–220] could potentially be responsible for precursors as well [147]. However, the stars considered here have neither phase transitions that result in density jumps inside the star, nor a solid crust separated from the fluid core, hence those modes are absent.

In general, identifying the precise conditions under which crustal failure can occur is complicated. In addition to the actual physics of fracturing not being perfectly understood (see Sec. (2.2) of [221] for a discussion), many factors participate in the straining mechanism, such as: the mass ratio of the binary [78, 79], the structure and strength of the stellar magnetic field [41,222], the degree of stellar stratification, which affects the g-mode spectrum in particular [140,147], the rotation rate [121,223,224], and the stellar EOS that characterises the internal structure [225, 226]. Moreover, NSs are compact enough that relativistic effects are not negligible in these last stage. For instance, QNM eigenfrequencies can differ from their Newtonian counterparts by $\gtrsim 10\%$ [120], which, if unaccounted for, results in errors in the estimation of parameters that allow for resonances to happen at certain times. Seeing that a search for realistic circumstances that connect with the observed precursors may thus shed light on the magnetic field structure, the rotation rate, and the EOS of progenitors (see, e.g., [227]), it is important therefore that realistic models of crust yielding due to mode resonance be constructed with the hope that they can eventually lead to predictions so that astrophysical information concerning NS structure can be extracted from precursor phenomenology.

Building on previous studies [39, 41, 147], we introduce a general-relativistic framework in this Chapter, and aims to (at least phenomenonologically) incorporate each of the above elements to better understand the connection between resonantly excited modes and crust yielding. Specifically, stellar QNMs are solved relativistically and the orbit evolution involves up to 3rd order PN order effects including a 2.5PN flux scheme for gravitational back-reaction. Furthermore, mixed poloidal-toroidal magnetic fields together with rotational and stratification effects are also included numerically in our evolutions.

4.2 Magnetised Stellar Models

We consider piecewise-polytropic approximations [68] to three different realistic EOS, namely the APR4, SLy, and WFF families. We choose these models because they are sufficiently soft to be compatible with the tidal deformability measured in GW170817 [22]. The aforementioned EOS are all barotropic [i.e., $p = p(\rho)$], which is a reasonable approximation for mature systems older than the relevant electroweak and diffusion timescales [228] where thermal fluxes are likely to be negligible, and the buoyancy comes primarily from composition gradients inside the star. Note, however, that tidal heating is expected to be able to raise the temperature of the (still relatively cold) NS crust to $\sim 10^8$ K prior to merger [124]. Thermal

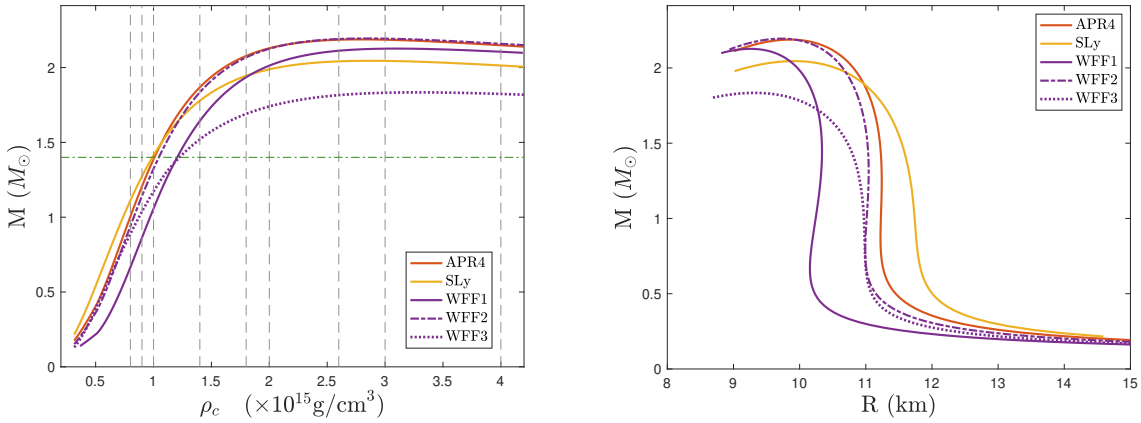

Figure 4.1: Mass of non-rotating equilibrium models constructed with various EOSs surviving the constraints of GW170817 (APR4, SLy, WFF1-3) as functions of central density (left panel) and stellar radius (right panel). We choose several models for each EOS to be studied. These models include those represented by the intersection of each EOS curve with the gray dashed lines, and those having masses of $1.4M_\odot$ (the intersection of each EOS curve with the green dashed line).

gradients may therefore become important at late times [229].

While each EOS considered here assumes that the stars consist of $npe\mu$ nuclear matter, the many-body problem is handled differently:

1. WFF families are obtained using variational methods applied to nucleon Hamiltonians, that contain pieces of two-body and three-body interactions. More precisely, different two- and three-nucleon potentials are used to model the bulk matter [see [158] for details].

2. SLy is derived from the Skyrme effective nucleon-nucleon interaction [160], consistent with WFF2 in the regime where the baryon density exceeds the nuclear value $n_0 = 0.16$ fm^{-3}.

3. APR4 is derived by variational chain summation methods [155] adopting a two-nucleon interaction [230] that accounts for Lorentz boost corrections not used in WFF1.

Masses $M_\star$ of the stars constructed with these EOS, as functions of central density, are shown in the upper panel of Figure 4.1. The intersections of each curves with the dashed lines (both green and gray) mark the models that we choose for later analysis. The mass-density relations [bottom panel of Fig. 4.1] tells us that the SLy EOS is the stiffest one and the WFF1 is the softest one.

4.2.1 Magnetic field structure

In this thesis, we treat stars as perfect conductors over which relativistic magnetic fields are constructed. Perturbed magnetic fields generate Lorentz forces according to the Faraday

induction equation (Sec. 4.2.2), which tunes the eigenfrequencies of QNMs through back-reaction (Sec. 4.4.1). In the event that a crustal yielding occurs on a magnetised star, the release of fracture energy may generate flares, such as precursors of short gamma-ray bursts. In general, perturbed magnetic fields would induce electric fields, accelerating charged particle and thermalising the electromagnetic emission; however, if the magnetic field is strong enough ($\gg 10^{13}$ G, i.e., magnetar-level [231]), the energy propagates along field lines as Alfvén waves [39]. The non-thermal properties of precursors thus support the possibility that at least one NS is a highly magnetised star in those events [41]. Timing of precursor will be examined in Sec. 4.6 as an application of the formalism that will be developed later.

The Viral theorem [232] sets an upper limit to the magnetic field strength for NSs of the order $\sim 10^{18}$ G [233–235]. Even for most magnetars, the (surface dipole) magnetic field strength is much smaller than this extreme, implying that the gravitational binding energy exceeds the magnetic energy by several orders of magnitude [218, 236]. One may therefore treat the magnetic field as a perturbation over a spherically symmetric background profile (2.1), in the style of [228, 237, 238].

We introduce the electromagnetic 4-potential A_μ, which defines the Faraday tensor

$$F_{\mu\nu} = \nabla_\nu A_\mu - \nabla_\mu A_\nu, \tag{4.1}$$

where each A_μ is a function of r and θ only. Maxwell's equations for the electromagnetic field are

$$F^{\mu\nu}_{\ \ ;\nu} = 4\pi J^\mu, \quad \nabla_{[\alpha} F_{\beta\gamma]} = 0, \tag{4.2}$$

for 4-current J^μ [effectively defined by the first of Eqs. (4.2)]. The Lorentz force is then given by $F^\mu_L = F^{\mu\nu} J_\nu$. The ideal MHD condition of vanishing electric field, defined by

$$E_\mu = F_{\mu\nu} u^\nu, \tag{4.3}$$

for a static and non-rotating star (i.e. $u^\mu = e^{-\Phi}\partial_t$), returns the condition $A_t = 0$. We have residual gauge freedom, which allows us to pick $A_\theta = 0$ [239]. Setting $A_r = B_\star e^{\lambda-\Phi}\Sigma$ and $A_\phi = B_\star \psi$, it can be shown that Maxwell's equations are solved exactly for [237]

$$\Sigma(r,\theta) = \int d\theta \zeta(\psi) \frac{\psi(r,\theta)}{\sin\theta}, \tag{4.4}$$

for some ζ, which is an arbitrary function of the stream function ψ and effectively defines the azimuthal (toroidal) component B_ϕ and generalises the Chandrasekhar (Helmholtz) decomposition in flat space [238, 240]. Here $B_\star$ sets the characteristic field strength.

The magnetic 4-field has covariant components

$$B_\mu = \frac{1}{2}\epsilon_{\mu\nu\sigma\eta} u^\nu F^{\sigma\eta}, \tag{4.5}$$

where $\boldsymbol{\epsilon}$ denotes the Levi-Civita symbol. Using the above expression for A_μ, the contravariant components B^μ can be readily evaluated, and we find

$$B^\mu = B_\star \left(0, \frac{e^{-\lambda}}{r^2 \sin\theta}\frac{\partial\psi}{\partial\theta}, -\frac{e^{-\lambda}}{r^2\sin\theta}\frac{\partial\psi}{\partial r}, -\frac{\zeta(\psi)\psi e^{-\Phi}}{r^2\sin^2\theta}\right). \tag{4.6}$$

The function ψ can now be expanded as a sum of multipoles. For simplicity, we take a dipole field with polynomial radial component (which generalises the Newtonian description in [238]), i.e.,

$$\psi(r,\theta) = f(r)\sin^2\theta, \tag{4.7}$$

with $f(r) = a_1 r^2 + a_2 r^4 + a_3 r^6$, where the a_i are to be constrained by appropriate boundary conditions. In particular, we impose that

- the field matches to a force-free dipole outside of the star ($r > R_\star$);
- there are no surface-currents ($J^\mu|_{r=R_\star} = 0$).

This leads to *four* constraints, which are that the 3-components (4.6) are continuous at the boundary ∂V of the star, and that the 4-current vanishes there (which only has one non-trivial component, J_ϕ, for an axisymmetric field). One of these is trivially satisfied by demanding that ζ vanishes on the surface, which we achieve, as in [238], by setting

$$\zeta(\psi)\psi = -\left[\frac{E^p\,(1-\Lambda)}{E^t\Lambda}\right]^{1/2}\frac{(\psi-\psi_c)^2}{R_\star^3}, \tag{4.8}$$

when $\psi \geq \psi_c$, and ζ is zero otherwise. Here ψ_c is the critical value of the streamfunction, defined as the value of the last poloidal field line that closes within the star, thus the toroidal component is confined to the region of closed poloidal field lines. The quantity Λ measures the ratio of poloidal and toroidal magnetic energies; typically $\Lambda \ll 1$ for a stable configuration [236, 241]. For the above choices, we find

$$\psi_c = -\frac{3R_\star^3\sin^2\theta}{8M_\star^3}\left[2M_\star\,(M_\star + R_\star) + R_\star^2\log\left(1-\frac{2M_\star}{R_\star}\right)\right]. \tag{4.9}$$

The energy stored in the *internal* magnetic field of the static equilibrium is (see, e.g., Eq. (41) in [237])

$$E = 2\int_{\text{primary}}\sqrt{-g}d^3x u_\mu u_\nu T^{\mu\nu} = \frac{1}{4\pi}\int_{\text{primary}}\sqrt{-g}d^3x B^2, \tag{4.10}$$

where $T^{\mu\nu}$ is the magnetic stress-energy tensor

$$T^{\mu\nu} = \frac{B^2}{4\pi}\left(u^\mu u^\nu + \frac{1}{2}g^{\mu\nu}\right) - \frac{B^\mu B^\nu}{4\pi}, \tag{4.11}$$

with $B^2 = B^\mu B_\mu$. For the dipolar field (4.6) considered here, the poloidal and toroidal energies are

$$E^p = \frac{B_\star^2}{4\pi}\int_{\rm primary}\sqrt{-g}d^3x\left[\left(\frac{\partial_\theta\psi}{r^2\sin\theta}\right)^2+\left(\frac{e^{-\lambda}\partial_r\psi}{r\sin\theta}\right)^2\right], \tag{4.12}$$

and

$$E^t = \frac{B_\star^2}{8\pi}\int_{\psi\geq\psi_c}\sqrt{-g}d^3x\left(\frac{\zeta(\psi)\psi e^{-\Phi}}{r\sin\theta}\right)^2, \tag{4.13}$$

respectively.

The force-free dipole outside of the star is found by setting $F^\mu_L = 0$ for $r > R_\star$. This leads to [242]

$$\psi_{\rm ext} = -\frac{3R_\star^3\sin^2\theta}{8M_\star^3}\left[2M_\star(r+M_\star)+r^2\log\left(1-\frac{2M_\star}{r}\right)\right], \tag{4.14}$$

where we note that, outside of the star, the geometry is Schwarzschild, i.e.

$$\Phi(r>R_\star) = \frac{1}{2}\log\left(1-\frac{2M}{r}\right) \text{ and } \lambda(r>R_\star) = -\Phi. \tag{4.15}$$

It is not hard to prove (use L'Hopital's rule) that, in the limit $M_\star \to 0$, $\psi_{\rm ext}$ reduces to the standard force-free dipole of Newtonian theory, $\psi \sim \sin^2\theta/r$. Finally, imposing the conditions (i) and (ii) discussed above leads to

$$a_1 = -\frac{3R_\star^3}{8M_\star^3}\left[\log\left(1-\frac{2M_\star}{R_\star}\right)+\frac{M_\star(24M_\star^3-9M_\star^2R_\star-6M_\star R_\star^2+2R_\star^3)}{R_\star^2(R_\star-2M_\star)^2}\right], \tag{4.16a}$$

$$a_2 = \frac{3(12M_\star-7R_\star)}{4R_\star(R_\star-2M_\star)^2}, \tag{4.16b}$$

and lastly

$$a_3 = \frac{3(5R_\star-8M_\star)}{8R_\star^3(R_\star-2M_\star)^2}. \tag{4.16c}$$

The above therefore completely defines the general-relativistic generalisation of the [238] mixed poloidal-toroidal field.

The magnetic field introduces a frequency shift in the spectrum of the star depending on the values $B_\star$ and Λ, defining the characteristic poloidal and toroidal strengths. To better understand the magnetic field, we transform the contravariant components of 4-field B^μ into the *Newtonian-like* components, denoted by a overhead tilde, through (cf. Eq. (4.8.5) in [243])

$$\tilde{B}_a = \sqrt{g_{aa}}B^a, \tag{4.17}$$

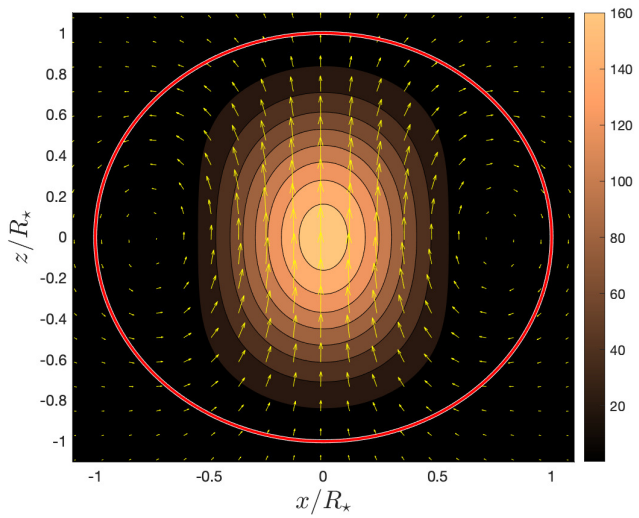

Figure 4.2: Field lines for the background magnetic field $\mathbf{B}$ with $\Lambda = 1$. The red rigid line marks the surface of the equilibrium star; the scale is given in unit of $B_\star$ for which brighter shades indicate stronger field strength.

and we show the cross section in Fig. 4.2, which is the whole picture of the magnetic field if the field is purely poloidal.

4.2.2 Perturbed Lorentz force and Faraday equations

We now study the backreaction onto the magnetic fields induced by the modes, which results in the frequency modulation 4.4.1. In this section, we ignore the spacetime variation of QNMs *from magnetic fields* in the perturbation equations (i.e., $\delta g^{\rm mag}_{\mu\nu} = 0$). Nonetheless we note that the difference between our approximation and the Cowling one is that we take the first order spacetime perturbations into account, viz. spacetime perturbations are involved in determining the mode frequency of the stars, and only the higher-order 'magnetic-backreaction' effects are disposed of. In this sense, our results are expected to be more accurate than those which adopt the Cowling approximation.

Following the derivation in [218] (see also [244]), the projection of the equation of motion onto the hypersurface orthogonal to u^μ,

$$h^\mu_\eta \nabla_\nu T^{\eta\nu} = 0, \tag{4.18}$$

gives

$$(\rho + p + \frac{B^2}{4\pi}) u^\nu \nabla_\nu u^\mu = -h^{\mu\nu}\nabla_\nu \left(p + \frac{B^2}{8\pi} \right) + h^\mu_\eta \nabla_\nu \left(\frac{B^\eta B^\nu}{4\pi} \right), \tag{4.19}$$

where the projection operator $h^{\mu\nu} = g^{\mu\nu} + u^\mu u^\nu$. The Lagrangian 4-displacement ξ^μ is related

to the perturbed velocity through the Lie derivative (see, e.g., Eq. (34) of [245])

$$\delta u^\mu = h^\mu_\nu \mathcal{L}_{\boldsymbol{u}} \xi^\nu. \tag{4.20}$$

In the simple case of a static fluid ($u^\mu = e^{-\Phi}\partial_t$), we find $\delta u^i = i\omega_\alpha e^{-\Phi}\xi^i$ for a certain QNM. After linearizing the equation of motion (4.19) and utilizing relation (4.20), the perturbing Lorentz force reads

$$\begin{aligned}\delta F^\mu_B =& \frac{i\omega_\alpha e^{-\Phi}}{4\pi}\bigg[B^2\bigg(\nabla_t(\xi^\mu e^{-\Phi}) + \xi^\nu\nabla_\nu u^\mu\bigg) + \frac{u^\mu\xi^\nu + u^\nu\xi^\mu}{2}\nabla_\nu(B^2)\\ &- (u^\mu\xi_\eta e^{2\Phi} + \xi^\mu u_\eta)\nabla_\nu(B^\eta B^\nu)\bigg] - \frac{1}{4\pi}h^\mu_\eta\nabla_\nu(B^\eta\delta B^\nu + \delta B^\eta B^\nu)\\ &+ \frac{1}{4\pi}h^{\mu\nu}\nabla_\nu(B_\eta\delta B^\eta) + \frac{1}{2\pi}B_\eta\delta B^\eta u^\nu\nabla_\nu u^\mu,\end{aligned} \tag{4.21}$$

while the perturbed magnetic field δB^μ can be determined by solving the linearized induction equation [218]

$$\begin{aligned}\nabla_t\delta B^\mu =& i\omega_\alpha\bigg[-\xi^\nu\partial_\nu B^\mu - \xi^\nu\Gamma^\mu_{\nu\eta}B^\eta - u^\mu\xi_\nu B^\eta\nabla_\eta u^\nu + e^\Phi B^\nu\nabla_\nu(e^{-\Phi}\xi^\mu)\\ &- e^\Phi B^\mu\partial_\nu(e^{-\Phi}\xi^\nu) - B^\mu\Gamma^\nu_{\nu\eta}\xi^\eta + u^\mu B^\nu i\omega_\alpha e^{-\Phi}\xi_\nu + u^\mu B^\nu\xi^\eta(\partial_\eta u_\nu + \Gamma^t_{\nu\eta}e^\Phi)\\ &- u^\mu B^\nu\Gamma^\eta_{\nu t}\xi_\eta + \xi^\mu B^r\Phi'\bigg] + \delta B^r u^\mu\Phi' e^\Phi.\end{aligned} \tag{4.22}$$

For the magnetic field given by Eq. (4.6), the induction equation gives

$$\begin{aligned}\frac{\partial}{\partial t}\delta B^\mu =& i\omega_\alpha\bigg[-\xi^r\partial_r B^\mu - \xi^\theta\partial_\theta B^\mu + B^\nu\partial_\nu\xi^\mu + B^\mu\Phi'\xi^r - B^\mu\partial_\nu\xi^\nu\\ &- B^\mu\Gamma^\nu_{\nu\eta}\xi^\eta + u^\mu B^\nu i\omega_\alpha e^{-\Phi}\xi_\nu\bigg] + \delta B^r u^\mu e^\Phi\Phi' - \Gamma^\mu_{t\nu}\delta B^\nu.\end{aligned} \tag{4.23}$$

Since some terms only appear in the temporal component of the first-derivative of δB^μ, one can make the equations more concise by separating the temporal component from the spatial, viz.

$$\frac{\partial}{\partial t}\delta B^t = -\omega_\alpha^2 e^{-2\Phi}B^\nu\xi_\nu, \tag{4.24a}$$

and

$$\frac{\partial}{\partial t}\delta B^i = -i\omega_\alpha\bigg[\bigg(\xi^r\partial_r + \xi^\theta\partial_\theta - \Phi'\xi^r + \partial_\nu\xi^\nu + \xi^\nu\partial_\nu\ln\sqrt{|g|}\bigg)B^i - B^j\partial_j\xi^i\bigg]. \tag{4.24b}$$

Accordingly, one can integrate the above equations to find

$$\delta B^t = i\omega_\alpha e^{-2\Phi}B^a\xi_a, \tag{4.25a}$$

and

$$\delta B^i = -\left[\left(\xi^r\partial_r + \xi^\theta\partial_\theta - \Phi'\xi^r + \partial_a\xi^a + \xi^r\left(\Phi' + \lambda' + \frac{2}{r}\right) + \frac{\xi^\theta}{\tan\theta}\right)B^i - B^j\partial_j\xi^i\right]. \quad (4.25b)$$

Expressions (4.25) will be used to define the perturbing Lorentz force in Sec. 4.2.2.

Though it is not considered in this work, we would like to point out the possibility that NSs as a member of a binary may be cold enough that they contain superconducting matters, which influences the magnetic properties of the star [246] and any resulting GWs [247]. For example, the force induced from the field perturbation has different influences to the Lorentz force, and the induction equation is also altered due to the altered nature of Ohmic and ambipolar dissipation [248]. On top of that, superfluidity increases the frequencies of g-modes, e.g., [57] found that the frequency of the $n = 1$, g_1-mode is of the order of a few hundred Hz (even up to 700 Hz) for a particular EOS with $M = 1.4M_\odot$ (see their Fig. 4). Adding that the overlap integral is found to be of the same order as the case where the superfluid is absent (see their Fig. 5), we expect a smaller amplitude for the g_1-mode due to its shorter resonance timescale. Although the inclusion of superfluidity brings higher-order modes into play, those overtones typically have a much weaker overlap integral (with respect to the normal fluid case). It may thus not be very plausible that these overtones can account for tidally-driven crustal failure.

4.3 Binary Evolution

We consider a close NSNS binary system with constituent masses $M_\star$ and $M_{\rm comp}$ for the primary and companion, respectively. The orbit is assumed to lie on the equatorial plane[2]. Each star perceives the other as a point mass to leading order, and thus we treat the companion as a point mass in the evolutionary code[3]. The relevant Hamiltonian consists of four parts [199, 253]:

1. The conservative orbital dynamics, for which we include up to 3rd order post-Newtonian (PN) corrections via the effective one-body formalism (since the equations are lengthy, we refer the reader to Eq. (4.28) of [254]; see also [255]).

2. Leading order GW dissipation of respective equatorial motions, which first appear at 2.5 PN order, is encapsulated by [256]

$$H_{\rm react} = \frac{2}{5}\left(p_ip_j - \frac{M_\star^2M_{\rm comp}^2}{M_\star + M_{\rm comp}}\frac{x_ix_j}{a^3}\right)\frac{d^3}{dt^3}\left[x_ix_j - \frac{a^2}{3}\delta_{ij}\right], \quad (4.26)$$

[2] In close binaries, tidal interaction aligns the stellar spins with the orbital angular momentum rapidly [249, 250]. Therefore, it is most likely that stellar spins are almost aligned with the orbital one in the late stage of inspiralling.

[3] Higher-order and finite-size effects have been looked at through the second-order gravitational self-force method [251] and, independently, by PN theory [252], where the leading correction comes beyond 5 PN.

where $x_i = (a\cos\phi, a\sin\phi)$ for $i = 1, 2$ denote the spatial coordinates of the companion (note the lack of dependence on θ because we consider equatorial motion), p_i are the associated momenta, and a is the distance between the companion and the center of the primary ($r = 0$).

3. The gravitational energy that the primary absorbs via the tidal field,

$$H_{\rm tid} = \int_{\rm primary} \phi^T \delta\rho(\mathbf{x}, t)\sqrt{-g}d^3x, \tag{4.27}$$

where Φ^T denotes the tidal potential as experienced by the primary, $\delta\rho$ is the physical variation in density, and the integral is taken over the volume of the primary. We note that the tidal potential ϕ^T is not to be confused with the metric function $\Phi(r)$. In true general relativity, the tidal potential ϕ^T (which is promoted to a tensor) has both electric and magnetic components [257–259] (see also [79, 260, 261] for the formalism of 1 PN interaction). However, the PN tidal response of NSs and the influence on the orbit evolution are insignificant except only the last few second of the insprial ($\gg$ 100 Hz). Therefore, we will neglect the PN tidal interaction and consider a Newtonian approximation here. As such, Φ^T admits a multipole expansion of the form [262] [see also [263] for the case of eccentric binaries]

$$\phi^T = -\frac{M_{\rm comp}}{a}\left[1 + \sum_{l=2}\left(\frac{r}{a}\right)^l P_0^l\left(\cos\tilde{\phi}\sin\theta\right)\right], \tag{4.28}$$

which depends on the difference $\tilde{\phi} = \phi - \phi_c$ between ϕ and the angular position of the secondary star, ϕ_c, as measured from the perihelion of the orbit. In general one needs to sum over the multipolar components of ϕ^T to complete the tidal Hamiltonian, though we specialize our attention to the $l = m = 2$ component of ϕ^T, which is the leading order term of the potential most relevant for tidally-forced oscillations [263, 264]. The tidal force associated with this component perturbs the primary with frequency two times the orbital frequency, $2\Omega_{\rm orb}$. In addition, $\delta\rho(\mathbf{x}, t)$ is induced by the small-amplitude motion ξ on the star,

$$\xi(\mathbf{x}, t) = \sum_\alpha q_\alpha(t)\xi_\alpha(\mathbf{x}, t), \tag{4.29}$$

which we have decomposed into modes ξ_α with amplitude q_α. Each ξ_α, having time dependence $e^{i\omega_\alpha t}$, is a solution to the eigenproblem

$$\mathcal{V}\xi_\alpha = \omega_\alpha^2\mathcal{T}\xi_\alpha, \tag{4.30}$$

where $\mathcal{V}$ and $\mathcal{T}$ are appropriate potential and kinetic operators [265]. The detailed form

of these potentials is crucial as one attempts to identify the impact of any perturbing forces in the problem, but is not important in building up the Hamiltonian itself, so we postpone their explicit definition until Sec. 4.4.

4. Pulsations on the primary, which are described by a harmonic-oscillators-type Hamiltonian

$$H_{\rm osc} = \frac{1}{2}\sum_{\alpha}\left(\frac{p_\alpha \bar{p}_\alpha}{M_\star R_\star^2} + M_\star R_\star^2 \omega_\alpha^2 q_\alpha \bar{q}_\alpha\right) + \text{H.c.}, \tag{4.31}$$

which is normalized according to

$$\int_{\rm primary} \sqrt{-g} d^3x e^{-2\Phi}(\rho+p)(\xi_\alpha)^\mu(\bar{\xi}_{\alpha'})_\mu = M_\star R_\star^2 \delta_{\alpha\alpha'} \tag{4.32}$$

for each QNM eigenfunction[4]. Here p_α are the canonical momenta associated with q_α, and the overhead bar denotes complex conjugation. Note that the momenta with Latin index are spatial ones, while those labeled by α are for pulsations. The Hermitian conjugate in Eq. (4.31) comes from the dual appearance of modes with eigenfrequency $-\bar{\omega}$ (see Sec. 4.3.1 for details). However, these are not the classic oscillators in the sense that dissipation rate of QNMs is not determined solely by the imaginary part of the eigenfrequencies, since the eigenfunctions are not real.

In summary, we work with the Hamiltonian

$$H(t) = \big(H_{\rm orb} + H_{\rm reac} + H_{\rm osc} + H_{\rm tid}\big)(t). \tag{4.33}$$

The orbital dynamics are then determined by numerically solving Hamilton's equations,

$$\frac{dp_\alpha}{dt} = -\frac{\partial H(t)}{\partial q_\alpha}, \quad \frac{dq_\alpha}{dt} = \frac{\partial H(t)}{\partial p_\alpha}, \tag{4.34a}$$

$$\frac{d\bar{p}_\alpha}{dt} = -\frac{\partial H(t)}{\partial \bar{q}_\alpha}, \quad \frac{d\bar{q}_\alpha}{dt} = \frac{\partial H(t)}{\partial \bar{p}_\alpha}, \tag{4.34b}$$

and

$$\frac{dp_i}{dt} = -\frac{\partial H(t)}{\partial x_i}, \quad \frac{dx_i}{dt} = \frac{\partial H(t)}{\partial p_i}, \tag{4.34c}$$

where we recall that x_i and p_i are defined in the sentence below Eq. (4.26).

The evolution is carried out up to the point that the orbital instability kicks in, which

[4]Eigenfunctions of QNMs, ξ^μ_α, in GR are not strictly orthogonal to each other for the coupling between the material motion to the gravitational radiation field, which extends to infinity, destroys the self-adjointness of the eigenvalue problem by a non-vanishing surface integral term from the perturbations in the spacetime (see, e.g., Eq. (2.4) in [266]; for the Cowling approximation case, see the last two terms of Eq. (16) in [267]). Nonetheless, that term is small for $g-$modes, whose dissipation timescales are extremely long. The omission of the surface integral term hence justifies the implementation of the normalization (4.32), which looks similar to the Newtonian case used in, e.g., [39].

happens at $a \lesssim 3q^{1/3}R_\star$ [268], where q is the mass ratio $M_{\rm comp}/M$ of the binary. Although this point need not coincide with the separation where NSs merge, the difference is small [269] and we effectively assume that mergers occur at $a \lesssim 3q^{1/3}R_\star$ [41, 153, 270].

4.3.1 Tidal resonances

For a spherically-symmetric (equilibrium) star, the components of the eigenfunction ξ_α can be expressed in terms of radial (W_{nl}) and tangential (V_{nl}) components, viz.

$$\begin{aligned}
\xi^r_\alpha &= r^{l-1}e^{-\lambda}W_{nl}(r)Y_{lm}e^{i\omega_\alpha t},\\
\xi^\theta_\alpha &= -r^{l-2}V_{nl}(r)\partial_\theta Y_{lm}e^{i\omega_\alpha t},\\
\xi^\phi_\alpha &= -r^{l}(r\sin\theta)^{-2}V_{nl}(r)\partial_\phi Y_{lm}e^{i\omega_\alpha t},
\end{aligned} \tag{4.35}$$

and $\xi^t_\alpha = 0$ [110, 111, 271]. In addition, the metric perturbed by (even parity) QNMs can be expressed in the Regge-Wheeler gauge[5] as

$$\begin{aligned}
ds^2 =& ds^2_{\rm eq} - e^{2\Phi}r^l H^0_{nl}Y_{lm}e^{i\omega_\alpha t}dt^2 - 2i\omega_\alpha r^{l+1}H^1_{nl}Y_{lm}e^{i\omega_\alpha t}dtdr\\
&- e^{2\lambda}r^l H^0_{nl}Y_{lm}e^{i\omega_\alpha t}dr^2 - r^{l+2}K_{nl}Y_{lm}e^{i\omega_\alpha t}d\Omega^2,
\end{aligned} \tag{4.36}$$

where $ds^2_{\rm eq}$ is the line element of the equilibrium (2.1), and H^0_{nl}, H^1_{nl}, and K_{nl} characterize the metric perturbations.

Two modes whose eigenfrequencies have real parts with opposite sign but share the same imaginary parts appear in pairs [135], and their eigenfunctions are complex conjugate to each other. The normalization (4.32) is satisfied for these dual modes, thus the Hermitian conjugate part in Eq. (4.31) attributes to them. The change in the (Eulerian) density induced by pulsations is therefore

$$\delta\rho(\boldsymbol{x},t) = \sum_\alpha \delta\rho(\boldsymbol{x},\omega_\alpha)e^{i\omega_\alpha t} + \text{H.c.}, \tag{4.37}$$

where the contribution of a particular mode, accompanying a Hermitian conjugate term due to the dual mode, is

$$\delta\rho(\mathbf{x},\omega_\alpha) = q_\alpha\left[-e^{-\Phi}\nabla_i\left((\rho+p)e^{\Phi}\boldsymbol{\xi}^i_\alpha e^{-i\omega_\alpha t}\right) + \left(\frac{H^0_{nl}}{2} + K_{nl}\right)(\rho+p)Y_{lm}\right] \tag{4.38}$$

to first order in the perturbation terms (cf. Eq. (8a) in [267]). The boldface symbol denotes the spatial part of a 4-vector and the divergence is taken with respect to the 3-geometry of the metric (4.36) at a constant time t. The physical perturbation in density induced by a

[5] Strictly speaking, this gauge assumes a fixed (l,m) and mode parity (cf. Eq. (A9) and (A11) in [271]), and so performing a summation, as we do in (4.29), is actually mixing gauges in a formally incorrect way. Fortunately, [134] have shown that one can simply superpose the QNMs using whatever gauge for each one.

pair of modes reads

$$\delta\rho(\mathbf{x},t) = 2\mathrm{Re}\left[\overline{\delta\rho}(\mathbf{x},\omega)\right]. \tag{4.39}$$

We use the complex conjugate $\overline{\delta\rho}$ in the bracket to maintain coherence with later use. The factor 2 comes from the fact that the modes appear in pairs with frequency of ω and $-\bar{\omega}$.

Substituting $\delta\rho$ and integrating by parts, the tidal Hamiltonian can be expressed as

$$\begin{aligned} H_{\rm tid} =& 2\int_{\rm primary}\sqrt{-g}d^3x(\rho+p)\mathrm{Re}\left[\overline{\delta\rho}(\mathbf{x},\omega)\phi^T\right] \\ =& \int_{\rm primary}\sqrt{-g}d^3x(\rho+p)\mathrm{Re}\left[(\bar{H}^0_{nl}+2\bar{K}_{nl})\bar{Y}_{lm}\phi^T\right] - \frac{2M_\star M_{\rm comp}}{aR_\star}\sum_\alpha W_{lm}\left(\frac{R_\star}{a}\right)^l \mathrm{Re}[\bar{q}_\alpha Q_\alpha e^{-im\phi_c}], \end{aligned} \tag{4.40}$$

containing a term resulting from the spacetime distortion, which does not have a Newtonian analogy. In Eq. (4.40), W_{lm} is given by

$$W_{lm} = (-)^{(l+m)/2}\left[\frac{4\pi}{2l+1}(l+m)!(l-m)!\right]^{1/2} \times \left[2^l\left(\frac{l+m}{2}\right)!\left(\frac{l-m}{2}\right)!\right]^{-1}, \tag{4.41}$$

where $(-)^k = (-1)^k$ if k is an integer, but equals zero otherwise. The relativistic "overlap integral", defined as [262]

$$Q_{nl} = \frac{1}{M_\star R_\star^l}\int_{\rm primary}\sqrt{-g}d^3x(\rho+p)\bar{\xi}^\mu_{nll}\nabla_\mu(r^l Y_{ll}), \tag{4.42}$$

is a complex, *dimensionless* number which measures the tidal coupling strength of the mode. The tidal overlap integral for the predominant effects ($l=m=2$ component of ϕ^T) reads[6]

$$Q_{n2} = \frac{1}{M_\star R_\star^2}\int_{\rm primary} e^{\Phi+\lambda}(\rho+p)\bar{\xi}^\mu_{n22}\nabla_\mu(r^2Y_{22})r^2d^3x. \tag{4.43}$$

For a binary system, the tidal force has the frequency of $2\Omega_{\rm orb}$ [263], thus pulsation modes, with (free mode) eigenfrequencies ω_α, would be brought into resonance when $\Omega_{\rm orb}$ satisfies [124]

$$|1-2\Omega_{\rm orb}/\omega_{\rm tot}| \simeq \epsilon, \tag{4.44}$$

where $\omega_{\rm tot} = \omega_\alpha + \delta\omega^B_\alpha + \delta\omega^T_\alpha + \delta\omega^R_\alpha$ denotes the shifted frequency (Sec. 4.4). In our numerical

[6] Note that this expression differs from that used by [223]. These latter authors ignored the pressure contribution in addition to the inertial mass in their expression.

results, we find that the definition

$$\epsilon = 10\sqrt{\frac{2\pi}{\Omega_{\rm orb}}\frac{|\dot{a}|}{a}} \tag{4.45}$$

is adequate for determining the onset and the end of resonance (see Fig. 4.4), which in turn yields the resonance duration $t_{\rm res} \approx \epsilon {\rm Re}(\omega_\alpha)$. Owing to the time-varying tidal strength, the tidal modification in the eigenfrequencies (cf. Sec. 4.4),

$$\delta\omega_\alpha^T = \frac{Q_{n2}}{2\omega_\alpha a^3} M_{\rm comp}, \tag{4.46}$$

depends on time as well. This indicates that the true eigenfrequencies — which include a shift due to the tidal field — must be solved for simultaneously with the orbital evolution equations, since Eq. (4.46) depends on the (time-dependent) orbital separation a.

The numerical scheme for evolving the modes of the primary is summarised in Fig. 4.3. We begin by evolving the binary with an initial separation of

$$a(0) = 2\sqrt[3]{\frac{M_\star + M_{\rm comp}}{\left({\rm Re}[\omega_\alpha]\right)^2}}. \tag{4.47}$$

The initial (non-resonant) mode amplitude is assumed to be zero. In Fig. 4.4 we show the mode amplitude for the $l = m = 2$, g_1-mode for a star with SLy EOS as a member of an equal-mass ($q = 1$) binary as a function of time. The resonance starts at orbital frequency $\nu_{\rm orb} = \Omega_{\rm orb}/2\pi = 43.89$ Hz (green point) and ends at 45.69 Hz (light green point) with duration of 0.29 s. The mode oscillates with amplitude $q \approx 2.4 \times 10^{-4}$ after resonance, though these oscillations decay exponentially as merger is reached.

We performed simulations for equal-mass binaries assuming the EOS APR4, SLy, and WFF1-3. We find that the maximal amplitudes of g_1-modes of the primary obey the following approximate relations

$$q_{\alpha,\rm max}(\omega_\alpha M_\star)^{5/6} \simeq (0.1092 \pm 0.0208) Q_{12}, \tag{4.48}$$

where the error is given by 1σ confidence level of least squares fitting. The analytic equation of the maximum mode amplitude under the stationary phase approximation suggests a slope of $\pi/32 \simeq 0.0982$ (cf. Eq. (6.3) in [124]), which agrees our result to within the stated confidence level.

Tidal effects accelerate the merger because orbital energy leaks into the QNMs [199, 200], especially the f-modes, whose coupling strengths are typically a few tenths. For modes with coupling strengths $Q \lesssim 0.01$, the effects on the orbital evolution are negligible. In Fig. 4.5, we present the separation of an equal-mass binary with $M_\star = 1.4M_\odot = M_{\rm comp}$ and $R_\star = 10$

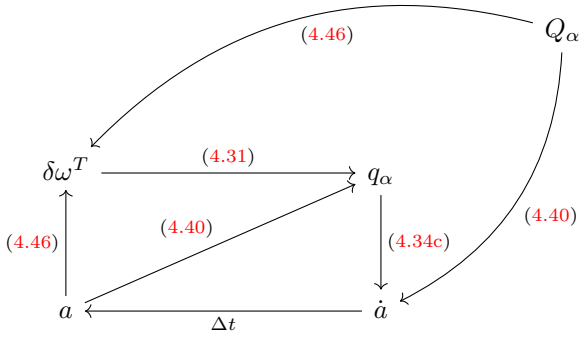

Figure 4.3: The numerical scheme used in this paper to evolve the modes of the primary. The only time-independent quantities are the tidal overlap integrals Q_α on the upper right, while the rest are iteratively solved for. Starting from the separation $a(t)$, the strength of tidal field by the companion of a specific binary is decided and gives rise to certain shift in eigenfrequencies of QNMs [Eq. (4.46)], which depends also on the tidal coupling strength of each QNM Q_α. Consequently, total eigenfrequencies $\omega_\alpha + \delta\omega_\alpha^T$ fixes the Hamiltonian of QNMs [Eq. (4.31)], which is solved to update mode amplitudes. Next, the change rate of the separation $\dot{a}$ is influenced by the amplitude of excited pulsations and the tidal coupling strength Q_α, and infers the separation at the next moment $a(t + \Delta t)$ for the time step Δt. Then the cycle runs again until $a \lesssim 3R_\star$ [41, 153]. Each arrow stands for a deduction via the relation labeled beside it.

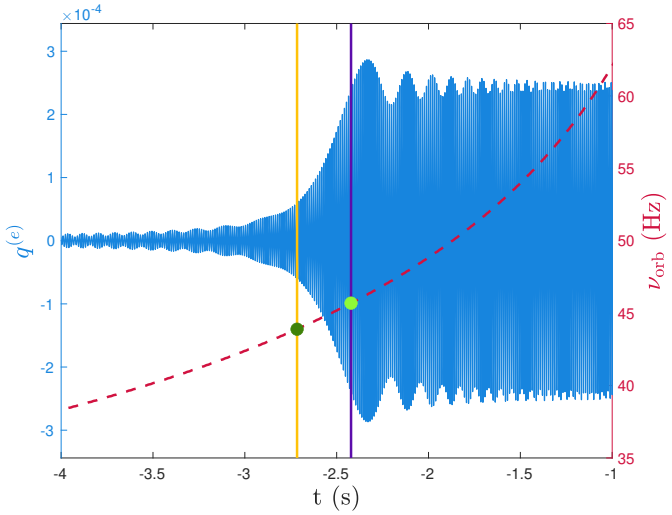

Figure 4.4: The amplitude $q^{(e)}$ (blue; left y-axis) of the $l = m = 2$, g_1-mode, whose unperturbed frequency is 89.25 Hz, and the orbital frequency (red; right y-axis) as functions of time. The horizontal axis records the time prior to an equal mass NS-NS coalescence, which is achieved once the separation decays to $a \lesssim 3R_\star$ [41, 153]. The yellow and the purple lines mark the beginning and the end of the resonance respectively; the corresponding orbital frequencies are 43.89 Hz and 45.69 Hz, marked by solid green points. We have taken an equal-mass binary with the SLy EOS with $M_\star = 1.27M_\odot = M_{\rm comp}$ and $R_\star = 11.78$ km. The radial displacement ξ^r of the first five g-modes are shown in Fig. 3.1.

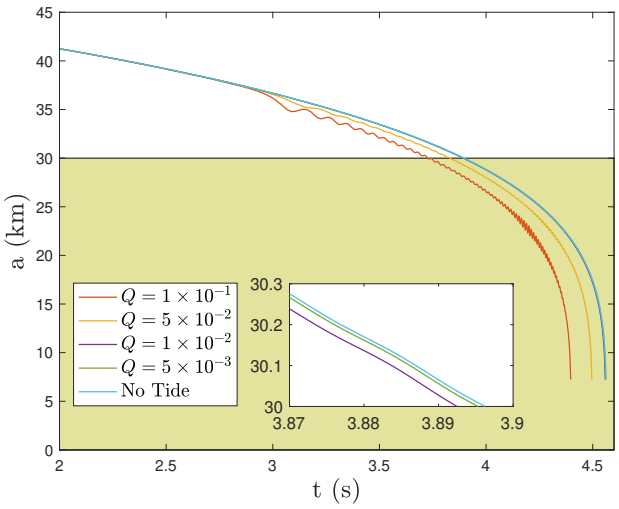

Figure 4.5: Binary separation with various tidal overlaps as a function of time. The maximal disagreement between $Q = 0.01$ and the case without tidal effect is $\lesssim 0.01$ s and is smaller for smaller tidal overlaps. Shaded area, where $a \lesssim 3R_\star$ [41, 153], marks the stage after the merger, which thus is not the virtual evolution. We have taken $M_\star = 1.4M_\odot = M_{\rm comp}$ and $R_\star = 10$ km, hence the collapse happens when the separation is around 30 km. The frequency of the resonant mode is 100 Hz. This Figure does not use any particular EOS.

km for four different strengths of tidal overlap Q as functions of time, together with an evolution on which the tidal effects are absent. As such, one can observe that for $Q \lesssim 0.01$ the tidal effect on the evolution is quite small. Given that the typical coupling strengths of a g-mode are both much smaller than 0.01, the effect in this case of the g-mode resonances on the orbital evolution are insignificant relative to measurement uncertainties in the timing of GWs and gamma ray-bursts.

4.4 Mode frequency modulations

The introduction of a perturbing force δF^μ into the Euler equations (2.5) leads to a modulation $\delta\omega$ in mode frequencies, while eigenfunctions are left unchanged to leading order [41, 272, 273]. The restriction of the Euler equation (2.5) of the unperturbed equilibrium to the hypersurface orthogonal to u^μ, i.e. $h_{\mu\nu}\nabla_\eta T^{\eta\nu} = 0$, gives

$$(\rho + p)u^\nu \nabla_\nu u^\mu = -h^{\mu\nu}\nabla_\nu p, \tag{4.49}$$

from which and Eq. (4.20), one can derive the linearized equation

$$\begin{aligned}(\rho + p)e^{-2\Phi}\omega^2\xi^\mu =& (\delta\rho + \delta p)u^\nu\nabla_\nu u^\mu + h^{\mu\nu}\nabla_\nu\delta p + i\omega e^{-\Phi}\xi^\mu u^\nu\nabla_\nu p \\ &+ i\omega e^{-\Phi}\left[(\rho + p)\nabla_\nu u^\mu + u^\mu\nabla_\nu p\right]\xi^\nu.\end{aligned} \tag{4.50}$$

The left hand side and the right hand side give, respectively, the kinetic operator $\mathcal{T}$ and the potential operator $\mathcal{V}$ that are defined in Eq. (4.30). This equation, with appropriate boundary conditions, forms an eigenvalue problem for ω_α^2.

For an mode with unperturbed frequency ω_α, the inclusion of a perturbing force δF^μ on the right hand side of (4.50), its eigenvalues would be amended accordingly by $\delta\omega_\alpha$. Substituting $\omega = \omega_\alpha + \delta\omega_\alpha$ and focusing on the leading order perturbation terms, (4.50) gives

$$2(\rho + p)e^{-2\Phi}\omega_\alpha \xi^\mu \delta\omega_\alpha = \delta F^\mu, \tag{4.51}$$

from which the frequency shift,

$$\delta\omega_\alpha = \frac{1}{2\omega_\alpha} \frac{\displaystyle\int_{\text{primary}} \delta F_\mu \bar{\xi^\mu} \sqrt{-g} d^3x}{\displaystyle\int_{\text{primary}} (\rho + p) e^{-2\Phi} \xi^\mu \bar{\xi}_\mu \sqrt{-g} d^3x}, \tag{4.52}$$

can be obtained. A similar derivation in the Newtonian case can be found in [272]. Equation (4.52) is numerically evaluated for some particular choices of δF^μ.

4.4.1 Magnetic field

As $\delta \boldsymbol{F}$ is given by the Lorentz force, (4.21) and (4.52) yield the expression of the correction in the frequency for a general magnetic field, which, after substituting the magnetic field as defined in Eq. (4.6) and adopting the normalization (4.32), becomes

$$\begin{aligned}\delta\omega_\alpha^B =& \frac{(M_\star R_\star^2)^{-1}}{8\pi\omega_\alpha} \int_{\text{primary}} \sqrt{-g} d^3x \Big[-\omega_\alpha^2 B^2 \xi^\mu \bar{\xi}_\mu e^{-2\Phi} \\ &+ 2B_\mu \delta B^\mu \bar{\xi^r} \Phi' - \bar{\xi}_\mu \nabla_\nu \Big(B^\mu \delta B^\nu + B^\nu \delta B^\mu \Big) + \bar{\xi^\nu} \nabla_\nu (B_\mu \delta B^\mu) \Big].\end{aligned} \tag{4.53}$$

In Fig. 4.6, we plot the mode frequency shifts for the $l = 2$, g_1- and g_2-modes ($n = 2$) with some fixed stellar parameters and EOS as functions of the poloidal-to-toroidal strength Λ (top panel). The range of Λ is chosen broadly compared to the ratio for a stable magnetic field configuration (shaded area), which is $10^{-3} \lesssim \Lambda \lesssim 0.3$ [236, 274]. The stability examined by the energy variation method gives the constraint

$$\tilde{B}^\phi \lesssim 10^{17} \sqrt{B_{15}} \left(\frac{\delta}{0.01} \right) \text{ G}, \tag{4.54}$$

on the toroidal strength, which implies $\Lambda \gtrsim 0.033$ (black line) for a magnetar-level surface field strength $B_\star \sim 10^{15}$ G. This constraint on the strength of toroidal component becomes loose for larger δ [236, 274]. On the other hand, we find that the Virial limit on the field strength of $\sim 10^{18}$ G inside the star [233–235] corresponds to $\Lambda \gtrsim 5 \times 10^{-4}$, which is a weaker

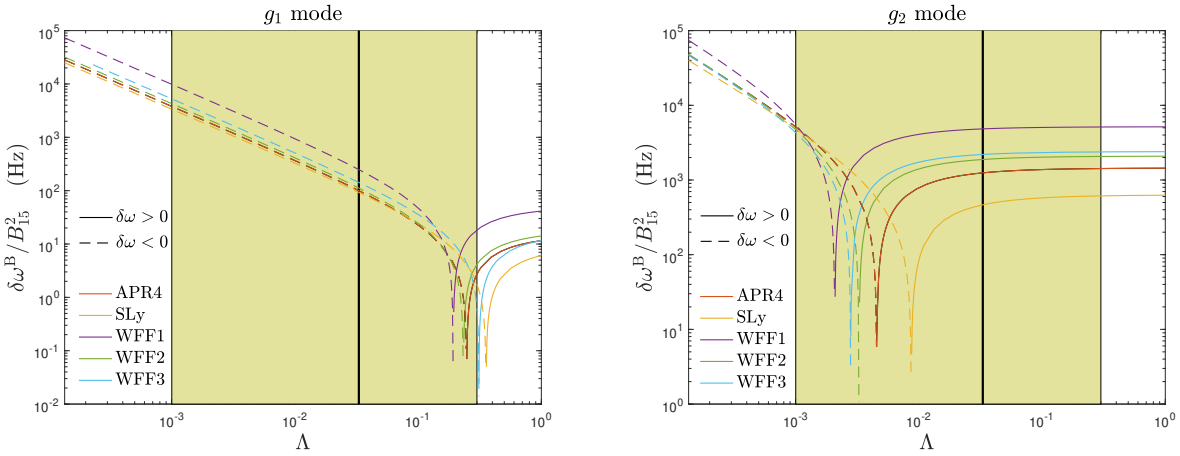

Figure 4.6: Eigenfrequency shifts $\delta\omega^B$ for the $l = 2$, g_1- (*top*) and g_2-modes (*bottom*) due to the magnetic field as functions of the poloidal-to-toroidal field-strength ratio Λ. The shaded areas represent the range of Λ for which the magnetic field is stable [236]. The black solid lines mark the ratio $\Lambda = 0.033$, which gives the maximal toroidal field strength for $B_\star = 10^{15}$ G inside the star [Eq. (4.54)]. We have used $\delta = 0.005$ and $\rho_c = 9\times10^{14}$ g/cm^3 for EOS APR, SLy, and WFF1-3, whose masses are $1.21M_\odot$, $1.27M_\odot$, $0.86M_\odot$, $1.14M_\odot$, and $1.04M_\odot$, respectively.

constraint than that coming from stability considerations. Unless $\Lambda \ll 1$, magnetic fields of the order $\gtrsim 10^{15}$ G are needed to noticeably shift the g_1-mode frequencies for any EOS, though marginally weaker (though still strong) fields of order $\gtrsim 10^{14}$ G can significantly adjust the g_2-mode frequencies. Given that the g_1-mode typically oscillates at ~ 100 Hz, the (rotating frame) frequency becomes negative when the ratio Λ is less than the value (black line) that implies the maximal toroidal strength for $B_\star = 10^{15}$ G, indicating the onset of instability. Moreover, the frequency shifts for overtones ($n > 1$) are less sensitive to Λ than g_1-modes, resulting from nodes of displacements in the region where the toroidal component of magnetic field is non-trivial. The coupling between these modes and the structure of magnetic field is thus more tenuous. For g_2-modes, a toroidal-to-poloidal ratio Λ of $\lesssim 0.01$ is needed in order that $\delta\omega^B$ becomes negative; and the shifts are always positive (for stable values of Λ) for g_3-modes, though not shown here. Fig. 4.7 shows modified mode frequencies of g_1-modes of a specific star for the cases $\Lambda = 1.0$ (top panel), $\Lambda = 0.3$ (middle panel), and $\Lambda = 10^{-3}$ (bottom panels), for various values of $B_\star$, as functions of δ. There ω_0 denotes the unperturbed frequency. As $\delta \lesssim 0.01$, the absolute values of frequency corrections increase as the stratification weakens, i.e. δ is lower, in that unperturbed frequencies in the denominator of the right hand side of (4.53) converges to zero faster than the numerator.

It is noticeable that the corrections are more severe for less compact stars when a purely poloidal ($\Lambda = 1$) field is considered, as shown in Fig. 4.8. For instance, defining the compactness as $\mathcal{C} = M_\star/R_\star$, we see that for $B_\star = 10^{15}$ G, $\delta = 0.005$, and EOS SLy, the correction for the g_1-mode is $\delta\omega^B = 42.40$ Hz for the model with $\mathcal{C} = 0.461$, while it is $\delta\omega^B = 20.32$ Hz for the model with $\mathcal{C} = 0.729$. Additionally, we find fitting relations for the effect of magnetic

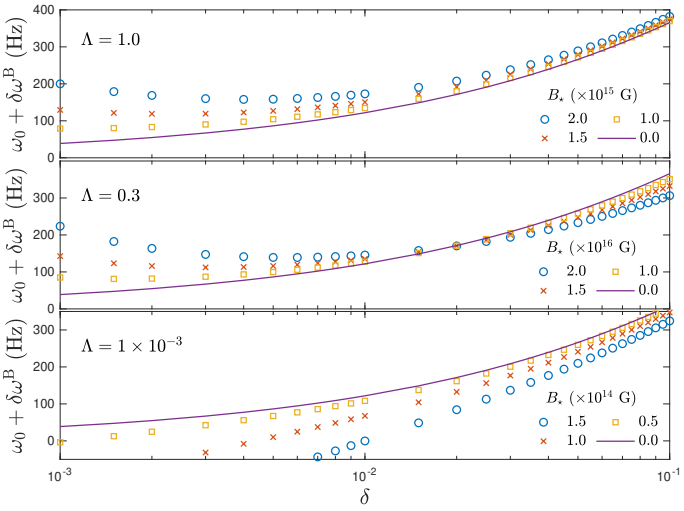

Figure 4.7: g_1-mode frequencies: the purple continuous line is for unperturbed star, while the rest for magnetized ones with different strengths of the magnetic field $B_\star$ as a function of δ. We set $\Lambda = 1.0$ (*top*), $\Lambda = 0.3$ (*middle*), and $\Lambda = 10^{-3}$ (*bottom*). The background star is constructed by EOS APR4 and has the central density of 8×10^{14} g/cm^3.

Table 4.1: Coefficients of the fitting functions (4.55a) for the magnetic-driven frequency modifications.

	APR4	SLy	WFF1	WFF2	WFF3
c_1	-0.493	-0.492	-0.498	-0.494	-0.495
c_0	0.279	-0.289	1.112	0.547	0.624
d_1	-3.489	-3.848	-3.707	-3.480	-5.150
d_0	5.126	4.811	5.645	5.213	5.937

field on the g_1-modes as

$$\delta\omega^B \approx B_{15}^2 e^{(c_1 \ln\delta + c_0)(d_1\mathcal{C}+d_0)} \text{ Hz}. \tag{4.55a}$$

The fitting coefficients for different EOS are summarised in Tab. 4.1.

4.4.2 Tidal forces

The tidal force generated by the companion, as exerted on the primary, reads

$$\delta F_\mu^T = \frac{M_{\rm comp}}{a^3}(\rho + p)\nabla_\mu(r^2 Y_{22}). \tag{4.56}$$

The equation for the frequency shift driven by this force is found to be

$$\delta\omega_\alpha^T = \frac{M_{\rm comp}}{2\omega_\alpha a^3} \frac{\displaystyle\int_{\rm primary} (\rho + p)\nabla_\mu \phi^T \bar{\xi^\mu}\sqrt{-g}d^3x}{\displaystyle\int_{\rm primary} (\rho + p)e^{-2\Phi}\xi^\mu\bar{\xi}_\mu\sqrt{-g}d^3x}. \tag{4.57}$$

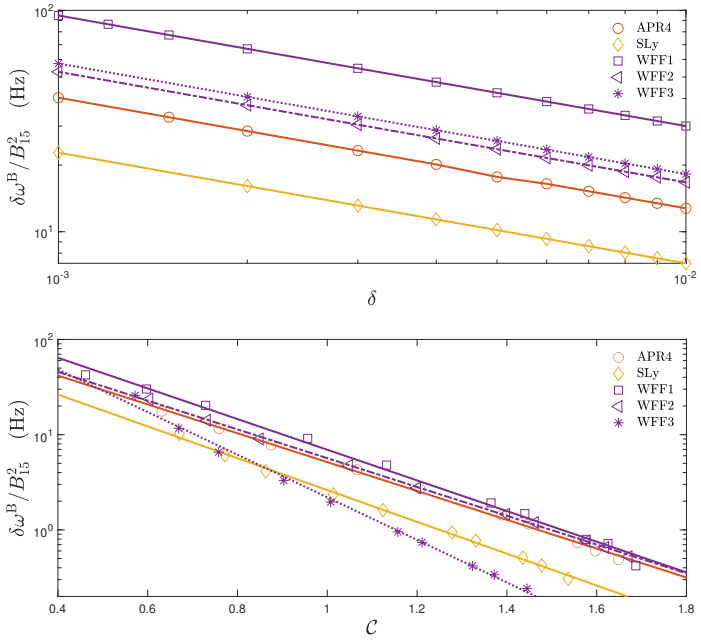

Figure 4.8: Magnetic-driven modifications in eigenfrequencies of $l = 2$, g_1-mode as functions of stratification δ (*top*), and the compactness $\mathcal{C}$ (*bottom*), respectively. The markers in the upper panel are the numerical results for the star of each EOS that has central denisty of 8×10^{14} g/cm^3, while the markers in the bottom panel represent the stars described in Fig. 4.1 with fixed $\delta = 0.005$. We have taken $B_\star = 10^{15}$ G and EOSs APR4, SLy, and WFF1-3 are included. In both plots, the rigid lines are the fitting results of corrections in magnetic frequencies for each EOSs.

This form is used in Eq. (4.46). The tidal force modifies the eigenfrequencies of QNMs via the interaction mediated by the pressure (hence density) variation. Consequently, it leads to minute frequency corrections ($\sim 0.01\%$) for g-modes since g-modes only perturb the pressure profile slightly.

4.4.3 Rotation

We treat the rotation of the star as a perturbation over the non-spinning equilibrium, since the Coriolis force is proportional to the square of the angular velocity, and thus a slow perturbation, to linear order, does not induce any hydromagnetic changes to the background structure [275]. We also omit the spin-orbit interaction. A (uniform) rotation Ω introduces a $g_{t\phi}$ component to the metric, causing frame dragging. When a slow rotation is considered, this effect is small and we therefore ignore it in this work. On top of the metric corrections, rotation also introduces the axial component

$$u^\mu_{\rm rot} = \Omega e^{-\Phi}\partial_\phi, \tag{4.58}$$

to the 4-velocity, when we are working in the inertial frame. The axial velocity $u^{\mu}_{\rm rot}$ adds an extra term to Eq. (4.20), resulting in

$$\delta u^{\mu} = i(\omega_{\alpha} + m\Omega)e^{-\Phi}\xi^{\mu}, \tag{4.59}$$

and thus leads to a perturbing force

$$\delta F^{r}_{R} = 2(\rho + p)e^{-2\Phi}\omega_{\alpha}\Omega(m\xi^{r} - ire^{-2\lambda}\sin^{2}\theta\xi^{\phi}), \tag{4.60a}$$

$$\delta F^{\theta}_{R} = 2(\rho + p)e^{-2\Phi}\omega_{\alpha}\Omega(m\xi^{\theta} + i\sin\theta\cos\theta\xi^{\phi}), \tag{4.60b}$$

$$\delta F^{\phi}_{R} = 2(\rho + p)e^{-2\Phi}\omega_{\alpha}\Omega\left(m\xi^{\phi} - i\frac{\xi^{r}}{r} - 2i\cot\theta\xi^{\theta}\right). \tag{4.60c}$$

Therefore, the relativistic leading order rotational corrections in the mode frequencies having the expression

$$\delta\omega^{R}_{\alpha} = -m\Omega(1 - C_{nl}), \tag{4.61}$$

with

$$C_{nl} = \frac{1}{M_{\star}R^{2}_{\star}}\int_{\rm primary}(\rho + p)e^{\Phi+\lambda}r^{2l}\big[-e^{-\lambda}(\bar{V}_{nl}W_{nl} + \bar{W}_{nl}V_{nl}) + V_{nl}\bar{V}_{nl}\big]dr. \tag{4.62}$$

In the Newtonian limit, this agrees with that of [272] and [126].

Fixing $\delta = 0.005$, we plot C_{nl} of g_1-modes (C_{12}; top panel) and of g_2-modes (C_{22}; bottom panel) as functions of compactness the mean density of the star in Fig. 4.9. The values for C_{12} and C_{22} differ only slightly [276–278], e.g. $C_{12} = 0.11$ and $C_{22} = 0.112$ for the star of WFF1 EOS that has $1.4M_{\odot}$. On the other hand, we find that C_{n2} depends only slightly on stratification δ for $n \lesssim 5$, e.g., the difference between the values of C_{12} for $\delta = 0.001$ and $\delta = 0.01$ is ~ 0.001 (percent level at most). The insignificant dependence on δ of C_{12} has also been shown in [224].

4.5 Crustal strain

Having considered modulations in mode eigenfrequencies by tidal and magnetic fields, and the (slow) rotation of the equilibrium in Sec. 3.5, we now turn to investigate the maximal strain exerted on the stellar crust as a result of resonant $g-$mode displacements.

Time-varying displacements $\boldsymbol{\xi}$ between the material elements of the neutron star generates a stress. However, in GR, the total strain is not only due to the displacement, and there is a contribution from the perturbation of the metric to the strain tensor [279–281], whose total

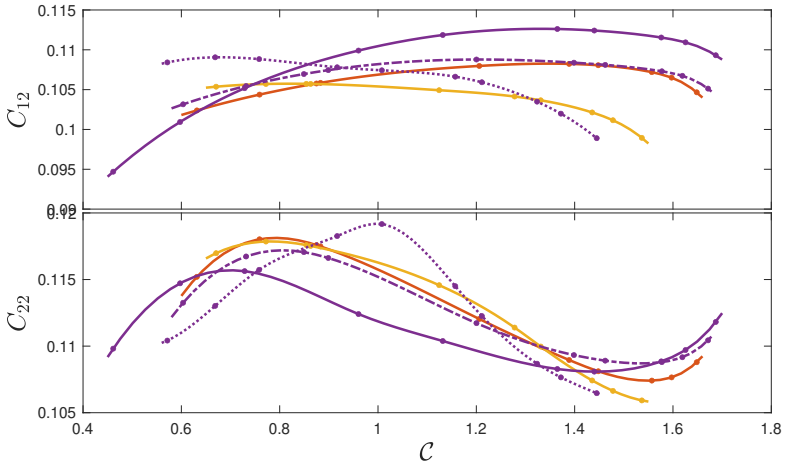

Figure 4.9: Coefficients C_{12} for g_1-modes (*top*) C_{22} for g_2-modes (*bottom*) as functions of compactness $\mathcal{C}$ assuming EOS APR4 (red curves), SLy (yellow curves), and WFF1-3 (purple solid, dashed, and dotted curves, respectively). We fix $\delta = 0.005$. Markers on each curve are models pointed out in Fig. 4.1.

form reads

$$\begin{aligned}\boldsymbol{\sigma}_{\mu\nu} =& \frac{1}{2}\left(\nabla_\mu \xi_\nu + \nabla_\nu \xi_\mu\right) + \frac{1}{2} h^\eta_\mu h^\kappa_\nu \delta g_{\eta\kappa} \\ =& \frac{1}{2}\left(\partial_\mu \xi_\nu + \partial_\nu \xi_\mu + \delta g_{\mu\nu}\right) - \Gamma^\sigma{}_{\mu\nu}\xi_\sigma,\end{aligned} \tag{4.63}$$

where we retain just the first order terms in the second line of the equation. Oscillations may lead to a crust failure for large enough stresses, which can be probed by the commonly used "von Mises stress" criterion, coming from classical elasticity theory [282]. Defining the strain as [283, 284]

$$\sigma \equiv \sqrt{\tfrac{1}{2}\boldsymbol{\sigma}_{\mu\nu}\bar{\boldsymbol{\sigma}}^{\mu\nu}}, \tag{4.64}$$

then the von Mises criterion implies that the crust breaks if σ exceeds some critical threshold, $\sigma_{\rm vM}$. In a recent semianalytic lattice stability models of [49], they calculate the threshold as $\sigma_{\rm vM} \approx 0.04$ while [45] follow molecular dynamics simulations to find $\sigma_{\rm vM} \approx 0.1$ for low temperature stars. We adopt the former in this article with a remark that if the latter had been adopted, the amplitudes of resonantly-excited modes would need to be much higher to instigate failure.

Equation (4.63) and definition (4.64) indicate that the stress generated by the displacement ξ_α is proportional to its amplitude q_α, which evolves according to equation (4.34a). Therefore we have

$$\sigma(t) = \sqrt{2}\sum_\alpha \sqrt{q_\alpha(t)\bar{q}_\alpha(t)}\sigma_\alpha, \tag{4.65}$$

where σ_α is the *unit* strain caused by ξ_α (i.e., for $q_\alpha = 1$) and the pre-factor $\sqrt{2}$ is attributed

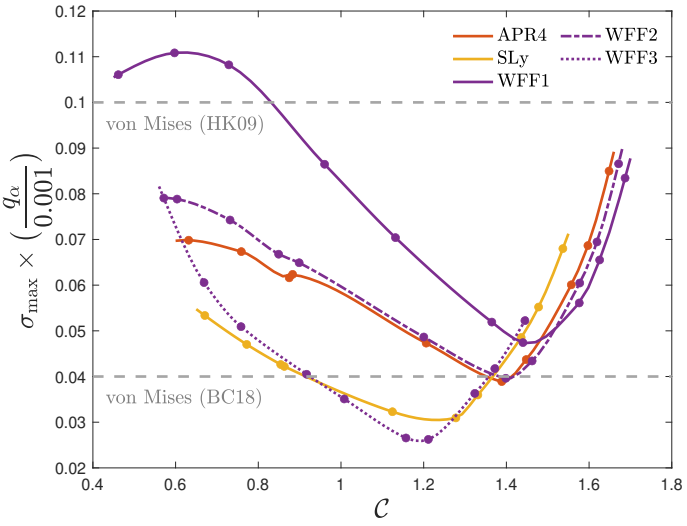

Figure 4.10: Maximal crustal strain $\sigma_{\max}$ due to g_1-modes for APR4, SLy, and WFF1-3 EOS as functions of $\mathcal{C}$. The gray dashed line represents the von Mises criterions by [49] and [45]. We have taken $\delta = 0.005$.

to the duality of modes with ω and $-\overline{\omega}$.

Taking crust as the part of star with $0.9R_\star < r < R_\star$, in Fig. 4.10 we plot the maximal values of strain strain $\sigma_{\max}$ in the crust due to the $(l = m = 2)$ g_1-modes for several EOS, where the stratification is taken to be $\delta = 0.005$. This latter value in particular is typical in the literature for mature NSs [140, 235]. As such, relation (4.48) implies that g_1-modes with tidal coupling strength $\gtrsim 8 \times 10^{-5}$ may be capable of generating a crustal strain that exceeds the von Mises criterion provided $\omega M \sim 0.003$ for g_1-modes. We therefore conclude that tidal resonances in NSNS binaries can excite g-modes to the point that the crust may yield, which can have important implications for observations of precursors of short gamma-ray bursts [39, 41]. This latter aspect will be covered in detail in paper II.

In addition to low order g-modes, it has been shown by [147] that the excitation of f-modes before the merger, though not resonantly instigated, can generate a strain that meets the von Mises criterion. For instance, we find the strain $\sigma_{\max} = 0.107$ for the f-mode of a particular primary with the SLy EOS and $M = 1.27M_\odot$. However, only within less than 10 ms prior to the merger can $\sigma_{\max}$ hit the critical value of 0.04. Though the excited f-modes are irrelevant to the precursors, their influences on the (phase of) GW waveforms may be measured with future GW detectors (see, e.g., [80, 181]).

4.6 Precursor Observations

GRBs show a bi-modal distribution in their durations, T_{90}, and are therefore often classified into two classes – long $(T_{90} > 2)$ and short $(T_{90} < 2)$ [208]. Classifying a given event however is not trivial, because one should take the duration, redshift, other observations

(e.g., precursors, afterglows [285]) and/or the possible limits of instruments (e.g. duration of measurement in different energy bands [286]) into account (see the discussion in [287]). Nonetheless, a simple but broadly used method to distinguish the short from the long is $T_{90} \lesssim 2$ s [208, 288, 289].

Although rare, precursor flares are sometimes seen before SGRB. The identification of these precursors from the main episode depends sensitively on the definition of preemissions. Therefore, the proportion of SGRBs hosting precursor activities varies within literature. For instance, some authors require that a genuine precursor flare has to precede the main episode by more than T_{90} [34, 35], whereas some allow for arbitrarily short periods of time prior to the main burst for preemissions to be classified as precursor status [37, 38, 125, 290]. In Table 4.2 we present relevant properties for the most statistically significant SGRB precursor candidates discussed in the above references. In the first column we show the associated SGRBs, and the second toward the penultimate ones are, respectively, the duration of the main bursts, the timing of precursor emissions prior to the main episodes (waiting time, $T_{\rm wt}$), and the statistical significance. The final column lists the inferred orbital frequency $\Omega_{\rm orb}$ by matching the time of the events with the binary evolution (Sec. 4.3), which indicates the frequency of the corresponding resonantly-excited mode (Sec. 4.3.1). We see that GRBs 071030, 090510b, 100717 and 130310 are temporally-separated, relative to the main burst, by at least couple of seconds ($T_{\rm wt} \gtrsim 2.5$ s), while others are prior to the main burst only within $\lesssim 1.85$ s.

There are three events in [38] having rather small or large $T_{\rm wt}$, viz. GRBs 100223110, 150922234 and 191221802. The first two precede the main episode by, respectively, $\gtrsim 80$ ms and 30 ms, and the waiting time for the latest is $T_{\rm wt} \gtrsim 20$ s. The closeness to the merger blurs the identification of the former two, i.e., these pre-emissions may not proceed the merger since the formation timescale of the main emission is likely comparable or longer than 80 ms (see Sec. 4.6.1 for the discussion). On the other hand, the latter happens at a very early stage ($a \gtrsim 200$ km), where the interaction between two stars in a binary, which is proportional to a^{-3}, is so weak that the mechanism behind this pre-emission may not be relevant to mutual interaction (unless the main burst was significantly delayed).

4.6.1 Precursor Timing

In reality, the main burst, occurring at t_B, will not be coincident with the coalescence at t_C, since the jet constituting the main burst has a finite formation timescale. Rather, the physical picture after the merger is complicated with several timescales participating in the SGRB mechanism, e.g., jet formation, jet break out, and GRB formation. In addition, each timescale varies with jet mechanism, making it almost impossible to make a conclusive statement about the separation between t_B and t_C (see Tab. 1 in [291] for more details). Though $t_B - t_C$ ranges from 0.01 to $\lesssim 10$ s, we assume that the burst occurs simultaneously with the merger, i.e.,

Table 4.2: Properties of SGRB precursor candidates as reported in [34,36–38]. The associated orbital frequencies are determined by the time prior to the main burst, which is assumed to happen immediately after the merger (i.e., $t_B \approx t_C$). We assume an equal-mass binary that comprises stars pertaining to EOS SLy with $M = 1.27 M_\odot = M_{\rm comp}$ and $R_\star = 11.78$ km (the same system used in Fig. 4.4). The binary evolution is solved according to the numerical scheme in Fig. 4.3, which involves up to 3PN terms in conservative orbital dynamics and 2.5 PN radiation-reaction. Tidal effects of f-modes are also taken into account.

Precursor Event	Duration [T_{90} (s)]	Time prior to main burst [$T_{\rm wt}$ (s)]	Significance (σ)	Orb. freq. [$\Omega_{\rm orb}$ (Hz)]
GRB 060502B	~ 0.09	0.32	6.1	573.74
GRB 071030	$\lesssim 0.7$	2.5	6.3	283.89
GRB 081216531	$0.15^{+0.05}_{-0.03}$	$0.53^{+0.04}_{-0.05}$	> 4.5	$484.27^{-11.78}_{+16.50}$
GRB 090510a [a]	0.05 ± 0.02	0.45 ± 0.05	$\lesssim 4.6$	$511.78^{-17.87}_{+20.68}$
GRB 090510b[a]	$\lesssim 0.4$	13	5.2	158.41
GRB 100213A	~ 0.44	0.68	11.1	445.00
GRB 100717	0.3 ± 0.05	3.3	12.8	257.58
GRB 100827455	$0.11^{+0.05}_{-0.04}$	0.34 ± 0.06	> 4.5	$562.24^{-29.77}_{+37.54}$
GRB 101208498	$0.17^{+0.12}_{-0.08}$	$1.17^{+0.10}_{-0.14}$	> 4.5	$369.51^{-10.31}_{+16.56}$
GRB 111117510	$0.18^{+0.05}_{-0.03}$	$0.22^{+0.03}_{-0.06}$	> 4.5	$649.61^{-26.84}_{-71.34}$
GRB 130310	0.9 ± 0.32	4.45 ± 0.8	10	$231.85^{-1.44}_{+1.29}$
GRB 140209A	~ 0.45	1.06	13.9	359.25
GRB 141102536	$0.06^{+0.10}_{-0.06}$	$1.26^{+0.11}_{-0.15}$	> 4.5	$360.18^{-10.27}_{+16.09}$
GRB 150604434	$0.17^{+0.25}_{-0.01}$	$0.64^{+0.02}_{-0.29}$	> 4.5	$454.27^{-4.72}_{+102.56}$
GRB 160726A	~ 0.08	0.39	10.2	537.00
GRB 170802638	$0.15^{+0.17}_{-0.11}$	$1.85^{+0.14}_{-0.21}$	> 4.5	$315.31^{-7.9}_{+13.48}$
GRB 181126413	$0.72^{+0.18}_{-0.27}$	$0.85^{+0.40}_{-0.29}$	> 4.5	$412.36^{-51.19}_{+62.97}$

Notes:

[a] GRB 090510a and GRB 090510b are not the official names of these two precursors. We label them by a and b to indicate the later and the earlier preemission episodes of GRB 090510.

$t_B \approx t_C$, with a caveat that the timing of precursor prior to the coalescence obtained under this assumption is actually the upper limit.

We consider a close NSNS binary system with constituent masses $M_\star$ and $M_{\rm comp}$ for the primary and companion, respectively. The coalescence is defined to occur when the separation of binaries $a \lesssim 3q^{1/3}R_\star$ [41, 153, 268, 270], where $R_\star$ is the radius of the primary and q is the mass ratio $M_{\rm comp}/M$ of the binary. The binary is evolved numerically until the point of coalesence defined above by including 3rd order PN effects and GW back-reaction induced from the orbit in the 2.5 PN order and from excited modes[7] (Sec. 4.3.1; see also [294]). The impacts of p- and g-modes on the binary evolution are, however, expected to be negligible as there is no resonance for the former and tidal couplings of the later is too small to affect binary evolution [295]. In principle the p- and g-mode can couple to each other strongly due to their similar radial wavelength, resulting in so-called p-g instability that may affect the binary evolution in a measurable way, e.g., heating up the star to $\gtrsim 10^{10}$ K and causing significant orbital phase errors [296, 297]. However, in the recent analysis of the gravitational wave event GW170817, the p-g instability seems to either be suppressed to induce only slight phase shifts to the gravitational waveform or to be difficult to distinguish the effects from other intrinsic parameters of GW170817 [298, 299]. Therefore, we do not consider these effects on the evolution, and ignore the nonlinear tidal effects in the evolution equations.

For a particular equal-mass binary ($q = 1$) inspiralling on the equatorial plane[8] (i.e., the companion sits in the plane $\Theta = \pi/2$ with respect to the inertial frame of the primary throughout the evolution) with both stars obeying the SLy EOS, we determine the orbital frequencies at the moment precursors occur. In [41], a Newtonian scheme was used, i.e., by the Kepler formula,

$$\Omega_{\rm Kep} = \sqrt{\frac{(M_\star + M_{\rm comp})}{a^3}}. \tag{4.66}$$

Here, however, we use a PN scheme for orbital evolution and take the relativistic tidal effects into account. First, the coalescence is expedited, thus the orbital frequency at a certain time prior to merger is less; secondly, the mode eigenfrequencies, which are relevant for precursor timing, are shifted. As a consequence, the inferred (PN) orbital frequencies (the last column of Tab. 4.2) are found to be less than the inferred Keplerian orbital frequency in [41] by $\lesssim 10\%$ of the PN orbital frequencies.

In addition, the frequencies of f-modes are $\gtrsim 2$ kHz and the typical frequencies of g_1-modes are $\gtrsim 100$ Hz. Since the tidal force perturbs stars at a frequency which is twice the value of the orbital one, the final column of Tab. 4.2 suggests, therefore, that the precursors

[7] While f-modes are likely to get resonant before merging for rapidly rotating primaries [41], in this work we only slow rotation, thus f-mode resonances are absent. However, it has been shown that tidal effects of f-modes are important in binaries evolution [181, 199, 292, 293] mainly due to their strong couplings with the tidal field.

[8] In close binaries, tidal interaction rapidly aligns the stellar spins with the orbital angular momentum [249, 250]. Therefore, the inclination angle is expected to be approximately zero.

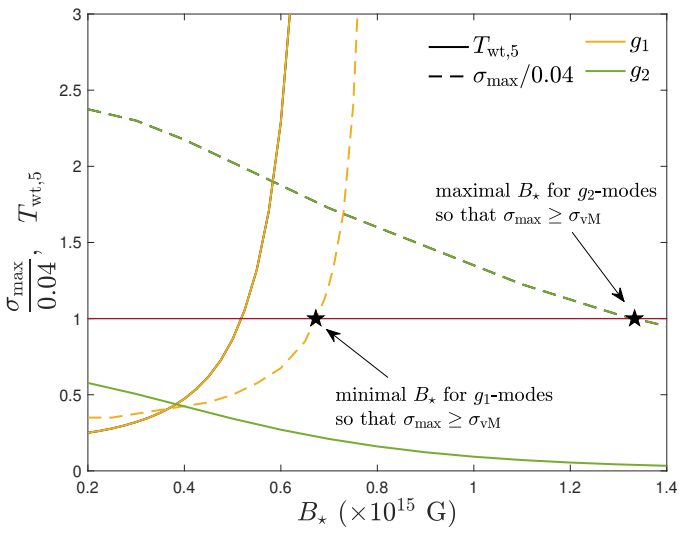

Figure 4.11: Time prior to the main burst, which is assumed to coincide with the coalescence, t (green and yellow solid lines) and maximal strain $\sigma_{\rm max}$ (dashed lines) as functions of $B_\star$. The black stars mark the minimal and the maximal value of $B_\star$, such that the von Mises criterion is met for g_1- and g_2-modes, respectively. We consider a binary with $q = 1$ and the non-rotating primary having EOS SLy and $M = 1.27 M_\odot$. Here $T_{\rm wt,5} = T_{\rm wt}/(5\ {\rm s})$.

are observed at the stage of inspiral prone to resonances of g-modes.

4.6.2 Resonant Shattering

As a practical application of the resonant shattering scenario to observations, we consider a particular primary, within an equal-mass binary, with[9] $\delta = 0.01$. The considered primary has a free g_1-mode resonance prior to the coalescence by ~ 1 s, while the resonance of its free g_2-mode occurs at ~ 3.2 s before the merger. For the stable range of Λ, the magnetic frequency modification is negative for the g_1-mode and is positive for the g_2-mode. Setting $\Lambda = 0.01$, we show $T_{\rm wt}$ and $\sigma_{\rm max}$ for g_1- and g_2-modes as functions of $B_\star$ in Fig. 4.11. We see that, when $B_\star$ approaches some certain values, both $T_{\rm wt}$ and $\sigma_{\rm max}$ become dramatically larger for g_1-modes, as a consequence of the neutral frequency ($\omega_{\rm tot} \to 0$) that triggers instability (cf. Fig. 7 in [41]). Additionally, to account for those precursors occur within 1 s prior to the merger, we vary $B_\star$ to match the resonant time of g_2-modes temporally with the aforementioned precursors.

In Tab. 4.3, we show in the second column the characteristic strength of the magnetic field $B_\star$ such that the orbital frequency starts sweeping through the resonance interval defined by modified mode frequency, i.e., $|1-2\Omega_{\rm orb}/\omega_{\rm tot}| \lesssim \epsilon$, at the moment the corresponding precursor

[9] The stratification $\delta = 0.01$ we used to match the data of precursors in Tab. 4.3 is higher than the typical value taken for NSs, which is $\delta = 0.005$ [140, 235]. This degree of stratification may still be sensible for the resonances of high order modes along the inspiral rapidly absorb tidal energy. Besides, the dissipation of mode energy via GW is extremely inefficient for g-mode [50, 53], which ranges from tens to thousands of years for g-modes in this work. Therefore, the energy absorbed by high order g-modes will retain in the star until final merger with negligible dissipation.

occurs. The third towards the final columns are, respectively, the resonance duration $t_{\rm res}$, the waiting time $T_{\rm wt}$, the energy restored in the (crustal) region where crust yields (see Sec. 4.6.3.2), and the orbital frequency inferred by the resonant time (We note that here g_2-mode resonances has been included, which was ignored in Tab. 4.2). With the same $B_\star$ as GRB 090510a, we find that for GRB 090510b one requires a stellar spin of $\nu = 68.62$ Hz so that the inertial frame frequency is reduced, else it is impossible to match the mode frequency with its waiting time of $T_{\rm wt} = 13$ s. However, this implies an unphysically steep spin-down between GRBs 090510b and 090510a, i.e., $\Delta\nu = 68.62$ Hz in less than 13 s. The tension can likely be alleviated if we also consider a rotation for GRB 090510a, then we find a $B_\star$ such that the rotation rates responsible for GRBs 090510a and 090510b are not so different. In any case, we analysis GRB 090510b by using the same $B_\star$ as GRB 090510a in Tab. 4.3.

In Fig. 4.12, we plot the precursors in Tab. 4.3 labeled by $B_\star$ in the second column, and the overplotted curve represents the orbital evolution with only tidal effects of the f-mode. The label of GRB 090510b includes the rotation rate mentioned above. We see that the inferred orbital frequencies involving the resonances of g_2-modes (coloured symbols) are almost the same as the values predicted when only f-mode effects are considered (blue curve, the final column of Tab. 4.2), reflecting the fact that the g_2-mode resonances barely affect the orbital evolution.

In addition, the resonances of the g_1-mode may precede the merger by more than 10 s for the toroidal-to-poloidal ratio in the range for a stable magnetic field, i.e. $10^{-3} \lesssim \Lambda \lesssim 0.3$ [236, 274]. The same stands even when stellar rotation is considered since rotation decreases the frequencies of $l = 2 = m$ g-modes. Therefore, instead of appealing to stellar rotation to account for GRB 090510b, one may use the resonance of g_1-mode to account for GRB 090510, viz. the two events could be accommodated by a g_1 and a g_2 excitations, respectively (see Sec. 4.6.2 for details).

Although not considered in the present article, we note that the situation will be adjusted to some extent if a solid crust is involved. In general, the (elastic) crust renders two damping mechanism in stars by the bulk and the shear viscosities. In a cold neutron stars, the dissipation by the shear viscosity dominates over the bulk viscosity for g-modes [300], which has the typical timescale of ~ 1000 years [301] thus may not suppress significantly the amplitude of the resonantly-excited g-modes in binaries. Accordingly, the proxies of the influence of the presence of the crust are the corrections in the tidal overlap, the mode frequencies, and the mode's eigen-functions.

As demonstrated in, e.g., [52], crust will expel the eigen-function of the core (surface) g-modes out of the surface (core), leading to higher mode frequencies for both classes. The crustal strain caused by the core g-modes is thus negligible, and the relevant g-modes for precursors are the surface g-modes. These latter modes have frequencies marginally larger than the frequencies of the g-mode of single component fluid stars, which is $\sim$100 Hz. As a

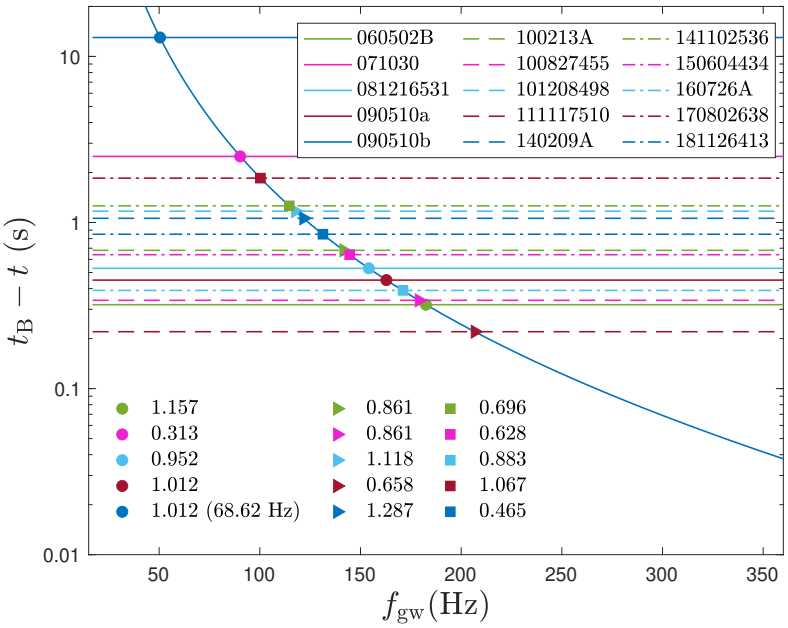

Figure 4.12: Time prior to the main burst, which is assumed to coincide with the coalescence, as a function of gravitational wave frequency $f_{\rm gw} = \Omega_{\rm orb}/\pi$. The solid line represents the evolution with tidal effect of f-mode but not g_1-mode for the non-rotating and non-magnetized star with EOS SLy and $M = 1.27M_\odot$. The time of precursors reported in Tab. 4.2 are plotted as horizontal dashed lines. Markers are labeled by the characteristic magnetic field strengths $B_\star$ given in the unit of B_{15} for which the resonance frequencies of g_2-modes $\omega_g = 2\pi f_{\rm gw}$ match the precursor events. The number in the parenthesis is rotation rate for GRB 090510b.

Table 4.3: The relative quantities of the resonances matching temporally with listed precursors in Tab. 4.2.We assume the resonances of g_2-modes for an equal mass binary, whose constituents obey the SLy EOS and have $M_\star = 1.27 M_\odot$. We set $\Lambda = 0.01$, $\nu = 0$ Hz, and $\delta = 0.01$. GRBs 100717 and 130310 are not included since they are not suitable for the g_2-mode of this star.

Precursor Event	$B_\star$ (B_{15})	$t_{\rm res}$ (s)	$T_{\rm wt}$(s)	$\sigma_{\rm max}$	Fracture Energy (E_{45}·s)	Orb. freq. [$\Omega_{\rm orb}$ (Hz)]
GRB 060502B	1.157	0.140	0.32	0.047	1.60	573.23
GRB 071030	0.313	0.286	2.50	0.091	1.13	283.49
GRB 081216531	0.952	0.140	0.53	0.056	1.76	484.15
GRB 090510a	1.012	0.133	0.45	0.053	2.24	511.64
GRB 090510b	1.012[a]	0.428	13.00	0.151	10.96 (+1.58) [b]	158.41
GRB 100213A	0.861	0.152	0.68	0.061	1.70	445.02
GRB 100827455	1.118	0.122	0.34	0.048	1.73	562.59
GRB 101208498	0.658	0.180	1.17	0.072	1.63	369.74
GRB 111117510	1.287	0.106	0.22	0.042	0.36	649.86
GRB 140209A	0.696	0.175	1.06	0.070	2.25	382.51
GRB 141102536	0.628	0.184	1.26	0.074	1.57	360.17
GRB 150604434	0.883	0.148	0.64	0.059	1.96	454.32
GRB 160726A	1.067	0.127	0.39	0.051	1.91	537.55
GRB 170802638	0.465	0.211	1.85	0.083	1.20	315.16
GRB 181126413	0.779	0.162	0.85	0.065	1.70	412.62

Notes:

[a] There is no $B_\star$ that can make the resonance happen at 13 s prior to the main burst; instead, for this event, we use the same $B_\star$ as GRB 090510a and vary the rotation frequency. Precursor time matches the resonant time as $\nu = 68.62$ Hz.

[b] The number in the parentheses is the rotational energy.

consequence, the corresponding resonance will occur at a later time comparing to those of the former. Additionally, the tidal overlap for surface g-modes are expected to be smaller than fluid g-modes due to their nearly vanishing eigen-functions over most of the interior. The delay in the g-mode resonances and the reduction of the associated tidal overlap due to the existence of the crust suppress the mode amplitude available during the resonance timescale. However, a detailed computation is needed to evaluate the applicability of this scenario if the crust is included.

4.6.3 Energetics

During the resonance, the mode amplitude increases rapidly, stretching the crust more strongly over time. We remain that here the crust is defined to be the region ranging from $0.9R_\star$ to the stellar surface ($\gtrsim$ 1 km). Denoting the maximal value of the crustal strain induced by a QNM when its amplitude reaches the peak during resonance as $\sigma_{\rm max}$, the crust fails when $\sigma_{\rm max}$ exceeds some maximal breaking strain $\sigma_{\rm vM}$ that the crust can sustain (Sec. 4.6.3.1).

4.6.3.1 Breaking Strain

The critical value $\sigma_{\rm vM}$ is hard to determine, and, in principle, it may depend on the duration of stress (or the timescale of the mechanism that generates the stress), density, temperature, and composition of the crust, and so on [46]. In recent molecular dynamics simulations, by adopting Zhurkov's model for breaking mechanism, [46] found a universal expression for $\sigma_{\rm vM}$ [see their Eq. (6)]. There are several combinations of density and temperature having been studied in literature, e.g., the crust with the density of 10^{13} g/cm^3 and $T = 0.1$MeV$\approx 10^9$K corresponds to $\sigma_{\rm vM} \approx 0.1$ [45], while $\sigma_{\rm vM} \gtrsim 0.11$ for a density of 10^{14} g/cm^3 and $T \gtrsim 10^8$ K [47].

In addition, [49] follow a semi-analytical approach to calculate $\sigma_{\rm vM}$ for low temperature stars (see also [48]). They found that, assuming the absence of the pasta phases, $\sigma_{\rm vM} \sim 0.04$ which is density independent. In this work, we adopt $\sigma_{\rm vM} \sim 0.04$ as in [41], while we note that if $\sigma_{\rm vM} \sim 0.1$ had been adopted, crustal failure would entail a larger mode amplitude. In Fig. 4.13 we show the distribution of crustal strain generated by the g_1- and g_2-modes of the primary as a member of an equal-mass binary at the peak of resonance with some fixed stellar parameters. Both show that the region under the relatively strong strain is narrow. Regions that fracture are restricted to the equatorial regions ($0.25\pi \lesssim \theta \lesssim 0.75\pi$), indicating the crack is more likely to happen at these areas.

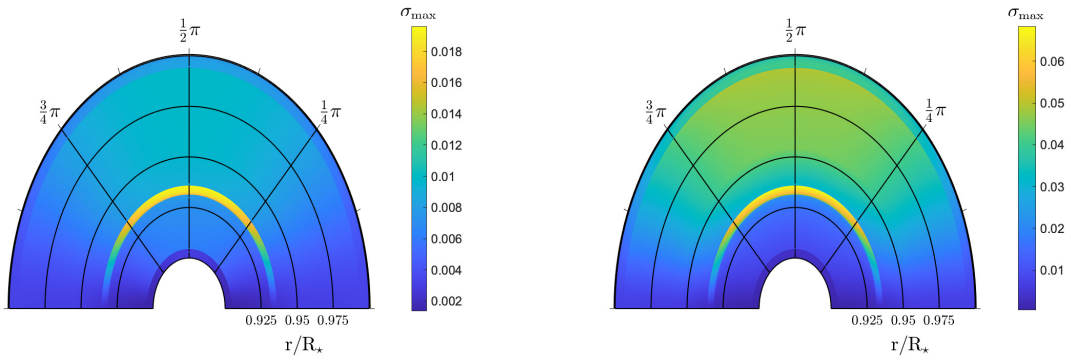

Figure 4.13: Configuration of crustal strain σ by the g_1-mode (left panel) and the g_2-mode (right panel) of the non-magnetized star with EOS SLy having $M_\star = 1.27M_\odot$ (the one used in simulating the orbital evolution in the final column of Tab. 4.2) at the offset of resonance. We fix $\delta = 0.005$ and adopt a log-linear grid to shrink the core region for illustration purposes.

4.6.3.2 Energy Release

To see if the precursor flares could fit in the context of SGRB precursors, it necessitates an estimation of the amount of energy potentially released due to crustal fracturing.

Assuming that the onset of the resonance is at $t = 0$ (this assumption is introduced for convenience and is valid only in this section), the liberated energy during the resonant shattering [221, 302],

$$\int dt E_{\rm quake} = \int_0^{t_{\rm res}} dt \int_{V_{\rm crack}(t)} \sqrt{-g} d^3x U(t, \mathbf{x}), \tag{4.67}$$

is obtained by temporally integrating the energy stored in the cracking area over the resonant duration $[0, t_{\rm res}]$, where $U(t, \mathbf{x})$ is the energy density (see below). In reality the cracking region, defined by

$$V_{\rm crack}(t) = \{p \mid \sigma(p) \geq \sigma_{\rm vM},\ p \text{ is a point in the crust}\}, \tag{4.68}$$

and the energy density, $U(t, \mathbf{x})$, are time-dependent. However, we approximate the energy released during a resonant timescale by integrating the energy density at the *onset* of resonance over the cracking area at the *offset* of resonance [41], namely

$$\int dt E_{\rm quake} \approx t_{\rm res} \times \int_{V_{\rm crack}(t_{\rm res})} \sqrt{-g} d^3x U(0, \mathbf{x}). \tag{4.69}$$

The available energy density includes the kinetic energy denisty of oscillation modes, $U_{\rm kin}$ [303], the rotational energy density, $U_{\rm rot}$ [304, 305], the magnetic energy density, $U_{\rm mag}$ [237], and the tidal energy density, $U_{\rm tid}$. The expressions for each of the contributions are,

respectively, given by

$$U_{\rm kin} = \frac{1}{2}(\rho + p)e^{-2\Phi}\frac{\partial \xi_i}{\partial t}\frac{\partial \bar{\xi}^i}{\partial t}, \tag{4.70a}$$

$$U_{\rm rot} = \frac{1}{2}\Omega^2 r^2 \sin^2\theta(\rho + p)e^{-2\Phi}, \tag{4.70b}$$

$$U_{\rm mag} = \frac{1}{8\pi}e^{-\Phi}B^\mu B_\mu, \tag{4.70c}$$

and

$$U_{\rm tid} = \phi^T \delta\rho, \tag{4.70d}$$

where we reduce $U_{\rm rot}$ to the uniform rotation case and the frame-dragging is not taken into consideration [306].

For those resonances explored in Tab. 4.3, the expected fracture energies are listed in the final column. We find that the kinetic energies of resonantly excited modes and the tidal energy contribute insignificantly ($\lesssim 10\%$) to the energy released as described by Eq. (4.69) unless the resonance onsets in the final stages of inspiral, $a \lesssim 6R_\star$, in agreement with the findings of [41].

4.7 Exploring the parameter space

The duration and timing of mode resonances are influenced by various parameters, including the mass of the primary $M_\star$ and the companion $M_{\rm comp}$ (or the mass ratio q between them), stratification δ, rotation frequency ν, characteristic magnetic strength $B_\star$, the poloidal-to-toroidal strength Λ and EOS. This section is devoted to a detailed investigation of mode resonances over a multidemensional parameter space spanned by these parameters. In Sec. 4.7.1 we investigate the impact of the mass ratio q on the maximal strain $\sigma_{\rm max}$ under fixed stratification strength δ and magnetic field. In Sec. 4.7.2 we assume equal-mass binaries to explore how other parameters affect $\sigma_{\rm max}$.

4.7.1 Unequal-Mass Binaries

We assume the same EOS for both of them, as that is the assumption adopted by [22]. The magnetic field is considered to be purely poloidal ($\Lambda = 1$), for which a field strength of a few 10^{15} G is needed to shift the frequencies of g_1-modes by a noticeable amount while a few 10^{14} G can already shift the frequencies of g_2-modes considerably (cf. Fig. (7) of Paper I). Consequently, we set $B_\star = 10^{15}$ G in this section. In addition, we fix $\delta = 0.005$ to evaluate the maximal crustal strains of the primary by g_1- and g_2-modes. Restricting the masses

of both components within the range[10] $(0.4, 2.2)M_\odot$, we find for aforementioned EOS that despite increasing with q, $\sigma_{\rm max}$ depends only slightly on q even in extreme cases. For g_1-modes, the difference in $\sigma_{\rm max}$ among binaries with a fixed $M_\star$ is $\lesssim 0.005$, while the difference is $\lesssim 0.01$ for g_2-modes. For the pure poloidal magnetic field considered here, only those extreme cases of binaries, whose primaries have either $M_\star \gtrsim 2M_\odot$ (for SLy, WFF1, and WFF3) or $M_\star \lesssim 0.9M_\odot$ (for WFF2-3 and APR4), $\sigma_{\rm max}$ by g_1- or g_2-modes can achieve the von Mises threshold.

While for a particular primary, $\sigma_{\rm max}$ depends only slightly on the companion (i.e., insensitive to q), the hosting-binary tends to have relatively small symmetric mass ratio $q_{\rm sym}$ [defined in Eq. (3.18) while we denote it as $q_{\rm sym}$ in the present Chapter], since the von Mises criterion is met for the primary with either large or small mass. Assuming a skewed normal distribution of the mass of NS in a NSNS binary, [309] estimates the proportion of NSNS binaries having a component with mass out of the range $(\sim 1.1, \sim 1.55)M_\odot$ is less than 5%, while [307] assumes a normal distribution instead, the result is almost the same. In addition, the authors of the former reference find that less than 0.64% for the mass lying out of $(\sim 1, \sim 1.7)M_\odot$. The rareness of precursor-hosting SGRBs, e.g. $\sim 0.5\%$ in *Swift* data [125] or $\sim 3\%$ in BATSE data [310], is compatible with the above estimation. Although the above point is certainly not conclusive, it does hint that a NSNS binary with relatively small symmetric mass ratio may be tied to precursor activity.

In Fig. 4.14 we plot the maximal strain $\sigma_{\rm max}$ available during the resonances of g_1- (left panels) and g_2-modes (right panels) for EOS WFF1, respectively, with a variety of chirp masses (3.17), and mass ratios q. We see that for a fixed $\mathcal{M}$, the von Mises criterion is met ($\sigma_{\rm max} \gtrsim \sigma_{\rm vM}$) by g_1 and g_2 excitations for small or large q. For instance, if a binary with the WFF1 EOS has a chirp mass at the similar level of GW 170817 ($\mathcal{M} = 1.186M_\odot$), the resonances of g_1- and g_2-modes can generate $\sigma_{\rm max} \gtrsim \sigma_{\rm vM}$ with a mass ratio $q \gtrsim 1.14$ and $q \lesssim 0.45$, respectively. In addition, the points with almost the same colour represent binaries with the same primary, which indicates that, for a given primary, $\sigma_{\rm max}$ depends mildly on q.

The region in the parameter space over which crustal failure may occur will be expanded, viz. more systems $(M_\star, M_{\rm comp})$ are likely to host a crack, if stars rotate moderately or the magnetic field has strong enough toroidal component in that mode frequencies are shifted downward resulting in longer resonances. In Fig. 4.15 we show $\sigma_{\rm max}$ as a function of ν. We can see that these systems are capable of producing $\sigma_{\rm max} \gtrsim \sigma_{\rm vM}$ at some certain range of ν, e.g., when 31.33 Hz $\lesssim \nu \lesssim$ 46.54 Hz for the binary with the APR4 EOS, $M_\star = 2.19M_\odot$, and $M_{\rm comp} = 1.39M_\odot$. The influences of Λ and ν on $\sigma_{\rm max}$ will be postponed until Sec. 4.7.

The leading-order (5PN) tidal effects in GW waveforms, measured by the advanced Laser Interferometer Gravitational-wave Observatory (aLIGO) and other ground-based GW detec-

[10] The considered range for $(M_\star, M_{\rm comp})$ covers a wide part of the parameter space compared to the NSs that have been observed (mostly from pulsar observation, cf. Fig. 2 of [307], see also Fig. 28 of [308]), which ranges from $\sim 1M_\odot$ to $\sim 2M_\odot$ with a few outliers. However, we also consider stars with $M < 1M_\odot$ for completeness.

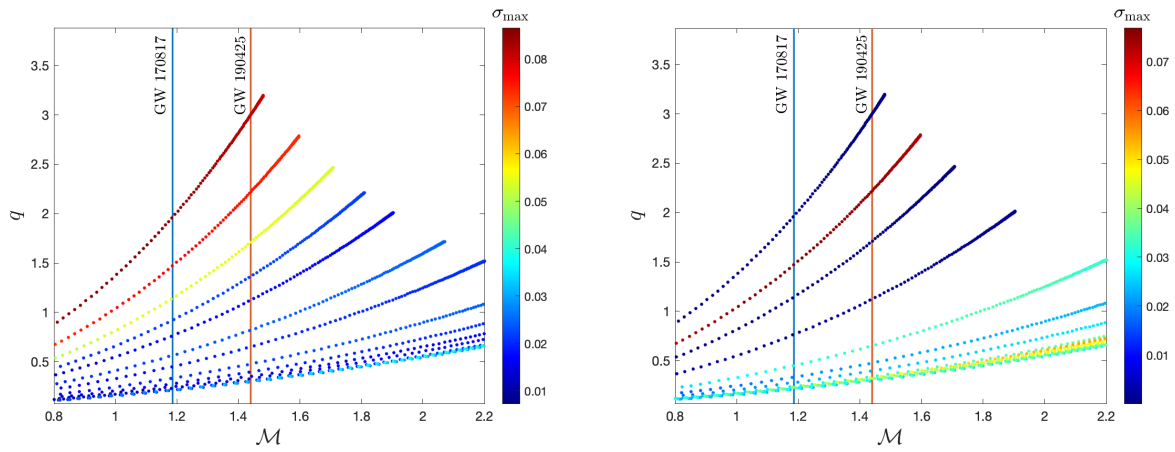

Figure 4.14: Maximal strain $\sigma_{\max}$ by g_1-modes (left panel) and g_2-modes (right panel) available during a resonant timescale for systems of EOS WFF1 with several chirps masses $\mathcal{M}$ and mass ratios q. The blue vertical line shows the chirp mass of the progenitor of GW 170817, while the red similarly corresponds to GW 190425.

tors, are encoded in the phase variation [76, 77, 311]

$$\Delta\varphi = -\frac{65}{4}\int \mathcal{M}^{-10/3} q_{\rm sym}\Lambda\Omega_{\rm orb}^{2/3} d\Omega_{\rm orb}, \tag{4.71}$$

where the tidal deformability Λ is given by

$$\Lambda \propto \frac{1+12q}{(1+q)^5}\Lambda_1 + \frac{1+12/q}{(1+1/q)^5}\Lambda_2, \tag{4.72}$$

with Λ_1 and Λ_2 being the (dimensional) tidal Love numbers of the primary and the companion, respectively [75, 312]. It has been shown that for $\mathcal{M} \lesssim 1.5M_\odot$ and under the common EOS assumption, Λ_1 and Λ_2 relate to each other via (see Eq. 8 of [116])

$$\Lambda_1 \simeq q^6\Lambda_2, \tag{4.73}$$

translating Eq. (4.72) to

$$\Lambda(q,\Lambda_1) \propto \frac{12+q+q^2+12q^3}{q^2(1+q)^5}\Lambda_1. \tag{4.74}$$

As a result, Λ decreases quite fast for large q, e.g., fixing Λ_1 and comparing a binary with $q = 1.3$ (or $q_{\rm sym} = 0.246$) to an equal mass binary ($q_{\rm sym} = 0.25$), we find $\Lambda(1.3,\Lambda_1)/\Lambda(1,\Lambda_1) = 0.47$. On that account, any GW-related constraints that might arise from the system are weaker. Further, the total emitted GW energy is a decreasing function of q during both the inspiral and the post-merger phase [313]. In the ideal situation in the future where one observes a precursor and GWs from the same inspiral, unequal mass binaries provide marginally worse information from GWs even if they are more likely to cause crustal fractures.

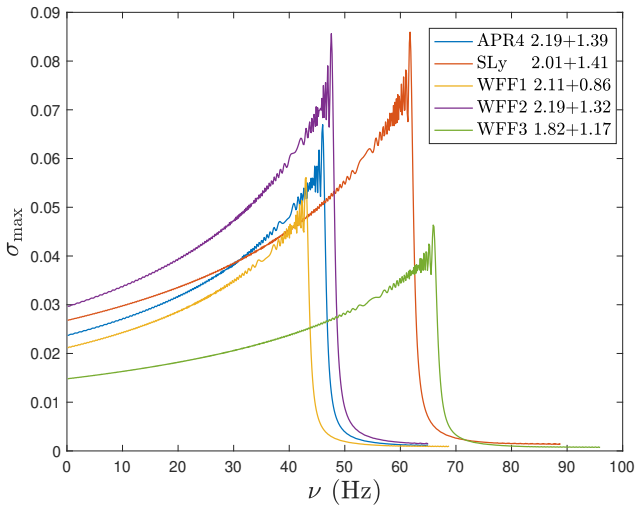

Figure 4.15: Maximal crustal strain $\sigma_{\max}$ induced by g_1-modes as functions of rotating rate ν. Labels of systems comprise the EOS that is obeyed by the primary and the companion, and the masses of these two components (in units of $M_\odot$).

There is a trade off of sorts therefore.

4.7.2 Dependence on Magnetic Field and Stratification

According to the previous discussion, although crust failure tends to occur in a primary that is a member of a binary with small symmetric mass ratio, $\sigma_{\rm vM}$ is insensitive to q for a fixed $M_\star$ (see the discussion of Fig. 4.14). In addition, studying the whole multidimensional parameter space is laborious so that we concentrate on equal-mass binaries ($q = 1$) in this subsection and emphasise the impact of magnetic field, which is parameterised by $B_\star$ and Λ, and stratification δ on $\sigma_{\max}$.

In Fig 4.16 we show $\sigma_{\max}$ of g_1-modes for some models with the EOS introduced above as functions of δ, where we set $\Lambda = 1$ (purely poloidal) and $B_\star = 2.5 \times 10^{15}$ G. Two kinds of tendencies are observed: (i) $\sigma_{\max}$ increases with δ for stars with either high or low compactness; (ii) $\sigma_{\max}$ decreases with increasing δ for stars having moderate compactness. We see that $\sigma_{\max}$ for stars of the first tendency are larger, suggesting again the tidally-driven shattering favours stars with strong or weak gravity. In addition, the frequency of g-modes, as well as the tidal overlap, decreases with δ; stipulating a small δ, resonances happen at low orbital frequency thus have longer resonant duration (NSs shrink slowly at large separation), while the weaker coupling strengths limit the growth of mode amplitudes. One thus weights these two effects in to determine $\sigma_{\max}$, which can be roughly estimated by the product of resonant duration and tidal overlap. Inflection points exist on some curves for moderate-compact stars, where the resonant duration and the tidal overlap strength offset each other most. Right to these points, the large overlap compensates the short resonant duration, while

the long resonance makes up the small tidal coupling for the other part. Additionally, we note that if we adopt $\sigma_{\rm vM} \sim 0.1$, then all the cases presented in Fig. 4.16 is not able to meet the von Mises criterion.

In line with recent suggestions by [147], our calculations show that crustal failure can happen for a wider range of stellar models when δ is larger (cf. Fig. 4.16), while the inclusion of magnetic fields and stellar rotation enriches the picture further. For both g_1- and g_2-modes, a pure poloidal magnetic field ($\Lambda = 1$) shifts mode frequencies upward, leading to shorter resonant time. On the opposite, either the toroidal component of magnetic field or the rotation of the equilibrium configuration can give rise to a larger $\sigma_{\rm max}$ due to the negative shifts in mode frequencies. GRBs 090510 *a* and *b* have been accounted for by the rotation of the primary (Tab. 4.3). In certain range of Λ, the mode modifications for g_1- and g_2-modes have different signs (see Fig. 4.6). The negative shifts for g_1-modes make them resonant with the earlier orbital frequency, while the positive shifts for g_2-modes delay their resonances. Therefore, g_1-modes will be resonantly excited *prior to* g_2-modes if strong magnetic field is present. For instance, setting $\Lambda = 0.18$ and $B_\star = 2.85 \times 10^{15}$ G, we find that the resonances of g_1- and g_2-modes for the primary with EOS WFF1 and $M_\star = 0.86 M_\odot$ occur at, respectively, $t = 12.95$ s and $t = 0.42$ s. Therefore, a magnetic field with toroidal component may present another scenario that may account for the two GRBs 090510a and 090510b.

In Fig. 4.17, we show $\sigma_{\rm max}$ by g_1- and g_2- modes for some fixed stellar parameters over the parameter space spanned by Λ and ν. It can be observed that $\sigma_{\rm max}$ for the g_2-mode reach values above 0.04 for a certain region of the two dimensional parameter space, while the von Mises criterion is not met for the non-spinning model with pure poloidal magnetic field (bottom left and right cells in Fig. 4.17). For both g_1- and g_2-modes, the optimal $\sigma_{\rm max}$ is two times higher than the non-rotating models with $\Lambda = 1$. Our results can be summerised as follows:

1. When other parameters are fixed, the maximal crust strain $\sigma_{\rm max}$ is an increasing function of stratification δ. Defining the optimal region as the set of combination of Λ and ν for which $\sigma_{\rm max}$ is at the greatest level of the colorbar beside the figures, a lower Λ (stronger toroidal field) or higher spin is necessary for the optimal case. In addition, the optimized $\sigma_{\rm max}$ does not depend on $B_\star$.

2. Although $B_\star$ changes the pattern of $\sigma_{\rm max}$ as a function of Λ and Ω, the value of $\sigma_{\rm max}$ remains unchanged. In addition, the optimal situation for g_1- and g_2-modes with stronger $B_\star$ requires faster spins.

3. Over the optimal region of each mode, g_2-modes cause stronger strains $\sigma_{\rm max}$ than g_1-modes. Yet, optimal cases of g_2-modes require the magnetic field to have a dominant toroidal field ($\Lambda \approx 10^{-2}$), which thus constrains the maximum alowed values of $B_\star$ [235].

Although the effects of rotation and magnetic field create some room for potential crust

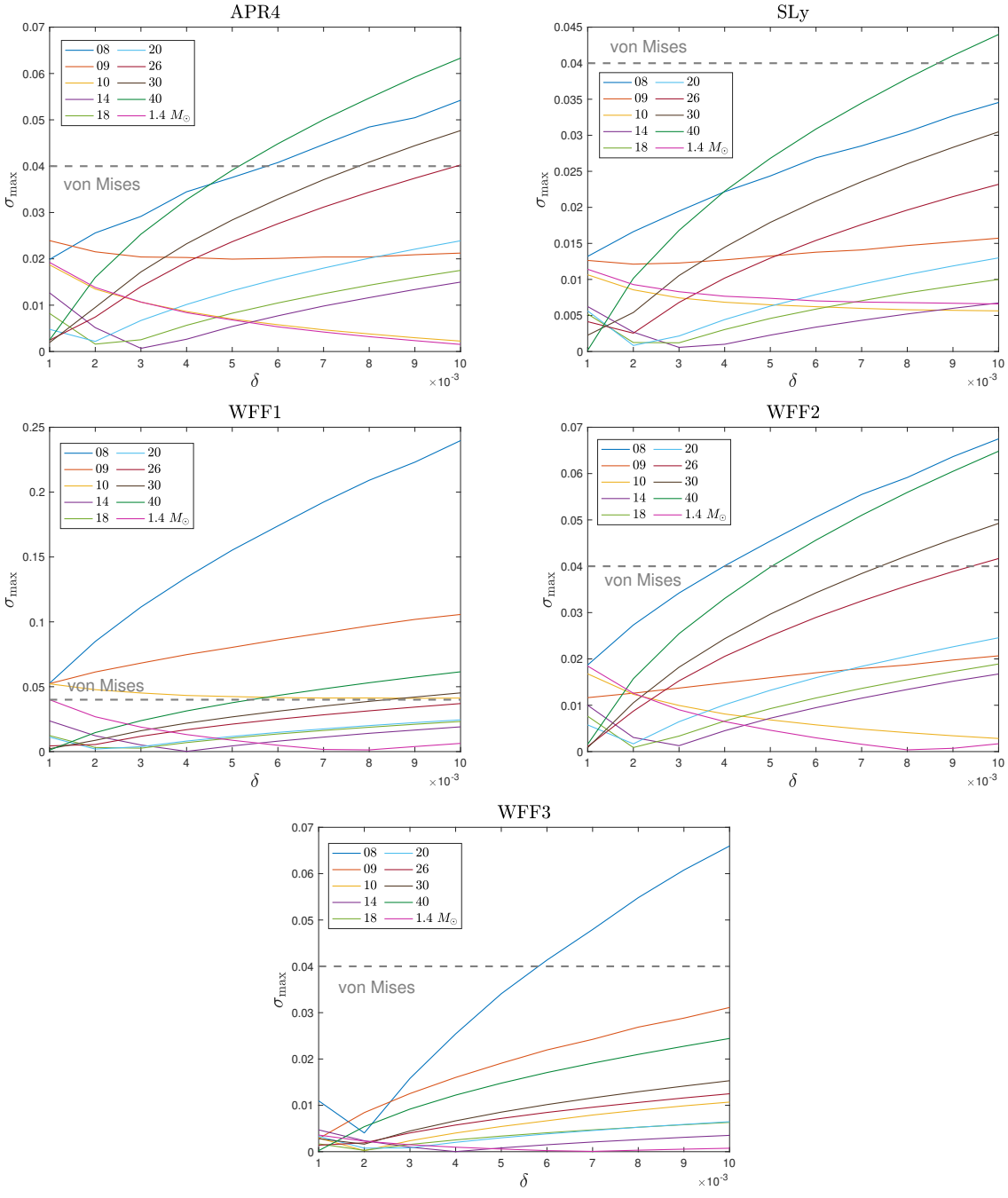

Figure 4.16: Maximal crustal strain $\sigma_{\max}$ due to g_1-modes of some chosen models of each EOS as functions of δ. The charateristic magnetic strength is fixed as $B_\star = 2.5 \times 10^{15}$ G. The horizontal dashed lines mark the von Mises criterion.

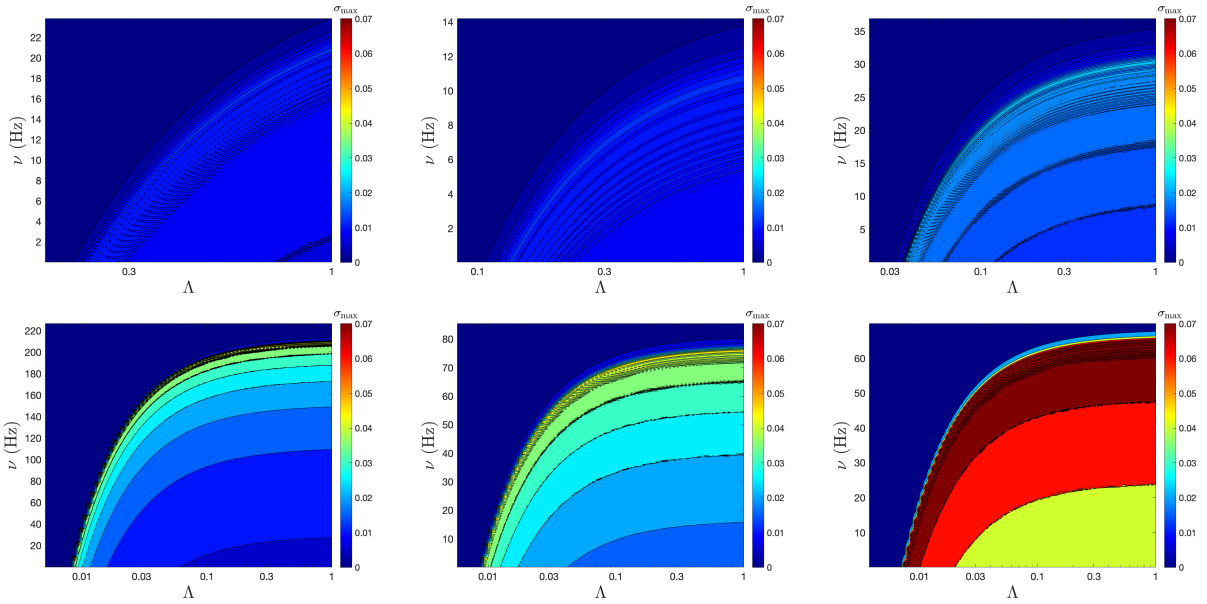

Figure 4.17: Maximal crustal strain by g_1- (top row) and g_2-modes (bottom row) as functions of δ and Λ for the star with EOS SLy and $1.27M_\odot$. Brighter shades indicate a greater value for $\sigma_{\max}$. The parameters $(B_\star, \delta)$ are, from left to right panel, taken as $(2, 0.005)$, $(1, 0.005)$, and $(1, 0.01)$ for the datum of g_1-mode, while they are $(0.8, 0.005)$, $(0.5, 0.005)$, and $(0.5, 0.01)$ for the datum of g_2-mode. Here $B_\star$ is given in the unit of B_{15}.

failure in the parameter space, the parameters should still be fine-tuned to generate a strain $\sigma_{\max} > \sigma_{\rm vM}$. In other words, a given precursor event may set stringent constraints on the properties of the individual stars in a binary.

4.8 Discussion

With multi-staged SGRBs, namely those including precursors, main events, and afterglows, we can garner better knowledge about the properties of the progenitors and fundamental physics governing NSs, such as their EOS. For instance, strongly magnetized remnants from binary mergers, as inferred from X-ray plateaus observed in some SGRB afterglow light curves [314, 315] or early X-ray flares observed in SGRB light curves [316], may hint that the progenitors consist of at least one highly magnetized NS from a flux conservation argument [317]. Detailed studies of SGRBs may also unveil the nature of their central engines. Analysing precursors may therefore shed light on the qualitative properties of the progenitors, and could tightly constrain the stellar parameters of the merging stars [39–41, 147, 227].

To explore the connection between crustal fractures and precursors, we adopt the theoretical framework detailed above: we consider the tidal resonance between QNMs and the orbit, where we treat general-relativistic QNM spectra, and the orbital dynamics involves up to the 3 PN effects including the 2.5 PN scheme for gravitational back-reaction. The modification of mode frequencies by perturbing forces from magnetic fields [Eq. (4.53)], tidal field

[Eq. (4.46)], and stellar rotation [Eq. (4.61)] are also taken into account. When a particular mode is brought into resonance – as defined by the time interval when the orbital frequency and the (modified) mode frequency are matched to some extent [Eq. (4.45)] – the mode amplitude increases rapidly. If the maximal amplitude available during a resonant timescale, the crustal fracture may be caused. Over the yielding area, stored energy will be released in some form [Eq. (4.69)]. Taking a particular binary and some fixed stellar parameters, we match the data of precursors by varying $B_\star$ to make the onset of resonances coincide with the moment (relative to the main event) precursors are detected (Tab. 4.3). Assuming all released energy is transformed into electromagnetic radiation (estimated in the 6th column of Tab. 4.3), SGRB precursor events may be accommodated, energetically speaking, by crust failure. On the other hand, we present two scenarios for SGRBs hosting two precursors, e.g. for GRB 090510 either the spin down of the primary leads to the same mode gets resonant twice at different moments [Tab. 4.3] or the resonances of g_1- and g_2-modes when the magnetic field has toroidal component.

We find that for a given primary, a relatively large mass ratio is more favourable for crustal fracture (Fig. 4.14). However, the price to pay is the detectability of the tidal imprints in GW [Eq. (4.74)]. In addition, we find that for certain combination of stellar parameters the von Mises criterion can be met. For instance, when ν and Λ are tuned to particular values (the brightest region in Fig. 4.17) the strain exceeds $\sigma_{\rm vM}$. In other words, as long as precursors prove to set constraints on the properties of progenitors, the constraints are going to be stringent because several parameters are limited simultaneously.

Tidal effects have been studied in various aspects, such as from the GW energy spectrum [318, 319], the NS tidal disruption signal for binaries having a least one NS [320, 321], and numerical simulations of NSNS mergers (see [322] for a detailed review). The aforementioned investigations are devoted to the prospect of extracting information about the EOS from the very final stage of inspiral ($f_{\rm GW} \sim 1000$ Hz [323]). Precursors, however, offer an extra probe into the details of EOS when $f_{\rm GW} \sim 100$ Hz (cf. Fig. 4.12), which is also the most sensitive band of (ground-based) interferometers such as aLIGO, Virgo, and KAGRA [324, 325]. Therefore, an application of this framework to future precursor data together with prospective GW detections may result in strong tests of the neutron star EOS [326].

Chapter 5

Measuring spin in coalescing binaries of neutron stars showing double precursors

Contents

Breakdown of Contributions

The code for evolving binaries is extended to the accuracy of 3rd post-Newtonian order by me from the previous code, which tackles at 2nd order motion, of Kostas D. Kokkotas. My contributions are producing all the plots and collaboratively writing the manuscript with Arthur G. Suvorov. Kostas D. Kokkotas assists with discussion and provides critical comments on the manuscript.

Overview

Short gamma ray bursts resulting from binary neutron-star mergers are sometimes preceded by precursor flares. These harbingers may be ignited by quasi-normal modes, excited by orbital resonances, shattering the stellar crust of one of the inspiralling stars up to $\gtrsim 10$ seconds before coalescence. In the rare case that a system displays two precursors, successive overtones of either interface- or g-modes may be responsible for the overstrainings. Since the

frequencies of these overtones have an almost constant ratio, and free-mode frequencies for rotating stars are shifted relative to static ones, we suggest that precursor timing in systems showing double events may be used to deduce the spin frequency of the flaring component. As a demonstration of the method, we find that the precursors of GRB090510 hint at a spin frequency of ~ 60 Hz for the star if g-modes account for the events.

5.1 Introduction

Some short gamma-ray bursts (SGRBs), which are thought to originate from binary neutron-star (NS) mergers, are preceded by precursor flares with time advance ranging from ~ 1 to $\gtrsim 10$ s [34, 36–38]. These early flashes may be caused by crust yielding in magnetised NS members, resulting from resonantly excited quasi-normal modes (QNMs) [39–41] (see also Chap. 4). In this context, the timing of a precursor relative to the SGRB, which depends on a jet formation timescale, estimates the frequency of the mode that leads to the crustal fracture. On rare occasions, more than one precursor precedes the SGRB, for which the frequencies of the two responsible modes may be acquired (see Sec. 4.6). Certain details of the fabric of the NS can thus be accessed since the QNM spectrum is sensitive to the particulars of the stellar interior; for instance, frequencies of pressure modes (f- and p-modes) strongly correlate to the interior mean density [118, 121], and g-modes encode microphysical temperature or composition gradients.

Here we discuss a novel way to learn the spin of a NS if a double precursor event is observed. In particular, mode frequencies in a rotating-NS attributable to the pre-emissions provide two relations between the free mode frequencies of these two modes and the stellar spin. In scenarios where the free mode frequencies have a constant ratio, such as for g- and i-modes as explained below, this additional relation then admits an inference of spin. In the current phase of gravitational-wave (GW) astrophysics, estimating the spins of binary NSs is crucial in shrinking down the error in other measurements [144, 327, 328]. For instance, the tidal deformabilites of GW170817 and GW190425 are only determinable under certain spin priors of the progenitors [12, 329]. In addition, simultaneous knowledge of the spin, and the mode frequencies may set strong constraints on EOS (e.g., [330]). A particular example to manoeuvre out stellar spin is implemented for SGRB 090510, an event preceded by two precursors occurring ~ 13 and $\lesssim 1$ s prior to the main burst, respectively [34]. Some discussion on blue/red kilonovae and GWs from the remnant is also offered.

5.2 GRB precursors via g-mode resonances

Although the definition of pre-emission in SGRBs is not uniquely given, e.g., some authors require the waiting time to be longer than the main burst duration [36] while others do

not [37], precursor flares have been confidently identified in rare ($\lesssim 10\%$) cases [38]. These early flares may be triggered by certain, resonantly-excited QNMs [39,41] (see also Chap. 4). The orbital (linear) frequencies of precursors, which are uncertain because there is a delay between the main episode and the merger through a jet formation timescale, suggest that modes with frequencies ~ 100 Hz are promising to account for the pre-emissions; in particular, shear-, interface-, and g-modes have attracted some attention [39,40]. We focus on the g-mode scenario in this Chapter, though a discussion about other modes is given in Sec. 5.4.3.

5.2.1 Resonant shattering via g-modes

Composition and/or the temperature gradients in NSs support g-modes, whose frequency is determined by the Brunt-Väisälä frequency. Adopting polytropic EOS, we introduced in Chap. 3 a simple parameterisation for the thermally-induced stratification by assuming a constant ratio δ between the adiabatic indices of the equilibrium and the perturbations to encapsulate the Brunt-Väisälä frequency. The parameter scales quadratically with the surface temperature, i.e., $\delta \propto T_{\rm surf}^2$; a typical value for mature NSs is $\delta \gtrsim 0.005$ [154]. This parameterisation is shown to capture well he feature of thermally-restored g-modes for internal temperatures $T \lesssim 10^{10}$ K, as relevant for mature stars in coalescing binaries. The mode frequencies then read

$$f = \alpha\delta \left(M_\star R_\star^{-3}\right)^{(1-\varsigma)/2} \text{ Hz} \tag{5.1}$$

for EOS- and quantum-number-dependent parameters α and ς (see Chap. 3 for more detail). Here $M_\star$ and $R_\star$ are, respectively, the mass and radius of the NS. Given the coldness and extreme density of old NSs, there may exist superfluidity and even a hadron-quark transition in the core, both leading to larger g-mode frequencies (see, e.g., [57,59]). However, we ignore these effects in this Chapter.

As the NSs inspiral, tidal fields induce perturbing forces that act mainly at frequencies that are twice the orbital frequency [39,263]. The forced system for QNMs suggests that a particular mode will be brought into resonance when its frequency matches the forcing rate. The amplitude of that mode increases rapidly during the resonance timescale, hitting a ceiling value that depends on the so-called overlap integral. After the mode leaves the resonance window, its amplitude decays according to the associated damping rate, which is generally much longer than the rest of the life of the coalescing binary. We recall that the crustal strain exerted by the mode is determined via Eqs. (4.63) and (4.64). The modes of interest in this context are those with quantum number $l = 2 = m$ since the dominant component of the tidal field is induced by the $l = 2 = m$ piece of the gravitational potential built by the companion [263]. Therefore, we specify ourselves to modes with $l = 2 = m$ hereafter.

In addition, QNM frequencies of forced systems deviate from those of free systems (see

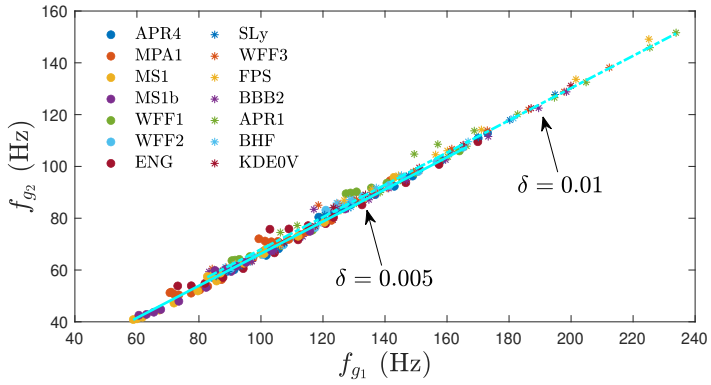

Figure 5.1: Correlation between the frequencies of g_1- and g_2-modes for EOS and two representative values of δ (see plot legends). To the modes of each δ, the relation between g_1- and g_2-modes [Eq. (5.4)] are shown as bright blue lines with the solid one for $\delta = 0.005$ while the dash-dot one for $\delta = 0.01$.

Sec. 4.4). Here we focus on the frequency shift due to rotation, and recall the equation for that: [cf. Eq. (4.61)]

$$f = f_0 - m(1 - C)\nu_\star, \tag{5.2}$$

where $\nu_\star$ is the stellar spin. The constant C is determined by Eq. (4.62), and depends on EOS and the mode quantum numbers, the azimuthal one of which, m, leads to a Zeeman-like splitting of the modes (e.g., [121]). The *free*-mode frequency of $l = 2 = m$ g_n-mode ($f_{g_n,0}$), whose radial eigenfunction has n nodes, thus relates to the *inertial-frame* one (f_{g_n}) through

$$f_{g_n} = f_{g_n,0} - m(1 - C_n)\nu_\star, \tag{5.3}$$

where C_n, defined in equation (5.2), quantifies the spin-correction. As shown in Sec. 4.4.3, rotation affects the frequencies of g_1- and g_2-modes to a similar extent. For a broad set of EOS detailed in Tab. 5.1, we find two facts about C_1 and C_2 valid for $10^{-3} \leq \delta \leq 0.05$: (i) both depend only weakly on $M_\star$ and EOS; (ii) for a given model and the described range of δ, they differ by only small amount, with the most extreme case having $|1 - C_1/C_2| \lesssim 0.13$. As such, the free mode frequency of the g_2-mode can be EOS-independently associated with that of g_1-mode, as plotted in Fig. 5.1, via

$$f_{g_2,0} = 0.62 f_{g_1,0} + 4.32 \text{ Hz} \tag{5.4}$$

for NSs with $\delta \leq 0.05$, or temperature less than 10^{10} K (see Chap. 3).

Table 5.1: Properties of the EOS used to analyse the precursors of GRB 090510. The second and the third columns show, respectively, the radius and the tidal deformability of a star with $M_\star = 1.4M_\odot$, while the final column presents the maximum mass of a static configuration supportable by each EOS.

EOS	$R_{1.4}$ (km)	$\Lambda_{1.4}$	$M_{\rm max}$ $(M_\odot)$	EOS	$R_{1.4}$ (km)	$\Lambda_{1.4}$	$M_{\rm max}$ $(M_\odot)$
WFF1	10.412	250.104	2.127	SLy	11.706	420.892	2.048
WFF2	11.124	341.859	2.194	ENG	11.969	519.308	2.238
APR4	11.446	386.820	2.168	MPA1	12.361	648.070	2.456

5.3 Spin frequency determination from precursor doubles

In this Chapter, we assume that both precursors are set off from the primary, defined as the heavier NS, and further that they are attributable to g_1 and g_2 resonances. There are other theoretical possibilities, however, notably that non-g modes are responsible or that each star releases a flare at different times rather than one star releasing both. These are discussed in detail in Sec. 5.4.3.

The orbital frequencies at which two precursors A and B are observed, denoted by ν_A and ν_B with $\nu_A > \nu_B$, should be determined by the their preceding time relative to the merger, while the measured quantity is the waiting time, i.e., the preceding time relative to the main burst. Therefore, ν_A and ν_B depend on the unknown jet formation timescale $\tau_{\rm jet}$ for the associated SGRB when the waiting time are given. Matching the tidal-driving frequency to the inertial-frame frequencies of g_1- and g_2-modes relates the mode frequencies, the NS spin, and the orbital frequencies via

$$\nu_\star(\nu_A, \nu_B, \tau_{\rm jet}) = \frac{0.62\nu_A(\tau_{\rm jet}) - \nu_B(\tau_{\rm jet}) + 2.16}{0.38 + C_2 - 0.62C_1}\ \text{Hz}. \tag{5.5}$$

Denoting the maximal, supportable mass for a particular EOS as $M_{\rm max}$, we surprisingly find that the denominator is roughly a *constant* 0.4268 with a standard variance of 0.0036 for stars having $1M_\odot \leq M_\star \leq M_{\rm max}$, for the considered EOS, and for the studied range of δ. This fact simplifies the above relation as

$$\nu_\star(\nu_A, \nu_B, \tau_{\rm jet}) = 2.343(1 \pm 0.0084)[0.62\nu_A(\tau_{\rm jet}) - \nu_B(\tau_{\rm jet}) + 0.34]\ \text{Hz}. \tag{5.6}$$

That δ is irrelevant in the above expression indicates the spin can be informed even without knowing the temperature of the star. It is conceivable somehow since here NSs are taken to be cold enough *ad hoc*, i.e., $T \leq 10^{10}$ K ($\delta < 0.05$), as appropriate for NSs in coalescing binaries (though see [331]).

5.3.1 Orbital dynamics and equations of state

The orbital frequencies associated with two precursors are determined by the numerical scheme detailed in Sec. 4.3 with the tidal effects of the $l = 2 = m$ f-modes involved. The

uncertainty of $\tau_{\rm jet}$, covering about 10-100 ms [291], gives rise to some errors in the inference of ν_A and ν_B [cf. Eq. (5.6)], while the error is narrower for the latter frequency since the changing rate of the orbital frequency is smaller at earlier stage.

Although the relation (5.6) holds for the EOS in Fig. 5.1, we, hereafter, will specify ourselves to those EOS able to support stars with mass $\gtrsim 2M_\odot$ or more – so as to be consistent with Shapiro delay measurements of PSR J0740+6620 [332] – the properties of which are listed in Tab. 5.1. The chosen EOS span a wide range of stiffness as evidenced by the radius of the star with canonical mass $1.4M_\odot$ (second column), where we see $R_{1.4}$ ranges from $10.4 - 12.4$ with 2 km wide uncertainty. The stiffness is also indicated by the tidal deformability of stars with $1.4M_\odot$ (third column) as $\Lambda_{1.4}$ ranges from ~ 250 to ~ 650 for this specific mass. These values of $\Lambda_{1.4}$ are consistent with those coming from GW170817, namely $120 \lesssim \Lambda_{1.4} \lesssim 800$ [12, 329].

5.3.2 Case study: GRB 090510

GRB 090510 displayed two precursors at 13 s and 0.45 s prior to the main event [34]. Using the orbital dyanmics procedure described in Sec. 5.3.1, and neglecting the jet formation timescale for now, i.e., taking $\tau_{\rm jet} = 0$ ms, we find $\nu_A = 72 - 83$ Hz and $\nu_B = 23 - 26$ Hz by considering a wide range of binaries for each of the EOS in Tab. 5.1: those with total mass $M_{\rm tot} = 2.5 - 3.1M_\odot$ and the mass ratio as long as the secondary having mass $> 1M_\odot$ (see below).

The spin of the primary is obtained via Eq. (5.6) for the chosen EOS, and is found to be well expressed as a function of the chirp mass via

$$\nu_\star = 57.2\,(\mathcal{M}/1.19M_\odot)^{-0.65}\ \text{Hz}. \tag{5.7}$$

The above is a consequence of the fact that the orbital frequency can be well represented as a function of the chirp mass, even though tidal deformabilities and the stellar f-modes influence the orbital dynamics. Taking two specific series of binaries, each characterised by a fixed total mass, we plot $\nu_\star$ in the left panel of Fig. 5.2 as a function of the mass ratio, q, for some particular EOS, where the solid lines represent the respective fittings (5.7). For $M_{\rm tot} = 2.5M_\odot$, one may expect the remnant to be supra-massive or even stable for the MPA1 EOS (see Tab. 5.1), surviving collapse long enough to produce an X-ray afterglow (see Sec. 5.4.2), as appropriate for GRB 090510. For this total mass, we do not consider values $q < 0.75$ since $q \sim 0.75$ implies a very light companion with $\sim 1.07M_\odot$; this would be in tension with the lightest known NS, viz. the secondary of J0453+1559 ($1.18M_\odot$; [333]). We see that $\nu_\star$ depends only mildly on both q (differs by less than 1 Hz between $q = 1$ and $q = 0.75$) and the EOS.

By contrast, a hypermassive remnant may be expected for $M_{\rm tot} \gtrsim 2.8M_\odot$. In this case,

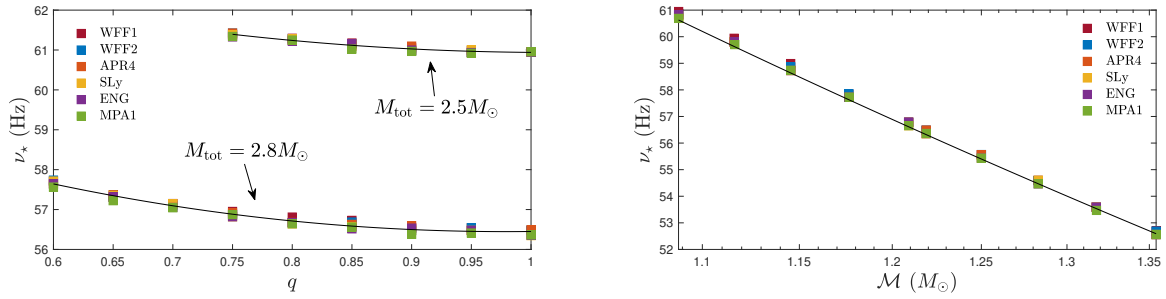

Figure 5.2: Derived spin of the primary [Eq. (5.6)] for double-precursor events with various EOS in binaries with fixed total masses $2.5M_\odot$ and $2.8M_\odot$ as functions of mass ratio q (left) and for symmetric binaries, as functions of the chirp mass $\mathcal{M}$ (right). Solid lines represent equation (5.7).

the primary (companion) has mass 1.4-1.75$M_\odot$ (1.05-1.4$M_\odot$) for q in the range $0.6-1$. The inferred spin rate again depends only slightly on q, while it is totally insensitive to the EOS. Noting that the mass ratio is rather irrelevant to the inferred spin rate from two precursors, we henceforth consider *symmetric* binaries to emphasise the dependence of $\nu_\star$ on the total mass $M_{\rm tot}$ of the system. In the right panel of Fig. 5.2, we plot $\nu_\star$ as a function of the system's chirp mass, where the EOS-independent relation (5.7) is drawn as solid line.

Allowing for a non-zero jet formation and breakout timescale, $\tau_{\rm jet}$, gives rise a to shift $\delta\nu_\star$ in the spin inference from equation (5.7). For $\tau_{\rm jet} \lesssim 0.3$ s [291], we find the quadratic fitting relation

$$\frac{\delta\nu_\star}{\nu_\star} = \left[7.99\left(\frac{\tau_{\rm jet}}{100\ {\rm ms}}\right) + 6.64\left(\frac{\tau_{\rm jet}}{100\ {\rm ms}}\right)^2\right]\%. \tag{5.8}$$

If the SGRB takes less than 100 ms to launch, for instance, the correction is $\lesssim 15\%$. We note that this relation is independent of $\mathcal{M}$.

5.4 Connections to other observational channels

In this section, we explore some connections that the double precursor scenario has to GWs (Sec. 5.4.1) and X-rays afterglow (Sec. 5.4.2), and also provide some discussion about how non-g-mode scenarios can still be used to constrain the stellar properties (Sec. 5.4.3).

5.4.1 Gravitational waves

There are two phases for which GW measurements may augment our knowledge about systems with precursors: during the merger and from the remnant. During merger, tidal resonances, and forces more generally, accelerate the inspiral. These influences on the waveform may be connected back to the properties of the pre-merging stars to infer not only $\mathcal{M}$ and q but also the stellar compactness via the mutual deformability, $\tilde{\Lambda}$. Generally speaking how-

ever, $\tilde{\Lambda}$ can only be tightly constrained by using priors for $\nu_\star$ [12,329]. Gravitational radiation from the remnant, which may be observed either directly or via the fall-off slope of electromagnetic emissions (see Sec. 5.4.2; [334]), allow us to infer properties of the final star. It was shown by [67] that many stellar parameters, such as the compactness, of a long-lived remnant NS (i.e., when $M_{\rm tot} \lesssim 2.5 M_\odot$; see Fig. 5.2) can also be inferred from the mutual tidal deformability. Furthermore, the mass of the remnant may be reliably estimated from the chirp mass to within an error of at most $\lesssim 0.1 M_\odot$ [65]. The frequency of the f-mode, from which independent constraints on the EOS can be placed, in the remnant can also be predicted if the spin frequency is known [121]. Additionally, large pre-merging spins may result in high degrees of mass asymmetry in the remnant [328], possibly revealing itself through the so-called "one-arm" instability in the GW spectrum or shifting the bar-mode peak [327]. Under favourable orientations, QNMs from the remnant may be observable with the Einstein Telescope out to $\gtrsim 200$ Mpc [335].

5.4.2 Afterglow light-curves

GRB 090510 (and many other SGRBs) displayed an afterglow 'plateau', which suggests that a NS was born from the merger [336]. Depending on the compactness and spin-down radiation efficiency of the remnant, analyses of the light curve indicate that the newborn star had a period in the range $1.8 - 8$ ms, surface magnetic field strength of $(5 - 17) \times 10^{15}$ G, and quadrupolar ellipticity between $10^{-4} - 10^{-2}$ [337–339]. These features impact the potential GW signal, e.g., the characteristic strain $h_0 \propto \epsilon \nu_\star^2$. From a purely electromagnetic standpoint, an eventual falloff slope of -2 in the X-ray emissions would be expected for dipolar spindown, while GW-dominated energy losses would be characterised by a slope of -1 instead, the crossover time and luminosity of which can be used to infer the ellipticity and magnetic field strength [334]. As the spin of the pre-merging stars has an impact on the properties of the remnant [144,327,328], information gleaned from double precursors may reduce the error bars from afterglow analysis. It is worth pointing out that a merger that leaves behind a stable NS, rather than a BH or hypermassive remnant (cf. Fig. 5.2), must be composed of relatively light stars, likely having formed through "bare collapse" or electron capture supernovae [340].

5.4.3 Other scenarios leading to double precursors

Although we focus on g-mode scenarios in this work, it is worth briefly commenting on other possibilities, and what one may infer under those circumstances. Indeed, precursors may arise from:

- ⋆ Resonances from other modes, such as i- or s-modes [39, 40], or even f- or r-modes in rapidly rotating or ultra-magnetised systems [41]

⋆ Each star undergoing a separate fracture, rather than one star undergoing two. Different atomic impurities in the crust, for example, could imply that the von Mises criterion is met at different strains and frequencies in each star. Such a scenario would be favoured if, for example, the stellar crust cannot "heal" in between fractures.

⋆ Scenarios unrelated to modes, such as the unipolar inductor model, where electromotive forces, generated across a weakly-magnetised star as it moves through the magnetosphere of a magnetar companion, spark precursor emissions [341, 342].

It is beyond the scope of this work to go into detail about each of these possibilities, though we explore the first point here. In an agnostic analysis, the two precursors of GRB 090510 corresponds to two $l = 2 = m$ modes (see Sec. 5.2.1) with inertial-frame frequencies of, respectively, ~ 160 Hz and ~ 50 Hz. Given the large difference in the frequencies of i- and s-modes (e.g., Fig. 3 in [343]), it seems difficult to connect each of these crust-induced modes to the two precursors of GRB090510. Among these two modes, the interface-mode is considered more promising to explain flares occurring at few seconds before the merger [39, 147].

In a three layers NS, there are two interface-modes originating from, respectively, the ocean-crust (Rayleigh-like mode) and the crust-core (Stoneley-like mode) transitions. The ratio between the frequencies of these two modes is roughly 2 with the Stoneley-like one being larger [51, 147, 344]. Those reported in [219] correspond to the crust/core transition thus belonging to the Stoneley-like mode, which oscillate at $\lesssim 50$ Hz (see Tab. 3 therein). The earlier flare may be accommodated by this i-mode for very low spins. On the other hand, as mentioned by [39], it is difficult to accommodate the later flare with i-modes. We note that a mix of i- and s-modes could also account for these two pre-emissions: the latter associated with the later precursors, while this calls for a s-mode with free mode frequency ~ 160 Hz since, for an i-mode to cause first precursor, we must have $\nu_\star \ll 10$Hz. This mixed-mode scenario will be investigated thoroughly elsewhere.

Some stars in coalescing binaries may spin fast, e.g., the secondary of GW190814 [330]. In such cases, modes with high free frequencies (e.g., f-modes) come into interest [41]. Nonetheless, if such high spins align with the orbit, we should see a rotation-induced modulations in the light-curves during the subsecond timescale of the observed precursors [345]. Unless the spin is misaligned with the orbit, the absence of substructure hints that $\nu_\star \lesssim 100$ Hz for precursor hosts[1].

[1] In principle, if the effective spinning rate of the signal, resulted from a large, aligned spin and the orbital frequency, is higher than the sampling rate for the data stream, the absence of the modulation is predicted as well. However, it will not be the case for the observed precursors since the observations are made with a sampling rate of 10^5 Hz (see, e.g., [34]).

5.5 Discussion

In this Chapter, we have shown how double precursor events, via a g-mode resonance interpretation (Chap. 4), can be used to measure the spin frequency of at least one component of a NS binary prior to coalescence. Our key results are relations (5.6) and (5.7), which connect the spin frequency to the orbital frequencies associated to precursor timings and the system's chirp mass, respectively.

A system that displays a double precursor, is bright/near enough ($\lesssim 100$ Mpc with aLIGO) to be detected in GWs at merger and late inspiral, and shows an X-ray plateau might be something of a holy grail for high-energy astrophysics. As shown here, the first two of these observation bundles may allow for the mass, radius, and spin of (at least one of) the pre-mergering stars to be determined with high accuracy. In principle, this can then be connected to the properties of the post-merger remnant by combining numerical, merger simulations [144,327,328] with the spin-down luminosity inferred from the jet energetics [336] and X-ray plateau [337]. One may thus be able to establish a magnetic field strength, compactness, and spin for the remnant [67, 338, 339], which imply constraints on the EOS (e.g., [330]). If the QNM spectrum of the remnant is also observable (out to $\gtrsim 200$ Mpc with the Einstein Telescope; [335]), the error bars may greatly shrink.

NSs in binaries tend to spin slowly; the fastest known pulsar in a binary is J0737-3039A with a spin of 44 Hz [346]. For GRB 090510 we predict that the primary has $\nu_\star \sim 60$ Hz, which is marginally faster than this value. Although only one double precursor event has thus far been observed, in the future one may be able to – assuming a resonance scenario – put statistical constraints on the spin dynamics of NS binaries that do not exhibit pulsations. This allows for an investigation of the evolutionary pathways of NSs that reside within the so-called pulsar 'graveyard'. It is conceivable also that even millisecond objects may enter into compact binaries in dense astrophysical environments through dynamical exchanges. What might the timing data of double precursors look like in such a case? For spin frequencies $\nu_\star \gg 10$Hz, equation (5.6) implies that the two events should be separated by at least 15 seconds, a prediction which is robust for different EOS. Depending on the spin alignment of the binary constituents, large values of $\nu_\star$ may excite the so-called "one-arm" instability in the GW spectrum of the remnant and enhance blue/red kilonovae [327, 328].

We close by noting that magnetic fields have not been considered at all in this work. It is likely that magnetic fields play a significant role in extracting the elastic energy from the crust that eventually fuels the precursor [40, 41]. However, unless the fields are of magnetar-level strength ($B_\star \gtrsim 10^{15}$ G), the Lorentz force will not be strong enough to significantly distort the QNM spectrum (Sec. 4.4.1), implying that the spin-fitting formula (5.6) would remain unchanged; see equation (4.52). Even so, it was argued by [41] that precursors with non-thermal spectra may be indicative of intense magnetic fields, so as to avoid thermalisations

from pair-photon cascades created via mode-induced backreactions (see also [37,39]; Chap. 4). These considerations imply that the error bars presented on the spin-frequency measurements may be slightly underestimated therefore, at least when applied to double precursors showing predominantly non-thermal spectra (as indeed was the case for GRB090510; [34]).

Chapter 6

f-mode Imprints in Gravitational Waves from Coalescing Binaries involving Spinning Neutron Stars

Contents

Breakdown of Contributions

The code for evolving binaries is extended to the accuracy of 3rd post-Newtonian order by me from the previous code, which tackles at 2nd order motion, of Kostas D. Kokkotas. My contributions are all the gravitational waveform analysis related computations, the preparation of figures, and the edition of manuscript. Kostas D. Kokkotas provides cardinal comments/suggestions while I was drafting the paper, and assists in implementing final edition on the manuscript.

Overview

The excitation of f-mode in a neutron star member of coalescing binaries accelerates the merger course, and thereby introduces a phase shift in the gravitational waveform. Emphasising on the tidal phase shift by rotating stars, we provide an accurate, yet economical, method to generate f-mode-involved, pre-merger waveforms using realistic spin-modulated

f-mode frequencies for some viable equations of state. We find for slow-rotating stars that the dephasing effects of the dynamical tides can be uniquely, EOS-independently determined by the direct observables (chirp mass $\mathcal{M}$, symmetric ratio η and the mutual tidal deformability $\tilde{\Lambda}$), while this universality is gradually lost for increasing spin. Although a high cutoff waveform frequency combined with large signal-to-noise ratio (SNR) is needed to trace the tidal dephasing if binary members rotate slowly, for binaries with fast rotating members ($\lesssim 800$ Hz) the phase shift due to f-mode will exceed the uncertainty in the waveform phase at reasonable SNR ($\rho = 25$) and cutoff frequency of $\gtrsim 400$ Hz. In addition, a significant phase shift of $\gtrsim 100$ rads can be found for a high cutoff frequency of 10^3 Hz. For systems involving a rapidly-spinning star (potentially the secondary of GW190814), neglecting f-mode effect in the waveform templates can therefore lead to considerable systemic errors in the relevant analysis.

6.1 Introduction

6.1.1 The Context

The macroscopic and microscopic properties of neutron stars (NSs) in coalescing binaries are imprinted in the emitted gravitational waveforms. The precise knowledge of the waveform morphology is of fundamental importance in the signal analysis and the extraction of the NS parameters therefore. Adopting the point-particle approximation for the gravitational wave (GW) analysis, the chirp mass and the symmetric mass of binaries can be estimated from the 1st order post-Newtonian (PN) phase evolution of GWs, though with different degree of accuracy [20, 21, 77, 300, 347, 348]. Beyond the point-particle baseline approximants, the internal structure of the NS members can also be probed: the quadrupole deformations induced by the tidal forces in the constituents will affect the binary evolution and thus the associated waveform. Two sorts of (gravito-electric) tidal effects are involved in the signal, viz. the equilibrium tides due to the induced tidal deformations, and dynamical tides due to the resonant excitation of the various neutron star quasi-normal modes (QNMs). Equilibrium tidal effects from Newtonian [76, 77], 1 PN [260, 349], up to 2.5 PN level [21], are encapsulated in the tidal deformability, and their traces in the signal have already been observed with the current detectors (see [12] and [350] for a recent review). Dynamical tides, while being subdominant in the low frequency regime, can affect the waveform to a similar extent as the equilibrium ones at the final stage of inspiraling, predominantly due to the f-mode excitation [78–80, 199].

For rotating NS progenitors, the spin-effects also contribute to phase shift thus introducing some degeneracy with the tidal contributions (cf. Eq. (3) of [351]). For instance, the spin-orbit (comes at 1.5 PN order), and the secondary spin-spin (comes at 2 PN order) terms appear in the PN expression of GW phase [184, 352, 353]. In addition, rotation will induce

a quadrupole deformation on the star, and its gravitational potential would be deformed accordingly. The deformation is larger for stiffer EOS [354] since NSs tend to have larger radius [355]. The change in the gravitational potential modifies the relation between the angular velocity and the separation of stars. The binary motion is affected by this self-spin effect at the same level as spin-spin effect (i.e., 2 PN) [356, 357], whose contribution to GW dephasing is however much smalelrthan the tidal one (see, e.g., Fig. 4 of [358]).

Rotation introduces shifting and splitting of the QNM spectrum of NSs, and thereby alters the tidal effects and as a consequence the waveform [182]. The effect of stellar rotation in the tidal dephasing is more profound for increasing spin rate since the downward-tuned QNM frequencies (counter rotating) lead to stronger tidal excitations. Although there are higher order couplings between tides and rotation, e.g., tide-spin terms, these are considerably weaker than the aforementioned effects, and even the accuracy of the state-of-the-art numerical relativity (NR) is incapable of sizing these effects [351]. Owing to the interplay between spin and tides, the ambiguity in the spins of inspiralling NSs would consequently obscure the determination of tidal dephasing especially if one of the NSs spins rapidly (e.g., [359, 360]). For the precise extraction of the source properties, it is thus important to discriminate tidal dephasing from the phase shift generated due to spin-contributions.

In addition to the degeneracy of spin and tidal dephasing, the uncertainty in equation of state (EOS) further messes up the attribution of the phase shifts to individual effects without knowing the "correct" EOS *a prior* (e.g., [361]); currently, several candidates survive the observations of pulsars [174, 362], and GW170817 as well as its electromagnetic counterparts [22, 198, 363]. Nonetheless, the f-mode effects in dephasing may overcome the uncertainty in phase originating from the EOS in some circumstances [73], where a neat clue of dynamical tidal effects can be observed. In a pursue of reliable analysis, it is necessary to take f-mode effect into account when constructing gravitational waveform templates for those cases [73, 74, 181].

The tidal effects of rotating NSs in binaries have been investigated in [182] by adopting an approximation for the frequency modulations [see Eq. (5.7) therein], which engulf a variance of $\lesssim 15\%$ among the realistic values (cf. Fig. 4.9). In the present article, we re-examine the measurability of dynamical tidal dephasing by using the realistic spin-modulation in the QNM spectrum, and a PN evolution for the inspiral part.

6.1.2 This Work

On top of a great body of existing literature, we collate in the following the original contribution of this article to address f-mode effect in GW:

- *EOS-independent Hamiltonian* — For slow-rotating binary NSs, the Hamiltonian of the binary evolution, including the tidal effects, is shown to be EOS-independently reconstructable from GW observable $\mathcal{M}$, η, and $\tilde{\Lambda}$ [Eq. (6.24)] since f-mode effects can be pre-

scribed universally by $\Lambda_\star$ [Eqs. (6.21)-(6.23)]. Assuming we have a well-measured chirp mass [20, 348, 364], say $\mathcal{M} = 1.146$ (the value for GW170817 [12]), the accumulated GW phase $\Psi_{\rm tot}$ is shown to be a universal function of the mass of the primary $M_\star$ (Fig. 6.4).

- *"Observability" of the spin effects in tidal dephasing* — Adopting five EOS with some representative spin rates, we find that the tidal dephasing piles up rapidly at the high frequency regime of GW (top panel of Fig. 6.5), hinting at that the information of dynamical tides concentrates in this part of waveform. On the other hand, the accumulated tidal dephasing from 20-1000 Hz of $f_{\rm gw}$ is larger for higher stellar spins for stiffer EOS (bottom panel of Fig. 6.5). For the highest stiffness EOS considered, viz. MPA1, we find a few tens rad of dephasing if two stars rotate moderately, while a few hundreds rad can be achieved when stars rotates rapidly. Although we consider symmetric binaries (masses and spins of both stars are the same) for Fig. 6.5, the conclusion is expected to be general since (i) faster rotation leads to further frequency reduction which will enhance the tidal dephasing, and (ii) NSs with stiffer EOS tend to have larger radii thus more notable tidal deformations. Despite of its dependence on EOS, the tidal dephasing can be expressed as a universal relation with respect to a dimensionless spin [Fig. 6.6; Eq. (6.25)].

- *Fast-spinning NS* — In general, the SNR needed to measure the tidal dephasing $\Delta\Psi^T$ depends on the cutoff frequency of the data stream $f_{\rm max}$, as well as the spin of the primary $\nu_{\star,\star} = 2\pi\nu_{{\rm s},\star}$. As an example, we assume a specific binary and trace that the error in GW phase decreases for increasing $f_{\rm max}$, while the tidal dephasing increases for larger $f_{\rm max}$ (top panel of Fig. 6.7). In this case, a data stream continuing beyond 600 Hz suffices to make the accumulated tidal dephasing exceed the uncertainty in the GW phase. Additionally, we see that a considerable improvement, in the measurability of tidal dephasing, can be made even by extending the cutoff frequency from 400 Hz to 500 Hz if the primary has a moderate spin ($\lesssim$ 400 Hz). Although the improvement for rapidly-spinning primary by extending $f_{\rm max}$ is weaker (bottom panel of Fig. 6.7), the required SNR for such system is much lower anyway; a mild SNR of $\rho \lesssim 20$ is sufficient to discriminate the tidal dephasing even for a cutoff $f_{\rm max} = 400$ Hz if the secondary of GW190814 is a fast-rotating NS with $\nu_{{\rm s},\star} > 800$ Hz. *The sizable f-mode effects quantified in the present article indicate that templates including f-mode effects are imperative for inferring EOS from more accurate GW observation in the near future.* That said, if a rapidly-rotating NS is involved in a coalescing binary, as it is claimed for the secondary of GW190814 [330, 365, 366], the f-mode effects enhanced by the fast rotation will be unambiguously measurable in the signal. Neglecting f-mode effects in such events will therefore result in biased inferences of stellar parameters.

The article is organised as following: We summarise the present status of the analytical waveform derived from the effective-one-body approach in Sec. 6.2. Tidal dephasing is numerically studied in Sec. 6.3, where the dependence on EOS, and the tidal effects of spinning NS are detailed. In addition, we illustrate how to discriminate tidal effects from spin-orbit

effects. A particular investigation on the influence in the GW phase produced by the spin-modified f-mode excitation is applied to GW190814 in Sec. 6.4. Finally, a discussion of the results is included in Sec. 6.5.

Unless stated otherwise, all quantities are given in the unit of $c = 1 = G$.

6.2 Tidal dephasing: Analytic Models

Under the stationary phase approximation (SPA) and by ignoring the PN modifications in the GW amplitude $\mathcal{A}$[1], the frequency-domain gravitational waveform can be expressed by: [300, 348]

$$h(f_{\rm gw}) = \mathcal{A} f_{\rm gw}^{-7/6} e^{i\Psi(f_{\rm gw})} \,. \tag{6.1}$$

This form is generic for all kinds of compact binaries. Here, $f_{\rm gw} = \Omega_{\rm orb}/\pi$ is the GW frequency, and $\Omega_{\rm orb}$ is the orbital frequency. The phase $\Psi(f_{\rm gw})$ is related to the time domain phase $\phi(t)$ via

$$\Psi(f_{\rm gw}) = 2\pi f_{\rm gw} t_o - \phi(t_o) - \frac{\pi}{4}, \tag{6.2}$$

and obeys the equation [21, 80, 368]

$$\frac{d^2\Psi}{d\Omega_{\rm orb}^2} = \frac{2Q_\omega}{\Omega_{\rm orb}^2}, \tag{6.3}$$

where t_o is a reference time with $\phi_o = \phi(t_o)$ being the corresponding phase, and Q_ω is a dimensionless measure of the phase acceleration defined as

$$Q_\omega = \Omega_{\rm orb}^2 \left(\frac{d\Omega_{\rm orb}}{dt} \right)^{-1}. \tag{6.4}$$

Constructing precise waveforms demands an accurate evolution of coalescing binaries. The PN equations of motion describe with adequate accuracy the largest part of the observed inspiralling evolution [369]. Still the PN approximation gradually fails as the binary approaches the plunge, merger, and finally the ringdown phases. This lack of applicability for high orbital frequencies and the post-merger dynamics motivated the so-called effective-one-body (EOB) formalism, which re-sums the PN expansions to account properly for the higher-order effects [255, 370]. In addition, the EOB analytic dephasing can be "calibirated" with the late-time NR results [371] even when tidal effects are taken into account [372, 373]. However, the latter hybrid EOB and NR model is much more time-consuming than the PN formalism.

[1] In general, the amplitude $\mathcal{A}(f_{\rm gw})$ depends on the internal structure (or finite size effects) of the binary members, the omission of these higher PN corrections does not affect the accuracy of SPA. In practice, SPA will be quite accurate up to the merger [21, 367], and thus this approximation will not affect significantly our results.

In the present article, we are not to study the tidal influence on high frequency waveform, but aim to offer an economical waveform variant capable to probe the internal physics of NSs from the low-frequency part of the waveform (before the actual "merger" begins; $\lesssim 10^3$ Hz). To this end, the PN framework proves sufficiently accurate [374–376] (see also below).

Tidal interaction among the binary members (i) accelerate the shrinking rate due to orbital energy transfer to QNMs [124,199], or, in another perspective, effectively amplify the strength of the gravitational potential in the EOB framework [376–378], (ii) enhance the energy flux carried by GW due to tidal deformations (see, e.g., Eq. (3.6) of [349]), and (iii) increase the angular momentum loss. As a result, certain tidally-driven modifications in $\mathcal{A}$ and Ψ will be encoded, while the change in $\mathcal{A}$ in minor.

The effect of equilibrium tides in the phase shift is mainly governed by the quadrupolar tidal deformability of the NSs in the binary [76,77],

$$\Lambda = \frac{2k_2}{3C^5} \tag{6.5}$$

where k_2 is the (dimensionless, quadrupolar) tidal Love number, and $C = M/R$ is the stellar compactness. The contribution of the higher-order Love numbers in the phase-shift is significantly smaller [351]. On the other hand, the dynamical tides are resulted from the excitation of oscillations in the individual NSs, which are predominantly excited by the quadrupolar ($l = 2$) component of the tidal potential built by the companion (see, e.g., the discussion in the Appendix A.2 of [21]). Among the various low or high frequency modes (p-, g-, i-, w-, etc.), the contribution of the f-mode is more significant to the tidal response, strictly the $l = 2 = m$ f-mode [21,199,351,379]. Therefore, we restrict ourselves to the physics (f-mode, tidal potential and deformability) at the quadrupolar level to study the leading order tidal phenomena. Although we focus on the quadrupolar f-mode, our methodology is applicable to higher-order ($l > 2$) f-modes and to other types of modes.

On top of the tidal interaction, the spins of the constituents also influence the binary evolution via spin-orbit, self-spin couplings [184,352,380,381], and some higher order terms such as spin-tidal coupling. Incorporating the aforementioned physics, and by denoting a certain parameter X of the primary (companion) as $X_\star$ ($X_{\rm comp}$), the GW phase can be expressed as

$$\Psi = \Psi(f_{\rm gw}; \mathcal{T}, \mathcal{S}, \mathcal{Z}), \tag{6.6}$$

where $\mathcal{T} = (\Lambda_\star, \Lambda_{\rm comp})$, $\mathcal{S} = (\nu_{{\rm s},\star}, \nu_{\rm s,comp})$, and $\mathcal{Z} = (M_\star, M_{\rm comp}, R_\star, R_{\rm comp})$. Here we will not investigate further the dephasing caused by spin coupling effects (spin-orbit, spin-spin, self-spin, etc.), while we note that $\mathcal{S}$ are not dummy as the spins affect the dynamical tides.

6.2.1 Analytic Tidal Dephasing

Equilibrium tides are usually addressed by extending the effective gravitational potential in EOB to include an enhancement due to higher-order PN contributions [376, 377], while dynamical tides can be investigated either by introducing associated kinetic terms to the Hamiltonian [79, 253] or by generalising the Love number k_2 to a running parameter (effective tidal responses) [78, 79, 382]. We adopt the PN evolution of binaries together with a kinetic term for dynamical tides to investigate the accumulated tidally-induced dephasing during the pre-merger stage ($f_{\rm gw} \lesssim 10^3$ Hz). This approach is numerically cheaper while agrees very well with the more sophisticated EOB method (cf. Fig. 1 in [80]; see also Fig. 6.2). To demonstrate the faithfulness of our code, we will compare our results with several analytical waveforms in this section.

To the leading order of the tidal deformability, the 1 PN order phase shift due to effects of the equilibrium tides in the primary, based on the TaylorF2 model, reads as [349]

$$\Delta\Psi_\star^{\rm eq} = -\frac{3\Lambda_\star}{128}(\pi\mathcal{M}f_{\rm gw})^{-5/3}x^5[a_0 + a_1 x] \approx \Psi(f_{\rm gw};\mathcal{T},\mathcal{S},\mathcal{Z}) - \Psi(f_{\rm gw};\mathcal{O},\mathcal{S},\mathcal{Z}), \tag{6.7}$$

where $x = [\pi(M_\star + M_{\rm comp})f_{\rm gw}]^{2/3}$, $\mathcal{O} = (0,0)$ denotes a null pair, $\mathcal{M}$ is the chirp mass [Eq. (3.17)], and η is the symmetric mass ratio [Eq. (3.18)]. The coefficient

$$a_0 = 12[1 + 7\eta - 31\eta^2 - \sqrt{1-4\eta}(1 + 9\eta - 11\eta^2)], \tag{6.8a}$$

is the Newtonian contribution, and

$$a_1 = \frac{585}{28}\left[1 + \frac{3775}{234}\eta - \frac{389}{6}\eta^2 + \frac{1376}{117}\eta^3 - \sqrt{1-4\eta}\left(1 + \frac{4243}{234}\eta - \frac{6217}{234}\eta^2 - \frac{10}{9}\eta^3\right)\right], \tag{6.8b}$$

is the 1 PN one. Although Eq. (6.7) encodes solely the tide in the primary, the effects from the companion can be linearly added to the gross influence, which can be simplified as [311, 383]

$$\Delta\Psi_\star^{\rm eq} + \Delta\Psi_{\rm comp}^{\rm eq} = -\frac{3\tilde{\Lambda}}{128}(\pi\mathcal{M}f_{\rm gw})^{-5/3}x^5\left[\frac{39}{2} + \left(\frac{3115}{64} - \frac{6595}{364}\sqrt{1-4\eta}\frac{\delta\tilde{\Lambda}}{\tilde{\Lambda}}\right)x\right], \tag{6.9}$$

where

$$\begin{aligned}\tilde{\Lambda} =& \frac{8}{13}\left[(1 + 7\eta - 31\eta^2)(\Lambda_\star + \Lambda_{\rm comp}) + \sqrt{1-4\eta}(1 + 9\eta - 11\eta^2)(\Lambda_\star - \Lambda_{\rm comp})\right] \\ =& \frac{16}{13(M_\star + M_{\rm comp})^5}\left[(M_\star + 12M_{\rm comp})M_\star^4\Lambda_\star + (M_{\rm comp} + 12M_\star)M_{\rm comp}^4\Lambda_{\rm comp}\right]\end{aligned} \tag{6.10}$$

is the mutual tidal deformability, and

$$\delta\tilde{\Lambda} = \frac{1}{2}\left[\sqrt{1-4\eta}\left(1-\frac{13272}{1319}\eta+\frac{8944}{1319}\eta^2\right)(\Lambda_\star+\Lambda_{\rm comp})+\left(1-\frac{15910}{1319}\eta+\frac{32850}{1319}\eta^2+\frac{3380}{1319}\eta^3\right)(\Lambda_\star-\Lambda_{\rm com}\right. \tag{6.11}$$

We note that $\delta\tilde{\Lambda}$ is typically much smaller than $\tilde{\Lambda}$, and will vanish for symmetric binaries.

The above 1 PN form can be extrapolated to 2.5 PN with the aid of EOB treatment as shown in [21]; for symmetric binaries, the equilibrium tidal effect of the primary leads to the dephasing

$$\Delta\Psi^{\rm eq}_\star = -\frac{117\Lambda_\star}{128}x^{5/2}\left[1+\frac{3115}{1248}x-\pi x^{3/2}+\frac{28024205}{3302208}x^2-\frac{4283}{1092}\pi x^{5/2}\right], \tag{6.12}$$

and can be doubled to include the influence of the companion.

The 2.5 PN correction to the phase acceleration (6.4) due to tidal contribution, on the other hand, reads as

$$\tilde{Q}^T_\omega = -\frac{65}{32}x^{5/3}\left[1+\frac{4361}{624}x^{2/3}-4\pi x+\frac{5593193}{122304}x^{4/3}-\frac{4283}{156}\pi x^{5/3}\right], \tag{6.13}$$

and is given along side the formula for GW phase in [21].

This 2.5 PN TaylorF2 model was later phenomenologically calibrated by numerical relativity simulations in [372] to capture dynamical tidal effects by replacing $\tilde{\Lambda}$ in Eq. (6.12) with $\tilde{\Lambda}(1+12.55\tilde{\Lambda}^{2/3}x^{4.240})$. The authors further show that one can directly generalise the above phase expression, which is for symmetric binaries, to asymmetric systems by substituting the denominator of the pre-factor with 256η, i.e.,

$$\Delta\Psi^{\rm eq}_\star+\Delta\Psi^{\rm eq}_{\rm comp} = -\frac{117}{256\eta}x^{5/2}\tilde{\Lambda}(1+12.55\tilde{\Lambda}^{2/3}x^{4.240})\left[1+\frac{3115}{1248}x-\pi x^{3/2}+\frac{28024205}{3302208}x^2-\frac{4283}{1092}\pi x^{5/2}\right]. \tag{6.14}$$

Although there is a mutation of 2.5 PN tidal phase approximant derived by Henry et al. [17], which is slightly different from the one in [371] (they match up to 1 PN tidal phasing, i.e., 6 PN effects in general), we will use the above NR-reshaped form for statistical estimation in Sec. 6.3.3. In addition to TaylorF2, the NR-calibrated form for TaylorT2 has also been derived in [351], which gives rise to the dephasing

$$\Delta\Psi^{\rm eq}_\star+\Delta\Psi^{\rm eq}_{\rm comp} = -\frac{117\tilde{\Lambda}}{64}x^{5/2}\frac{1-17.428x+31.867x^{3/2}-26.414x^2+62.362x^{5/2}}{1+(-17.428-3115/1248)x+36.089x^{3/2}}. \tag{6.15}$$

Although several models for equilibrium tides have been developed, dynamical tidal dephasing due to the quadrupolar f-mode in the primary is just provided in [80] recently, given

by

$$\Delta\Psi_{\star}^{\rm dyn} = -\frac{10\sqrt{3}\pi - 27 - 30\log 2}{96\eta}(\pi M_{\star} f_{\rm gw})^{11/3}\frac{M_{\star}^4\omega_f^{-2}}{(M_{\star}+M_{\rm comp})^6}\left(155 - 147\frac{M_{\star}}{M_{\star}+M_{\rm comp}}\right), \tag{6.16}$$

where ω_f is the frequency of the f-mode. This analytical phase shift agrees with the tidal EOB model for $f_{\rm gw} \lesssim 10^3$ Hz [80].

6.3 Tidal Dephasing: Numerical results

The Hamiltonian describing the binary evolution is (Chap. 4; see also, e.g., [199, 253])

$$H(t) = \big(H_{\rm orb} + H_{\rm reac} + H_{\rm osc} + H_{\rm tid}\big)(t), \tag{6.17}$$

where $H_{\rm tid}$ and $H_{\rm osc}$ are the Hamiltonians describing the equilibrium and dynamical tidal effects, respectively. We consider the conservative motion, $H_{\rm orb}$, up to 3 PN level, and include the gravitational back-reaction, $H_{\rm reac}$, at 2.5 PN order. The explicit forms for the point-particle part of $H(t)$, viz. $H_{\rm orb}$ and $H_{\rm reac}$, are rather long and are not the subject of the present article, which are thus omitted here but we refer the interested reader to [254, 384]. Nonetheless, we will give the form of the tidal parts $H_{\rm osc} + H_{\rm tid}$ in due course, for which the coupling strength of modes to the external tidal field is a crucial parameter (Sec. 6.3.1).

The determination of Λ via the phase shift due to equilibrium tides can set constraints on the EOS as demonstrated by the analysis of GW 170817 [22]. However, we need to take also dynamical tides into account since more accurate observations will be available in the next years. This entails a good handle on the QNM effects on the waveforms especially in the high frequency window, where the influence of tidal effects in the GW signal is encoded (cf. Fig. 2 of [385]). Ignoring the dynamical tide contribution in the phase shift will therefore deteriorate the accuracy in constraining the EOS. Furthermore, for binaries involving rapidly-rotating NSs the effect will be more pronounced since the f-mode frequency will be lowered, leading into larger tidal dephasing. In this article, we consider the GW phase accumulated when $f_{\rm gw}$ ranges between $f_{\rm min} = 20$ Hz and $f_{\rm max} = 1000$ Hz, given by

$$\Psi_{\rm tot} = \int_{f_{\rm min}}^{f_{\rm max}} df_{\rm gw}\left(\frac{\partial\Psi}{\partial f_{\rm gw}}\right)_{\Lambda_{\star},\Lambda_{\rm comp},\nu_{{\rm s},\star},\nu_{\rm s,comp}} = \Psi_{\rm pp} + \Delta\Psi^T. \tag{6.18}$$

Here $\Psi_{\rm pp}$ is the part of point-particle contribution, and $\Delta\Psi^T$ is the tidal dephasing due to both equilibrium and dynamical tides.

In Fig. 6.1, we compare our result of phase acceleration Q_{ω}^0, for a particular symmetric binary with a non-spinning primary, with $\tilde{Q}_{\omega}^T$ given by Eq. (6.13). We see that our result, which includes the f-mode effect, has a deviation $\leq 20\%$ from the analytic result for $f_{\rm gw} <$

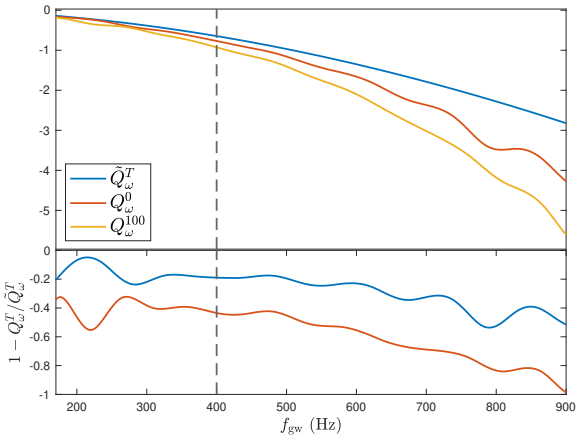

Figure 6.1: Ratio between the numerically estimated phase acceleration $Q^T_\omega = \{Q^0_\omega, Q^{100}_\omega\}$ [Eq. (6.4)] and the analytic 2.5 PN form $\tilde{Q}^T_\omega$ [Eq. (6.13)].

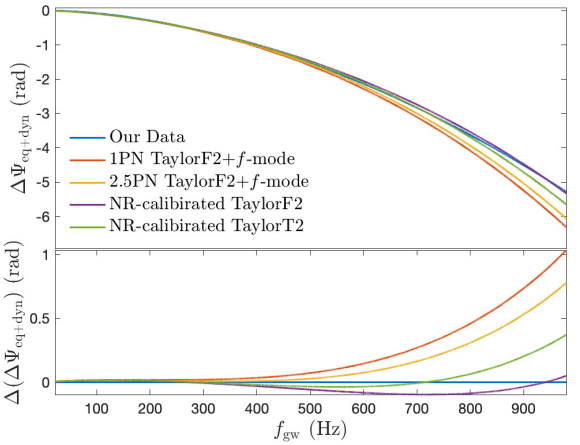

Figure 6.2: Tidal dephasing, including equilibrium and dynamical tides, from our code (blue) and several analytic models (see the main text) as functions of $f_{\rm gw}$. For this plot, we consider a symmetric binary with $M_{\rm comp} = 1.3M_\odot = M_{\rm comp}$ and MPA1 EOS [156] The results shown here account only for the tides in the primary, thus the total effect is twice as big.

500 Hz, while larger deviation is observed for high frequencies. The growing deviation can be attributed to f-mode excitation, which is absent in the analytic expression (6.13). To demonstrate that the deviation originates from the presence of f-mode, we add in the plot the phase acceleration Q_ω^{100}, for the same binary but with the primary spinning at 100 Hz. The enhanced f-mode effect in the latter spinning case manifests as the larger deviation from Eq. (6.13). In addition, the inclusion of f-mode effect gives rise to a more negative phase acceleration, suggesting a faster merging (the so-called"tidally induced plunge" [199]).

On the other hand, in Fig. 6.2, the GW phase of our simulation (blue curve) is compared to the following approaches: (i) 1 PN TaylorF2 + f-mode [Eq. (6.9) and Eq. (6.16)], (ii) 2.5 PN TaylorF2 + f-mode [Eq. (6.12) and Eq. (6.16)], (iii) NR-calibrated TaylorF2 [Eq. (6.14)], and (iv) NR-calibrated TaylorT2 [Eq. (6.15)]. Denoting the difference between our tidal phase shift to a certain model as $\Delta(\Delta_{\rm eq+dyn}) = \Delta^{\rm ours}_{\rm eq+dyn} - \Delta^{\rm model}_{\rm eq+dyn}$, we see that the deviation from the aforementioned models is less than 1 rad overall, and most of the deviation piles up after $f_{\rm gw} \gtrsim 400$ Hz. Our numerical scheme produces smaller dephasing compared to the two non-NR-corrected models, meaning the tidal effect in our scheme is a bit weaker. However, the shifts are greater than those of NR-calibrated models when $f_{\rm gw}$ is less than a certain value. This "sign-changing" behaviour is often seen when it comes to comparing different waveform models (e.g., [80, 373, 386]). Among the considered models, the model using TaylorF2 with NR waveforms fits to our result the best with difference only between ± 0.1 rads.

As the QNM spectrum depends on EOS and spin, we will address how these affect the tidally-induced phase shift, notably the dependence on EOS (Sec. 6.3.1) and the tidal effects of spinning stars (Sec. 6.3.2). In general the spin itself will lead to certain dephasing due to, e.g., spin-orbit, spin-spin, and self-spin couplings. The total dephasing thus consists of the tidal and spin-included contributions. Identifying of tidal part accurately is crucial in acquiring source parameters; some discussion on this issue will be provided at the end. Before we investigate the aforementioned aspects, we first attain confidence on the results of our code by comparing with the analytic forms obtained via PN expansions, the EOB scheme, and the phenomenological models fitting to NR simulations.

6.3.1 An EOS-independent Tidal Hamiltonian

In general, stellar oscillations in GR will cause perturbations in metric fields, thus damping in a certain timescale set by the imaginary part of mode frequencies. However, we are studying the very last moment of coalescence, where the few minutes is not enough for modes to decay. Therefore, we ignore the small contributions from the mode-induced metric perturbation and from the imaginary part of the mode in the tidal parts of Hamiltonian, which then has the

form [cf. Eqs. (4.31) and (4.40)]

$$H_{\rm tid} = -\frac{2M_\star M_{\rm comp}}{aR_\star}\sum_\alpha W_{lm}\left(\frac{R_\star}{a}\right)^l \Re\left[\bar{q}_\alpha Q_\alpha e^{-im\phi_c}\right], \tag{6.19}$$

$$H_{\rm osc} = \frac{1}{2}\sum_\alpha\left(\frac{p_\alpha\bar{p}_\alpha}{M_\star R_\star^2} + M_\star R_\star^2\sigma_\alpha^2 q_\alpha\bar{q}_\alpha\right) + \text{H.c.}, \tag{6.20}$$

where we focus on the tidal activity in the primary. Here α labels different QNMs, ϕ_c is the phase coordinate of the companion, q_α are the mode amplitudes, and p_α are the canonical momenta associated to q_α. The (inertial-frame) eigenfrequency of the excited mode is $\sigma_\alpha = \omega_\alpha + i/\tau_\alpha$, where ω_α is the frequency, and τ_α the damping timescale. The overhead bar denotes complex conjugation. As stated above, we will limit our study to the $l = 2 = m$ f-mode hence we will drop the subscript α hereafter, and denote its coupling strength as Q_f, which should not be confused with the phase acceleration Q_ω defined in Eq. (6.4).

We introduce the primary-based, dimensionless quantities

$$\mathcal{A}(\Lambda_\star) = Q_f R_\star/M_\star, \tag{6.21a}$$

$$\mathcal{B}(\Lambda_\star) = R_\star\omega_f, \tag{6.21b}$$

which, if the primary is non-spinning (i.e., ω_f is the mode frequency), can be expressed as functions of Λ. In particular, we find the universal relations for these two quantities, given by

$$\log\mathcal{A} = -0.250 + 0.306\log\Lambda_\star - 0.008(\log\Lambda_\star)^2, \tag{6.22}$$

and

$$\log\mathcal{B} = -0.270 + 0.013\log\Lambda_\star - 0.013(\log\Lambda_\star)^2. \tag{6.23}$$

The relations are plotted in Fig. 6.3, where the considered set of EOS is labeled in the legend. This set of EOS is the same as those adopted in Chap. 3, and we note that the latter formula (6.23) has been introduced there. The former universal relation connects the tidal overlap of f-mode to the tidal deformability, which is newly pointed out here, while that for r-mode has been developed in [387] (see the right panel of Fig. 7 therein).

Substituting the previous quantities into the tidal Hamiltonian, we get

$$H^T = H_{\rm tid} + H_{\rm osc} = -\frac{2M_\star^2 M_{\rm comp}}{a^3}\mathcal{A}q\cos(m\varphi_c) + \frac{p\bar{p}}{M_\star R_\star^2} + M_\star q\bar{q}\mathcal{B}^2. \tag{6.24}$$

which is a functional depending on the individual masses $M_\star$ and $M_{\rm comp}$, the tidal deformability of the primary $\Lambda_\star$, and $M_\star R_\star^2$. The latter quantity is related to moment of inertia [388]

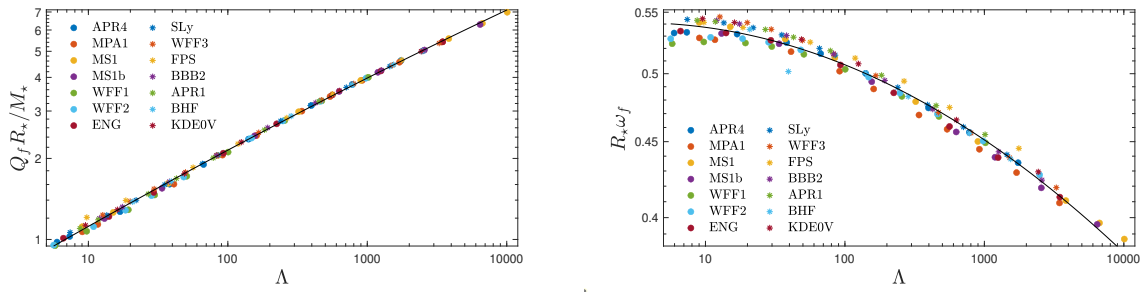

Figure 6.3: Universal relations connecting $Q_f R_\star/M_\star$ [Eq. (6.23); left panel] and $R_\star^2\omega_f^2$ [Eq. (6.22); right panel] to the tidal deformability of the primary $\Lambda_\star$.

[see Eq. (12) therein]. The dependencies are all detectable in GW analysis either directly or indirectly; the measurement of the chirp mass $\mathcal{M}$ and the symmetric mass ratio η determine the individual masses, while the measurement of $\tilde{\Lambda}$ returns $R_\star$ in a manner independent of the $M_{\rm comp}$ if the chirp mass is known [115, 389]. In addition, the mass ratio together with $\tilde{\Lambda}$ estimate the individual tidal deformabilities since $\Lambda_\star$ and $\Lambda_{\rm comp}$ relate to each other via Eq. (4.73) [116]. The tidal Hamiltonian can therefore be *EOS-independently reconstructed* from $\mathcal{M}$, η, and $\tilde{\Lambda}$. The "hierarchy" of the three arguments in GW phasing goes from the chirp mass to the tidal deformability.

In Fig. 6.4, we plot the accumulated GW phase from $f_{\rm gw} = 20$ Hz to $f_{\rm gw} = 1000$ Hz for binaries with fixed chirp mass $\mathcal{M} = 1.186M_\odot$ as functions of $M_\star$ for some EOS. We note that the chosen EOS span a wide range of stiffness going from the stiffest MPA1 down to the softest KDE0V. The binaries considered in Fig. 6.4 undergo ~ 2260 orbits in the last ~ 150 s of the coalescence, during which $f_{\rm gw}$ climbs from 20 Hz to 10^3 Hz. This corresponds to ~ 4560 cycles of *time-domain* gravitational waveform, while the *frequency-domain* gravitational waveform (6.1) is found to oscillate ~ 4775 cycles, i.e., $\Psi_{\rm tot} \lesssim 3 \times 10^4$ rads. The phase varies $\lesssim 1\%$ for different η, while the variance of the finite size effects encoded in $\tilde{\Lambda}$ is even smaller. Following the EOS-independent nature of the Hamiltonian, the accumulated phase is thus, to a large degree, uncorrelated to the EOS. *To our knowledge, the universality of the GW phase shift when fixing the chirp mass has not yet been recognised in the literature.* In addition, the phase peaks at $M_\star = M_{\rm comp} \simeq 1.37M_\odot$, indicating that symmetric binaries will undergo more cycles before merger regardless the stellar constitution.

Although this Hamiltonian is EOS-independent, it is not indicating that we cannot place any constraints on EOS from the GW phasing detection. On the contrary, from the analysis of GW phase, we may determine the properties of the binary members to place certain constraints on EOS, e.g., the predicted $\tilde{\Lambda}$ of GW170817 favours soft candidates.

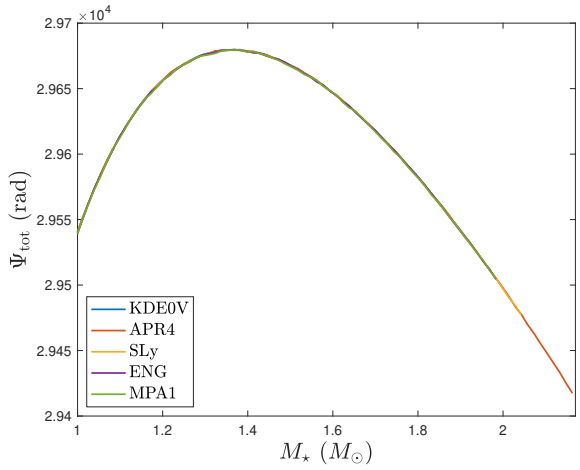

Figure 6.4: $\Psi_{\rm tot}$ [Eq. (6.18)] for binaries with a fixed chirp mass $\mathcal{M} = 1.186 M_\odot$ as functions of $M_\star$ for the chosen EOS. Each curve terminates at the maximal mass of the associated EOS.

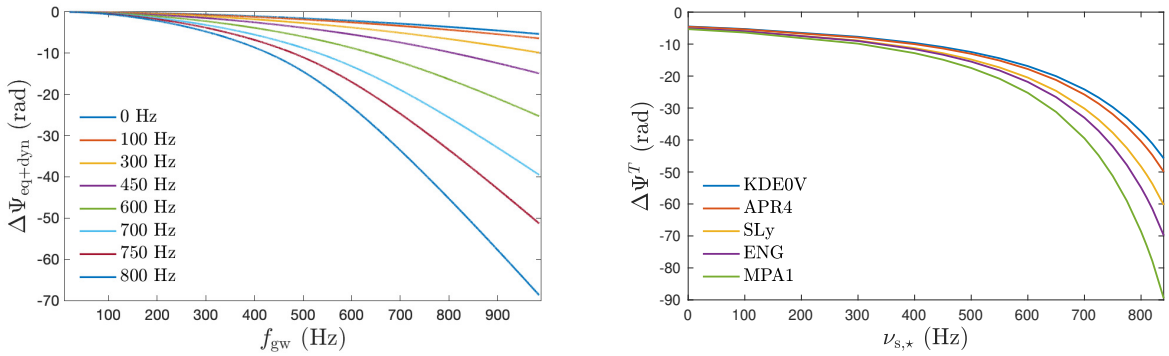

Figure 6.5: *Top panel*: Evolution of GW phase for various spin rates of the primary, $\nu_{{\rm s},\star}$, as functions of $f_{\rm gw}$ for a particular binary (we assumed the MPA1 EOS). *Bottom panel*: Accumulated phase shift $\Delta\Psi^T$ due to tidal effects in both NSs as a function of $\nu_{{\rm s},\star}$, here we used the same EOS as in Fig. 6.4. For both panels, we consider the tidal effect of the primary in symmetric binaries.

6.3.2 Spin modification in Tidal Dephasing

In spinning neutron stars the oscillation frequency splits into co- and counter-rotational components. In the inertial frame, the f-mode frequency in the primary shifts according to Eq. (4.61). For a fast-rotating primary, the frequency shift formulae involving extra terms quadratic in $\nu_{{\rm s},\star}$ has been proposed in [121,390,391]. This quadratic term is however negligible up to high spin $\nu_{{\rm s},\star} \gtrsim 800$ Hz, and the linear modification shown in Eq. (4.61) is adequate for our purpose. The counter-rotating shift in the frequency of the $l = 2 = -m$ f-mode is always negative since the coefficient of the linear correction $C_f \approx 0.3$. A reduced frequency indicates an earlier resonant coupling between the mode and the orbital frequency, thus the accumulation of tidal effects in the waveform will be more significant.

For particular symmetric binaries with two NSs spinning at the same rate and having the same mass, we plot in the top panel of Fig. 6.5 the tidal dephasing induced by the primary

for various spins, as functions of $f_{\rm gw}$. We see that the phase shift increases monotonically with $\nu_{{\rm s},\star}$, while a noticeable, rapid growth is observed in the high GW frequency regime. For instance, the dephasing piles up to about 20 rads for the case with $\nu_{{\rm s},\star} = 800$ Hz during $f_{\rm gw} < 500$ Hz, while the accumulated dephasing is $\lesssim 150$ rad from $f_{\rm gw} = 500$ to 10^3 Hz. In the bottom panel of Fig. 6.5, we show the tidal dephasing $\Delta\Psi^T$ defined in Eq. (6.18) as function of $\nu_{{\rm s},\star}$ for the five EOS used in Fig. 6.4. We observe that the waveform dephasing depends on the EOS, and is smaller for softer EOS due to the smaller radius of the star. Again, we witness a rapid increase of $|\Delta\Psi^T|$ for higher spin due to a different reason. For cases with fixed spin, the dephasing grows faster for a cutoff $f_{\rm max} > 500$ Hz since the information of dynamical tides lies in the high frequency part of waveforms; on the other hand, for cases assuming a fixed $f_{\rm max}$, the dephasing enlarges due to early excitation of f-mode. In particular, a tidal correction of for $f_{\rm max} = 10^3$ Hz and $\nu_{{\rm s},\star} = 850$ Hz, the dephasing of $\Delta\Psi^T \lesssim 100$ rad [right end of the green curve in the bottom panel of Fig. 6.5] is mainly caused by f-mode excitation since the contribution of the equilibrium tide is only $\lesssim 10$ rad.

In addition, we find that there exists a universal relation between $\Delta\Psi^T$ and the dimensionless spin $\nu_{{\rm s},\star} M_\star^2/R_\star$, given by

$$\begin{aligned}\Delta\Psi^T =& -4.850 - 2.539\times10^{-2}\tilde{\nu} + 2.449\times10^{-4}\tilde{\nu}^2 - 1.429\times10^{-6}\tilde{\nu}^3 \\ &+ 3.026\times10^{-9}\tilde{\nu}^4 - 2.482\times10^{-12}\tilde{\nu}^5 \text{ rad}\end{aligned} \tag{6.25}$$

for a normalised spin

$$\tilde{\nu} = \nu_{{\rm s},\star}\left(\frac{M_\star}{1.2M_\odot}\right)^2\left(\frac{R_\star}{12\text{ km}}\right). \tag{6.26}$$

The relation (6.25) is plotted in Fig. 6.6.

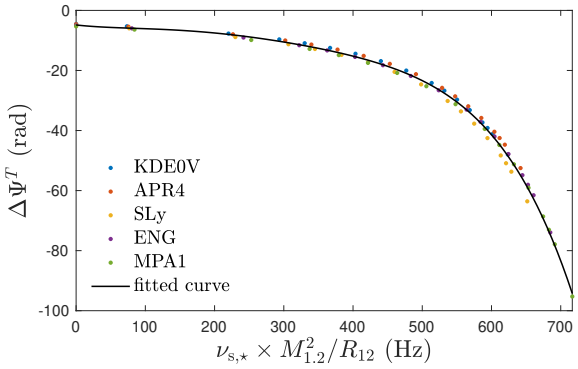

Figure 6.6: Tidal dephasing as a universal function of the dimensionless, normalised spin defined in Eq. (6.26).

Although the EOS-independent Hamiltonian (6.24) is allowed by a non-spinning primary, its universality survives for spins $\nu_{{\rm s},\star} \lesssim 100$ Hz. For example, we see that the phase shift $\Delta\Psi^T$ is EOS-independent for $\nu_{{\rm s},\star} \lesssim 100$ Hz (bottom panel of Fig. 6.5). In reality, mode frequency

will be modified differently depending on the EOS. Although this difference is minor for small spins, the dependence of the phase shift on the EOS is becoming observable as the stellar spin increases.

The Hamiltonian is EOS-independent for most of the coalescing NS binaries since its members are typically old and tend to rotate slowly. Nevertheless, there may still be a number of NSs in binaries with moderate and higher spin rates. A potential case is the secondary of GW190814 [392], we will discuss the specific case in we will Sec. 6.4.

Apart from the rotation-induced modifications to the f-mode frequency ω_f, rotation will induce a correction δQ_f to the tidal overlap integral Q_f. This term, however, is of quadratic order to $\nu_{\mathrm{s},\star}$ [257, 393], and is typically $\delta Q_f \lesssim 10^{-3} Q_f$ even for the fastest rotating NS in a binary observed to-date, viz. PSR J0737-3039A, whose dimensionless spin is $\chi \lesssim 0.05$ (~ 44 Hz; [346]). However, the secondary of GW190814 has a finite chance to set a new record with $\chi \sim 0.47$ (~ 1170 Hz [330]; see also below). In the latter system, a correction of $\delta Q_f \gtrsim 0.2 Q_f$ is expected. However, we will not explore this interesting case in the present article, and we will base our estimations on the tidal overlap integral for non-rotating stars.

6.3.3 Statistical Error

The phase of the (frequency-domain) GW waveform is particularly crucial in estimating parameters in the matching filter algorithm [300, 364, 394], which we summarise in the following.

Defining a sensitivity-curve-weighted inner product in the waveform-space as

$$(g|h) = 2 \int_0^\infty \frac{g^*(f)h(f) + h(f)^* g(f)}{S_n(f)} df, \tag{6.27}$$

for two frequency-domain waveforms f and g, the SNR can then be express as

$$\rho^2[h] = (h|h) = 4 \int_0^\infty \frac{|h(f)|^2}{S_n(f)} df = 4\mathcal{A}^2 \int_0^\infty \frac{f^{-7/3}}{S_n(f)} df, \tag{6.28}$$

where h is the input waveform template, and the latter equality holds if SPA (6.1) has been adopted. Here $S_n(f)$ is the sensitivity curve set by the detector, and the superscript asterisk denotes complex conjugate.

As any measurement comes along with errors, we have to handle the posterior possibility of getting a somewhat different set of parameters θ, which deviates from the true parameters θ_o, by a minute inaccuracy $\Delta\theta_o$ for a given signal s, i.e., $p(\theta|s)$ must be under controlled. For a large S/N, the approximation for the posterior possibility,

$$p(\theta|s) \propto \exp\Big[-\frac{1}{2} \Gamma_{ab} \Delta\theta^a \Delta\theta^b \Big], \tag{6.29}$$

exhibits a Gaussian distribution around θ_o [300, 348], which is characterised by the Fisher

information matrix

$$\Gamma_{ab} = \left(\frac{\partial h}{\partial \theta^a} \middle| \frac{\partial h}{\partial \theta^b} \right). \tag{6.30}$$

The measurement error of θ^a is then defined as

$$\sigma_a = \sqrt{(\Gamma^{-1})^{aa}}, \tag{6.31}$$

where Γ^{-1} is the inverse of the Fisher matrix.

Neglecting explicitly spin-related terms, which is appropriate when the spin is well-constrained or rather small[2] [21], we have the symbolic expression

$$h = h(f_{\rm gw}; \mathcal{A}, f_0 t_o, \phi_o, \mathcal{M}, \eta, \tilde{\Lambda}, \omega_f) \tag{6.32}$$

focusing on the explicit dependencies. Here f_0 is the frequency at the minimum of the sensitivity curve, and we recall that t_o and ϕ_o are the reference time and phase often set as the values of as of merger [defined in Eq. (6.2)]. Although the Fisher matrix is 7 dimensional, we can suppress one of its dimensions by factoring out the elements related to $\mathcal{A}$ since the amplitude is uncorrelated with the other quantities involved in the inner product Eq. (6.27) in SPA.

For the measurement of $\mathcal{M}$ and η, it has been demonstrated in [21] that 2 PN order approximants for point-mass waveform suffice the purpose of estimating errors in tidal parameters. For later convenience, we provide the derivatives (cf. Eq. (3.10) of [348])

$$\frac{\partial \ln h_{\rm pp}}{\partial (f_0 t)} = 2\pi i (f_{\rm gw}/f_0), \tag{6.33a}$$

$$\frac{\partial \ln h_{\rm pp}}{\partial \phi_o} = -i, \tag{6.33b}$$

$$\frac{\partial \ln h_{\rm pp}}{\partial \ln \mathcal{M}} = -\frac{5i}{128}(\pi \mathcal{M} f_{\rm gw})^{-5/3} \left[1 + \left(\frac{743}{252} + \frac{11}{3}\eta \right) x - \frac{32\pi}{5} x^{3/2} + \left(\frac{3058673}{508032} + \frac{5429}{504}\eta + \frac{617}{72}\eta^2 \right) x^2 \right], \tag{6.33c}$$

and

$$\frac{\partial \ln h_{\rm pp}}{\partial \ln \eta} = -\frac{i}{96}(\pi \mathcal{M} f_{\rm gw})^{-5/3} \left[\left(\frac{743}{168} - \frac{33}{4}\eta \right) x - \frac{108}{5}\pi x^{3/2} + \left(\frac{3058673}{56448} - \frac{5429}{224}\eta - \frac{5553}{48}\eta^2 \right) x^2 \right] \tag{6.33d}$$

for the point-mass approximants. We will approximate the variance of the strain (6.32) with

[2] As of the time this article is prepared, the known, fastest spinning NS in binaries is PSR J0737-3039A, whose dimensionless spin, though depending on the EOS, is estimated to be $\lesssim 0.03$ [21].

infinitesimal changes of non-tidal parameters by the point-mass formulas (6.33), i.e.,

$$\frac{\partial h}{\partial X} \simeq \frac{\partial h_{\rm pp}}{\partial X} \tag{6.34}$$

for $X = \{f_0 t,\, \phi_o,\, \ln \mathcal{M},\, \ln \eta\}$. On the other hand, we numerically evaluate $\frac{\partial h}{\partial \tilde{\Lambda}}$ by first constructing two waveforms with slightly different tidal deformabilities $\tilde{\Lambda} \pm \epsilon$, while fixing other parameters, then dividing the difference of the two waveforms by the difference in $\tilde{\Lambda}$, viz.

$$\frac{\partial h}{\partial \tilde{\Lambda}} = \frac{h(\tilde{\Lambda}+\epsilon) - h(\tilde{\Lambda}-\epsilon)}{2\epsilon}. \tag{6.35}$$

The scheme admits that the variation of $h(\Lambda)$ does not feel the variance of the others (even though via the inversion of the Fisher matrix there is some mixing). The same procedure is performed for the parameter ω_f to obtain $\partial h/\partial \omega_f$. Measurement errors, (6.31), can then be calculated by inverting the Fisher matrix (6.30).

Adopting the sensitivity curve of aLIGO and assuming that the data streams are measured across the frequency band $20 \leq f_{\rm gw} \leq 10^3$ Hz with a SNR $\rho = 25$, we estimate the errors $\Delta\mathcal{M}/\mathcal{M}$, $\Delta\eta/\eta$, $\Delta\tilde{\Lambda}/\tilde{\Lambda}$ and $\Delta\omega_f/\omega_f$ in Table 6.1. We see that the magnitude of tidal phase shift $\Delta\Psi^T$ increases with stellar spin due to earlier excitation of f-mode, allowing for a more accurate extraction of tidal parameters. In particular, the error in $\tilde{\Lambda}$ and ω_f reduce rapidly for increasing spin, where the error can be $< 1\%$ for the former and $< 15\%$ for the latter if the NS spins at 800 Hz. The improvement in the measurability of both $\tilde{\Lambda}$ and ω_f is due to the earlier excitation of the f-mode whose frequency was shifted by the rotation. An earlier mode excitation increases significantly the transfer of orbital energy to stellar oscillations affecting significantly the dephasing. As a result, f-mode frequency will be estimated with significantly smaller error. Actually, even thought the dephasing due to the equilibrium tide is not directly affected, the increasing influence of the dynamical tides encodes certain information of the equilibrium tides since the latter is the adiabatic limit of the former – notice that Λ factors out in $\Delta\Psi^{\rm dyn}_\star$ in Eq. (6.16). Therefore, by including the dynamical tides in the Fisher analysis for $\tilde{\Lambda}$ we effectively place extra emphasis on the high-frequency part of waveform.

For the considered data stream, the tidal dephasing $|\Delta\Psi^T|$ is larger than the uncertainty of phase $\Delta\phi_o$ even for a non-spinning star. However, the tidal dephasing may be hidden in the uncertainty in phase $\Delta\phi_o$ for a lower cutoff. In general, tidal dephasing is a function of $\nu_{{\rm s},\star}$ and $f_{\rm max}$ [i.e., $\Delta\Psi_T = \Delta\Psi_T(\nu_{{\rm s},\star}, f_{\rm max})$], while the uncertainty in phase is a function of SNR and $f_{\rm max}$ [i.e., $\Delta\phi_o = \Delta\phi_o(\rho, f_{\rm max})$]. For a particular binary with the spin of the primary being $\nu_{{\rm s},\star} = 45$ Hz and the SNR of the associated waveform being $\rho = 25$, we integrate Eq. (6.18) and Eq. (6.27) from $f_{\rm gw} = 20$ Hz to a varying cutoff $f_{\rm max}$. We plot $\Delta\phi_o$ and $\Delta\Psi^T$

Table 6.1: Statistical estimation of the measurement error for the accumulated tidal dephasing $\Delta\Psi^T$ [Eq. (6.18)] (3rd column), the GW phase $\Delta\phi_o$ (4th column), the chirp mass $\Delta\mathcal{M}/\mathcal{M}$ (5th column), the symmetric mass ratio $\Delta\eta/\eta$ (6th column), the mutual tidal deformability $\Delta\tilde{\Lambda}/\tilde{\Lambda}$ (7th column), and the frequency of the f-mode in the primary $\Delta\omega_f/\omega_f$ (8th column) assuming the cutoff as $f_{\rm max} = 10^3$ Hz. We additionally considered the uncertainty of $\tilde{\Lambda}$ for $f_{\rm max} = 450$ Hz in the final column so as to be compared to the results in [21], which are shown in the final column of their Tab. 2 though there the authors adopted $\rho = 1$ and did not present by percentage. We assumed symmetric binaries with $\tilde{\Lambda} = 920$ while the EOS used are listed in the 1st column. We used four representative spin rates (given in Hz): 0 (non-spinning), 45 (fastest known NS in binaries), 500 (moderate fast), and 800 (rather fast) of the primary. In general, the errors scale as $1/\rho$, while the results derived assuming an SNR value of $\rho = 25$. The table are prepared by considering only the tidal effects of the primary.

EOS	$\nu_{{\rm s},\star}$ (Hz)	$\Delta\Psi^T$ (rad)	$\Delta\phi_o$ (rad)	$\Delta\mathcal{M}/\mathcal{M}$	$\Delta\eta/\eta$	$\Delta\tilde{\Lambda}/\tilde{\Lambda}$	$\Delta\omega_f/\omega_f$	$[\Delta\tilde{\Lambda}/\tilde{\Lambda}]_{450}$
KDE0V	0	-4.4982	1.5231	0.0037%	1.1383%	5.0868%	664.5%	83.67%
	45	-4.8299	1.5150	0.0037%	1.1335%	4.4050%	568.3%	73.23%
	500	-12.4849	1.6379	0.0038%	1.2128%	0.6339%	74.08%	5.940%
	800	-37.3150	1.4969	0.0037%	1.1274%	0.2266%	14.92%	2.080%
APR4	0	-4.5928	1.5220	0.0038%	1.1496%	4.8817%	634.9%	79.62%
	45	-4.9372	1.5138	0.0038%	1.1447%	4.2180%	541.5%	69.74%
	500	-13.0437	1.4196	0.0037%	1.0886%	0.7189%	70.23%	11.99%
	800	-40.4013	1.5165	0.0038%	1.1514%	0.2151%	13.79%	1.777%
SLy	0	-5.0406	1.5218	0.0039%	1.1630%	4.3130%	557.2%	69.71%
	45	-5.4287	1.5137	0.0039%	1.1581%	3.7168%	473.6%	60.76%
	500	-14.8164	1.4367	0.0038%	1.1124%	0.6322%	60.40%	9.857%
	800	-48.2919	1.5813	0.0040%	1.2057%	0.1956%	12.18%	1.300%
ENG	0	-5.0167	1.5184	0.0042%	1.1828%	4.1548%	531.8%	66.64%
	45	-5.4175	1.5110	0.0042%	1.1782%	3.5738%	450.8%	57.58%
	500	-15.4857	1.4449	0.0041%	1.1388%	0.5933%	54.78%	8.660%
	800	-54.8652	1.6344	0.0044%	1.2623%	0.1858%	10.93%	0.9655%
MPA1	0	-5.3222	1.5179	0.0045%	1.2083%	3.7394%	473.2%	58.69%
	45	-5.7651	1.5102	0.0045%	1.2034%	3.2010%	398.6%	49.91%
	500	-17.4710	1.2997	0.0042%	1.0679%	0.6222%	17.48%	14.19%
	800	-68.6082	1.7409	0.0049%	1.3587%	0.1700%	9.410%	0.6029 %

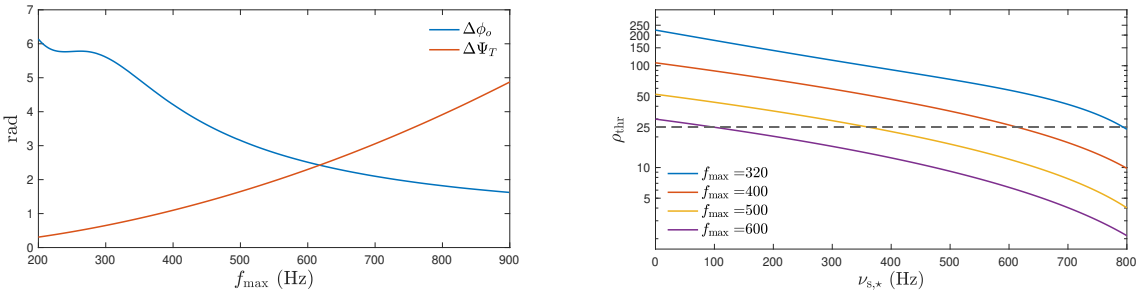

Figure 6.7: *Top panel*: Uncertainty in the GW phase $\Delta\phi_o$ (blue) and tidally-induced phase shift $\Delta\Psi^T$ (red) [Eq. (6.18)] as functions of the cutoff frequency $f_{\rm max}$. The spin of the primary and the SNR are set as, respectively, $\nu_{\rm s,\star} = 45$ Hz and $\rho = 25$. *Bottom panel*: SNR $\rho_{\rm thr}$ for the uncertainty in phase $\Delta\phi_o$ to equate the tidal dephasing $|\Delta\Psi^T|$ [Eq. (6.36)] for four cutoff frequencies as functions of $\nu_{\rm s,\star}$. In both panels, the symmetric binary with $\tilde{\Lambda} = 920$ and EOS MPA1 is considered.

as functions of $f_{\rm max}$ in the top panel of Fig. 6.7. In this example, the tidal dephasing becomes noticeable if the cutoff is $\gtrsim 600$ Hz. In general setting, there is a minimal SNR $\rho_{\rm thr}$ for a specific spin ν_o and cutoff $f_{{\rm max},o}$, defined by the equality

$$\Delta\Psi^T(\nu_o, f_{\rm max,o}) = \Delta\phi_o(\rho_{\rm thr}, f_{\rm max,o}). \tag{6.36}$$

To grasp how the increasing spin improves the detectability of tidal effects, we find $\rho_{\rm thr}$ as function of the NS spin assuming some cutoff frequencies for a particular binary in the bottom panel of Fig. 6.7. Improvement of measurability is observed when $f_{\rm max}$ is extended.

6.4 Case Study: GW190814

The event GW190814, reported by the LIGO-Virgo-Kagra collaboration at a SNR of $\rho = 25$ [395], consists of one black hole, weighting $22.2 - 24.3 M_\odot$, and a compact object with $2.50 - 2.67 M_\odot$. The mass of the latter intriguingly falls in the so-called "lower mass gap" $(2.5 - 5 M_\odot)$, and may be either the lightest black hole or the heaviest NS known to-date. A possibility that the secondary is a mass-gap, fast-rotating NS has been raised in [330,365,366], with the highest suggested spin being $\nu_{\rm s,\star} \sim 1170$ Hz [330]. Although the spin parameter for this presumably, rapidly-rotating NS has not been well constrained, an estimation of the dimensionless spin χ via the relation (cf. Eq. (3) of [392]),

$$\chi \approx 0.4\ (\nu_{\rm s,\star}/10^3\ {\rm Hz}), \tag{6.37}$$

gives $\chi \approx 0.47$ for the rate $\nu_{\rm s,\star} \sim 1170$ Hz, which is about 65% of maximum spin ($\chi \sim 0.7$) attainable by an isolated NS [396]. This peculiar system may originate from a dynamical process, such as dynamical encounters in a star cluster [81,82], hierarchical triple system [83], and tidal capture [84] of a natal NS kicked off from its born site by a BH.

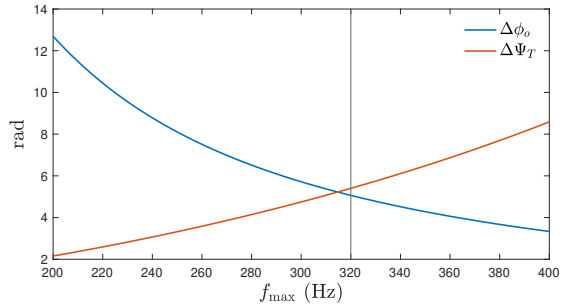

Figure 6.8: Same plot as the top panel of Fig. 6.7, while the spin of the primary is $\nu_{\rm s,\star} = 800$ Hz here. The vertical line marks the merger frequency 360 Hz.

Table 6.2: Parameters relevant to Eq. (6.38) for the chosen EOS. The inertial-frame, spin-modified f-mode frequency is listed in the second column, and the fitting parameters defined in Eq. (6.38) are presented from the third to the final column. Here we assume $\nu_{\rm s,\star} = 800$ Hz.

EOS	$\omega_f/2\pi$ (Hz)	a_1	a_2	b_1	b_2
KDE0V	817.57	509.55	-2.46	9.05	-2.34
APR4	789.65	436.70	-2.49	7.86	-2.36
SLy	748.47	321.41	-2.53	5.91	-2.38
ENG	697.92	241.25	-2.60	4.59	-2.42
MPA1	637.01	151.46	-2.70	3.04	-2.47

Compared to the other tidal contributions, dephasing due to spin effects is secondary. Still, it seems that the estimation of spin parameter via its impact on the tidal dephasing may be promising. In this section, we discuss the tidally-induced phase shift for a fast-spinning NS, and estimate how can we probe both the f-mode frequency and the stellar spin rate from the waveform of GW190817 if the secondary turns out to be a fast-rotating NS. We will focus on the tidal dephasing caused by the fast spinning secondary, which is taken as the primary.

6.4.1 Estimation of Source Parameters

Adopting the definition of the onset of the merger as [397], i.e., when $\pi(M_\star + M_{\rm comp}) f_{\rm gw} = 0.2$, the total mass of $\sim 27 M_\odot$ of GW190814 suggests that the merger occurred at $f_{\rm gw} \lesssim 360$ Hz. In our simulation of the binary having two constituents with the masses and radii of those for GW190814, we find the separation between the two bodies is ~ 95 km when $f_{\rm gw} = 360$ Hz, which is larger than the sum of the two radii, viz. ~ 75 km. We therefore set the cutoff at $f_{\rm max} = 360$ Hz and the "competition" between $\Delta\Psi^T$ and $\Delta\phi_o$ is plotted in Fig. 6.8. We see that the tidal dephasing in the waveform is exceeding the error of phase even with this low cutoff since the spin is rather fast. Ignorance of the tidal effect in this case will therefore deteriorate the extraction of source parameters to an extent worse than ignoring the uncertainty in the reference phase ϕ_o.

Although we show that the inclusion of tidal dephasing is necessary since the primary spins rapidly, the uncertainties for $\tilde{\Lambda}$ and ω_f are however large for this low $f_{\rm max}$. We investigate

the uncertainties of these two parameters as functions of $f_{\rm max}$ in a neighbourhood of 360 Hz. In particular, we find the following relations

$$\frac{\Delta\omega_f}{\omega_f} = a_1 \left(\frac{f_{\rm max}}{360\ {\rm Hz}}\right)^{a_2} \%, \quad \text{and} \quad \frac{\Delta\tilde{\Lambda}}{\tilde{\Lambda}} = b_1 \left(\frac{f_{\rm max}}{360\ {\rm Hz}}\right)^{b_2} \%, \tag{6.38}$$

for the chosen EOS and $f_{\rm max} \in [200, 400]$ Hz, where the fitting parameters a_i and b_i are listed in Tab. 6.2. The b_2 parameter is consistent with the trend showed in the Fig. 10 of [372].

Although we have assume the knowledge of the spin in the above analysis, we note that we may estimate the spin by exploiting the universality of the tidal dephasing as a function of the dimensionless spin [Fig. 6.6; Eq. (6.25)], together with the mass measurement and the radius inferred by $\tilde{\Lambda}$ in the fashion of [115].

6.5 Discussion

The phase of gravitational waveform is sensitive to several stellar parameters, which elevates it into an invaluable position in the GW physics era. Among other factors, the tidal contribution to the GW phasing encodes the details of internal motions of NSs, consisting of the equilibrium tide, described by the tidal deformability (Sec. 6.2.1), and the dynamical, f-mode oscillation, captured by the mode frequency ω_f and its coupling strength to the external tidal field Q_f [Eq. (6.19)].

As we mention earlier, both spin and tidal effects will influence the GW phasing though the spin contribution is smaller [313]. Therefore, it is crucial to estimate the phase shift caused by each one of them for the precise estimation of the tidal parameters (e.g., [358]). If we can determine independently the stellar spin through, e.g., the range of dynamical ejecta [398, 399], a shift in the main pulsating mode in hypermassive NS remnant [327, 400], or a system showing double precursors (Chap. 5), we can construct a point-particle waveform for that spin. Subtracting the point-particle waveform from the data then returns the tidal dephasing. In addition, the tidal effects are encoded in the high frequency part of GW data stream, while the spin affects mainly the low frequency part [361, 385]. We may acquire the individual spins in the early waveform by firstly measuring the mutual, effective spin via spin-orbit contribution in GW phase shift, then solving for the individual ones via dephasing due to spin-spin effect. Although the latter spin-spin contribution is degenerate with the self-spin effect as discussed in Introduction, the I-Love-Q relation can help break the degeneracy since the spin-induced quadrupole moment can be estimated from the adiabatic tidal parameter [183, 401]. The tidal dephasing can then be obtained by subtracting the template including the spin effects but no tidal effects, as stated above. On the other hand, GW luminosity during the inspiralling is more sensitive to the tidal effects rather than spin-orbit terms [402].

In particular, the tidal contribution of the primary to the luminosity reads [77]

$$\mathcal{L}^{T}_{\rm GW} = \frac{192\eta^2 x^{10}(M_\star + 3M_{\rm comp})M_\star^4 \Lambda_\star}{5(M_\star + M_{\rm comp})^5}, \tag{6.39}$$

while the spin-orbit effects give only negligible amount to it. Therefore, by correlating the tidal imprints in the phasing and the luminosity, we may be able to determine better the tidal parameters. Nonetheless, we note that the above equation applies to non-spinning NSs.

In reality, the effect of tides in the tidal evolution and dephasing is 3-fold: *gravito-electric*, *gravito-magnetic* tides, and the *change in the waveform* shape induced from the gravito-electric tidal field [259, 403, 404]. We focus in the present article the gravito-electric tides, while we note that some excitations ignited by the gravito-magnetic tidal field [387, 405] may become comparable to the gravito-electric excitations under certain conditions [406]. In addition, although we consider the spin-influenced tidal effects in GW phase, we do not include the spin-corrected orbital motion, and the rotation-induced deformation of NSs in the present article. Despite the minor spin contribution in the GW dephasing compared to the tidally-induced phase shift (e.g., [400]), the uncertainty in the spin contribution will deteriorate the estimation of the tidal parameters. Detailed analysis accounting for the other types of tides, and including the spin-induced dephasing would be useful in this direction. In addition, during the preparation of this article, there is an investigation [407] pointing out the importance of tidal-spin interaction in the waveform modeling if the NS spins rapidly with $\chi \gtrsim 0.1$.

Part II

Dynamics of Scalarized Compact Objects

Chapter 7

Equilibrium and Stability of Scalarized Neutron Stars

Contents

Breakdown of Contributions

I contribute to producing all the plots, while datum for Fig. 7.2 are prepared by Daniela D. Doneva. The numerical, nonlinear simulations are carried out with a code generalised from the open-source code GR1D by me in order to study the dynamical behaviours of spherical, isolated compact objects in tensor-multi-scalar theories. The perturbative analysis is executed by Jasbir Singh, and Daniela D. Doneva. The analytic proof for the stability of polar-dependent scalar fields is provided by Stoytcho S. Yazadjiev. Although we focus on the one of the scalar field that plays the major role in predicting stability of scalarized neutron stars, an analytic proof for the stability of other scalar fields is derived by S. S. Yazadjiev, which better illustrates the major role of the scalar field to which we specialised ourselves. K. D. Kokkotas provides constructive comments on the manuscript written partially by me and D. D. Doneva, and recommends additional numerical manipulations to improve the robustness of our results.

Overview

It was recently shown, that in a class of tensor-multi-scalar theories of gravity with a nontrivial target space metric, there exist scalarized neutron star solutions. An important property of these compact objects is that the scalar charge is zero and therefore, the binary pulsar experiments can not impose constraints based on the absence of scalar dipole radiation. Moreover, the structure of the solutions is very complicated. For a fixed central energy density up to three neutron star solutions can exist — one general relativistic and two scalarized, that is quite different from the scalarization in other alternative theories of gravity. In the present Chapter we address the stability of these solutions using two independent approaches — solving the linearised radial perturbation equations and performing nonlinear simulations in spherical symmetry. The results show that the change of stability occurs at the maximum mass models and all solutions before that point are stable. This leads to the interesting consequence that there exists a stable part of the scalarized branch close to the bifurcation point where the mass of the star increases with the decrease of the central energy density.

7.1 Introduction

Perhaps the most widely studied models of compact stars in alternative theories of gravity are the scalarized neutron stars in the Damour-Esposito-Farese (DEF) scalar-tensor theory of gravity [89, 408]. The reason is that these were the first models that offered the possibility to have a theory perturbatively equivalent to General Relativity (GR), and thus no constraints from the weak field observations can be imposed, while still allowing for large deviations in the strong gravitation regime due to a nonlinear development of the scalar field. This mechanism for development of a nontrivial scalar field is possible for other compact objects, such as black holes [91, 105, 106, 409–411], but it requires either some not very realistic astrophysical conditions, or further modifications of the Hilbert-Einstein action such as the inclusion of curvature invariants. For neutron stars, the matter itself can act as a source of the scalar field due to the nonzero trace of the energy momentum tensor, and thus scalarized neutron stars became naturally the primary target for investigating the possible effects of nontrivial scalar hair and its observational implications.

Scalarization indeed can produce very large deviations from GR, but in the standard DEF model it leads to the emission of scalar dipole radiation that is severely limited by the binary pulsar observations [408, 412–415]. An elegant way to evade these constraints is to consider a nonzero scalar field mass, that suppresses the scalar dipole radiation [416–419]. Another more sophisticated and also viable approach is to allow for the presence of multiple scalar fields. This is possible in the tensor-multi-scalar theories (TMST) of gravity that are the generalization of the standard scalar-tensor theories to multiple scalar field. These theories are mathematically self-consistent and well posed, and can pass through all known

experimental and observational tests [420–424]. Moreover, (quantum motivated) higher-order generalizations of GR often predict the existence of multiple scalar fields [420, 425].

In TMST different kinds of interesting compact objects can be constructed including solitons [422, 426], mixed soliton-fermion stars [423], topological and scalarized neutron stars [424, 427, 428]. The variety of solutions is controlled mainly by the choice of target space for the scalar fields φ and the metric defined on it, and the choice of the map $\varphi : \textit{spacetime} \to \textit{target space}$. In particular, for a nontrivial map $\varphi : \textit{spacetime} \to \textit{target space}$ where the *target space* is a maximally symmetric 3-dimensional space ($\mathbb{S}^3$, $\mathbb{H}^3$ or $\mathbb{R}^3$), there exists non-topological, spontaneously scalarized neutron stars in this theory [428]. These are mathematically similar to topological neutron stars [424], but with an important difference: the value of the scalar field at the center of the star is zero and thus the topological charge vanishes. A very important property of these solutions is that they have a zero scalar charge and thus no emission of scalar dipole radiation is possible. Therefore, the strong observational constraints on the standard scalar-tensor theories obtained on the basis of the binary pulsar observations simply do not apply for the TMST under consideration that allows for strong possibly observable deviations from GR.

As discovered in [428], the scalarized TMST neutron stars show a very interesting property related to the uniqueness of the solutions. This constitutes in the fact that for a fixed central energy density up to three neutron star solutions can exist – one GR solution with zero scalar field and up to two scalarized solutions. This is in sharp contradiction with the standard scalar-tensor theories [89] where only one scalarized neutron star solution can exist for a given central energy density. The preliminary stability analysis performed in [428] based on the turning point method, suggested that all three of the solutions are stable (where exist). In the present Chapter we go further by performing a stability analysis (both a linear and nonlinear one) in order to determine the (in)stability of the scalarized neutron stars. Radial perturbations of neutron stars in scalar-tensor theories have already been studied in [429, 430] while the linear stability of TMST for topological neutron stars was examined in [427].

In section 7.2, we give a brief overview of the theory of scalarized neutron stars and in section 7.3 we present the background neutron star solutions. The stability of these solutions is examined in sections 7.4 and 7.5 in the linear and nonlinear regimes respectively. Finally, the conclusions are presented in section 7.6.

7.2 Neutron stars in tensor-multi-scalar theories of gravity

In this section, we will briefly describe the basics of TMST and especially the subclass of these theories that allows for the construction of scalarized neutron stars. For a more extensive discussion, we refer the reader to the original paper where these solutions where constructed [424].

The most general action of TMST in the Einstein frame can be written in the form [420, 421]:

$$S = \frac{1}{16\pi G_*}\int d^4\sqrt{-g}\left[R - 2g^{\mu\nu}\gamma_{ab}(\varphi)\nabla_\mu\varphi^a\nabla_\nu\varphi^b - 4V(\varphi)\right] + S_m(A^2(\varphi)g_{\mu\nu}, \Psi_m), \tag{7.1}$$

where G_* is the bare gravitational constant, ∇_μ and R are the covariant derivative and Ricci scalar respectively, both associated with $g_{\mu\nu}$. $V(\varphi) \geq 0$ denotes the potential of the scalar fields and Ψ_m represents collectively the matter fields. The theory is equipped with N scalar fields φ_a that define a map φ : *spacetime* $\rightarrow$ *target space*, where the *target space* is a N-dimensional Riemannian manifold $\mathcal{E}_N$ with $\gamma_{ab}(\varphi)$ as a positively definite metric defined on it. The function $A(\varphi)$ is the conformal factor connecting the metrics in the Einstein frame ($g_{\mu\nu}$) and the physical Jordan frame ($\tilde{g}_{\mu\nu}$) via the relation

$$\tilde{g}_{\mu\nu} = A^2(\varphi)g_{\mu\nu}. \tag{7.2}$$

In our calculations we will adopt the Einstein frame for mathematical simplicity while all final quantities will be transformed to the physical frame. Unless otherwise specifies, tilde will denote the quantities in the Jordan frame.

By varying the action (7.1) with respect to the metric and the scalar fields, metric equations and the equations of motion for scalar fields in the Einstein frame,

$$R_{\mu\nu} = 2\gamma_{ab}(\varphi)\nabla_\mu\varphi^a\nabla_\nu\varphi^b + 2V(\varphi)g_{\mu\nu} + 8\pi G_*\left(T_{\mu\nu} - \frac{1}{2}Tg_{\mu\nu}\right),$$

and

$$\nabla_\mu\nabla^\mu\varphi^a = -\gamma^a_{bc}(\varphi)g^{\mu\nu}\nabla_\mu\varphi^b\nabla_\nu\varphi^c + \gamma^{ab}(\varphi)\frac{\partial V(\varphi)}{\partial\varphi^b} - 4\pi G_*\gamma^{ab}(\varphi)\frac{\partial \ln A(\varphi)}{\partial\varphi^b}T, \tag{7.3}$$

can be obtained, where $\gamma^a_{bc}(\varphi)$ denotes the Christoffel symbols of the target space metric $\gamma_{ab}(\varphi)$. The Einstein frame energy-momentum tensor $T_{\mu\nu}$ satisfies the following conservation relation:

$$\nabla_\mu T^\mu_\nu = \frac{\partial \ln A(\varphi)}{\partial\varphi^a}T\nabla_\nu\varphi^a. \tag{7.4}$$

The energy-momentum tensor in the Jordan frame is given by $\tilde{T}_{\mu\nu} = A^{-2}(\varphi)T_{\mu\nu}$. We only consider perfect fluid stars in our analysis and thus the energy density, the pressure and the 4-velocity are connected in the two frames by $\varepsilon = A^4(\varphi)\tilde{\varepsilon}$, $p = A^4(\varphi)\tilde{p}$ and $u_\mu = A^{-1}(\varphi)\tilde{u}_\mu$ respectively.

We are interested in static, spherically symmetric and asymptotically flat solutions. As in

Chap. 2, the metric takes the following general form

$$ds^2 = -e^{2\Phi(r)}dt^2 + e^{2\Lambda(r)}dr^2 + r^2(d\theta^2 + \sin^2\theta d\phi^2). \tag{7.5}$$

where we change the notation for the $\{rr\}$-component of the metric (2.1) from $\lambda(r)$ to $\Lambda(r)$. We note that $\Lambda(r)$ denotes, in this second part of the present thesis, the exponent of the lapse function, and should not be confused with the adiabatic index for the perturbation defined in Part I of this thesis. Accordingly, Eq. (2.4) has a new expression:

$$e^{-2\Phi} = 1 - \frac{2m(r)}{r}. \tag{7.6}$$

The 4-velocity of a generic fluid moving radially is

$$\tilde{u}^\mu = \frac{1}{\sqrt{1-v^2}}(e^{-\Phi}\partial_t + ve^{-\Lambda}\partial_r), \tag{7.7}$$

with the characteristic strength v.

The simplest setup that can lead to the existence of the desired scalarized solutions is the following [428]. We consider three scalar fields $\varphi_a = \{\chi, \Theta, \Xi\}$, with the target space manifold being $\mathbb{S}^3$, $\mathbb{H}^3$ or $\mathbb{R}^3$. Thus the 3-dimensional target space metric takes the following form:

$$\gamma_{ab}d\varphi^a d\varphi^b = a^2\left[d\chi^2 + H^2(\chi)(d\Theta^2 + \sin^2\Theta d\Xi^2)\right], \tag{7.8}$$

where Θ and Φ are the standard angular coordinates on the 2-dimensional sphere $\mathbb{S}^2$ and the parameter a is related to the curvature of $\mathbb{S}^3$ and $\mathbb{H}^3$. The function $H(\chi)$ represents the target space geometry: for spherical geometry $\mathbb{S}^3$, $H(\chi) = \sin\chi$; for hyperbolic geometry $\mathbb{H}^3$, $H(\chi) = \sinh\chi$; and finally for flat geometry $\mathbb{R}^3$, $H(\chi) = \chi$. We will only consider theories where the coupling function $A(\varphi)$ and the potential $V(\varphi)$ depend only on χ, which in turn allows the equations for Θ and Ξ to separate. This guarantees that the spacetime will be spherically symmetric in both the Einstein and the Jordan frames for the ansatz defined below.

In this Chapter we choose a nontrivial map φ such that the field χ is assumed to depend on the radial coordinate r while Θ and Ξ are independent from r and are given by $\Theta = \theta$ and $\Xi = \phi$ [424, 428]. This ansatz is compatible with the spherical symmetry and in addition, ensures that the equations for Θ and Ξ are satisfied.

Using the ansatz stated above and the general form of the field equations (7.3), the dimensionally reduced field equations governing the neutron star equilibrium solutions can be derived. Since they are somewhat lengthy and also not the main focus of the present Chapter, we will not present them here and refer the reader to [428]. They have to be supplemented with boundary conditions and we consider the standard ones – regularity at the center of the

star and asymptotic flatness.Thus we impose $\Phi(\infty) = 0$, $\Lambda(\infty) = 0$ and $\chi(\infty) = 0$, while at the stellar center $\Lambda(0) = 0$ and $\chi(0) = 0$. As a matter of fact for a target space being $\mathbb{S}^3$, the scalar field χ can have a more general boundary condition at the center $\chi(0) = n\pi$ with $n \in \mathbb{Z}$ being the stellar topological charge [424, 427]. In the present Chapter, though, we will be focusing only on non-topological scalarized neutron stars and thus consider $n = 0$.

At infinity the scalar field χ behaves as

$$\chi \approx \frac{\text{const}}{r^2} + O(1/r^3). \tag{7.9}$$

In this expansion, the $1/r$ term is missing and thus the scalar charge is zero. This implies that these starts do not emit any scalar dipole radiation and therefore they comply with the binary pulsar observations by construction. Furthermore, since the leading order term in the expansion is proportional to $1/r^2$, the ADM masses in both frames are the same.

7.3 The background solutions

Here, we will briefly present the behavior of the background solutions that will be later evolved. More details can be found in [428]. To construct scalarized neutron stars, the conformal factor function $A(\chi)$ has to be chosen to satisfy the following conditions

$$\frac{\partial A}{\partial \chi}(0) = 0, \quad \frac{\partial^2 A}{\partial \chi^2}(0) \neq 0. \tag{7.10}$$

Taking these conditions into account, we employ the following standard form of the conformal factor

$$A(\chi) = e^{\beta\alpha(\chi)}, \tag{7.11}$$

where $\alpha(\chi)$ is a function of the scalar field and can be, e.g., a periodic function such as $\sin^2\chi$, or simply χ^2. It is straightforward to show that these coupling functions satisfy the conditions (7.10). The dimensionally reduced field equations together with the above mentioned boundary conditions are solved numerically using a shooting method. The shooting parameters are the central values of the scalar field derivative $(d\chi/dr)(0)$ and the metric function $\Phi(0)$, which are determined so that χ and Φ tend to zero at (numerical) infinity.

Fig. 7.1 shows the neutron star mass M as a function of the central energy density $\tilde{\varepsilon}_c$ for a conformal factor $A(\chi) = \exp(\beta \sin^2\chi)$ and the three possible choices of $H(\varphi)$. In this figure, we used a hybrid equation of state (EOS) to account for the stiffening of the matter at nuclear density $\tilde{\rho}_{\text{nucl}} = 2 \times 10^{14}$ g/cm^{-3}, where the pressure and the internal energy are

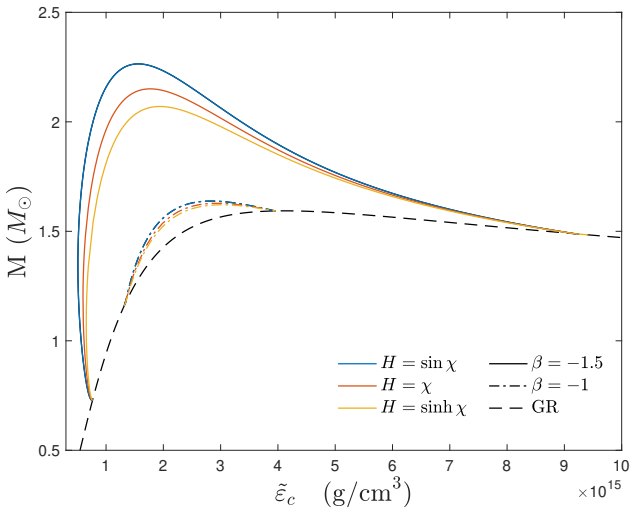

Figure 7.1: The mass as a function of the central energy density for the fundamental branch of scalarized neutron stars possessing nodeless scalar field. Solutions for the cases with $A(\chi) = \exp(\beta \sin^2 \chi)$ and $H(\chi) = \{\sin\chi, \chi, \sinh(\chi)\}$ are shown. The values of the parameters are fixed to $a^2 = 0.1$ and $\beta = \{-1, -1.5\}$. The neutron stars with zero scalar field are plotted with a black line.

given by

$$\tilde{p} = K_1 \tilde{\rho}^{\Gamma_1}, \quad \tilde{\varepsilon}_i = \frac{K_1}{\Gamma_1 - 1} \tilde{\rho}^{\Gamma_1 - 1}, \quad \text{for} \quad \tilde{\rho} \leq \tilde{\rho}_{\text{nucl}}, \tag{7.12}$$

$$\tilde{p} = K_2 \tilde{\rho}^{\Gamma_2}, \quad \tilde{\varepsilon}_i = \frac{K_2}{\Gamma_2 - 1} \tilde{\rho}^{\Gamma_2 - 1}, \quad \text{for} \quad \tilde{\rho} > \tilde{\rho}_{\text{nucl}}. \tag{7.13}$$

The energy density and the internal energy are related to each other via $\tilde{\varepsilon} = \tilde{\rho}(1 + \tilde{\varepsilon}_i)$. This equation of state clearly does not reach the two solar mass barrier, but it was widely used for example in the nonlinear simulations of stellar evolution in scalar-tensor theories [431–435]. Since our nonlinear code for examining the stability is based on [434, 435] we decided to keep this EOS for consistency with the canonical values $\Gamma_1 = 1.3$, $\Gamma_2 = 2.5$. We have performed calculations for other piecewise polytropic EOS [436] and the results remain qualitatively the same.

As one can easily check, the GR neutron star solutions with zero scalar field are always solutions of the field equations (7.3) if it obeys the conditions (7.10). At a certain energy density $\tilde{\varepsilon}_c^{\text{crit}}$ a nontrivial scalar field develops and the solutions bifurcate from GR. As discussed in [428], $\tilde{\varepsilon}_c^{\text{crit}}$ is controlled only by the values of β/a^2 and it is independent on the particular form of the coupling function (as long as it allows for scalarization of course). These scalarized solutions coexist with the GR solutions indicating non-uniqueness and they are energetically favorable. However, at a particular higher value of the central energy density, the scalarized branch of solutions merges again with the GR one and the neutron stars with nonzero scalar field cease to exist. With the decrease of β/a^2 the range of central energy

densities, where scalarized solutions exist, gets larger and the deviations from GR increase. It is interesting to note a well known fact in scalar-tensor theories – the scalarization increases the maximum mass and thus an EOS that in GR leads to neutron star masses lower than the two solar mass barrier, can reach above this threshold in the presence of nontrivial scalar field. What is different from all the other examples of scalarized neutron stars in standard (massless) scalar-tensor theories, though, is that for the TMST solutions the scalar charge is zero. Thus, they can not be constrained by the binary pulsar observations and allow for large deviations from GR.

For larger values of β (e.g. $\beta = -1$), the mass of the scalarized neutron stars increases monotonically as the central energy density increases till the maximum of mass is reached and after that the mass keeps on decreasing until the branch merges with the GR solutions. On the other hand, for lower values of β, after the first bifurcation point the mass of the scalarized neutron stars increases whereas $\tilde{\varepsilon}_c$ decreases. This happens until a minimum value of $\tilde{\varepsilon}_c$ is reached and after that the behavior of the branch is similar to the larger β case. This different behavior of the smaller β branch implies that at certain lower values of $\tilde{\varepsilon}_c$, there exist simultaneously three solutions – two scalarized ones and one solution with zero scalar field, which indicates non-uniqueness. This is a new results that has not been observed in standard scalar-tensor theories.

We should note that the particular choice of the coupling function only deforms the scalarized branch, while keeping the position of the bifurcation points unaltered [428]. That is why, even though we have presented here the $M(\tilde{\varepsilon}_c)$ dependence only for $A(\chi) = \exp(\beta \sin^2 \chi)$, the results are qualitatively the same for other couplings such as $A(\chi) = \exp(\beta\chi^2)$.

Below we will study the stability of the scalarized solutions with two independent approaches – by examining the linearized field equations and by considering the full system of nonlinear field equations in spherical symmetry. Even though the former approach should in principle constitute a subclass of the latter one, we have decided to apply both of them in order to have an independent verification of (in)stability especially taking into account the observed very interesting non-uniqueness of solutions.

7.4 Linear Scheme

7.4.1 Perturbation Equations

To derive the perturbation equations for the radial stability analysis, in the field equations we impose perturbations of the form

$$f(t, r) = f_0(r) + \delta f(t, r), \tag{7.14}$$

where f represents a perturbed variable which in our case is the metric functions, the Jordan frame pressure $\tilde{p}$ and energy density $\tilde{\varepsilon}$, and the scalar field χ. The static background functions are denoted by a subscript "0" in f_0 and the time dependent radial perturbations are represented by δf. As a matter of fact, the fluid perturbations can be expressed in terms of the Lagrangian displacement $\zeta = \zeta(t, r)$ as we will see below.

In a perturbed state, the star pulsates around the spherically symmetric equilibrium configuration, with the line element as

$$ds^2 = -e^{2\Phi_0+2\delta\Phi}dt^2 + e^{2\Lambda_0+2\delta\Lambda}dr^2 + r^2(d\theta^2 + \sin^2\theta d\varphi^2). \tag{7.15}$$

The equations governing the fluid perturbation ζ and the scalar field perturbation $\delta\chi$ are given as

$$\begin{aligned} 0 =&(\tilde{\varepsilon}_0 + \tilde{p}_0)e^{2\Lambda_0-2\Phi_0}\ddot{\zeta} + (\tilde{\varepsilon}_0 + \tilde{p}_0)\delta\Phi' + [\Phi_0' + \alpha(\chi_0)\chi_0'](\delta\tilde{\varepsilon} + \delta\tilde{p}) + \delta\tilde{p}' \\ &+ \alpha(\chi_0)(\tilde{\varepsilon}_0 + \tilde{p}_0)\delta\chi' + \tilde{\beta}(\chi_0)(\tilde{\varepsilon}_0 + \tilde{p}_0)\chi_0'\delta\chi, \end{aligned} \tag{7.16}$$

and

$$\begin{aligned} 0 =& - e^{-2\Phi_0}\ddot{\delta\chi} + e^{-2\Lambda_0}\delta\chi'' + e^{-2\Lambda_0}\left[\Phi_0' - \Lambda_0' + \frac{2}{r}\right]\delta\chi' + e^{-2\Lambda_0}\chi_0'[\delta\Phi' - \delta\Lambda'] \\ &+ \left[- \frac{2}{r^2}\left(\frac{d}{d\chi}H^2(\chi)\right)_{\chi_0} + \frac{2}{a^2}\partial_\chi V(\chi_0) - 8\pi G_*\frac{\alpha(\chi_0)}{a^2}A^4(\chi_0)(\tilde{\varepsilon}_0 - 3\tilde{p}_0)\right]\delta\Lambda \\ &- \left[\frac{1}{r^2}\left(\frac{d^2}{d\chi^2}H^2(\chi)\right)_{\chi_0} + \frac{1}{a^2}\partial_\chi^2 V(\chi_0) + 4\pi G_*\frac{\beta(\chi_0)}{a^2}A^4(\chi_0)(\tilde{\varepsilon}_0 - 3\tilde{p}_0)\right. \\ &\left. + 16\pi G_*\frac{\alpha^2(\chi_0)}{a^2}A^4(\chi_0)(\tilde{\varepsilon}_0 - 3\tilde{p}_0)\right]\delta\chi - 4\pi G_*\frac{\alpha(\chi_0)}{a^2}A^4(\chi_0)(\delta\tilde{\varepsilon} - 3\delta\tilde{p}), \end{aligned} \tag{7.17}$$

where dot and prime represent derivatives with respect to time and radial coordinates, respectively, and $\alpha(\chi) = \frac{d\ln A(\chi)}{d\chi}$ and $\tilde{\beta}(\chi) = \frac{d^2\ln A(\chi)}{d\chi^2}$. These equations represent a system of coupled, second order wave equations for the perturbations ζ and $\delta\chi$ and in the $H(\chi) = \sin(\chi)$ case they reduce to the ones in [427]. The perturbations of the metric functions, the energy density and the pressure in terms of ζ and $\delta\chi$ are as follows:

$$\delta\Lambda = a^2 r\chi_0'\delta\chi - 4\pi G_* A^4(\chi_0)(\tilde{\varepsilon}_0 + \tilde{p}_0)e^{2\Lambda_0}r\zeta, \tag{7.18}$$

$$\delta\tilde{\varepsilon} = -(\tilde{\varepsilon}_0 + \tilde{p}_0)\left[r^{-2}e^{-\Lambda_0}\left(e^{\Lambda_0}r^2\zeta\right)' + \delta\Lambda\right] - [\tilde{\varepsilon}_0' + 3\alpha(\chi_0)(\tilde{\varepsilon}_0 + \tilde{p}_0)\chi_0']\zeta - 3\alpha(\chi_0)(\tilde{\varepsilon}_0 + \tilde{p}_0)\delta\chi, \tag{7.19}$$

$$\delta\tilde{p} = \tilde{c}_s^2\delta\tilde{\varepsilon}, \tag{7.20}$$

and

$$\delta\Phi' = \frac{1}{r}\left[1 - 2a^2H(\chi)^2 + r^2\left(8\pi G_* A^4(\chi_0)\tilde{p}_0 - 2V(\chi_0)\right)\right]e^{2\Lambda_0}\delta\Lambda + 4\pi G_* e^{2\Lambda_0} r A^4(\chi_0)\delta\tilde{p} + re^{2\Lambda_0}\left[-\partial_\chi V(\chi_0) - 2\frac{a^2}{r^2}H(\chi)\frac{d}{d\chi}H + 16\pi G_*\alpha(\chi_0)A^4(\chi_0)\tilde{p}_0\right]\delta\chi + a^2 r\chi_0'\delta\chi', \tag{7.21}$$

where $\tilde{c}_s^2$ is the sound speed in the Jordan frame and is defined by $\tilde{c}_s^2 = \frac{d\tilde{p}_0}{d\tilde{\varepsilon}_0}$.

The boundary conditions at the center of the star are derived from the requirement for regularity of the perturbations and we have $\zeta(t, r = 0) = 0$ and $\delta\chi(t, r = 0) = 0$. Similar to pure GR case, the Lagrangian perturbation of the pressure $\Delta\tilde{p}$ has to vanish at the surface of the star. Only the perturbation of the scalar field $\delta\chi$ can propagate outside the star while ζ vanishes there. For large distances $\delta\chi$ has to satisfy the radiative (outgoing) asymptotic condition, expressed as

$$\partial_t(r\delta\chi) + \partial_r(r\delta\chi) = 0. \tag{7.22}$$

7.4.2 Results Linear Stability

To perform the stability analysis in the linear regime, we convert the linearized wave equations (7.16) and (7.17) into a form more suitable for numerical analysis by adapting a standard approach from pure GR [427, 437]. Namely, we introduce a new dimensionless function

$$Z(t, r) = (\tilde{\varepsilon}_0 + \tilde{p}_0)r\zeta e^{2\Lambda_0}. \tag{7.23}$$

Since this function is zero at the stellar surface where $\tilde{\varepsilon}_0$ and $\tilde{p}_0$ vanish, applying the boundary conditions is easier in terms of Z.

To evolve the perturbation equations (7.16) and (7.17) in time, we use the Leapfrog method. As initial data for $\delta\chi$ we use a Gaussian pulse which is located several neutron star radii away from the stellar surface, with zero initial velocity at $t = 0$. Z is set to be zero initially and is always zero outside the star by construction. It will remain zero until the $\delta\chi$ pulse reaches the star and will get excited only then through the coupling of the fluid and scalar field perturbations.

Using the method described above, we solved the system of equations for different forms of $H(\chi)$ and $A(\chi)$ for different values of β. We found that for all of the considered scalarized neutron star branches, the perturbation $\delta\chi$ decays in time for the scalarized models before the maximum of the mass, which implies the branch is stable up to this point [1]. Whereas, for neutron star models located after the maximum of the mass $\delta\chi$ grows exponentially which clearly indicates instability. For smaller values of β (for example the $\beta = -1.5$ branch in Fig. 7.1) an interesting observation has been made. In the region where two scalarized

[1] Let us point out that contrary to the GR case, the radial oscillations in TMST will have an amplitude decaying in time because the scalar field carries away energy to infinity.

solutions exist for the same central energy densities, it was found that both solutions are stable. This implies that at these central energy densities, three radially stable solutions exist simultaneously: one general relativistic and two scalarized solutions. In addition, in the part of the scalarized branch just after the bifurcation point, the mass increases with decreasing central energy density while the neutron stars is still stable.

Fig. 7.2 shows the waveforms of the central scalar perturbation $\delta\chi_c$ for three representative scalarized neutrons stars belonging to the $\beta = -1.5$ branch in Fig. 7.1. The *top* figure depicts $\delta\chi_c$ of a star from the initial part of the branch where the mass increases with decrease of the central energy density. The *middle* figure refers to a star from the part of the branch where the mass increases as central energy density increases, but having an energy density smaller than the solution with maximum mass. Finally, the *bottom* figure represents the perturbations of an unstable star with central energy density slightly higher than the maximum mass solution. As one can see, after a few milliseconds the perturbation function $\delta\chi$ shooting off exponentially. The time at which instability sets in reduces for stars with higher central energy density. Here we will not comment in detail on the frequencies of the radial oscillations since the focus of the Chapter is on the stability, but our analysis shows that, as expected, these frequencies decrease monotonically with the increase of the stellar mass and they cross zero exactly for the maximum mass models.

7.5 Nonlinear Scheme

Having done the linear analysis of the stability of scalarized models, we now turn to address the issue within fully non-linear framework. Among the advantages of the non-linear analysis is that one can access more information about how the instabilities grow and saturate. As a whole, the evolutionary equations in TMST (Sec. 7.5.1) resemble those in DEF theories with some additional terms owing to the non-trivial geometry of target spaces. It thus justifies the appliance of the numerical approach (reconstruction method and high-performance-shock-capture algorithm) that has been implemented in DEF theories in [434, 435] to TMST. We construct a grid adequate for our purpose in this work (Sec. 7.5.2) for solving the evolutionary equations. It has been checked, that the results summarized in Sec. 7.5.3 show only slight deviations by doubling the resolution.

7.5.1 Evolution Equations

The Euler equation,

$$\nabla_\mu \tilde{T}^{\mu\nu} = 0, \tag{7.24}$$

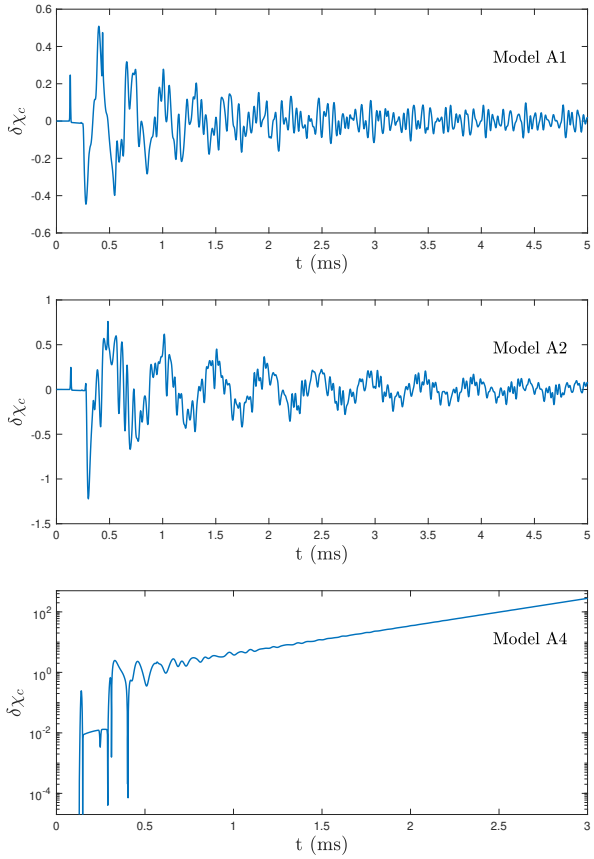

Figure 7.2: The evolution of the scalar field perturbations $\delta\chi_c$ extracted at a point located several neutron star radii away from the surface, with $A(\chi) = e^{\beta \sin^2 \chi}$, $H(\chi) = \sin\chi$, $a^2 = 0.1$ and $\beta = -1.5$. Three models are considered, including two stable (top and middle panel) and one unstable (bottom panel). These are models A1, A2 and A4 listed in Table 7.1 and discussed in detail in the next section.

can be presented as a first-order flux conservative system [438, 439],

$$\partial_t \mathbf{U} + \frac{1}{r^2}\partial_r \left[r^2 \frac{\alpha}{X} \mathbf{f}(\mathbf{U}) \right] = \mathbf{s}(\mathbf{U}), \tag{7.25}$$

constituting the *conserved* quantities $\boldsymbol{U} = \{D, \tau, S^{r)}\}$ and the corresponding fluxes $\mathbf{f(U)}$ and sources $\mathbf{s(U)}$. The Jacobian of this (differential equation) system, $\frac{\partial \mathbf{f(U)}}{\partial \mathbf{U}}$, offers information about the characteristic speeds of the *conserved* quantities. Defining the *conserved* quantities and the fluxes via

$$D = \frac{A^4 e^{\Lambda}}{\sqrt{1-v^2}}\tilde{\rho}, \qquad S^r = \frac{A^4 v}{1-v^2}(\tilde{\varepsilon} + \tilde{p}), \qquad \tau = \frac{A^4 \tilde{\varepsilon}}{(1-v^2)} - A^4 \tilde{p} - D, \tag{7.26a}$$

and

$$f_D = Dv, \qquad f_{S^r} = S^r v + A^4 \tilde{p}, \qquad f_\tau = S^r - Dv, \tag{7.27a}$$

we find the source terms

$$s_D = D e^{\Phi}(\psi + \eta v) A \frac{d \ln A}{d\chi}, \tag{7.28a}$$

$$s_{S^r} = (S^r v - \tau - D) e^{\Phi+\Lambda} \left(8\pi r A^4 \tilde{p} + \frac{m}{r^2} + e^{-\Lambda} A \frac{d \ln A}{d\chi} \eta - r V_{\rm eff} \right) + e^{\Phi+\Lambda} \frac{A^4 \tilde{p} m}{r^2} - 2 r e^{\Phi+\Lambda} S^r \eta \psi A^2 a^2$$
$$+ 2 e^{\Phi-\Lambda} \frac{A^4 \tilde{p}}{r} + 3 e^{\Phi} A^5 \tilde{p} \frac{d \ln A}{d\chi} \eta - e^{\Phi+\Lambda} A^4 \tilde{p} r V_{\rm eff} - \frac{r}{2} e^{\Phi+\Lambda} (\eta^2 + \psi^2) \left(\tau + A^4 \tilde{p} + D \right) (1+v^2) A^2 a^2, \tag{7.28b}$$

$$s_\tau = -\left(\tau + A^4 \tilde{p} + D \right) r e^{\Phi+\Lambda} \left((1+v^2)\eta\psi + v(\eta^2 + \psi^2) \right) A^2 a^2 - e^{\Phi} A \frac{d \ln A}{d\chi} \left[Dv\eta + \left(S^r v - \tau + 3 A^4 \tilde{p} \right) \psi \right]. \tag{7.28c}$$

In addition, it has been illustrated in [435] that the characteristic speeds, determined by $\mathbf{f(U)}$ and $\mathbf{U}$, for the conservative system in DEF theories are exactly the same as those in GR due to their independence on the coupling function A. In our formulation for TMST, we stick with the same definition of $\mathbf{f(U)}$ and $\mathbf{U}$ as [435], indicating that the characteristic properties for the system (7.25) are identical to GR.

Having assumed $\Theta = \theta$ and $\Phi = \phi$, the nonlinear evolution equation for the scalar fields reads

$$\Box \chi - \frac{2H}{r^2}\frac{\partial H}{\partial \chi} - \frac{1}{a^2}\frac{\partial V}{\partial \chi} = -\frac{4\pi}{a^2}\frac{\partial \ln A}{\partial \chi} T, \tag{7.29}$$

which can be reduced to two first order, decoupled equations having the form

$$\dot{\eta} = \frac{e^{-\Lambda}}{A}(Ae^{\Phi}\psi)' - re^{\Phi+\Lambda}\eta\left(a^2A^2\psi\eta - 4\pi s^r\right) - \psi\eta e^{\Phi}A\frac{d\ln A}{d\chi}, \tag{7.30a}$$

$$\begin{aligned}\dot{\psi} =& \frac{e^{-\Lambda}}{Ar^2}(Ae^{\Phi}r^2\eta)' - re^{\Phi+\Lambda}\psi\left(a^2A^2\psi\eta - 4\pi s^r\right) - \psi^2e^{\Phi}A\frac{d\ln A}{d\chi} \\ & - \frac{4\pi e^{\Phi}}{Aa^2}\frac{d\ln A}{d\chi}\left(\tau - s^rv + D - 3A^4\tilde{p}\right) - \frac{e^{\Phi}}{Ar^2a^2}\frac{d}{d\chi}\left(r^2V_{\rm eff}\right),\end{aligned} \tag{7.30b}$$

with $\psi = e^{-\Phi}\dot{\chi}$ and $\eta = e^{-\Lambda}\chi'$. The effective potential is defined as

$$V_{\rm eff} = V + \frac{a^2H^2(\chi)}{r^2}, \tag{7.31}$$

where the second term on the right hand side attributes to the geometry of the target space manifold. The Einstein equations reduce to two linearly independent equations,

$$\Phi' = e^{2\Lambda}\left[\frac{m}{r^2} + 4\pi r\left(s^rv + A^4\tilde{p}\right) + \frac{a^2r}{2}A^2(\psi^2+\eta^2) - rV_{\rm eff}\right], \tag{7.32a}$$

$$m' = 4\pi r^2(\tau + D) + \frac{a^2r^2}{2}A^2(\psi^2+\eta^2) + r^2V_{\rm eff}, \tag{7.32b}$$

relating the spatial derivative of the metric functions to the fluid quantities and the scalar field. We note that the theory will be reduced to DEF theory if $a = 1$ and the effective potential is replaced with the bare potential V.

7.5.2 Numerical setup

The code used in this work to solve the above system of nonlinear evolution equations is a modification of the `GR1D` code [434, 440] (for the DEF theory version of `GR1D`, readers can refer to, e.g., [90, 435, 441, 442]). In this spherical symmetric simulation, the computational domain ranges from the stellar center to $r = 10000$ km (~ 1000 times the radius of the star), securing that the radial boundary is sufficiently far away from the strong-field region where the spacetime is well approximated by Minkowski metirc. The grid used has uniform size of 30 m from center to $r = 40$ km and the grid size increases exponentially from $r = 40$ km toward the outer boundary in the rate that the number of grid points amounts to 10000. There are, therefore, ~ 330 grids point inside stars.

At the center and the outer boundary, the boundary conditions are applied to every metric functions and fluid variables. The radial velocity v is antisymmetric across the origin since the radial fluxes vanish there, while the remaining variables are symmetric. All variables are symmetric about the outer edge. In addition, we do not perturb artificially any quantities (Φ, Λ, χ, ...), but only the error due to numerical truncation serves as perturbation to the equilibrium.

Table 7.1: Properties of symbolic models with the target space geometry $H(\chi) = \sin\chi$ and the coupling function $A(\chi) = \exp(\beta \sin^2\chi/2)$. There are two classes of the chosen models, where models in the "A" class are solutions for $\beta = -1.5$ and models in the "B" class are solutions for $\beta = -1$. The second toward the final columns are, respectively, the central energy density, the radius, and the (baryon) mass of stars.

Model	$\tilde{\varepsilon}_c$ (g/cm^3)	Radius (km)	Mass ($M_\odot$)	Model	$\tilde{\varepsilon}_c$ (g/cm^3)	Radius (km)	Mass ($M_\odot$)
A1	5.6536×10^{14}	10.0876	1.0002	B1	1.5828×10^{15}	10.4074	1.3923
A2	5.6933×10^{14}	10.9379	1.6872	B2	2.7857×10^{15}	9.5503	1.6380
A3	1.5298×10^{15}	11.0621	2.0426	B3	2.8708×10^{15}	9.4966	1.6380
A4	1.6000×10^{15}	11.0094	2.2644	B4	3.6997×10^{15}	9.0108	1.6077
A5	2.5181×10^{15}	10.2366	2.2643				
A6	3.1163×10^{15}	9.7595	2.1507				

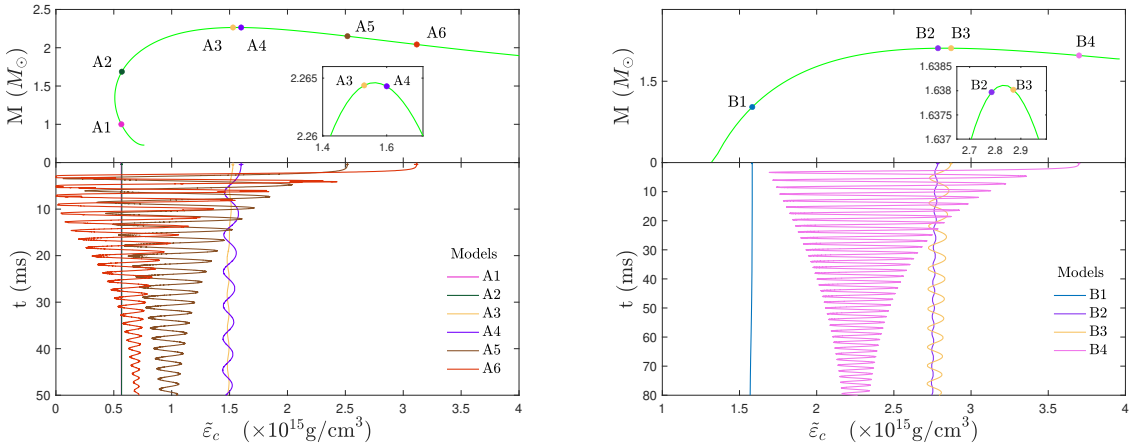

Figure 7.3: The non-GR part of the sequence of solutions with $H(\chi) = \sin\chi$ and $a^2 = 0.1$ for $\beta = -1.5$ (left panel) and $\beta = -1$ (right panel), along which the chosen models in Tab. 7.1 are marked by different colors. The magnified window in the left panel shows the A3 and A4 models, while the one in the right panel shows the B2 and B3 models. Each pair of these models have, respectively, slightly smaller and larger mass than the maximal mass in each case, where the instability kinks in. Evolutions of central energy density of the chosen models are presented at the bottom row of the two panels.

7.5.3 Results

We examine the stability of scalarized neutron stars along the sequences of equilibrium models depicted in Fig. 7.1. To balance the completeness of our results and the compactness of this Chapter, we choose without loss of generality some symbolic models with $H = \sin\chi$ to illustrate our results, whose properties are listed in Table. 7.1.

In the left panel of Fig. 7.3, we summarize the evolution of $\tilde{\varepsilon}_c$ of models A1-A6, where each history is arranged in the order of the initial values of $\tilde{\varepsilon}_c$. The models A1 and A2 oscillate about the equilibrium slightly, whereas the model A3 shifts a bit toward left and oscillates around a non-zero residual with respect to its initial value, which converges to zero as second order with increasing resolution. The results for A1-3 reflect that the segment, which is non-GR and yet reaches the maximal mass, is stable. The stability is lost when the maximal mass is reached; particularly, model A4 exhibits instability and deforms into a stable model.

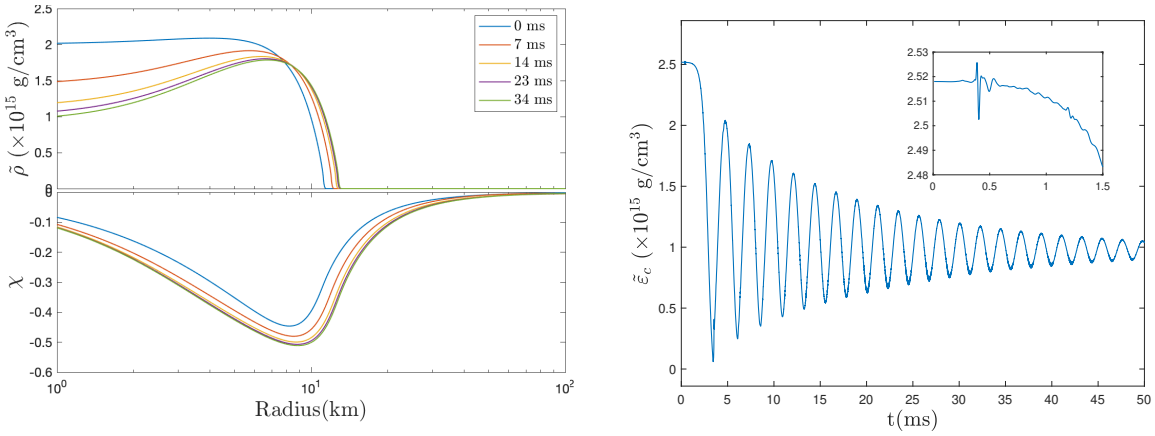

Figure 7.4: *left*: Distributions of the baryon mass density $\tilde{\rho}$ and the scalar field χ at several moments, whereby one can see that the material part of star settles to the final state at ~ 34 ms, while χ has already reached to the final profile at ~ 23 ms. *right*: For model A5 the central energy density $\tilde{\varepsilon}_c$ is plotted as a function of time. In the magnified window, the onset of instability is shown. Model A5 has been considered for both panels.

The point representing A4 on upper row of the left panel in Fig. 7.3 drifts toward left then oscillates around another point on the curve with the same baryon mass, as expected. The unstable models A5 and A6 also show the deformation into a stable model with same baryon mass.

In particular, the translation of model A5 from the initial unstable star to the stable one is shown by the evolution of the radial profiles of the baryon density $\tilde{\rho}$ and the scalar field χ (top panel of Fig. 7.4). One can observe that the material part of the star settles to the final state at ~ 34 ms, while χ has already reached to the final profile at ~ 23 ms. The development of the instability is depicted by the evolution of $\tilde{\varepsilon}_c$ and the central value of scalar field χ_c (bottom panel of Fig. 7.4), where the magnified windows show the onset of the instability and the following saturation is apparent in the main figure. On the other hand, the evolution of models B1-B4 are given in the right panel of Fig. 7.3, which confirms as well that the non-GR segment left to the maximal mass, is stable and the segment right to the maximal mass is unstable. We note that in general an unstable neutron star could migrate to a stable star with same baryon mass but less compact, or collapse to a black hole, i.e. there should be a third channel that an unstable star collapses into a BH. However, our tests show that this channel probably requires additional perturbation.

Since the solutions to $H(\chi) = \sin\chi, \chi$, and $\sinh\chi$ differ only quantitatively while remaining qualitatively the same, it is expected that the stability properties for each branches do not change among these three choices of $H(\chi)$. In practice, we confirm this hypothesis by analyzing the stability of some representative models of each branches, and conclude the same – a model lighter than the maximal mass is stable, otherwise is unstable.

Having evolved and checked stability for a large number of models, we find that each

sequence contains exactly one stable segment and one unstable, converging towards the maximum mass models. The non-GR parts of the stable segments for $\beta = -1.5$ can be further divided into two classes: one before the central energy density reaches the minimal value, and one after. It is of particular interest that the scalarized models belonging to the part of the branch before the minimal $\tilde{\varepsilon}_c$ are stable even though they have larger masses for smaller $\tilde{\varepsilon}_c$. It indicates roughly that these models are "glued together" more by the non-trivial scalar field rather than by the self-gravitating fluid. In some sense, this is also the reason why the maximal mass of the solutions in TSMT (also in DEF theories) is larger than the predicted one by GR.

7.6 Conclusions

In the present Chapter we have investigated the (in)stability of scalarized neutron stars in tensor-multi-scalar theories. These models posses two very intriguing properties. First, their scalar charge is vanishing leading to zero scalar dipole radiation. Therefore, no constraints can be imposed by the binary pulsar observations, contrary to the DEF model in standard scalar tensor theories. Second, there exists a region of non-uniqueness of the scalarized solutions themselves, i.e. for a certain range of central energy densities two scalarized solutions can co-exist with the GR (zero scalar field) one. Clearly, this interesting structure calls for an investigation of the stability. We used two approaches in order to be able to confirm independently the results – solving the linearized perturbation equation and addressing the full nonlinear evolution in spherical symmetry. The equations governing the evolution of the scalar field and the metric were derived independently in the considered class of tensor-multi-scalar theories and they were solved numerically.

The linear stability analysis showed, that for all combinations of parameters we have studied, the critical point for stability occurs at the maximum of the mass. Thus the scalarized branches before this point are stable, independent on whether they posses a region of non-uniqueness in terms of the central energy density or not. This is a very interesting conclusion leading to the fact that there is a part of the branch where the total mass of the neutron stars increases with the decrease of the central energy density that is in sharp difference with GR and even with most of the known alternative theories of gravity. As expected, the GR solutions with trivial scalar field loose stability at the point of the first bifurcation. Their stability is restored once the scalarized branch merges again with the GR one (only in case the second bifurcation point is before the maximum mass of the GR sequence of course).

In the fully non-linear investigation, we again identified the parts on the sequence of scalarized models that are unstable and the results agree perfectly with the ones from the linear perturbation analysis. A particular merit of the non-linear treatment is that apart from demonstrating the development of the instability we can follow the evolution towards a final

stable state. The transition from an unstable model to a stable one with the same baryon mass is numerically revealed in our simulations. However, the dynamics (damping timescale of instabilities, the emission via the scalar channel during the drift from an unstable model to a stable one, etc.) behind the phenomenon is not addressed in the present work. The knowledge of the detailed dynamics is crucial in connecting the instabilities of the objects discussed here to observations, thus research towards this direction will be helpful providing possible constraints on TMST.

Chapter 8

Gravitational waves from accretion-induced descalarization in massive scalar-tensor theory

Contents

Breakdown of Contributions

I contribute to producing all the plots, and carrying out the numerical simulations with a code modified by me to adopt realistic equation of state from the previous code of P. C. K. Cheong which is based on GR1D but tailored into scalar-tensor theory. The fitting results are obtained by me, and the manuscript is jointly completed by me (discussion of the results and the observation perspectives), Arthur G. Suvorov (motivation and the observation perspectives), and D. D. Doneva (connection to the material phase transition). S. S. Yazadjiev helps check all the formulae, and provides useful comments on the manuscript.

Overview

Many classes of extended scalar-tensor theories predict that dynamical instabilities can take place at high energies, leading to the formation of scalarized neutron stars. Depending on the theory parameters, stars in a scalarized state can form a solution-space branch that shares a lot of similarities with the so-called mass twins in general relativity appearing for equations of state containing first-order phase transitions. Members of this scalarized branch have a lower maximum mass and central energy density compared to Einstein ones. In such cases, a scalarized star could potentially over-accrete beyond the critical mass limit, thus triggering a gravitational phase transition where the star sheds its scalar hair and migrates over to its non-scalarized counterpart. Such an event resembles, though is distinct from, a nuclear or thermodynamic phase transition. We dynamically track a gravitational transition by first constructing hydrostatic, scalarized equilibria for realistic equations of state, and then allowing additional material to fall onto the stellar surface. The resulting bursts of monopolar radiation are dispersively-stretched to form a quasi-continuous signal that persists for decades, carrying strains of order $\gtrsim 10^{-22}(\mathrm{kpc}/L)^{3/2}$ $\mathrm{Hz}^{-1/2}$ at frequencies of $\lesssim 300$ Hz, detectable with the existing interferometer network out to distances of $L \lesssim 10$ kpc, and out to a few hundred kpc with the inclusion of the Einstein Telescope. Electromagnetic signatures of such events, involving gamma-ray and neutrino bursts, are also considered.

8.1 Introduction

General relativity (GR) has historically provided an excellent description for both local (e.g., solar system) and global (e.g., cosmology) gravitational phenomena. It is well known however that the theory cannot by itself be fully complete, and the non-renormalizability of the action implies that additional ingredients, possibly in the form of non-minimally coupled fields [443, 444], should activate at extreme scales. Nevertheless, any theoretical extension must be virtually invisible at low energies, and also somehow suppressed in certain strong-field environments. For example, binary pulsar experiments restrict the possibility for significant sub-quadrupolar radiation over super-Compton length scales [414, 415, 445–447], and gravitational-wave (GW) experiments suggest that (at least some) black holes should be approximately, if not exactly, Kerr [448]. An observationally-viable class of extensions that can survive these issues is massive scalar-tensor theory (STT): the mass of the scalar field suppresses the scalar dipole radiation [417,418], and the classical no-hair theorems tend to be respected [449], implying that astrophysically stable black holes would be indistinguishable from their GR counterparts.

Material degrees of freedom in these theories however allow for the possibility of *scalarized* stars [89]. This phenomenon can be generally thought of as a consequence of the effective curvature-coupled mass term, which appears in the relevant Klein-Gordon equation, changing

sign once some critical threshold is breached, thereby inducing a tachyonic instability (though see also Ref. [450]). Thus for neutron stars a critical compactness exists at which a branch of strongly scalarized solutions emerges. In some cases, the heaviest scalarized neutron star has lower baryon mass and lower central energy density compared to the maximum mass (stable) non-scalarized neutron star [451] and there is a gap between the two branches where no stable neutron star solutions exist. This picture resembles very closely the so-called mass twins in pure GR that are manifestations of the presence of first order phase transition in the equation of state [452–455] This implies that if a near-critical scalarized star were to acquire additional mass through accretion, the system may promptly discharge its scalar hair. Importantly, the neutron star needs not to collapse to a black hole in this scenario, as considered in, e.g., [456–459], but rather may undergo a *gravitational* phase transition, distinct from a *material* (e.g., hadron-quark) phase transition [460], and migrate to the GR branch pertaining to the same equation of state (EOS). This novel scenario is considered in this Chapter. We begin by constructing hydrostatic equilibria in a massive STT, and then allow additional material to fall onto the stellar surface until the point of descalarization, so as to dynamically track the migration process.

A migration to a new branch is likely to carry a variety of observational signatures. As a scalar shedding necessarily compactifies the star over a short, dynamical timescale ($\gtrsim$ ms), abrupt changes in the electromagnetic output of the source, most notably those associated with gamma-ray burst (GRB) afterglows and neutrino bursts [461–463], would point towards such a transition. These signatures could, however, be imitated by a nuclear phase transition [464–469], thus highlighting the well-known degeneracy between effects coming from a modification of gravity and the uncertainties in the nuclear EOS (e.g., Sec. 4 of [96]). One key difference is that a gravitational transition will unleash a burst of scalar radiation which, for a massive theory, will be dispersively stretched into a quasi-continuous signal, as higher frequency components are first to arrive at the detector(s) [458]. GW afterglows lasting up to a ∼kyr may therefore be expected following a gravitational phase transition. We quantify the distances, as a function of the theory's coupling parameters, out to which such events may be observable with existing and upcoming GW interferometers.

8.2 Formalism and equations of motion

The action of a STT of whichever flavor [e.g., Brans-Dicke, Bergmann-Wagoner, and even $f(R)$ theories] can be transformed into the Einstein frame (cf. the action (7.1) for the TMST)

$$S = \int \frac{\sqrt{-g}}{16\pi} d^4x \left(R - 2\partial_\mu\varphi\partial^\mu\varphi - 4V\right) + S_M[\Psi, A^2 g_{\mu\nu}], \tag{8.1}$$

for matter portion S_M, metric tensor g, scalar field φ, Ricci scalar R and scalar field potential for which we take the following form[1]

$$V(\varphi) = \frac{1}{2} m_\varphi^2 \varphi^2. \tag{8.2}$$

The saddle point of V poses the boundary condition $\varphi_0 := \varphi(r \to \infty) = 0$ for φ. The transition to the physical Jordan frame metric $\tilde{g}_{\mu\nu}$ is done via a Weyl scaling (7.2), where we choose the conformal factor

$$A(\varphi) = \exp(\alpha_0 \varphi + \beta_0 \varphi^2/2). \tag{8.3}$$

We adopt the spherically-symmetric Jordan frame metric ansatz:

$$\tilde{g}_{\mu\nu} = \mathrm{diag}[-\alpha^2, X^2, A(\varphi)^2 r^2, A(\varphi)^2 r^2 \sin^2\theta], \tag{8.4}$$

for which the metric functions in the Einstein frame, i.e., Φand Λ [Eq. (7.5)], can be expressed as $e^\Gamma = A^{-1}\alpha$ and $e^\Lambda = A^{-1}X$, respectively. The time-independent field equations of the above metric can be obtained from Eq. (7.32) by setting $a = 1$ and replacing $V_{\rm eff}$ [Eq. (7.31)] with V, notably (see also Eqs. (2.21) and (2.23) in [435] together with Eq. (6) in [90])

$$m' = 4\pi r^2 A(\varphi)^4 \left(\frac{\rho h}{1-v^2} - P\right) + r^2 \left[\frac{A(\varphi)^2}{2}(\psi^2 + \eta^2) + V\right], \tag{8.5a}$$

and

$$\Phi' = X^2 \left[\left(\frac{m}{r^2} - rV\right) A(\varphi)^{-2} + 4\pi r^2 A(\varphi)^2 \left(\frac{\rho h v^2}{1-v^2} + P\right) + \frac{r}{2}(\psi^2 + \eta^2)\right], \tag{8.5b}$$

where we recall that the local mass $m(r)$ relates to the lapse function via Eq. (7.6), and the gravitational mass of the star is defined as the the value of $m(r)$ at infinity. In addition, we have, in a dynamical process, the following time-depend equation

$$\dot{m} = r^2 \frac{\alpha}{X} \left[A(\varphi)^2 \psi\eta - 4\pi A(\varphi)^4 \left(\frac{\rho h v}{1-v^2}\right)\right]. \tag{8.5c}$$

For cold EOS, ϵ and P are functions of ρ, i.e., barotropic. In contrast to Chap. 7, we adopt in this Chapter the APR4 EOS approximated by piecewise polytropic EOS ([69]; see below).

In addition, the equation for φ for the considered coupling function reads [cf. Eq. (7.29)]

$$\Box\varphi = -4\pi \frac{d\ln A}{d\varphi} T + \frac{dV}{d\varphi} = -4\pi(\alpha_0 + \beta_0\varphi)T + m_\varphi^2 \varphi := m_{\rm eff}^2 \varphi, \tag{8.6}$$

which can be rephrased as a set of first-order hyperbolic differential equations in a conservative-

[1] The massless theory is also investigated in Appendix C, where the totally distinct picture appears, and the accretion-induced descalarization will instead launch a burst-like GW.

flux form for the variables $\{\varphi, \eta, \psi\}$ [cf. Eq. (7.30)]. On the other hand, the hydrodynamic equations,

$$0 = \nabla_\mu T^{\mu\nu} - \frac{d\ln A}{d\varphi} T \nabla^\nu \varphi, \tag{8.7}$$

can also be written as a system of hyperbolic conservation laws (Sec. 7.5.1; refer also to Eqs. (21)-(29) in [458]). From the field equations we can derive the energy E_φ and luminosity $\mathcal{L}_\varphi$ of the scalar field as

$$E_\varphi = \int \frac{r^2 A(\varphi)^2}{2}(\psi^2 + \eta^2) + V dr, \qquad \mathcal{L}_\varphi = r^2 X \alpha \psi \eta, \tag{8.8}$$

which defines the corresponding energy leakage as

$$E_{\rm GW}^{\rm (scalar)} = \int \mathcal{L}_\varphi dt. \tag{8.9}$$

We note that no conservation law applies to the quantity $E_\varphi - E_{\rm GW}^{\rm (scalar)}$, since the scalar field couples to the material energy. Instead, the conserved energy is $M - E_{\rm GW}^{\rm (scalar)}$ for the (gravitational) mass M of the star; this conservation law is satisfied in our code within an error of $\lesssim 10^{-6} M_\odot$.

8.2.1 Scalar-induced Gravitational Waves

Two additional GW modes are raised by φ, viz. the breathing ('B') and longitude ('ℓ') modes, which carry the same response functions up to a sign flip (see Eq. (134) of [470]). The strain of the latter mode is reduced by a factor of $(\lambda_\varphi f)^{-2}$ relative to the former, which reads $h_\varphi = 2\alpha_0 \varphi$. The strain felt by a LIGO-VIRGO-like array (two orthogonal antennas) is thus

$$h(L,t) = \frac{h_\varphi}{2}(L,t)\left\{1 - [\lambda_\varphi f(L,t)]^{-2}\right\}, \tag{8.10}$$

when the source orients optimally, where

$$\lambda_\varphi = 2\pi\hbar/m_\varphi \tag{8.11}$$

is the Compton length-scale for the massive scalar field, t is the retarded time post-emission, and $f(L,t)$ is the characteristic frequency of the signal. Low frequency modes are screened at $r > \lambda_\varphi$, while the near-zone ($r \ll \lambda_\varphi$) dynamics of φ are to a large measure unaffected by the dispersion and reduce to the results of the massless case. On the other hand, high frequency components propagate at subluminal velocities. As a result, the dispersively-stretched waveform becomes quasi-monochromatic over a L- and m_φ-dependent timescale [90, 458]. In contrast to the burst-like data stream, the full spectrum of the power-spectral density

(PSD) $2\sqrt{f}|\tilde{h}(f)|$ will not reach the observatory simultaneously, but will arrive sequentially; therefore, there is an implicit time-dependence, encoded in the characteristic frequency, for the witness. The quasi-monochromatic feature implies that a phase-coherent search can be implemented, to which the signal-to-noise ratio (SNR), $4\int df\left[|\tilde{h}(f)|^2/S_n(f)\right]$, can be obtained by integrating over a narrow frequency interval around $f(t)$. In the limit $Tf \gg 1$, i.e., when many cycles are observed, Parseval's theorem states that the frequency-domain integral equates to the time-domain integral for the strain over the observation timescale, thus the SNR depends on the observation duration T (e.g., [247]) as well as the retarded time that is relevant to the characteristic frequency $f(t)$ of the signal. Specifically, [458] shows that the SNR can be obtained by dividing the *effective* PSD resulting from the aforementioned time-domain integration,

$$\sqrt{S_f} = \frac{\sqrt{T}\alpha_0 A(L,t)}{2}\{1-[\lambda_\varphi f(L,t)]^{-2}\}, \tag{8.12}$$

by the noise spectral curve $\sqrt{S_n(f)}$, where we assume an optimally-oriented detector. Here the amplitude is

$$A(L,t) \simeq 2\mathcal{A}(f)L^{-3/2}\lambda_\varphi\left[f^2-(\lambda_\varphi)^{-2}\right]^{3/4}, \tag{8.13}$$

with $\mathcal{A}(f)$ the Fourier component of the scalar-GW extracted at some distance $\lambda_\varphi < r \ll L$ so that it contains the content of the wave that will later propagate to a detector at L (cf. Eq. (57) in [458], while noting that our definition for A differs from theirs by a factor of L^{-1}).

8.3 Scalarized neutron stars

In the present Chapter, we adopt the APR4 EOS, and more precisely its piecewise polytropic approximation [69], which withstands constraints coming from GW 170817 [22], and supports masses which accommodate the heaviest neutron star observed to-date, viz. PSR J0740+6620 ($M = 2.14^{+0.10}_{-0.09}M_\odot$) [109]. In the considered STT and for large enough stellar compactness, the neutron star scalarizes, meaning it develops a strong, localized scalar field. This is demonstrated in Fig. 8.1 where we plot stellar equilibria for $\alpha_0 = 10^{-2}$, $\beta_0 = -5$, and $m_\varphi = 10^{-14}$ eV (yellow and red curves; see below) as well the GR branch ($\alpha = 0$) for comparison. This value of m_φ mitigates the tension with binary-pulsar constraints since radiation is suppressed over super-Compton length-scales $r \gg \lambda_\varphi$ [417,418,445]. The parameters are chosen such that a picture close to the so-called mass twins in pure GR [452–455], connected to first order phase transitions in the high density matter equation of state, is observed. Thus, a phase transition (descalarization) starting from the yellow to the red branch can be realized.

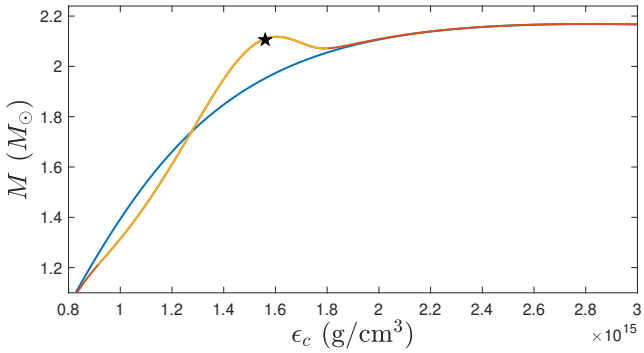

Figure 8.1: Hydrostatic equilibria for $\alpha_0 = 10^{-2}$, $\beta_0 = -5$ and $m_\varphi = 10^{-14}$ eV, for the APR4 EOS. The scalarized branch is divided in two parts, with the yellow one being strongly-scalarized and the red one possessing a very weak scalar field, which virtually coincides with the GR case ($\alpha = 0$; blue curve). The maximum mass of the blue and red sequences is $2.168M_\odot$, while the strongly-scalarized configuration (yellow line) can only support masses up to $2.118M_\odot$. The black star represents the initial state for the simulations.

This is possible due to the fact that the maximal mass for the scalarized branch ($2.118M_\odot$) is less than that for the GR branch ($2.168M_\odot$). We should note that strictly speaking, in the STT we consider, the red branch will always have some small nonzero value of the scalar field due to the nonzero α, i.e., it will be very weakly scalarized. A phase transition from the yellow to the red branch will shed off most of scalar energy but a tiny residual scalar field will always be left. For practical purposes, however, the blue (GR) and the red branch are virtually indistinguishable at high densities and thus with a slight abuse of language, we call the red branch of neutron star solutions *descalarized* ones.

8.4 Accretion dynamics

A neutron star that over-accretes beyond the peak of the scalarized curve displayed in Fig. 8.1 will undergo a phase transition to the GR branch. This scenario may occur either for a newborn star after a merger or collapse through fallback accretion, or a mature star in a binary undergoing Roche-lobe overflow. In the former case, debris disks containing $\lesssim 0.2M_\odot$ worth of material [462], though potentially much more in a core-collapse [471], will form around the birth site. A sizeable fraction of it may eventually fall back onto the stellar surface [472]. Accreted masses may total $\lesssim 0.8M_\odot$ in some X-ray binaries [473], though such amounts can accumulate only over long (potentially $\sim$ Gyr) timescales. The details of the accretion process itself are complicated however, since the neutron star may be spinning rapidly enough that material is repelled by a centrifugal barrier ('propeller' effect [471]), pressure gradients from nucleosynthetic heating can accelerate ejecta before it has a chance to return [474], and material will not fall isotropically onto the surface but rather may be guided onto the magnetic poles by the Lorentz force [475].

Here, however, our main goal is not to simulate a realistic accretion process in a STT, but

rather to illustrate qualitatively how the dynamical acquisition of additional mass can trigger a descalarization. To this end, accretion is artificially simulated by considering two sorts of mass excess in order to verify that our results are not overly sensitive to the particulars of the chosen accretion profile, which we call

- *Type I* — Superposing a Gaussian bulk centred at $0.9R_\star$, for stellar radius $R_\star$, with a width ("standard deviation") of 1 km, every 4 ms. The process is then halted when a total (baryon) mass of $0.015M_\odot$ has been added (after 16.01 ms). The average accretion rate is $\dot{M}_a \simeq 0.94 M_\odot \mathrm{s}^{-1}$.
- *Type II* — Superposing a Gaussian bulk out of but close to the surface of the neutron star every 4 ms, which is centred at $1.2R_\star$ with standard deviation width of 1 km, and terminates when a total (baryon) mass of $0.014M_\odot$ has been added (after 16.1 ms). We find again $\dot{M}_a \simeq 0.87 M_\odot \mathrm{s}^{-1}$.

The average accretion rates of both types are marginally slower than the numerical result of $\lesssim 1 M_\odot \mathrm{s}^{-1}$ over the first few ms of merger simulations (cf. Fig. 7 of [177]). The (post-)descalarization dynamics described here remains the same if the bulk is accreted with longer waiting time; in particular, we see just negligible changes in the emitted energy, the duration of scalar-peeling process, and the scalar GW waveform for the double interval, viz. 8 ms, between consecutive bulks. Nevertheless, we stress that neither profile is representative of a realistic astrophysical process, though they allow us to capture the salient features of a gravitational phase transition.

8.5 Results

The left-hand plot in Fig. 8.2 shows the evolutionary track of a particular scalarized model, initially with gravitational mass of $\sim 2.106 M_\odot$. The strongly scalarized star undergoes a phase transition after the accretion completes, and heads to the non-scalarized branch. The descalarization lasts ~ 4.4 ms. We have numerically verified that the final state indeed coincides with the descalarized, equilibrium one within an error of less than 2% that decreases monotonically with increasing simulation resolution. The onset and offset of the phase transition to the scalar-free state are chosen as the moments when the last bulk has been accreted and the final state is formed, respectively. After the descalarization, the model oscillates about a certain, stable state as shown in the inset in the bottom-left panel.

The left panel of Fig. 8.2 shows the scalar energy (top row), the flux of the scalar radiation at some radii (middle row), and the associated energy loss (bottom row) as functions of retarded time. The scalar energy (8.8) drops very close to zero after descalarization (top panel). The near zone ($r \ll \lambda_\varphi$) extraction of the luminosity at a point where its value has already saturated suggests an energy loss (blue curve in the bottom panel) $\gtrsim 40$ times less

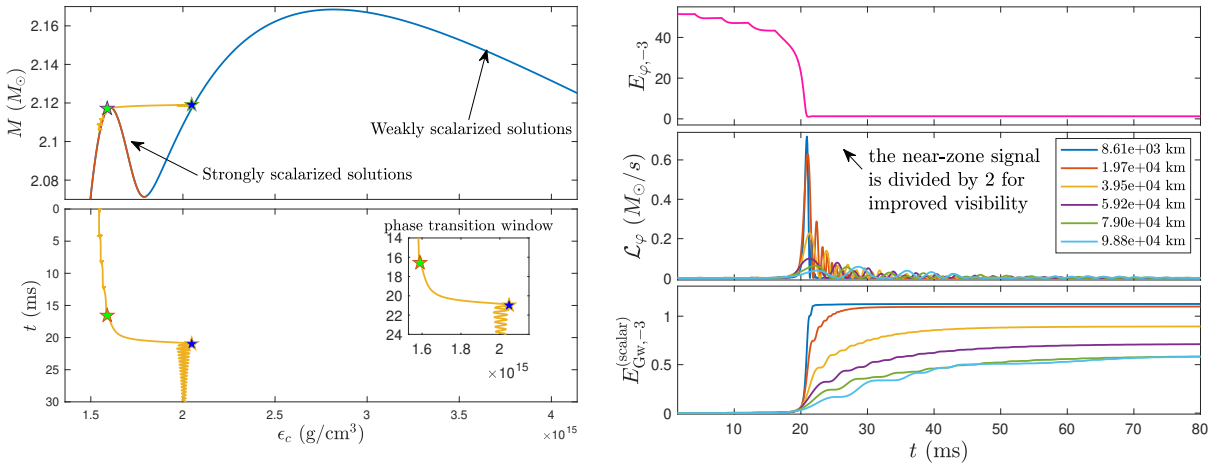

Figure 8.2: *Left*: Evolutionary track of a near-critical scalarized star under accretion: gravitational mass M as a function of central energy density ϵ_c (top panel), and the temporal dependence of the central energy density (bottom panel). The green and blue stars mark the onset and the termination of descalarization, respectively. *Right*: Evolution of scalar energy: scalar energy integrated from the centre to the outer boundary of the grid $r_{\mathrm{out}}/c = 3$ s (top panel), scalar luminosity extracted at some different distances (middle panel) [Eq. (8.8)], and energy emitted via scalar sector associated with the luminosity coded with same colour [Eq. (8.9)] (bottom panel), all as functions of retarded time. Here $E_{\varphi,-3}$ and $E^{(\mathrm{scalar})}_{\varphi,-3}$ are given in units of $10^{-3}M_\odot$.

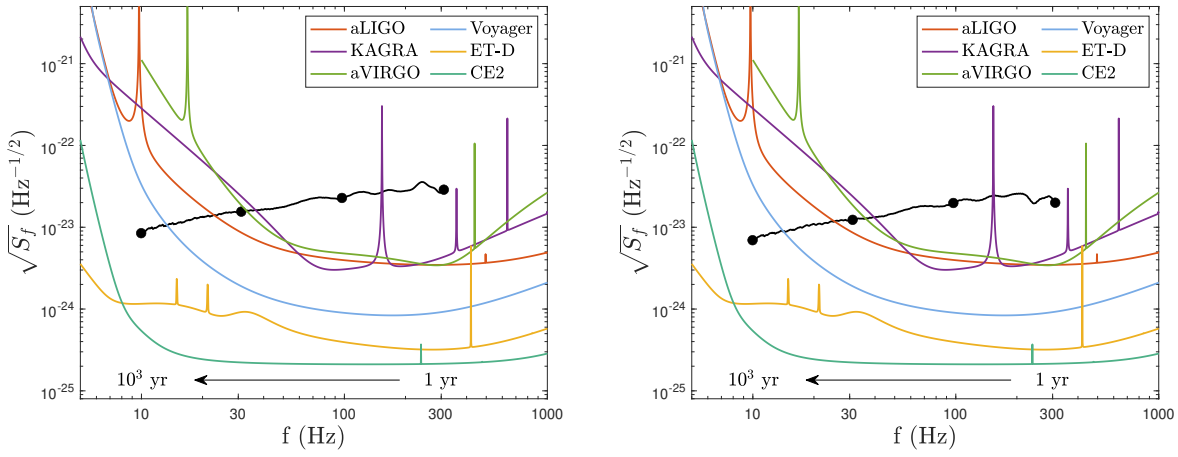

Figure 8.3: Square root of the PSD $\sqrt{S_f}$ at $L = 10$ kpc of the strain of the scalar-induced GW mode [Eq. (8.10)] for the Type-I (left) and Type-II accretion as functions of retarded time from 1 to 10^3 years (black curve; the k-th dot from the right along the curve represents $10^{(k-1)}$ years of retarded time). Overlapped are the sensitivity curves of current and considered GW interferometers.

than the decrease of E_φ, indicating that most of the scalar energy transforms into gravitational binding energy since the stellar radius shrinks from 11.56 km to 10.36 km between the initial and the final states, while the (gravitational) mass increases by $\approx 0.013 M_\odot$. After the emission propagates to those distances comparable to λ_φ, the dispersion suppresses the low frequency component and leads to a stretching on the waveform. In the bottom panel, we see that the energy leakage to infinity in the scalar sector is $\sim 6 \times 10^{-4} M_\odot$ (green and light blue curves), which is less than the energy carried by the scalar radiation in the near zone (blue curve) by a factor of ~ 2 due to the dispersion.

Assuming an observation duration of $T \sim 2$ months for the GW, over which the signal is slowly evolving for $m_\varphi = 10^{-14}$ eV [458], we present the numerical result of the signal amplitude (8.12) for scalar GW with the retarded time spanning from 1 to 10^3 years in the left panel of Fig. 8.3. The k-th notch, starting from the right, plotted over the signal (black) curve stands for $t = 10^{(k-1)}$ years. Together with the results for models with smaller α, though not shown here, we find a fitting to the *effective* PSD, in units of $\mathrm{Hz}^{-1/2}$, as

$$\frac{\sqrt{S_f}}{10^{-23}} \approx 3 \left(\frac{\alpha_0}{10^{-2}}\right) \left(\frac{T}{5 \times 10^6 \text{ s}}\right)^{\frac{1}{2}} \left(\frac{10\text{kpc}}{L}\right)^{\frac{3}{2}} \left(\frac{f}{300\text{Hz}}\right)^{0.34}, \tag{8.14}$$

with the frequency of the signal approximated as (cf. Eq. (53) in [458])

$$f(L,t) \approx 2.42 \frac{t+L}{\sqrt{t(t+2L)}} \text{ Hz}. \tag{8.15}$$

We note that larger T may be used for greater retarded times since the timescale for the frequency evolution, $f/\dot{f}$, scales as t, thus opening the possibility for much larger *effective* PSD. In particular, since the signal (8.14) is quasi-continuous, an extended narrow-band search could be carried out if one knew when the system descalarized, as the dispersion relation directly equates the relative delay with a frequency. Furthermore, multiple sensors can act to 'fuse' data together in a way that improves the overall signal-to-noise ratio beyond that inferred from equation (8.14) (see Sec. IV. E. of [476] for a detailed comparison of achievable sensitivities with different networks). It is natural also to ask whether the change of some theory parameters, namely α_0 and m_φ, will influence significantly our results. The equilibrium with a fixed mass would not change much for sufficiently small α_0 (cf. Fig. 2 of [419]) and m_φ (cf. Fig. 1 of [417]); therefore, the scalar-shedding processes for a range of α_0 and m_φ would be different but similar to each other. Of course, what scales with α_0 is the effective (PSD) of the resulting scalar radiation.

On the other hand, in Fig. 8.4, we plot the evolution track of the star undergoing Type-II accretion (left panel), and the scalar emission during the descalarization (right panel), while the GW strain caused by the emanating scalar field is presented in the right panel of Fig. 8.3. We see that the process is both qualitatively and quantitatively similar to that of the Type-I

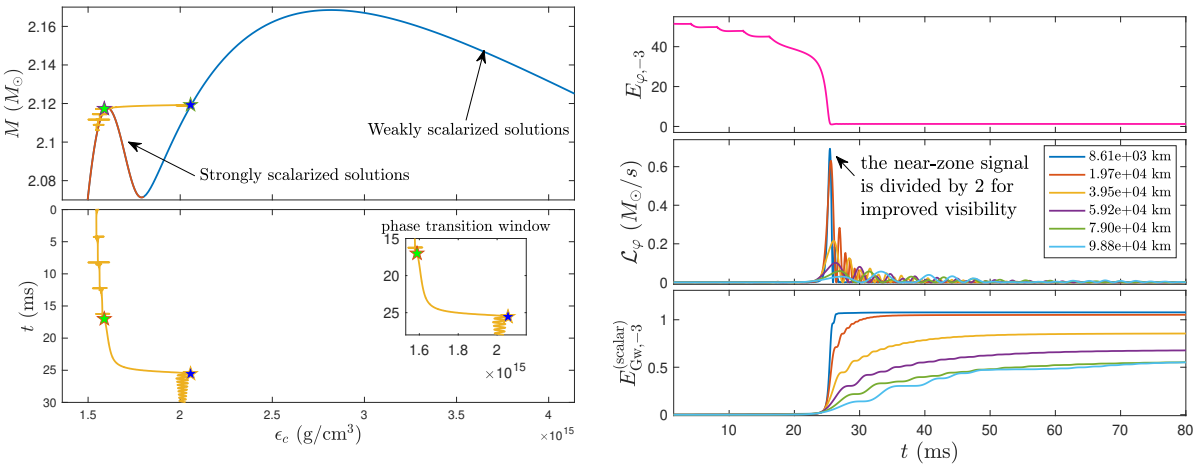

Figure 8.4: Same as Fig. 8.2 but for Type-II accretion (see main text for the definition).

accretion while with the descalarization lasting ~ 8.54 ms, indicating that for the two distinct types of accretion we get practically the same results thus strengthening the confidence that the process is more or less independent of the initial setup.

8.6 Connection to matter phase transitions

The phase transitions from scalarized to non-scalarized states considered here bear striking similarities to the material phase transitions from confined hadronic to deconfined quark matter. In both cases, there can be stars of equal mass but different radii, that are separated by a range of central energy densities where the stable solution space is empty (i.e., twin stars [452–455]). The astrophysical implications of matter phase transitions, and especially the GW signatures, have attracted considerable attention recently (see, e.g., [464–469]). In each case there will be a descalarization analogue, with the main difference being an additional channel for energy loss – the scalar radiation. Thus the degeneracy between effects coming from a modification of gravity and from EOS uncertainty goes far beyond the standard paradigm, demonstrating once again the importance of searching for strategies to break this degeneracy.

Although we concentrate on accretion in this Chapter, some interesting examples of such analogues can be found also in cases without accretion. For a hot, newborn neutron star with an EOS that permits negatively charged, non-leptonic particles (e.g., hyperons or quarks), the hydrostatic support available to the star will reduce when neutrinos diffuse out of the core as the system cools [477]. This can lead to a delayed phase transition with a number of interesting observational signatures [466]. Naturally, a descalarization analogue of this delayed transition will exist: depending on the chemical composition and theory parameters, the scalarized star may migrate to a non- or weakly-scalarized branch when the temperature

drops below a critical threshold (cf. superfluid phase transitions also [478]). A similar picture exists for the case of differential rotation, which is likely to be damped out (or at least reduced to a Ferraro profile) in a few tens of ms post-formation due to the magnetically-driven, turbulent viscosity [176]. Studying these processes in detail lies beyond the scope of the present paper since it requires a nonlinear evolution of a hot and differentially-rotating, scalarized neutron star. It is clear, though, that complementing the scalar-flavour phase transition to the studies of neutron star mergers in STT will offer rich phenomenology as concerns the evolutionary track of neutron stars (see also below). This will be on one hand due to the additional channel of energy loss that, even if not detectable, will alter the merger remnant evolution. On the other hand, some properties of the post-merger remnant, such as its oscillations frequencies, can be very different compared to GR, due to the change in the stellar structure for scalarized neutron stars [479].

8.7 Discussion and observational prospects

While a detection of scalar GWs of the form shown in Fig. 8.2 could be used to unambiguously identify that a descalarization took place, (massive) STTs may already leave traces in the events that lead up to the transition. In particular, a promising avenue for the formation of scalarized stars, which are then particulary prone to over-accretion and descalarization, comes from binary mergers. The scalar field associated with the binary constituents may become excited during the late stages of inspiral, leaving a clear imprint on the GW signal by accelerating the coalescence and reducing the number of orbital cycles [479] (see also [480–482]). Despite progress though, certain key effects, such as rotation, are still missing from numerical simulations of mergers in STTs. This means that direct waveform comparisons with observed inspirals cannot be achieved yet. On the electromagnetic side, however, binary neutron-star merger events are also the progenitors for short GRBs, which offer avenues for indirectly observing a descalarization.

Many GRBs exhibit extended emissions at short-wavelengths following the main burst. Emission profiles that display a prominent and long-lived X-ray ‘plateau’ are especially suggestive of persistent energy injections from a massive, newborn neutron star [461, 462]. Suppose that tensorial GWs were coincidentally observed with a short GRB (as occurred for GW170817 [12]), followed by a plateau-like X-ray afterglow. The detection of a *scalar* GW afterglow some time after the main event, which may persist for $\sim$ centuries, would clearly indicate that the remnant peeled its scalar hair. Note in particular that the time at which the descalarization occurred can be determined from the radiation frequency given a field mass m_φ; see Fig. 8.2. Even without such a detection, the nature of the afterglow will be affected by a scalar shedding as the star compactifies. The spindown power associated with magnetic dipole braking scales as $L_{\rm dip} \propto R_\star^6$ (e.g., [462]), for example, and so a decrease in

$R_\star$ by $\sim 5\%$ may then lead to a drop in the X-ray flux by $\lesssim 30\%$ over the descalarization timescale ($\sim$ 5 ms). Afterglow light-curves in this case may appear as 'broken plateaus', such as observed in GRB 170714A [483]. Conservation of angular momentum however implies that the star should spin-up as a result of descalarization, and thus the drop may be less pronounced because $L_{\rm dip} \propto \Omega^4$. Likewise, the temperature of the star should increase from the compactification. Magnetohydrodynamic processes involving magnetic field reorganization may also take place, extending the dip timescale and enriching the phenomenology. Modelling magnetized, rotating stars with hot EOS is much more challenging than for static, cold ones, and studying such cases lies beyond our current computational tools. This would be worth investigating in future though, as a number of possibilities arise. For example, the star's centrifugal barrier may activate, halting further accretion after descalarization, which may carry its own brand of signatures [471]. Furthermore, a descalarization-induced compactification may itself instigate a nuclear phase transition (e.g., quark deconfinement) due to the sudden increase in the core density [466, 477]. If consecutive transitions like this occurred in a massive STT, the tensorial GWs from the nuclear transition would be expected to arrive at the detectors before the scalar mode(s) because of dispersion.

It is also worth pointing out that a descalarization event could also occur in the collapse of a scalarized neutron star to a hairless black hole. From a scalar-GW perspective, these events would be indistinguishable [459], though they can be told apart via the nature of the X-ray afterglow. If the plateau persisted after the scalar radiation was emitted, a gravitational phase-transition would be the favoured scenario since black hole formation, which would effectively terminate the stellar wind that is providing the radiation energy, should instead manifest as a sharp drop in the flux (as is often observed [463]).

The closest GRBs that have thus far been observed are GRBs 980425 and 170817A at distances of $\sim$ 40 Mpc [12, 484]. This distance is a factor $\sim$ 4000 times larger than that plotted in Fig. 8.2. As such, unless α_0 takes a value larger than that which we have used by a factor $\gtrsim 10$ and year-long ($T \gtrsim$ yr) searches are carried out, we are unlikely to observe this scenario in its full capacity even with Cosmic Explorer (CE) [485] or Einstein Telescope (ET) [486, 487] – ET-D in particular [488]. given the $L^{-3/2}$ dependence in the effective PSD (8.14), should such stars exist. Other multi-messenger possibilities for identifying a neutron star post-descalarization come from neutrino bursts (from Urca cooling or shocks triggered by compactification; cf. [489]) or indeed a burst of GWs (if the now descalarized star collapses) at some later time, either of which again would be hard to explain with a black hole remnant. It is also not necessarily the case that a neutron star must descalarize shortly after birth. Mature stars residing in the disks of active galactic nuclei or in high-mass X-ray binaries [490] are particularly disposed to over-accretion, with accretion-induced collapse rates reaching anything up to $\lesssim 20\ {\rm Gpc}^{-3}\ {\rm yr}^{-1}$ from the former channel [491]. Overall, however, in the absence of a detection of scalar GWs, one may not be able to tell whether a phase transition

was of a nuclear or gravitational nature. This exemplifies further the degeneracy between modifications of gravity and EOS uncertainty.

Chapter 9

Scalarization and Its Gravitational Wave Imprint in Scalar-Tensor Theory

Contents

Breakdown of Contributions

I contribute to producing the plots and implement the numerical simulation for massive theories by utilising the code modified by me from the previous code of P. C. K. Cheong which is a code based on GR1D but is tailored into scalar-tensor theory. The plots and numerical results for self-interacting theories are provided by D. Huang by extending my code aforementioned. The manuscript is mainly written by me, while the part of self-interaction theories is drafted by D. Huang. At certain stages of this Chapter, L. W. Luo and C. Q. Geng assist in discussions and suggestions. In addition, L. W. Luo has contributed to partially polishing the manuscript, and C. Q. Geng helps the final edition of the whole manuscript.

Overview

The spontaneous scalarization during the stellar core collapse in the massive scalar-tensor theories of gravity introduces extra polarizations (on top of the plus and cross modes) in gravitational waves, whose amplitudes are determined by several model parameters. Observations of such scalarization-induced gravitational waveforms therefore offer valuable probes

into these theories of gravity. Considering a triple-scalar interactions in such theories, we find that the self-coupling effects suppress the magnitude of the scalarization and thus reduce the amplitude of the associated gravitational wave signals. In addition, the self-interacting effects in the gravitational waveform are shown to be negligible due to the dispersion throughout the astrophysically distant propagation. As a consequence, the gravitational waves observed on the Earth feature the characteristic inverse-chirp pattern. Although not with the on-going ground-based detectors, we illustrate that the scalarization-induced gravitational waves may be detectable at a signal-noise-ratio level of $\mathcal{O}(100)$ with future detectors, such as Einstein Telescope and Cosmic Explorer.

9.1 Introduction

Even though general relativity (GR) has so far withstood all experimental tests [96, 448, 470, 492], many theoretical considerations signal the need of alternative theories of gravity beyond the GR, e.g., the non-renormalizability of GR [493], and numerous astrophysical and cosmological observations [494] (see Ref. [96] for a recent review). An abundance of modified theories of gravity have been constructed to extend GR to overcome the aforementioned obstacles. Among them, the most widely explored one may be the scalar-tensor (ST) theories of gravity [495–497] in which the gravitational interaction is mediated not only by the metric tensor but also by an additional scalar field.

Due to its simplicity and well-posedness [498, 499], ST theories have been subjected to a wide range of experimental tests [420, 500–503], while most are performed in the weak-field regime (mainly in the solar system) [504–507]. Nonetheless, with appropriate ST parameters and strong enough spacetime curvature (see, e.g., [508]), strongly-scalarized neutron star (NS) solutions are energetically favoured over the ordinary weakly-scalarized ones [509]. The ST gravity therefore allows a nonperturbative strong-field phenomenon known as the *spontaneous scalarization* [89, 408] in NSs. Such phenomenon induces a non-vanishing dipole charge of the scalar field, which is (strigently) constrained by observations such as the Cassini spacecraft [507] and binary pulsar timings [413, 414, 510]. However, in massive ST theories, the introduction of the scalar mass $\mu \gtrsim 10^{-15}$ eV effectively weakens these experimental constraints on the parameters [417, 511] so that the theory leaves more room for parameters that can lead to strongly-scalarized NS solutions. In addition, the recent detections of gravitational waves (GWs) have opened a novel window to limit the ST gravity, which has already set severe constraints on the possible models [64, 448, 512, 513]. A further constraint on the ST gravity arises from the equivalence between the Jordan and Einstein frames (see below).

As the evolutionary endpoint of a star, the core collapse to form a NS or a black hole (BH) constitutes another testbed for the strong-field dynamics of the ST gravities [96, 417, 514]. In particular, if a scalarized proto-NS forms during the collapse, the sharp transition from

the weakly-scalarized star configuration into the strongly-scalarized state generates scalar- or monopole-polarized GWs, which is a critical feature of the ST gravity that is absent in GR. Early studies on the spontaneous scalarization and scalar GW production were concentrated on the massless ST gravity [435, 456, 457, 515]. In order to evade the strong experimental constraints listed above, Refs. [90, 458] initiated a line of studies on the core collapse in the massive ST theories. In Refs. [441, 442], the theory was further extended to the case with scalar self-interactions which generically suppressed the degree of the scalarization and the amplitude of the scalar GW radiation.

However, previous studies only focused on the effects of the even-power scalar self-interactions [441, 442] defined in the Einstein frame. Odd-power scalar self-interactions have not been explored yet. Given the importance of the stellar collapse in testing ST gravity by, e.g., scalarization-induced GW signals that are potentially measurable with the ground-based GW detectors, any ST model warrants further investigations. In the present paper, we study the core collapse and the monopole GW radiations in the massive ST theories, including the simplest odd-power scalar self-interaction in the Einstein frame, viz. the triple-scalar coupling effects. In order to ensure the stability of the theory, we take the absolute value of the triple-scalar interaction in the scalar potential. The influence of this scalar interaction on the spontaneous scalarization and the scalar GW production during the core collapse is explored by considering two particular collapse progenitors, which have been treated in the massless [435] and massive [90] ST theories. One of them leads to a NS remnant and the other settles to a BH. We also consider the impact of the triple-scalar coupling on the astrophysically long-distance dispersive propagation of the scalar GWs in our galaxy, which generically leads to the inverse-chirp feature of the GW signals detected on the Earth. Finally, we assess the detectability of the possible scalar GW signals in the on-going and up-coming ground-based GW detectors by computing the corresponding signal-to-noise ratios (SNRs).

Unless stated otherwise, we adopt the geometric unit, viz. $G = 1 = c$, in the present Chapter.

9.2 Formalism

In the previous two Chapters, we only look at the Einstein-frame action of the (multi-)scalar-tensor theories. Although we are solving the matter and metric fields in the Einstein frame [see Eqs. (7.32), (8.5b), and (8.5c)], these quantities can always be transformed back to the Jordan frame to connect to the physics (see the statement below Eq. (7.4) for the transformation). The results of the scalar field φ in the Einstein frame may, on the other hand, nonconvertible to the Jordan frame, suggestive of a "frame-choosing" problem: the solutions in the Einstein can be irrelevant to the physical fields. We note however this does not indicate the Einstein frame formalism losses its applicability in these theory. Rather, it hints at that

we should be carefully about our results if the scalar field fails to fulfill certain condition (see below).

In this Chapter, we are interested in the ST gravity first proposed by Bergmann [516] and Wagoner [517], in which (i) the single scalar field non-minimally couples to the metric tensor; (ii) the theory is diffeomorphism invariant; (iii) the variation of the action gives rise to second order field equations; and (iv) the weak equivalence principle is satisfied in the Jordan (physical) frame. In the literature, the most general action of this class of theories can be written as [96]

$$S_J = \int d^4x \frac{\sqrt{-\tilde{g}}}{16\pi}\left(F(\phi)\tilde{R} - \frac{\omega(\phi)}{\phi}\tilde{g}^{\mu\nu}\partial_\mu\phi\partial_\nu\phi - U(\phi)\right) + S_m[\psi_m, \tilde{g}_{\mu\nu}]\,, \tag{9.1}$$

where $F(\phi)$, $\omega(\phi)$ and $U(\phi)$ are C^2 functions of the Jordan-frame scalar field ϕ, and S_m represents the action of matter fields that are collectively denoted by ψ_m. We note that matter fields couple to the gravity sector only through the (physical) metric tensor $g_{\mu\nu}$ without any dependence on ϕ, so that the weak equivalence principle holds.

One can also formulate the same theory in the so-called Einstein's frame, which relates to the Jordan frame via a Weyl transformation (7.2) for $F = A^{-2}$, and a redefinition of the scalar field:

$$\frac{d\varphi}{d\phi} := \pm\sqrt{\frac{3(F_{,\phi})^2}{4F^2} + \frac{\omega}{2\phi F}}. \tag{9.2}$$

The action Eq. (9.1) can then be rewritten as Eq. (7.1) in the Einstein frame, where the scalar potential $V(\varphi)$ is related to the one in the Jordan frame through

$$V(\varphi) := U(\phi)/(4F^2). \tag{9.3}$$

We see that the ST theory in the Einstein frame is specified by the scalar potential $V(\varphi)$ and the conformal factor $F(\varphi)$. The latter controls the coupling between the scalar field φ and ordinary matters. We adopt the coupling function (8.3) same as that has been considered in, e.g., [408, 420, 500], while the free parameters α_0 and β_0 will be chosen to allow strong scalarization in proto-NSs so as to generate significant scalar GW signals for each of our simulations (see below).

9.2.1 Scalar Field in The Two Frames

Although formulating the theory in the Einstein frame makes numerical implement more convenient since the equations are slightly dressed by some extra terms to the GR counterparts, the issues on the physical interpretation and equivalence of these two frames have been debated for a long time (e.g. [102, 104]). In spite of many efforts to show that these two

conformal frames are equivalent, there are two general problems regarding the redefinition of the scalar field, notably

- For the scalar field ϕ to be describable in terms of the new field φ, the two inequalities,

$$\frac{d\phi}{d\varphi} \neq 0 \quad \text{(Jordam to Einstein frame)}, \tag{9.4a}$$

$$\frac{d\varphi}{d\phi} \neq 0 \quad \text{(Einstein to Jordam frame)}, \tag{9.4b}$$

  should hold, i.e., a bijection $s : \phi \to \varphi$ exists between the scalar fields in the two frame. In addition to being *non-zero*, we also require the derivatives to be *finite*. We call (9.4) as the *derivative constraints*. For the studies of the ST theories in the Einstein frame, it is important that the aforementioned conditions are regarded, or the results may not be able to be transformed back into the Jordan frame, which is assumed to be the physical frame.

- The Einstein-frame scalar field φ is defined via a differential relation $d\varphi/d\phi$, whose sign can be either "+" or "−" as mentioned in [518] but without further discussions therein. Although many just consider the positive sign (e.g., [90, 501, 519]), the negative version is equally reasonable. Therefore, starting from a given ST model in the Einstein frame, it usually corresponds to two different models in the Jordan (physical) frame, arising a uniqueness problem of a model in the Jordan frame. In addition, the condition that the relation $d\varphi/d\phi$ is regular indicates that there is a critical value of φ dividing the solution space of φ into two branches. Conversely, the value of φ can restrict the choice of the sign of the relation $d\varphi/d\phi$ in some cases. (see below)

On top of the above two issues, for theories with non-trivial potential for the scalar field, the existence of the latter one-to-one mapping between φ and ϕ is essential for the model in the Jordan frame being uniquely determined by the one in the Einstein frame. In particular, a potential $V(\varphi)$ in the Einstein frame should admit that $U(\phi) = 4A^{-4}(\phi)V(\varphi(\phi))$ exists and is a unique function of ϕ since $U(\phi)$ is a physical potential as it is defined in the Jordan frame, whereas $V(\varphi)$ is an auxiliary one. It is apparent that V can be a function of ϕ if and only if the derivative constraints hold.

For a specific coupling function A that allows for GR solutions, i.e., $dA/d\varphi(0) \neq 0$, the mapping $s : \phi \to \varphi$ is reversible if and only if

$$\frac{d\ln A}{d\varphi} = -\frac{F_\phi}{2F}\frac{d\phi}{d\varphi} \neq 0. \tag{9.5}$$

The above relation thus returns the condition,

$$\boxed{\varphi \neq -\frac{\alpha_0}{\beta_0}}, \tag{9.6}$$

for the coupling function (8.3) adopted here, defining a critical value $\varphi_{\rm crit} = -\alpha_0/\beta_0$ for φ. Although we have focused on the specific coupling function (8.3) to achieve (9.6), the restriction (9.5) applies to general choices of the coupling function; see Appendix B for some other cases. The existence of a critical value for φ can set certain constraints on the coupling-function parameters α_0 and β_0, which will be explained in Sec. 9.3.1.

9.3 Spherical Collapse

The stellar core collapse into a compact object such as NS and BH marks the endpoint of a massive star with the zero-age main sequence (ZAMS) mass in the range of $10M_\odot \lesssim M_{\rm ZAMS} \lesssim 130M_\odot$ [520–522] with $M_\odot$ denoting the solar mass. At the end of the nuclear burning phase of a star, the nuclear matter thermal pressure and the electrons' degenerate pressure can no longer balance the huge gravitational attracting force [523], leading to a sudden radial compression of the matter. The collapse increases the central (baryon) mass density up to the nuclear density $\rho_{\rm nuc} \simeq 2 \times 10^{14}$ g/cm^3 [433] beyond which the compression is halted and the inner core bounces due to the repulsive force stemmed from the stiffening of the nuclear matter. The core bounce launches a hydrodynamic shockwave outwards and a core-collapse supernova explostion (CCSNe) may then be generated[1].

We assume a spherically symmetric core-collapse in this Chapter with a hybrid EOS (7.12), together with a mixture of thermal component regulated by

$$p_{\rm th} = (\Gamma_{\rm th} - 1)\rho\epsilon_{\rm th}. \tag{9.7}$$

for the thermal contributions to pressure $p_{\rm th}$ and special internal energy $\epsilon_{\rm th}$. Our simulations are based on the open-source code `GR1D` [434], which was originally developed to model the spherically symmetric hydrodynamics in GR by employing the high-resolution shock capturing scheme [529, 530]. The code was extended to include massless scalar fields in [435], massive ones in [90, 458], and an even-power scalar potential in [441, 442]. Here we adopt all dynamical equations, grid types and boundary conditions in our simulations identical to those in [90].

For the initial data, we focus on two specific progenitors of supernovae (pre-SN) with primordial metallicities of $M_{\rm ZAMS} = 12M_\odot$ (denoted by WH12) and $M_{\rm ZAMS} = 40M_\odot$ (denoted

[1] After emanating from the inner core, the out-going shock will then be stalled by the inflowing material. If the shockwave successfully revives by some mechanisms, such as the standing accretion shock instability [524, 525], and the neutrino heating [526, 527], the explosion will be instigated and lead to a CCSNe. The mechanism that accounts for the revival is still an on-going problem (see, e.g., [528] for a recent review and the references therein).

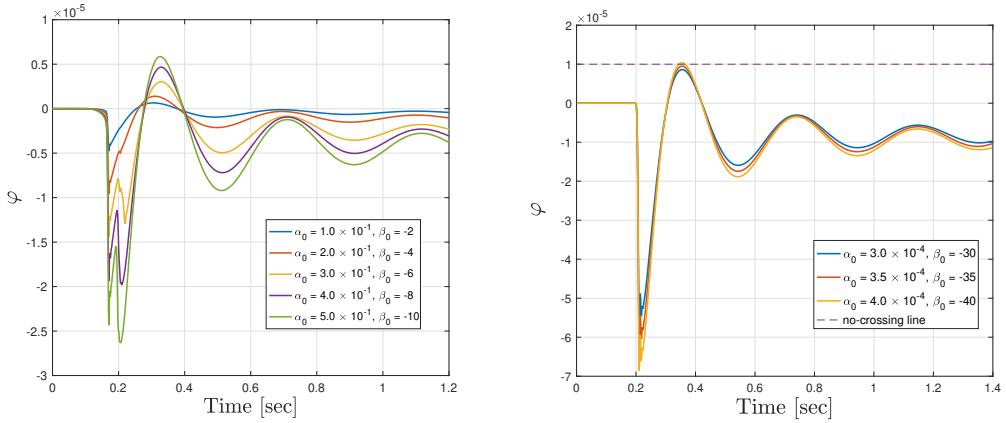

Figure 9.1: Waveforms of the scalar GW, extracted at $r_{ex} = 5 \times 10^9$ cm away from the supernovae core for two specific critical values $\varphi_c = k = 0.05$ (left) and $\varphi_c = k = 1 \times 10^{-5}$ (right). The scalar field labeled by $\beta_0 = -40$ in the left panel is ruled out by the argument made clear in the main context.

by WH40) from the catalog of realistic non-rotating pre-SN models of Woosley and Heger (WH) [531], respectively. In massive ST gravity [435], as well as in GR (see Fig. 10.3), it has been shown that WH12 will collapse to form a NS remnant, while WH40 will eventually result in a BH after a stage of proto-NS (though see later). We note that the initial value of the scalar field at every grid point is taken to be zero.

We will first study the massive scalar-tensor theories with the mass term same as that used for Chap. 8 in Sec. 9.3.1. In Sec. 9.3.2, we then turn to consider additionally a self-interaction at the triple-scalar level, where the scalar potential reads

$$V(\varphi) = \frac{m_\varphi^2}{2\hbar^2}(\varphi^2 + \lambda|\varphi|^3). \tag{9.8}$$

Here λ is assumed to be positive, and the absolute value is taken in the scalar self-interaction term so as to guarantee the semi-positivity and stability of the potential. For these investigations, we use the coupling function (8.3) introduced in Chap. 8. For the later convenience, we also define the characteristic frequency associated with the scalar mass, which is the reciprocal of the Compton length (8.11), viz.

$$f_\varphi = 1/\lambda_\varphi = m_\varphi/(2\pi\hbar). \tag{9.9}$$

9.3.1 Collapse in Massive Theory

Following Chap. 8, the scalar field mass is set a $m_\varphi = 10^{-14}$ eV, which not only alleviates the strong constraints from binary pulsars and weak field tests of GR [417, 511], but also allows the propagating monopole GW signals to be detectable [90, 458] in the LIGO/Virgo sensitivity window. To illustrate our results, we consider the set of parameters (α_0, β_0) for

the coupling function with a constant ratio of $-k$, namely

$$S_k = \left\{(\alpha_0, \beta_0)\middle|\alpha_0/\beta_0 = -k\right\}. \tag{9.10}$$

S_k effectively defined a hypersurface of constant $\varphi_{\rm crit} = k$, and the solutions of φ for (α_0, β_0) within S_k can be viewed as an *one-parameter family* curve, where one of α_0 and β_0 is redundant for specifying the coupling function. We choose β_0 as the parameter – thus α_0 is redundant – for the later analysis.

In the left panel of Fig. 9.1, we show that the amplitudes of the GW signals at the distance of $r = 5 \times 10^9$ are too small by comparing with the critical value $k = 0.05$, which corresponds to a horizontal line far above the signals. We see that φ for different parameters have similar waveform morphology, while the two associated with $\beta_0 = -2$ and -4 are different from the others since they do not or barely possess the second twist before reaching the peak around $0.3s$. As introduced in [458], the amplitudes of the signals at the wave zone of their propagations with different Compton lengths [Eq. (8.11)] of the scalar field have an approximate universal relation. If we ignore the φ-independent source term of $-4\pi G\alpha_0 T$ in (8.6), the Compton length will be a function of β_0. The signals belong to a particular hyperspace S_k have a homologous form, while this universality will be broken if $-4\pi G\alpha_0 T^\star$ is present. We quantify the deviation by the absolute value of the ratio between the coefficients of the zeroth and first order terms on the right hand side of (8.6), given by

$$\delta := \frac{-4\pi G\alpha_0 T^\star}{-4\pi G\beta_0 T^\star + m^2} = \frac{-k}{1 - (4\pi G\beta_0)^{-1}\gamma}, \tag{9.11}$$

for $\gamma = m^2/T^\star$. Consequently, we have that $\delta \approx -k = -0.05$ for $S_{0.05}$ as the linear term dominates, and $\delta \to 0_-$ otherwise. The behaviors of δ as a function of β_0 with several values of γ are plotted on the left panel of Fig. 9.2, while the right panel depicts the case with $\gamma = 1$. For the signals in Fig. 9.1, our simulation on the right panel of Fig. 9.2 illustrates that the deviation is $\lesssim 1.31\%$ from the leading order limitation for $\beta_0 \leq -6$, whereas deviations with twice and three times magnitude are resulted for, respectively, $\beta_0 = -2$ and -4. From Fig. 9.1, we see that the homologous form has been distorted for the later two cases.

For $S_{1\times10^{-5}}$ in the right panel of Fig. 9.1, the amplitudes of the GW signals at the same extraction distance are comparable to those at the critical value $\varphi = k = 1 \times 10^{-5}$, and hence the constraint is more stringent in this case. Any solution crossing the dashed line $\varphi = k$ will be ruled out. For the cases here, δ is minor compared to $-k = -1 \times 10^{-5}$ ($-\delta/k = 0.20 - 0.26\%$), thus the shapes of the signals do not deviate much. In addition, we see that the peaks of the curves increase for decreasing β_0 until they touch the non-crossing line. We can define the corresponding parameter as the critical value of β_0, denoted by β_c. As a result, there exists a value of β_c such that the peak of φ reaches the value of $\varphi_{\rm crit}$. Consequently, any case with $|\beta_0| > |\beta_c|$ will be forbidden due to its crossing with the line of

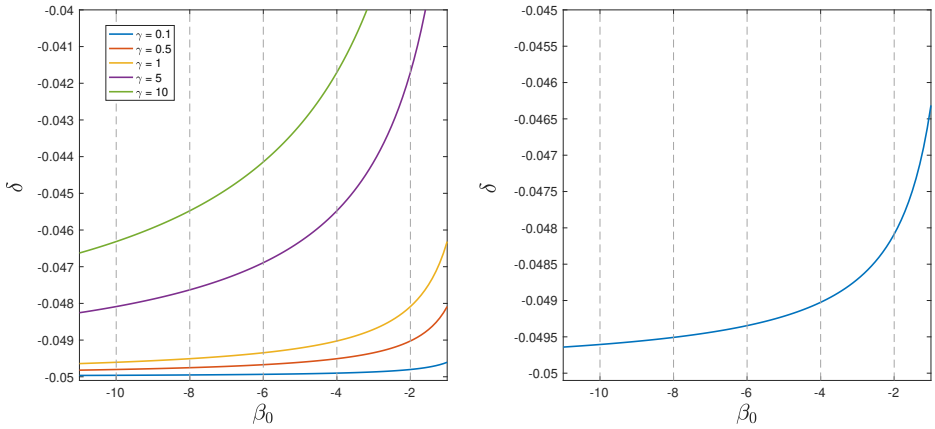

Figure 9.2: Behaviors of δ as a function of β_0, where the left panel represents the cases in Fig. 9.1 with $S_{k=0.05}$ for some γ listed in the legend, while the right panel is our simulation with $\gamma = 1$. For both panels, the vertical dashed lines for β_0 are the values for the signals in Fig. 9.1.

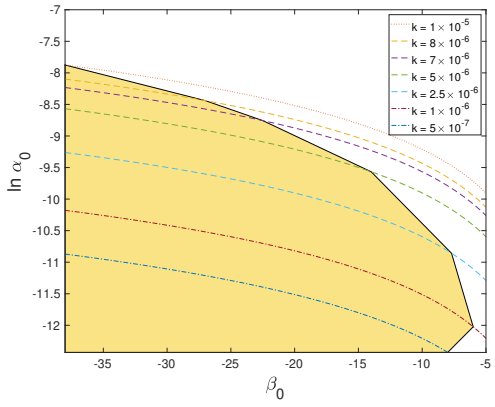

Figure 9.3: Constraints on the coupling parameters α_0 and β_0 for several k's shown in the legend: the shaded region of $(\beta_0, \ln \alpha_0)$ are enclosed by the boundary tracing the critical values β_c for each k, and marks the inviable parameters.

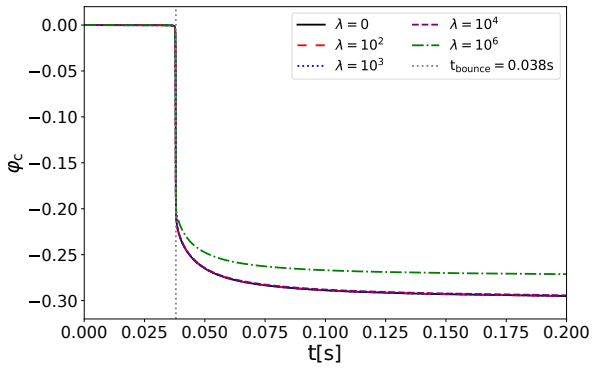

Figure 9.4: Evolutions of the central value of the scalar field φ_c during the core-collapse into a NS for the model WH12 with the self-interaction couplings of λ =0, 10^2, 10^3, 10^4 and 10^6, respectively, where the vertical dashed line denotes the time of the stellar core bounce.

$\varphi_{\rm crit}$.

In Fig. 9.3, we consider some particular values of k, and find the constraints on β_0 for each k. The parameter space is split into two pieces bounded by the solid curve, in which the parameters in the yellow region are ruled out as far as the reversibility between two frames is considered. We note that the shade area will change for the different initial data/progenitors as well as EOS.

9.3.2 Collapse in Self-Interacting Theory

9.3.2.1 Core Collapse to Neutron Stars

For the particular progenitor WH12, the ST parameters are fixed to be $\alpha_0 = 10^{-2}$ and $\beta_0 = -20$, which trigger the strong scalarization in the remnant NS as shown in Refs. [90,441]. Our main interest here is to investigate how the triple-scalar interaction in Eq. (9.8) affects the scalar field dynamics during the core collapse and its subsequently produced GW signals.

In Fig. 9.4, we show the scalar field value at the stellar center as a function of time, i.e., $\varphi_c(t) \equiv \varphi(t, r = 0)$. We can see that the strong spontaneous scalarization occurs at the time of the core bounce, $t \simeq 0.038$ s, for all triple-scalar coupling strength λ considered. The departure of the scalar dynamics around the star center from the non-interacting ST gravity ($\lambda = 0$) is found to be inconsiderable for a moderate coupling strength $\lambda \lesssim 10^4$. However, when λ approaches or exceeds $\sim 10^6$, we can observe the significant suppression in the magnitude of the scalarization (the green dashed line in Fig. 9.4).

The suppression of the spontaneous scalarization is more evident in the rescaled field

$$\sigma \equiv r\varphi. \tag{9.12}$$

Extracting σ at a fixed distance of $r_{\rm ex} = 5 \times 10^4$ km, in Fig. 9.5 we plot $\sigma_{\rm ex} \equiv \sigma(r_{\rm ex})$ in the

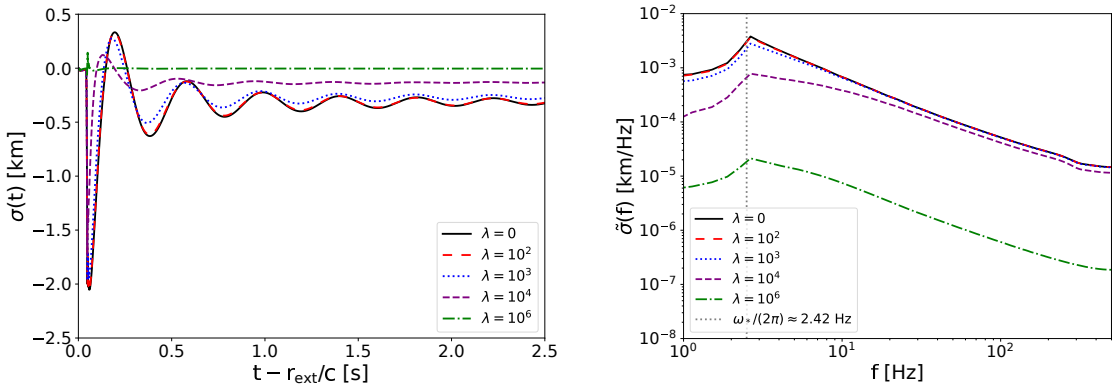

Figure 9.5: Scalar GW signals for WH12 extracted at the radius $r_{\rm ex} = 5 \times 10^4$ km for the self-interaction couplings of λ =0, 10^2, 10^3, 10^4 and 10^6, respectively, where the vertical line on the right plot denotes the characteristic frequency $f_\varphi = 2.42$ Hz [Eq. (9.9)].

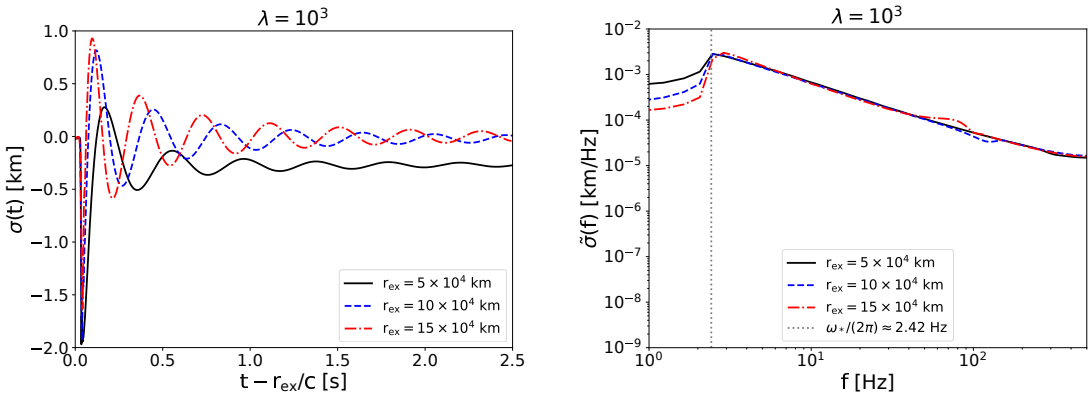

Figure 9.6: Scalar GW waveforms for WH12 extracted at different radii $r_{\rm ex} = (5, 10, 15) \times 10^4$ km.

time domain (left panel), and the associated Fourier transformed signals $\tilde{\sigma}_{\rm ex}(f)$ [532] in the frequency domain (right panel). For the self-coupling up to $\lambda \sim 10^2$, the difference in $\sigma_{\rm ex}$ from the non-self-interacting ST gravity is negligible. However, when λ approaches $\sim 10^3$, we begin to see a mild suppression and a small phase shift. The suppression and the phase shift are enlarged with increasing λ as a consequence of the frequency-related quenching due to the scalar self-interaction, similar to that found in [441]. In particular, the scalarizaion is reduced from the case without the self-interaction by more than two orders for $\lambda \gtrsim 10^6$.

In addition, the right panel of Fig. 9.5 plots the frequency-domain, where we see that the suppression is more significant for $f \lesssim f_\varphi = 2.42$ Hz. Due to their smaller group velocities, the low-frequency modes spend more time propagating out of the (strong) interaction regime near the star so that they experience more suppressions by self-interactions. To illustrate this effect, we plot σ at three radii $r_{\rm ex} = (5, 10, 15) \times 10^4$ km with $\lambda = 10^3$ in Fig. 9.6. These distances lie in the wave zone [458] and are much larger than both the reduced Compton wavelength (8.11) of the massive scalar and the gravitational radius $r_G = GM_{\rm NS}/c^2$ with

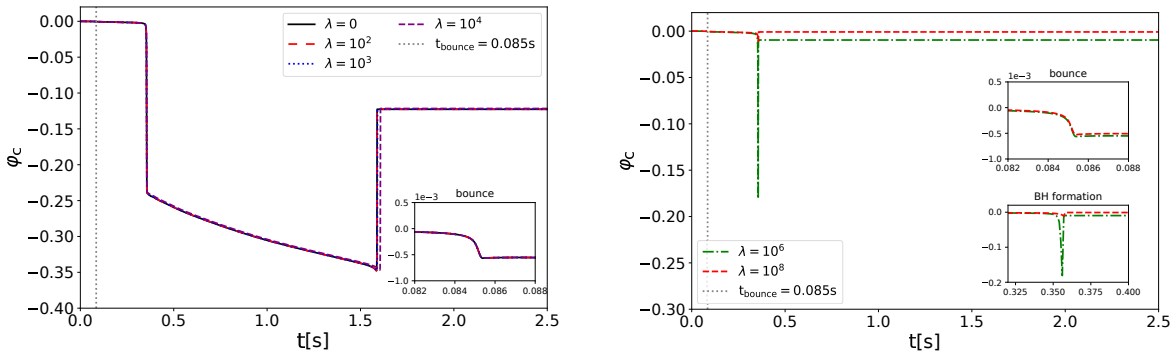

Figure 9.7: Evolutions of the central value of the scalar field φ_c for the progenitor WH40 during the core-collapse into a BH for $\lambda = 0$, 10^2, 10^3 and 10^4 in the left panel and $\lambda = 10^6$ and 10^8 in the right panel, respectively, where the inset of left panel shows the scalar field behavior zoomed in on the core bounce part, while ones on the right panel correspond to the region near the core bounce and the BH formation, respectively.

$M_{\rm NS}$ denoting the NS mass. In the left panel of Fig. 9.6, we see that the time-domain signal becomes much more oscillatory since the dispersion during the propagation screens out the low frequency modes for a distant observer, as expected. When transformed into the frequency domain (the right panel of Fig. 9.6), the modes with frequencies higher than f_φ remain unchanged, while the spectra below this critical frequency decay exponentially. This implies that only the high-frequency scalar signals can travel astrophysically long distance to be detectable on the Earth. Focusing on the high frequency signals, the choice of the extraction radius is irrelevant therefore.

9.3.2.2 Core Collapse to Black Holes

Now we turn to simulation results for the progenitor model WH40. In order for the strong scalarization to occur in the proto-NS prior to the BH formation, we set the ST parameters as $\alpha_0 = 3\times10^{-3}$ and $\beta_0 = -5$. We shall repeat the above analysis to see the effects of the self-interaction term in Eq. (9.8) on the dynamics of the stellar evolution and the scalar-polarized GW radiations.

Fig. 9.7 presents the evolutions of the scalar field at the center of the compact objects for the WH40 progenitor. Obviously, the dynamics is much more complicated than the WH12 model. We begin our discussion with the non-self-interacting case, *i.e.*, $\lambda = 0$. The stellar core bounce firstly produces a weakly scalarized NS with $\varphi_c \sim -5\times10^{-4}$ at $t_{\rm w} \simeq 0.085$ s, which then transits to a strongly scalarized NS at $t_s \simeq 0.35$ s due to the accretion of ambient materials. In this particular model, the continuous infalling material makes the stellar core massive enough to cause the gravitational instability, i.e., the mass of the remnant exceeds the maximal mass that can be supported by the EOS considered. Eventually, a BH forms at some point $t_{\rm BH}$, which depends on λ (see below).

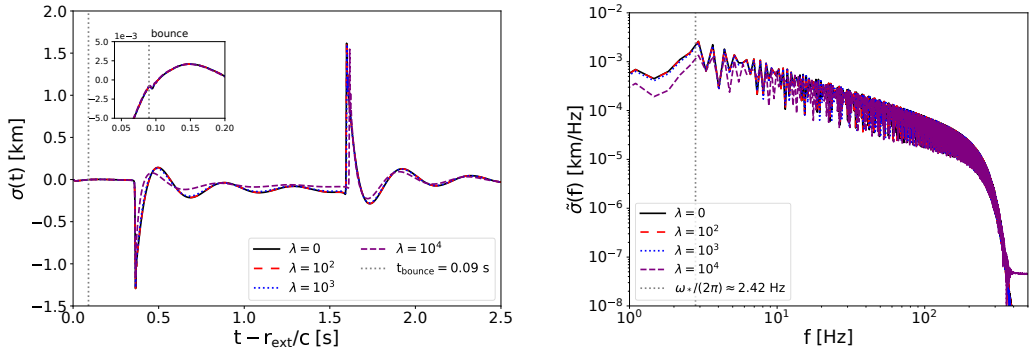

Figure 9.8: Scalar GW signals in the time domain (left panel) and frequency domain (right panel) for the progenitor model WH40 extracted at the radius $r_{\rm ex} = 5 \times 10^4$ km for different values of the self-interaction coupling λ =0, 10^2, 10^3 and 10^4, respectively. The inset in the left panel illustrates the scalar GWs around the core bounce which generates a weakly-scalarized NS.

The extent to which the scalarization is triggered and the lifetime of the strongly-scalarized state ($t_{\rm BH} - t_{\rm s}$) depend on λ. The left panel of Fig. 9.7 shows the cases with a moderate level of λ, where we see that φ_c goes down to ~ -0.25 at $t_{\rm s}$, and then the scalarizaion is progressively strengthened to $\varphi_c \sim -0.35$ at the moment right before the BH formation. The strong scalarization lasts for ~ 1.24 s, and is followed by a transient decrease of the scalarization at $t_{\rm BH}$ in accordance with the BH no-hair theorem. In addition, when $\lambda \lesssim 10^3$, we do not see any visible deviation from the case without self-interactions. As λ increases to $\gtrsim 10^4$, the degree of the scalarization during the strong-scalarization stage is weakened a little, but the duration $t_{\rm BH} - t_{\rm s}$ becomes a bit longer owing to a delay in the BH formation. Such trend continues and becomes more evident with increasing λ until $\lambda \sim 10^6$. In the right panel of Fig. 9.7, we plot the case with strong coupling strengths $\lambda = 10^6$ and 10^8. For $\lambda = 10^6$, the degree of the scalarization is a bit slighter than the aforementioned case with the moderate λ and the lifetime of the proto-NS becomes very short with $t_{\rm BH} - t_{\rm s} \lesssim 0.01$ s. When $\lambda = 10^8$, we find that the strongly-scalarized proto-NS stage completely disappears, leading to a scenario that a weakly-scalarized NS directly collapses to a BH.

Having shown the influence of λ on φ_c, we now turn to investigate how λ affects σ, especially $\sigma_{\rm ex}$. In Figs. 9.8 and 9.9, we present $\sigma_{\rm ex}$ in both the time and the frequency domains. As illustrated in the left panel of Fig. 9.8, we can find clear time-domain signatures corresponding to the transitions between different stages of the multi-stage BH formation scenario. In the inset figure, we see a small variation in the amplitude at the retarded time $t_r \equiv t - r_{\rm ex}/c = 0.085$ s, which matches the timing of the core bounce. The sudden drop at $t_r \simeq 0.35$ s and the sharp peak around $t_r \simeq 1.59$ s reflect the transition from weakly- to strongly-scalarized configurations and the descalarization caused by the BH formation. Moreover, compared with the non-self-interacting case, the evolution of $\sigma_{\rm ex}$ keeps intact for $\lambda \lesssim 10^3$. When λ increases to 10^4, the suppression of the amplitude for GW signals can

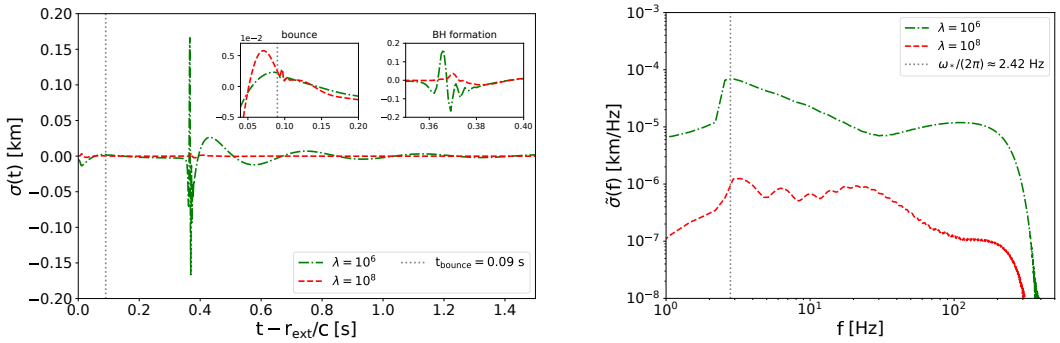

Figure 9.9: Label is the same as Fig. 9.9, except for $\lambda = 10^6$ and 10^8. The two insets in the left panel correspond to the scalar GW signals at the core bounce and the BH formation, where we have artificially enlarged the field values by a factor of 10 for the case with $\lambda = 10^8$ in order to make its dynamical evolution clearer.

be seen in both the time and frequency domains. On the other hand, as shown in the left panel of Fig. 9.9, besides the small structure at the core bounce, we only see some rapid oscillations around the BH formation for $\lambda \gtrsim 10^6$, which indicates the disappearance of the strongly-scalarized NS stage. Furthermore, the right panel of Fig. 9.9 illustrates that the scalarization is diminished greatly by several orders for $\lambda = 10^6$ and 10^8 in comparison with the case of $\lambda = 0$.

9.4 Scalar Detectability

For the scalar GW signals in the ST gravity, there exist several search strategies [90], such as monochromatic continuous-wave searches, stochastic searches, and burst searches. For instance, for a CCSNe that is detected by optical observations or all-sky GW searches, the best strategy is through the continuous quasi-monochromatic GW search [90, 442, 458, 533] pointed to the location of that source. In this subsection, we present our prediction of the detectabilities of such source-targeted continuous searches of the scalar GW signals for the progenitor models WH12 and WH40.

By implementing a fourier transformation to the scalar GW waveforms extracted at $r_{\rm ex} = 5 \times 10^4$ km, we can obtain the spectral power densities for both progenitor models. In Fig. 9.10, we plot $\sqrt{S_o(f)}$ at several time points after the GW emission with various triple-scalar coupling strengths. Here, the distance between the Earth and the source is assumed to be of the galactic scale, i.e., $D = 10$ kpc. Since the signal would keep nearly monochromatic for the period of $\mathcal{O}$(month), the observational duration is taken to be $T = 2$ months. For both WH12 and WH40, we see that

- the quasi-monochromatic signal slowly moves to low frequencies in accord with the inverse-chirp formula (8.15) [cf. also Eq. (53) in [458]],

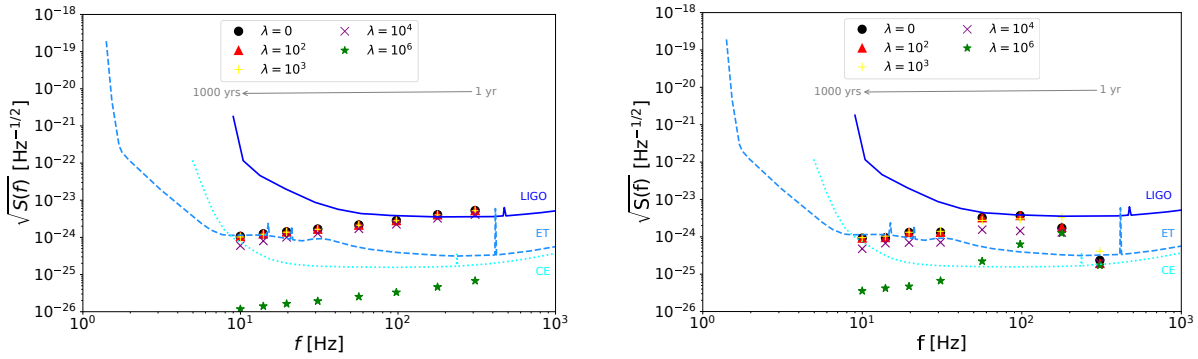

Figure 9.10: Power spectrum densities of the core collapse into a NS for the progenitor models WH12 (upper panel) and into a BH for WH40 (lower panel) with the self-interaction couplings λ =0, 10^2, 10^3, 10^4 and 10^6, respectively, where the points of various types correspond to the inverse-chirp scalar GW signals observed at different times after the supernova: t =1, 3, 10, 30, 100, 250, 500, and 1000 years from right to left on each plot. In comparison, we also plot the noise power spectral density of LIGO, ET, and CE.

- $\sqrt{S_o(f)}$ varies within two orders over time for a given coupling strength,
- the triple-scalar self-interaction suppresses the magnitude of the scalar gravitational radiation generated by the stellar core collapses.

The predicted scalar GW signals are similar to the non-interacting case for up to $\lambda \sim 10^3$, whereas we observe a small reduction in the signal amplitude when λ increases to $\sim 10^4$. When $\lambda \gtrsim 10^6$, the scalar-polarized GW is suppressed by two orders for the WH12 model, while for the WH40 progenitor the suppression is frequency-dependent, viz. the low-frequency modes decrease in amplitude more than the high-frequency part of the spectrum.

On top of the scalar GW strain of our models, Fig. 9.10 also shows the noise curves of the current LIGO detectors, and the near-future ET and CE experiments, whereby we can estimate the SNRs of signals. It turns out that, even though the scalar GW signal amplitude of the WH12 model with $\lambda \lesssim 10^4$ observed for 2 months in the first 3 years after the core collapse can be higher than the LIGO noise curve, the SNR in this optimal case can only reach $\rho \simeq 2$ at most, which is unlikely to be detected. For other choices of the coupling constant values, progenitor models and observation duration would result in power spectral densities $\sqrt{S_o}$ lower than the LIGO sensitivity curve, implying that it is impossible to measure them with LIGO. In contrast, with the future ET and CE detectors, some signals may reach SNRs of $\rho \sim \mathcal{O}(100)$ and remains visible for several centuries.

9.5 Conclusions and Discussions

The stellar core collapse provides us with valuable tests of ST theories due to the possible formation of the NS in the intermediate stage or as the final state of the process. The spontaneous scalarization may be induced in those NS and produces strong scalar or monopole GW

signals. In the present Chapter, we have studied the effects of the triple-scalar self-interaction [Eq. (9.8] on the scalar field dynamics and the subsequent scalar GW generation. In order to achieve this goal, we have performed simulations based on the open-source code `GR1D` which is extended to the massive ST gravity with the triple-scalar self-interaction. We have focused on two specific pre-SN models with the primordial metallicity in the WH list, viz. WH12 and WH40, corresponding to stars with ZAMS mass of $12M_\odot$ and $40M_\odot$, respectively. These two progenitors are representative of two typical collapse processes: WH12 collapses into a NS, while WH40 ends up to a BH. The ST parameters α_0 and β_0 are chosen specifically for each model so that the strong scalarization can take place in simulations.

As a result, we find that the triple-scalar self-interaction generically suppresses scalarization during collapse, consistent with the conclusions of [441, 442]. Such suppressions can be shown either from the scalar dynamics at the center, or from the produced scalar GW signals. However, the suppression is considerable only for sufficiently large self-interaction coupling λ; in particular, it should be $\lambda \gtrsim 10^3$ for WH12 and $\lambda \gtrsim 10^4$ for WH40. In addition, the self-interaction can alter the scalar evolution of the collapse of WH40, where the strongly scalarized stage during the BH formation can be completely eliminated if λ reaches $\gtrsim 10^6$.

For the massive scalar GWs propagate over astrophysically long distances, the self-interaction effects have been shown to be negligible, and the dispersion of GWs is solely determined by the scalar mass. It turns out that scalar GW signals detected on the Earth have the inverse-chirp feature as in massive ST theories [90]. We have accessed the detectability of the scalar GW signals produced by the galactic WH12 and WH40 pre-SN sources by estimating their SNRs. Although it is unlikely to observe the inverse-chirp signals for both progenitors with the current LIGO detectors, signals of these two models can reach SNRs of $\mathcal{O}(100)$ with the future ET and CE detectors and remain visible for several centuries.

In this study, our simulations have been performed with fixed nuclear matter EOS parameters and specific values of the ST gravity parameters (α_0, β_0). However, it is well known that the nuclear matter property would significantly affect the hydrodynamic evolution of matter fields during the core collapse [534, 535], which would in turn dramatically modify the dynamics of the scalar field and the generated GW waveforms. Additionally, it has been pointed out in Ref. [458] that the stellar collapse scenarios changes with the different choices of the ST parameters (α_0, β_0). Especially, as the value of β_0 becomes more and more negative, the degree of scalarization tends to be intensified and the corresponding GW signals are expected to be stronger. Moreover, there have been several studies on the spectrum of radial quasinormal modes (QNMs) of NSs in the ST gravity theory [430, 536, 537]. It is well expected that the radial QNMs would show themselves in the scalar GW spectrum at the late stage of the stellar collapse. According to the discussion in Ref. [430] which has also addressed the spontaneously scalarized NSs with a negative β_0, there are two classes of radial QNMs: the pressure-led fluid modes and the scalar ϕ-modes. It is seen from the plots of

Fig. 2 in this reference that typical frequencies of the fluid modes are of $\mathcal{O}$(kHz) and that of the fundamental ϕ-mode is around or below 1 kHz, while the damping times of these modes are of $\mathcal{O}(0.1-1)$ ms. However, in our simulation, the minimal sampling time interval is only 1 ms, which means that we do not have enough precision to resolve the QNM signals for both modes. In order to see these modes clearly, one needs to improve the simulation precision in time interval at least by one to two orders. Nevertheless, the full exploration of all these aspects is well beyond the scope of the present article, and will be deferred to the future work.

Chapter 10

Scalarization and Descalarization in Scalar Gauss-Bonnet Theory

Contents

Breakdown of Contributions

I contribute to producing almost all the plots (one is generated by D. D. Doneva), and carrying out the numerical simulations with a code modified by me from the previous code of P. C. K. Cheong which is based on GR1D but has been tailored into scalar-tensor theory. The manuscript is jointly completed by me (illustration of the numerical results), and D. D. Doneva (motivation and general discussion). S. S. Yazadjiev assists in discussion and complements a theoretical capture of the conception of "lost hyperbolicity" to account for the termination of the numerical simulations.

Overview

In a certain class of scalar-Gauss-Bonnet gravity, the black holes and the neutron stars can undergo spontaneous scalarization – a strong gravity phase transition triggered by a tachyonic instability due to the nonminimal coupling between the scalar field and the spacetime curvature. Studies of this phenomenon have, so far, been restricted mainly to the study of the tachyonic instability and stationary scalarized black holes and neutron stars. To date, no

realistic physical mechanism for the formation of isolated scalarized black holes and neutron stars has been proposed. We study, for the first time, the spherically symmetric fully nonlinear stellar core collapse to a black hole and a neutron star in scalar-Gauss-Bonnet theories allowing for a spontaneous scalarization. We show that the core collapse can produce scalarized black holes and scalarized neutron stars starting with a nonscalarized progenitor star. The possible paths to reach the end (non)scalarized state are quite rich leading to interesting possibilities for observational manifestations.

10.1 Introduction

Among the modified gravity theories, the scalar-Gauss-Bonnet (SGB) gravity takes a special place. This theory is an extension of general relativity (GR) and contains a dynamical scalar field coupled to the Gauss-Bonnet (GB) invariant. The roots of SGB gravity lay in the low-energy limit of quantum gravity and unification theories [86, 87] as well as in the effective field theories. As in GR, the field equations of SGB gravity are of second order and the theory is free from ghosts. There exists a particular class of SGB theories which gives rise to spontaneously scalarized black holes (BHs) and neutron stars (NSs) [91, 105, 106, 538]. More precisely, the spacetime curvature itself can induce a tachyonic instability that spontaneously scalarizes the black holes or the neutron stars. This class of SGB theories is indistinguishable from GR in the weak field limit and is yet unconstrained by gravitational wave (GW) observations. Since this interesting phenomenon is the only known dynamical mechanism for endowing black holes and neutron stars with scalar hair, it has attracted a lot of interest in recent years (though a novel nonlinear mechanism that can lead to dynamical formation of scalar hair beyond the standard spontaneous scalarization was recently proposed by [450]).

Thanks to the efforts of many researchers, the spontaneous curvature induced scalarization in SGB gravity has been extensively studied, and now, we have a pretty good understanding of this phenomenon. In particular, the tachyonic instability that triggers the spontaneous scalarization is, to a large extent, well understood [91, 92, 105, 106, 538–540]. The same applies to the static or stationary BH and NS solutions that are the end states of the tachyonic instability [91, 106, 538, 541–544]. Even the highly nonlinear dynamics of the curvature induced spontaneous scalarization is, to some extent, well understood from a mathematical point of view [93, 545] including the dynamical descalarization during black hole merger [95, 546] (see, also, [547]). However, there is a very important link missing in our understanding of the curvature induced spontaneous scalarization. Up to now, no realistic physical scenario for the formation of isolated, scalarized BHs and NSs has been investigated. The purpose of the present Chapter is to show that the scalarized compact objects can be formed under gravitational core collapse (CC) of a nonscalarized progenitor star and to explore the different

scenarios depending on the theory parameters and the progenitors.

Numerical simulations that demonstrate the core-collapse process with a scalarized compact object as the remnant have been limited in scalar-tensor theories [90, 435, 441, 442, 456, 458] until now. In this case, though, scalarization of BHs is typically not possible (for interesting, though not so astrophysically relevant exceptions, we refer the reader to [409–411]). Since SGB theories allow for nonlinear development of BH scalar hair, they provide a richer phenomenology of the core collapse. However, the complexity of the field equations is significantly increased. In the present Chapter, we go beyond the commonly employed decoupling limit approximation [93,546,547] and consider the coupled evolution of the spacetime, matter and the scalar field.

10.2 Gauss-Bonnet theory

The action of the sGB gravity in the presence of matter is the following:

$$S = \frac{1}{16\pi}\int d^4x\sqrt{-g}\Big[R - 2\nabla_\mu\varphi\nabla^\mu\varphi + \lambda^2 f(\varphi)\mathcal{R}^2_{\rm GB}\Big] + S_{\rm matter}(g_{\mu\nu},\Psi_m). \tag{10.1}$$

where $f(\varphi)$ is the coupling function of the scalar field φ to the GB invariant $\mathcal{R}^2_{\rm GB} = R^2 - 4R_{\mu\nu}R^{\mu\nu} + R_{\mu\nu\alpha\beta}R^{\mu\nu\alpha\beta}$. The GB coupling constant λ has dimension of length, and the matter fields are collectively denoted by Ψ_m.

The field equations derived from the action are

$$R_{\mu\nu} - \frac{1}{2}Rg_{\mu\nu} + \Gamma_{\mu\nu} = 2\nabla_\mu\varphi\nabla_\nu\varphi - g_{\mu\nu}\nabla_\alpha\varphi\nabla^\alpha\varphi + 8\pi T_{\mu\nu}, \tag{10.2}$$

$$\nabla_\alpha\nabla^\alpha\varphi = -\frac{\lambda^2}{4}\frac{df(\varphi)}{d\varphi}\mathcal{R}^2_{\rm GB}, \tag{10.3}$$

where $T_{\mu\nu}$ is the matter energy-momentum tensor that can be proven to satisfy $\nabla^\mu T_{\mu\nu} = 0$ and

$$\begin{aligned}\Gamma_{\mu\nu} =& -R(\nabla_\mu\Psi_\nu + \nabla_\nu\Psi_\mu) - 4\nabla^\alpha\Psi_\alpha\left(R_{\mu\nu} - \frac{1}{2}Rg_{\mu\nu}\right)\\ &+ 4R_{\mu\alpha}\nabla^\alpha\Psi_\nu + 4R_{\nu\alpha}\nabla^\alpha\Psi_\mu - 4g_{\mu\nu}R^{\alpha\beta}\nabla_\alpha\Psi_\beta + 4R^\beta_{\ \mu\alpha\nu}\nabla^\alpha\Psi_\beta\end{aligned} \tag{10.4}$$

with $\Psi_\mu = \lambda^2[df(\varphi)/d\varphi]\nabla_\mu\varphi$.

We consider asymptotically flat spacetimes with zero cosmological value of the scalar field $\varphi_\infty = 0$. The GB coupling function $f(\varphi)$ allowing for spontaneous scalarization has to obey the condition $(df/d\varphi)(0) = 0$. In addition we can impose $f(0) = 0$ and $(d^2f/d\varphi^2)(0) = \epsilon$ with $\epsilon = \pm 1$.

10.2.1 Evolution equations

In the present Chapter, we will study the coupled evolution of the scalar field, the matter, and the spacetime in spherical symmetry [cf. the metric Eq. (2.1), while we change the notation from $\lambda(r)$ to $\Lambda(r)$ to leave the symbol λ for the coupling strength of Gauss-Bonnet term], which is a simplification also adopted in previous studies on core collapse in alternative theories of gravity [90, 435, 441, 442, 456, 458]. We will model the matter as a perfect fluid with energy-momentum tensor $T_{\mu\nu} = \rho h u_\mu u_\nu + p g_{\mu\nu}$ and particle density current $J^\mu = \rho u^\mu$. Here ρ is the rest-mass (baryonic) density, p is the fluid pressure, $h = 1 + e + \frac{p}{\rho}$ is the specific enthalpy with e being the specific internal fluid energy, and u^μ is the fluid 4-velocity. Due to the spherical symmetry, the 4-velocity of the fluid can be written as

$$u^\mu = \frac{1}{\sqrt{1-v^2}}(e^{-\Phi}, v e^{-\Lambda}, 0, 0) \tag{10.5}$$

with $v = v(t, r)$ being the fluid velocity.

A well established approach to handle the shock discontinuities appearing in the fluid is the use of the high-resolution shock-capturing schemes. This approach requires the equations of motion to be written in flux conservative form using conserved variables. In our case the conserved variables are D, S^r and τ, and they are related to the standard primitive variables ρ, v and p by

$$D = \frac{\rho e^{\Lambda}}{\sqrt{1-v^2}}, \; S^r = \frac{\rho h v}{1-v^2}, \; \tau = \frac{\rho h}{1-v^2} - p - D. \tag{10.6}$$

The flux conservative equations of the relativistic hydrodynamics take then the form

$$\partial_t \mathbf{U} + \frac{1}{r^2}\partial_r \left(r^2 e^{\Phi-\Lambda} \mathbf{f}(\mathbf{U}) \right) = \mathbf{s}(\mathbf{U}). \tag{10.7}$$

where $\mathbf{U}$ is the state vector of the conserved variables, namely $\mathbf{U} = [D, S^r, \tau]$. The flux vector $\mathbf{f}(\mathbf{U})$ and the source vector $\mathbf{s}(\mathbf{U})$ are defined by

$$\mathbf{f}(\mathbf{U}) = [Dv, S^r v + p, S^r - Dv], \tag{10.8}$$

$$\mathbf{s}(\mathbf{U}) = [0, (S^r v - \tau - D) e^{\Phi+\Lambda}(8\pi r p + \frac{m}{r^2}) + e^{\Phi+\Lambda} p \frac{m}{r^2} + 2 e^{\Phi-\Lambda}\frac{p}{r}, 0]. \tag{10.9}$$

The dimensionally reduced field equations, in terms of the conserved variables, for the

metric functions Φ and m and the evolutionary equations for the scalar field are

$$(1+\mathcal{A})\Phi' + \mathcal{B}\frac{X^2}{r}\dot{m} = X^2\left(4\pi r(s^r v + p) + \frac{m}{r^2}\right) + \frac{(P^2+Q^2)r}{2} + \frac{4m\lambda^2}{r^2}\left(\frac{d^2 f}{d\varphi^2}P^2 + \frac{df}{d\varphi}e^{\Lambda-\Phi}\dot{P}\right), \tag{10.10a}$$

$$(1+\mathcal{A})m' + \mathcal{B}\dot{m} = 4\pi r^2(\tau + D) + \mathcal{A}\frac{m}{r} + \frac{r^2}{2X^2}(P^2+Q^2) + \frac{4m\lambda^2}{rX^2}\left(\frac{d^2 f}{d\varphi^2}Q^2 + \frac{df}{d\varphi}Q'\right), \tag{10.10b}$$

$$\mathcal{C}m' + (1+\mathcal{A})\dot{m} = -4\pi r^2\alpha X^{-1}s^r + \mathcal{C}\frac{m}{r} + e^{\Phi-3\Lambda}r^2 PQ + \frac{4m\lambda^2}{r}e^{\Phi-3\Lambda}\left(\frac{d^2 f}{d\varphi^2}PQ + \frac{df}{d\varphi}P'\right), \tag{10.10c}$$

$$\begin{aligned}\partial_t P = {} & e^{\Phi-\Lambda}Q' + e^{\Phi-\Lambda}(\Phi' - \Lambda' + \frac{2}{r})Q - \frac{1}{4}\frac{dV(\varphi)}{d\varphi}e^{\Phi+\Lambda} + 2\frac{df(\varphi)}{d\varphi}\frac{\lambda^2}{r^2}e^{\Phi+\Lambda} \\ & \times\left\{(1-e^{-2\Lambda})\left[\frac{1}{r}(\Phi'-\Lambda')e^{-2\Lambda} - 8\pi p + (Q^2-P^2)e^{-2\Lambda} + \frac{\Gamma_{\theta\theta}}{r^2}\right] - 2\Phi'\Lambda' e^{-4\Lambda} + 2\dot{\Lambda}^2 e^{-2\Phi-2\Lambda}\right\},\end{aligned} \tag{10.10d}$$

and

$$\partial_t Q = e^{\Phi-\Lambda}[P' + (\Phi'-\Lambda')P]. \tag{10.10e}$$

where $Q = \partial_r\varphi$ and $P = e^{\Lambda-\Phi}\partial_t\varphi$. We see that the scalar field couples to the metric functions via

$$\mathcal{A} = \lambda^2 Q\frac{df}{d\varphi}\frac{2}{r}(1-3e^{-2\Lambda}), \quad \mathcal{B} = \frac{4m\lambda^2}{r^2}e^{\Lambda-\Phi}P\frac{df}{d\varphi}, \quad \text{and} \quad \mathcal{C} = \frac{4m\lambda^2}{r^2}e^{\Phi-\Lambda}P\frac{df}{d\varphi}. \tag{10.11}$$

The aforementioned equations are solved numerically with the scheme of [548]. Equations (10.10b) and (10.10c) form a system of equations

$$\begin{pmatrix} 1+\mathcal{A} & \mathcal{B} \\ \mathcal{C} & 1+\mathcal{A}\end{pmatrix}\begin{pmatrix} m' \\ \dot{m}\end{pmatrix} = \begin{pmatrix}\text{LHS of (10.10b)} \\ \text{LHS of (10.10c)}\end{pmatrix}; \tag{10.12}$$

however, equation (10.10a) should be solved for simultaneously with the $\theta\theta$ component of the equation for $\Gamma_{\mu\nu}$ (can be found in the main text of the paper) and (10.10d), symbolized by

$$\mathbf{T}\begin{pmatrix}\Phi' \\ \dot{P} \\ \Gamma_{\theta\theta}r^{-2}\end{pmatrix} = \mathbf{V} \tag{10.13}$$

where $\mathbf{T}$ and $\mathbf{V}$ can be obtained after a lengthy manipulation of relevant equations. We solve the mass function [Eq. (10.12)] and the redshift Φ [Eq. (10.13)] iteratively until the computational error drops below a predefined threshold. In solving Eq. (10.13), $\dot{P}$ is obtained

simultaneously, which then is used to evolve the scalar field. In order to close the hydrodynamical system of equations we have to specify the EOS giving the pressure and other thermodynamical quantities as a function of the mass density, internal energy and possibly the chemical composition. We adopt the hybrid EOS (7.12) introduced in Chap. 7 together with the termal treatment introduced in Chap. 9.

As the final piece to be specified about the numerical setup, let us briefly comment on the grid we employ. Due to the fact that the functions we compute exhibit much stronger spatial variation in the central region of the star compare to the outer wave zone, the computational domain in the `GR1D` code [434, 435] is divided in two parts – an inner grid with a constant spacing and an outer grid where the spacing increases exponentially. This provides us with the opportunity to follow the dynamics in the inner core with a good resolution while allowing to extend the computational domain to large distances at acceptable computational cost. For an extensive discussion on the grid construction in the `GR1D` code we refer the reader to [434, 435]. Unless otherwise specified, in our simulations the two pieces of the grid are matched at 40 km and the outer boundary is located at 9×10^5 km. The inner grid bin (cell width) is equal to 15m. For the numerical calculations, we employ the `GR1D` code [434, 435] with a significant modification implemented in order to deal with the SGB field equations in the fashion of [545, 548].

Although different coupling functions satisfying the scalarization criteria can be introduced, the difference between the stable scalarized solutions (if exists; such solution is absent for, e.g., the simplest choice $f(\varphi) = \varphi^2$) and their dynamics is mainly quantitative [93, 549]. From a numerical point of view, one of the least problematic, generic, and widely used coupling functions for which stable scalarized BHs can exist is the following [95, 106, 538, 541, 543]

$$f(\varphi) = \frac{\epsilon}{2\beta}\left[1 - \exp(-\beta\varphi^2)\right], \quad \epsilon = \pm 1, \tag{10.14}$$

where $\beta > 0$ is a parameter that has not been constrained by the observations yet. Based on [93, 549], we expect that the main results in this Chapter will remain qualitatively similar for a broad class of couplings that lead to scalarization.

10.2.2 Hyperbolicity

If strong enough scalar field is realised, the evolutionary differential equations will lose locally their hyperbolicity, i.e., the discriminant of the characteristic equation D becomes negative at some places [545, 550]. As a consequence, the set of equations is no longer well-posed in the sense that the solution is not unique for the mix-type differential equations, and thus the predictability of the theory is polluted. However, for certain range of the parameters the influence of scalar field on the matter sector will maintain small enough that the hyperbolicity holds everywhere throughout the evolution [95, 545, 548]. In particular, for the framework

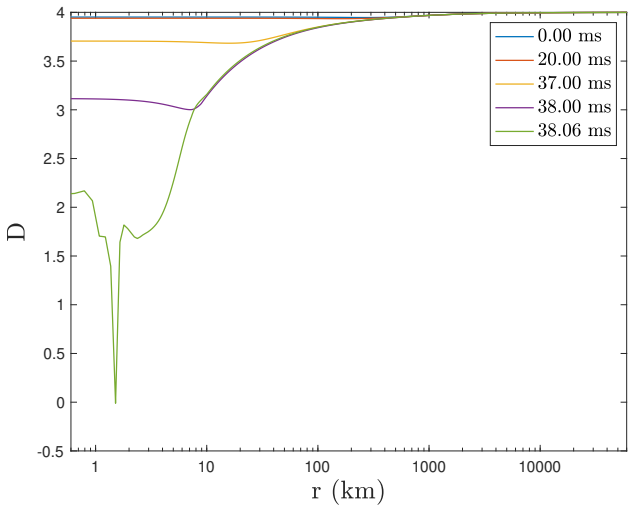

Figure 10.1: The discriminant of the characteristic equation as a function of r at several moments. We consider z12 progenitor, and set $\lambda = 80$ and $\beta = 5000$. The chosen parameters and the progenitor model correspond to the channel "$\epsilon = -1$: CC$-\varphi$NS".

adopted in this Chapter, the scalar hair of an equilibrium is weaker with increasing β when λ is fixed [538]. The hyperbolicity will be preserved throughout the dynamical formation of the equilibrium for small enough β therefore.

Although the simulation results will be detailed below, here we make an early advantage of the result of the channel "$\epsilon = -1$: CC$-\varphi$NS" (defined in Fig. 10.3, and the simulation result is plotted in Fig. 10.4 below), we show in Fig. 10.1 the discriminant of the characteristic equation as a function of r for $\lambda = 80$ and $\beta = 5000$ at several moments. The numerical evolution of the model crashes at $\sim$38.06 ms due to the violation of hyperbolicity at $\sim$1.51 km, which indicates the onset of the ill-posedness of the evolutionary equations.

10.3 Possible core-collapse scenarios

As initial data for the scalar field, we consider a Gaussian pulse with a mean of 200 km, minute amplitude of 10^{-10}, and standard deviation of 100 km, while we note that the results are independent of the explicit form of the initial data.

Depending on the progenitors, the coupling constants β and λ, and the sign of ϵ, the final outcome of the core collapse and the path to reach it can vary significantly. Fig. 10.3 represents all possible outcomes, which are divided into two major classes: $\epsilon = 1$ and $\epsilon = -1$. While in the former case ($\epsilon = 1$), both NSs and BHs can scalarize, in the latter case ($\epsilon = -1$) scalarization is not possible for static BHs and only NSs can develop nontrivial scalar field [91, 106, 538]. In addition, scalar field can develop during the formation of either the protoneutron star (PNS) or the BH. For $\epsilon = -1$, scalarization can appear only temporarily at the PNS stage. Let us note that if a relatively fast rotating BH is formed after the core

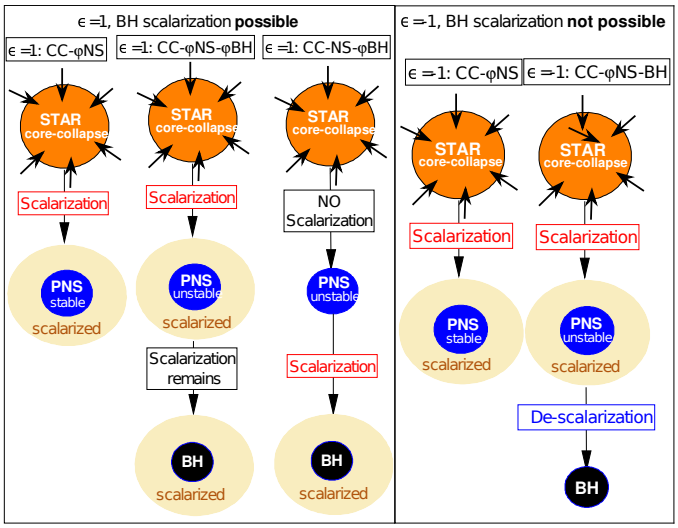

Figure 10.2: Possible outcomes of stellar core collapse in SGB gravity.

collapse, it might be possible to have another scenarios for $\epsilon = -1$ because of the spin-induced scalarization [92, 539, 540, 543, 544]; however, production of a rapidly rotating protoneutron star after a core collapse seems to be a rare event [551, 552].

We set λ and β to appropriate values for the aforementioned scenarios to be realized. The critical central energy density $\rho_{\rm bifurc}$, above which scalarization is possible, is controlled by λ, while β is responsible for the "degree" of scalarization [538]. In general, larger β leads to weaker scalar fields (for a fixed λ).

10.3.1 Progenitors

For the progenitors of stellar core collapse, we use some models provided in Woosley & Heger's catalog [531]. The simulated results are qualitatively the same. In particular, for the remnant with the central density larger than the λ-dependent $\rho_{\rm bifurc}$, scalarization is observed, whose degree then depends on β. Without loss of generality, here, we present the simulations with two progenitors $z12$ and $z40$, having primordial metallicity, that have also been investigated in scalar-tensor theory [90, 435, 441] and are good for comparison.

The model $z12$ has the zero-age-main-sequence (ZAMS) mass of $M = 12M_\odot$ and collapses to a stable PNS. The steep density gradient outside its iron core results in a low accretion rate after bounce. On the other hand, the model $z40$, more massive with $M = 40M_\odot$, evolves into a short-lived PNS which then collapses to a BH as its shallow density leads to high accretion rate after bounce. Simulations adopting an approximation of deleptonization show the index for the softer, cold piece of EOS to be $\Gamma_1 \sim 1.3$ [534], while $\Gamma_2 = 2.5 - 3$ is found to be approximants for some realisitc finite-temperature EOS [535], e.g., Shen [553] and Lattimer and Swesty [554] EOS, for the stiffer, cold component. The thermal description of a mixture of relativistic and non-relativistic gas can be translated to $4/3 < \Gamma_{\rm th} < 5/3$. As in Chap. 9,

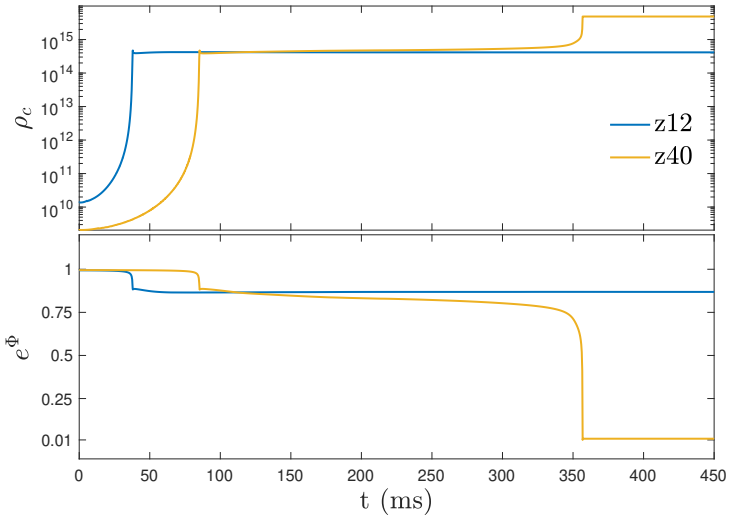

Figure 10.3: Central densities (top panel) and central values of redshift (bottom panel) of supernova progenitors $z12$ (blue line) and $z40$ (yellow line) [531] as functions of time in GR. The formation of a black hole is numerically defined to form as central redshift $e^{\Phi} < 0.01$.

the values of $\Gamma_1 = 1.3$, $\Gamma_2 = 2.5$, and $\Gamma_{\rm th} = 1.35$ have been taken as canonical following, e.g., [90, 435, 441, 442, 458]. We note that our simulations show that different combinations of parameters, each falling in the aforementioned range, does not phenomenologically alter the scalar field dynamics. The evolution of the progenitors' central density and redshift in GR is shown in Fig. 10.3. The evolution will remain qualitatively and quantitatively similar for weak to moderate scalar fields. A significant change is expected for strong scalar fields, but they might lead to loss of hyperbolicity and deserve special attention (see below).

10.3.2 Core collapse to a scalarized neutron star

For the model $z12$, the remnant of the collapse is PNS, which may be imbued with scalar field for both $\epsilon = 1$ and $\epsilon = -1$. However, the profiles of the scalar hair differ considerably from each other. We first show the case with $\epsilon = -1$ in fig. 10.4, where a spontaneous scalarization occurs upon the formation of the PNS remnant. We see that the PNS forms at ~ 38 ms resulting in a rapid development of a scalar field. Afterward, the hot mantle ranging from $\sim 10 - 20$ km still accretes matter onto the remnant as illustrated by the velocity profile; the extent to which the scalar field is excited is enhanced with increasing compactness [the third from top panel of Fig. 10.4]. Clearly, the scalarization first develops in the immediate vicinity of the remnant, and then, it propagates to infinity as the profile of φ settles to a quasiequilibrium one. The spontaneous appearance of $r\varphi$ at the associated retarded time indicates that the scalar wave propagates at the speed of light in SGB. We have checked $r\varphi$ at three different places, viz. 500 km, 5000 km, and 50 000 km, to confirm it does saturate.

As it is well known, in certain regions of the parameter space, the SGB field equations lose

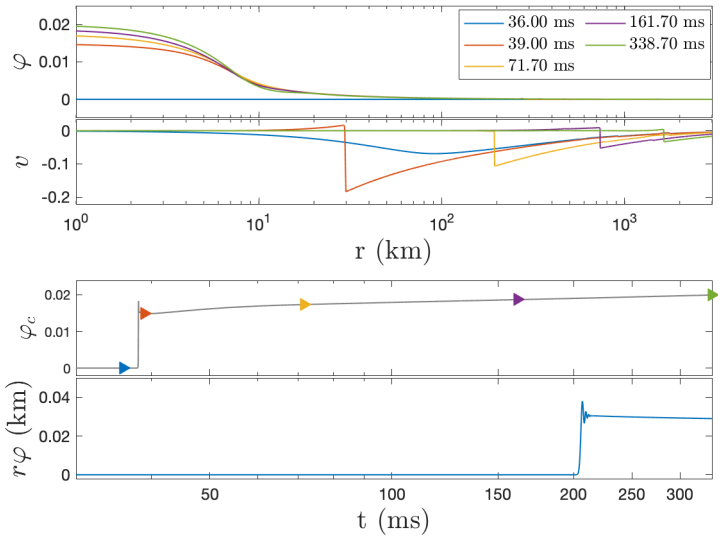

Figure 10.4: (scenario "$\epsilon = -1$: CC-φNS") Temporal snapshots of scalar field φ and fluid velocity v as functions of the distance from the core $r = 0$ for the $z12$ progenitor are plotted in the upper panel. In the lower panel, the evolution of the central value of the scalar field φ_c and the scalar charge $r\varphi$ taken at a very large distance, 50 000 km, are displayed. Markers in the bottom panels indicate the time of snapshots having the same colors in the corresponding upper panels. We have taken $\epsilon = -1, \lambda = 80$, and $\beta = 7000$.

their hyperbolic character [95, 545, 550]. How to deal with this problem in SGB theories is still an open question and is beyond the scope of the present Chapter. In our simulation, we observed that, if we fixed λ, there is a threshold β below which the system loses its hyperbolic character (see Sec. 10.2.2). In practice, this effectively limits the strength of the scalar field since larger β leads to weaker scalar field (for fixed λ). The parameter β for the simulations presented in this Chapter is chosen to be close to this threshold β, and the results remain qualitatively similar for larger β. For the presented model, the change of the metric function with respect to GR is relatively small, of the order of 1%, and the total energy of the scalar field reach $\lesssim 1\%$ of the compact object mass. The threshold for loss of hyperbolicity will also depend on the progenitor properties, the employed EOS, and the parameters of the theory. A thorough investigation of this threshold as different parameters of the system are varied will be considered somewhere else.

We then turn to consider the case with $\epsilon = 1$ that leads to the formation of a scalarized protoneutron star for the z12 progenitor in Fig. 10.5. As observed in [538], for the same mass neutron star, the case with $\epsilon = 1$ requires larger λ to scalarized compared to $\epsilon = -1$ and that is why we have chosen to work with $\lambda = 120$. Qualitatively the scalar field evolution has the same characteristic as for the "$\epsilon = 1$: CC-φNS" case. The only major difference is the scalar field profile that is drastically different for positive and negative ϵ. The reason lies in the fact that $\mathcal{R}^2_{\rm GB}$ of the protoneutron star remnant is positive(negative) for $r \gtrsim (\lesssim)$ 7.77 km, implying the source term in the scalar field equation has the minimal value at some point $r < (>)7.77$ km for $\epsilon = -1(+1)$. Naturally, the scalar field will have a maximum where the

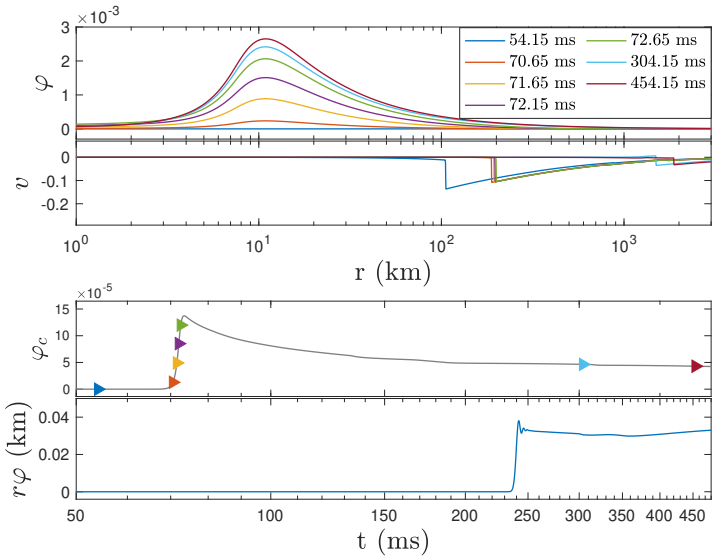

Figure 10.5: (collapse to a scalarized neutron star "$\epsilon = 1$: CC-φNS") Temporal snapshots of scalar field φ and fluid velocity v as functions of the distance from the core $r = 0$ for the z12 progenitor are plotted in the upper panel. In the lower panel the evolution of the central value of the scalar field φ_c and the scalar charge $r\varphi$ taken at a very large distance, 50000 km, are displayed. The time delay between the formation of protoneutron star and the excitation of scalar charge is consistent with the fact that scalar fields propagate with the light speed in scalar-Gauss-Bonnet gravity. Markers in the bottom panels indicate the time of snapshots having the same colors in the corresponding upper panels. We have chosen $\epsilon = 1, \lambda = 100$, and $\beta = 14000$.

source term has a negative minimum that explains the differences in the scalar field profile.

10.3.3 Collapse to a black hole

Now, we turn to study collapses with a middle PNS stage followed by a BH formation due to continuous accretion by exhibiting the evolution of $z40$. As plotted in Fig. 10.3, the PNS forms at ~ 85 ms and lives for ~ 300 ms. Afterward, the BH remnant appears at ~ 360 ms, and matter and scalar field cease evolving inside the event horizon once it has formed. The parameter β is chosen to be close to the threshold where loss of hyperbolicity is observed (for the corresponding λ).

Two channels are possible in collapses leading to a BH for $\epsilon = 1$, namely, scalarization is absent or present during the middle PNS stage of the collapse (see Fig. 10.3). In Figs. 10.6 the channel "$\epsilon = 1$: CC-NS-φBH" is presented. Temporal snapshots of scalar field φ as a function of the distance from the center $r = 0$ are plotted in the upper panel. In the lower panel, the evolution of the central value of the scalar field φ_c and the scalar charge $r\varphi$ are displayed. The evolution of φ_c is just symbolic since it is uncertain how the fields (ρ, p, φ, ...) evolve inside the event horizon, and we plot φ_c as constant since we freeze the fields interior to the event horizon similar to [435, 456].

Scalarization is only possible for NSs for $\epsilon = -1$. Thus, a scalarized PNS will undergo a

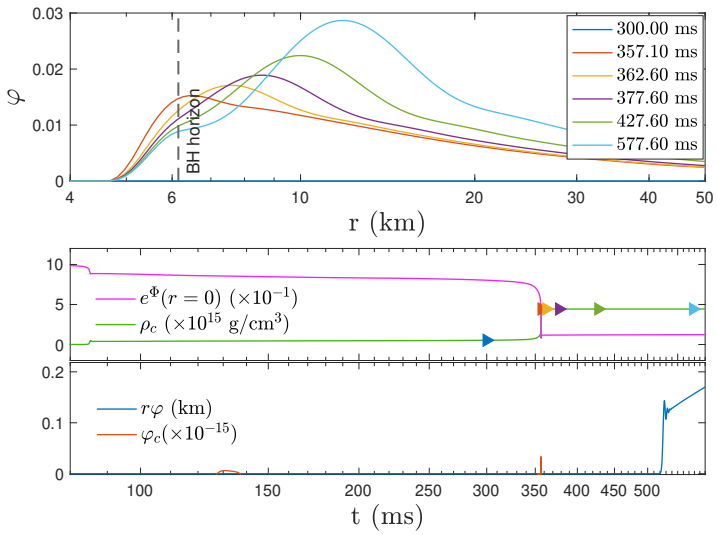

Figure 10.6: (scenario "$\epsilon = 1$: CC-NS-φBH") Temporal snapshots of scalar field φ as a function of the distance from the core $r = 0$ is potted for the $z40$ progenitor in the upper panel. In the lower group of panels, central value of scalar field φ_c and the scalar charge $r\varphi$ are displayed as functions of time. The notations are the same as in Fig. 10.4. We have taken $\epsilon = 1$, $\lambda = 30, \beta = 20\ 000$.

descalarizaion before it collapses into a BH. This scenario, "$\epsilon = -1$: CC-φNS-BH", is depicted in Fig. 10.7. We see that, upon the formation of the final state BH, the excited scalar field is eliminated (blue curve in the bottom panel of Fig. 10.7). During the descalarization, most of the energy stored in the scalar field is swallowed by the BH ($\gtrsim 90\%$), while a small portion of the energy is radiated away (curves in the top panel of Fig. 10.7). The dynamical result proves that static BHs can not scalarize for $\epsilon < 0$ [93, 106], illustrating how the scalar field fades away in SGB.

The emitted scalar radiation E_s as a function of time is presented in Fig. 10.8. We see that, at late times, E_s varies in the range $10^{48} - 10^{51}$ergs depending on the core collapse model. Given that the typical energy emitted through tensorial GWs during core collapse is $10^{46} - 10^{47}$ergs [555, 556], the scalar waves produced during the (de)scalarization of a compact object offer a much more efficient channel of energy loss. In the considered SGB gravity, though, the so-called breathing modes, that are potentially detectable, do not exist. If a more general form of sGB gravity is considered such breathing modes can be easily present that would allow us to set constraints on the corresponding SGB theory. Moreover, if one considers the problem beyond the spherical symmetry approximation, other observational manifestations of the scalarization can be expected. This is a very complicated task, though, that has not yet been solved in any alternative theory of gravity.

The second core-collapse scenario we will consider here is "$\epsilon = 1$: CC-φNS-φBH", where a collapse to a scalarized black hole, through a scalarized protoneutron stars, is observed. This case is depicted in Fig. 10.9. We find that, in accordance with [538], the channel for which

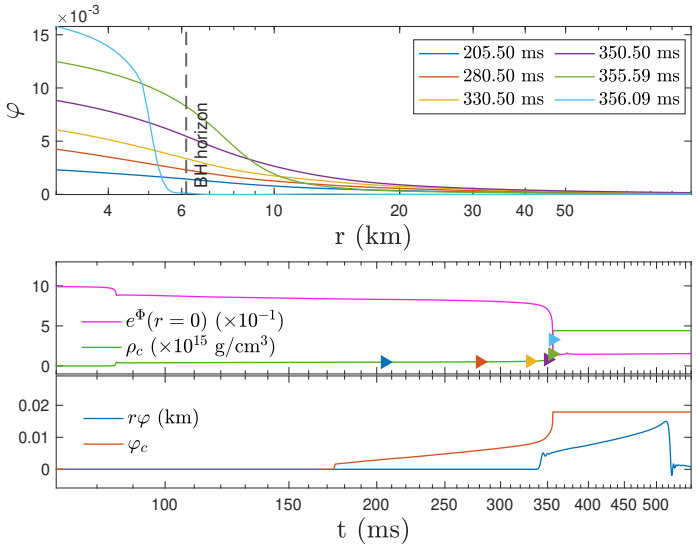

Figure 10.7: (scenario "$\epsilon = -1$: CC-φNS-BH") The same as Fig. 10.6 but for $\epsilon = -1$, $\lambda = 40, \beta = 25\ 000$. Scalarization of protoneutron star reveals (light red and yellow curves in the upper panel); nonetheless, once the black hole is formed, the scalar field condensates into the event horizon. Descalarization is apparent as shown by the disappearance of the scalar charge after a period of scalarized protoneutron star stage (blue line in the bottom panel).

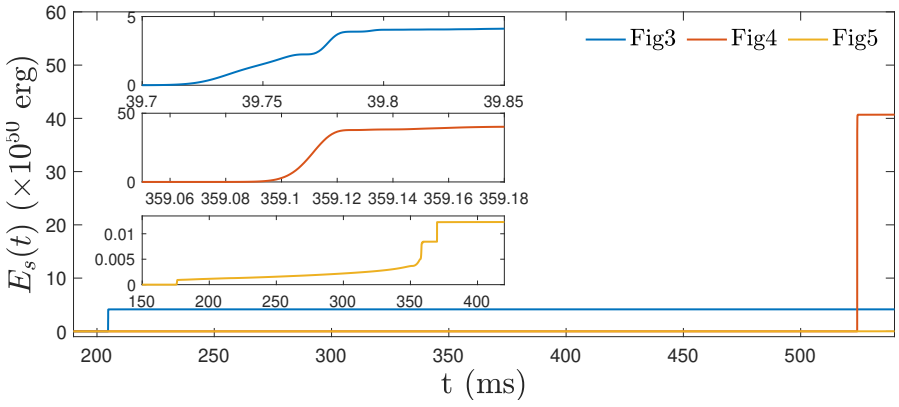

Figure 10.8: The scalar radiation emitted during core collapse for the cases presented in Figs. 10.4, 10.6, and 10.7. $E_s(t)$ is practically independent of r for large distances, and in the figure, it is extracted at the same point as the scalar charge, i.e., at 50 000 km. The insets represent a magnification around the most interesting regions for each case.

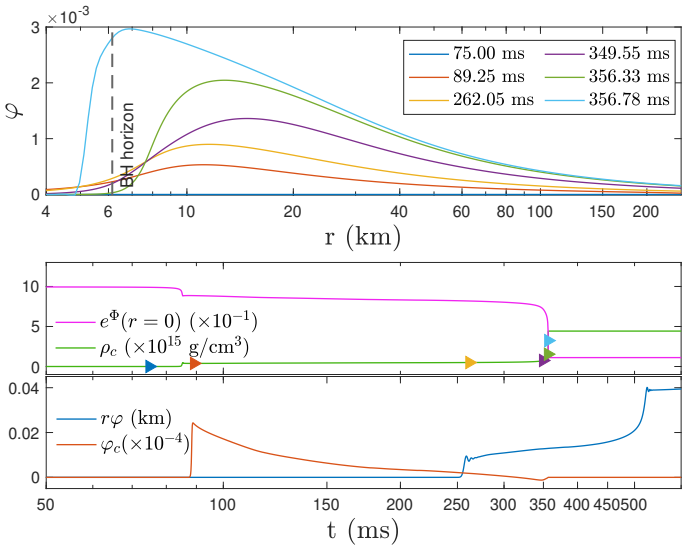

Figure 10.9: (collapse to a scalarized black hole through a scalarized protoneuton star "$\epsilon = 1$: CC-φNS-φBH") Temporal snapshots of scalar field φ as a function of the distance from the core $r = 0$ is potted for the z40 progenitor in the upper panel. In the lower group of panels central value of scalar field φ_c and the scalar charge $r\varphi$ taken at a very large distance, 50000 km, are displayed as functions of time. We have taken $\epsilon = 1$, $\lambda = 120, \beta = 900000$

scalarization is present in the middle state of protoneutron star ("$\epsilon = 1$: CC-φNS-φBH") needs larger λ compared to "$\epsilon = 1$: CC-NS-φBH". The scalarization is clearly visible e.g. in the evolution of the scalar charge where the collapse to an intermediate protoneutron stars produces a nonzero scalar charge. The charge is further enhanced during the black hole formation and remains practically constant afterwards.

10.4 Consistency and convergence tests

In this section we detail the reliance of our numerical results with two-fold reasoning. The equations we utilised to evolve the metric functions Φ and Λ are three of the four extended Einstein's field equation; the solved functions must then obey the remaining one, viz. the $\{\theta\theta\}$-component of the extended Einstein's field equation. Denoting the difference between the right and the left hand sides of the extended Einstein's field equation as $E_{\theta\theta}(r)$, which in the perfect simulation should vanish everywhere, we measure the self-consistency of our code via the L^2 norm of $E_{\theta\theta}$ defined by

$$\mathcal{E} = \frac{\int (E_{\theta\theta})^2 dr}{\text{grid number}}, \tag{10.15}$$

where we divide the usual L^2-norm by the grid number or else the parasitical truncate error at each grid will pile up.

In Fig. 10.10, we plot $\mathcal{E}$ as a function of time for the case "$\epsilon = -1$: CC-φNS" discussed in

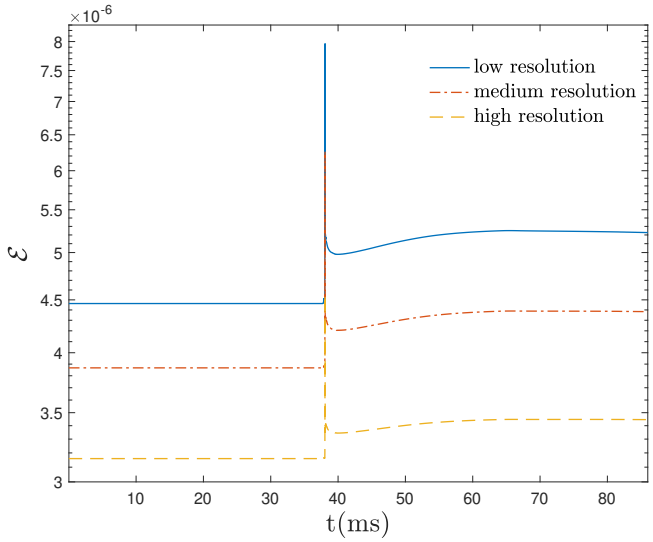

Figure 10.10: The L^2 norm of $E_{\theta\theta}$ [Eq. (10.15)] as a function of time for the case "$\epsilon = -1$: CC-φNS" discussed in the main test of the Chapter with three resolutions.

the main test of the Chapter with three resolutions; in particular, the grid sizes are chosen to have the ratio of $2 : 1.5 : 1$ with the coarsest grid chosen to be the same as the one used in our simulations. We see that the residuals of the $\{\theta\theta\}$-component of the extended Einstein equations are $\lesssim 10^{-5}$ and have a sharp peak around the time when scalarization happens. In addition, the heights of this peak and the overall value of $\mathcal{E}$ decreases with increasing grid resolution.

The convergence of the code can be quantified by comparing a certain quantity q yet computed with different resolutions; stipulating we solve q with three resolutions characterised by the bin sizes of the grid points $\Delta r_{\rm low}$, $\Delta r_{\rm medi}$, and $\Delta r_{\rm high}$, the convergence order n for q is defined through

$$\frac{q_{\rm low} - q_{\rm medi}}{q_{\rm medi} - q_{\rm high}} = \frac{(\Delta r_{\rm low})^n - (\Delta r_{\rm medi})^n}{(\Delta r_{\rm medi})^n - (\Delta r_{\rm high})^n}, \tag{10.16}$$

where $q_{\rm low}$, $q_{\rm medi}$, and $q_{\rm high}$ are the particular quantity q solved with low, medium, and high resolutions. We note that Eq. (10.16) is designed for uniform grid simulation.

The convergence order of the `GR1D` code is mainly influenced by the fluid dynamics. The reason is that as shock forms and propagates outwards the convergence deteriorates from second to first order that is characteristic feature of high-resolution shock-capturing schemes. This ultimately influences the scalar field as well since its evolution is coupled to the fluid. Thus, the convergence order will vary in time as well as location within the computational domain. For an extensive discussion and quantification of these effects we refer the reader to [435]. In order to test convergence of our modification of the `GR1D` code we followed [435] and we collapsed a polytropic star with a low central density, thus large radius, instead of

z12 and z14. The reason falls in that Eq. (10.16) is designed for uniform grid simulation, while we adopt for the latter progenitors a grid whose bin size is uniform inside $r = 40$ km but then starts exponentially increasing until reaching to the outer boundary ($r = 9 \times 10^5$ km). Within this setup we managed to confirm that the convergence is of the same order as for the original `GR1D` code [435]. Generally speaking, we see that the convergence order of our code is of second order prior to the formation of sharp wave due to the bounce, which also triggers the scalarization, while it becomes first order afterwards.

10.5 Discussion

In this Chapter, we presented the first numerical fully nonlinear simulations of the spherically symmetric stellar core collapse to a BH or a NS in SGB theories allowing for a spontaneous scalarization. We showed that, in this process, scalarized BHs and NSs can be produced starting with a nonscalarized progenitor star. In this way, we also demonstrated that the stellar gravitational collapse is the natural physical mechanism for the formation of isolated scalarized compact objects in SGB gravity. There is a variety of collapse scenarios that can be realized with different progenitors, and the SGB parameters that will have different astrophysical manifestations. Thus, with the improvement of the sensitivities of the observations, it might be possible to put strong constraints on the SGB theory. In order to quantify the observational manifestations, though, one has to examine, in much greater detail, the parameters space consisting of the theory parameters, the possible progenitors, and realistic EOS. This is a study underway.

Considering the full system of coupled fluid, metric, and scalar field evolution also allows us to observe the loss of hyperbolicity of the system that occurs for certain ranges of parameters. The system of differential equations turns to a mixed type in the vicinity of the region where shocks appear as the core collapse proceeds. The interpretation of such loss of hyperbolicity is a very involved, open problem in SGB gravity that has not received a proper treatment or interpretation until now. Still, the region where the system behaves well and the Cauchy problem is well defined is large enough, while the scalar field is bounded to relatively low values.

For the considered SGB theories, in contrast to some standard scalar-tensor theories, for example, the spherically symmetric scalar field dynamics does not lead to the emission of gravitational waves (the so-called breathing modes are absent). Scalar waves will be present, though, and they constitute an additional channel for dissipation of energy and angular momentum that can leave an imprint on the emitted gravitational waves. The collapsing scenarios we considered lead to relatively weak scalar fields, but on the other hand, the scalar radiation is a quite efficient channel of energy dissipation. For the models we considered in the present Chapter, the energy dissipation of the scalar waves can be much stronger compared

with the expected gravitational wave signal in case of nonspherical core collapse [555, 556] that can potentially lead to constraints on Gauss-Bonnet theories.

Appendix A

Tidally-neutral g-modes

In binaries, QNMs will be driven by the exertion of tidal forces from the companion. The resulting motions generate excess in gravitational energy by absorbing and localising the orbital energy into the star. The "efficiency" of the energy-soaking process for a specific mode is appraised by the overlap between the associated motion ξ_{lnm} and the gravitational potential Φ^T of the companion [262], where $\{nlm\}$ are conventional quantum numbers for harmonic oscillators. Considering solely the quadrupolar component ($l = 2$) of the potential due to its predominant contribution to tidal effects (see, e.g., the discussion in the Appendix A.2 of [21]), tidal coupling strength Q_{nl} of QNMs to the (leading-order) external tidal field is given by Eq. (4.43), which is independent of the winding number m. We recall that only $l = 2$ QNMs are relevant to the leading-order tidal phenomena due to the orthogonality between spherical harmonic functions Y_{lm} (see Chap. 4 for details).

Although only the absolute value of the tidal coupling Q_{nl} matters in the context of energy absorption, we find that the $n = 1, l = 2$ g-mode (quadrupolar g_1-mode) may have positive and negative values of Q_{12}, implying that there are some g_1-modes with $Q_{12} = 0$

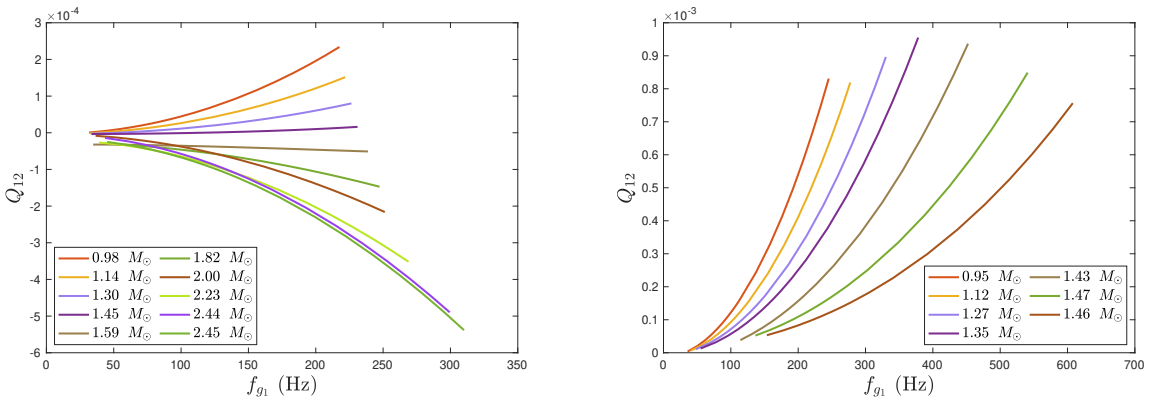

Figure A.1: Q_{nl} [Eq. (4.43)] as a function of g_1-mode frequency for several models of EOS MPA1 (left) and PCL2 (right). The mass of the star is held fixed for each curve shown here, which is drawn by increasing the stratification index δ.

from continuity (Rolle's theorem). For instance, we plot the tidal coupling of g_1-modes for several masses with EOS MPA1 in the left panel of Fig. A.1, where each curve shows the g_1-modes with different stratification. We see that g_1-modes in the star with $1.59M_\odot$ have nearly vanishing Q_{12}, and may thus be fitting called 'tidally-neutral'. By contrast, we find that Q_{12} is always positive for the EOS belonging to *Group III* (see, e.g., EOS PCL2 in the right panel of Fig. A.1) except for EOS H7 and GNH3, whose models with mass close to the maximum have $Q_{12} \simeq 0$.

Appendix B

Reversibility of the Einstein frame in the Scalar-Tensor Theories

In a specific model, the condition (9.5) would manifest itself as a critical value φ_c. We will show that the scalar field can be nowhere equal to φ_c as it cannot be a solution to the scalar equation in the Jordan frame. Hence, the solution space of the scalar field in the Einstein frame is separated by φ_c into two pieces. Here we consider the potential

$$V(\varphi) = m^2\varphi^2, \tag{B.1}$$

in the Einstein frame .

B.0.1 General Jordan Frame Action

In the action (9.1), we have to specify the coupling function $F = A^{-2}$, which is chosen so that

$$\ln F = -2\alpha_0\varphi - \beta_0\varphi^2 \tag{B.2}$$

in this Appendix. The parabola of (B.2) is shown as Fig. B.1. From the above relation, we obtain

$$\varphi = \pm\frac{\sqrt{\alpha_0^2 - \beta_0 \ln F}}{\beta_0} \tag{B.3}$$

with one relation $\varphi(\phi)$ for each sign. Therefore, a given model in the Einstein frame may correspond to two potentials $U(\phi)$, thus two models in the Jordan frame.

We consider two situations: (a) φ is *not* always positive and (b) φ is always positive. For (a), like all the solutions in [90], oscillating across $\varphi = 0$, we should choose the "+" sign in (B.3), which indicates $\varphi < \varphi_c$.[1] Therefore, once the sign in (B.3) is determined, the other

[1] If we choose the "−" sign in (B.3), φ must be positive and greater than φ_c due to $\beta_0 < 0$.

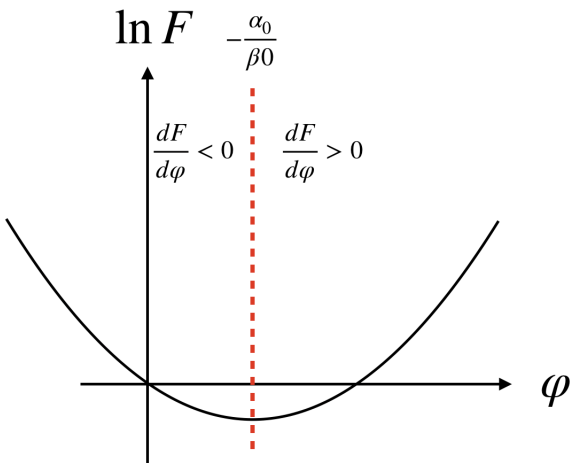

Figure B.1: The parabola reveals the relation between $\ln F$ and φ, where the dashed line represents the forbidden value φ_c for φ.

branch of the solution space represented by $\varphi > \varphi_c$ should not realise. In this sense, φ_c can be viewed as a ceiling of φ, which is independent of the potential. Any φ exceeding this ceiling in certain region is not viable as, strictly speaking, it is not a solution to the Jordan-frame scalar equation. With the restriction $\varphi < \varphi_c$, we can see from Fig. B.1 that the inequality

$$F_\phi \frac{d\phi}{d\varphi} < 0 \tag{B.4}$$

holds, while no more can be said about the sign of $d\phi/d\varphi$ due to the ambiguity in the sign of F_ϕ. In particular, the positivity of F_ϕ implies that the sign of (9.2) should be minus and vice versa. Therefore, two Jordan-frame models depending on the "±" signs of F_ϕ remain possible even if the condition $\varphi < \varphi_c$ is imposed. The sign of F_ϕ can only be acquired once the specific form of the $F(\phi)$ is given however.

For (b), there are two cases. The first one corresponds to the "−" sign in (B.3) with $\varphi > \varphi_c$. Similar to the argument above, there exists two models in the Jordan frame related to the sign of F_ϕ. In this case with the equivalence of $\alpha < 0$, we have the relation

$$F_\phi \frac{d\phi}{d\varphi} > 0. \tag{B.5}$$

By contrast, the case for the "+" sign requires $0 < \varphi < \varphi_c$. The solution space is bounded, which is the most restrictive one among the cases.

By differentiating both sides of (B.3) with respect to ϕ, one gets an additional equation

$$\frac{d\varphi}{d\phi} = \frac{\mp F_\phi}{2F\sqrt{\alpha_0^2 - \beta_0 \ln F}}, \tag{B.6}$$

which suggests that F_ϕ determines the sign of $d\varphi/d\phi$ since $F > 0$. We note that the sign in

(B.6) is opposite to the one chosen in (B.3). The requirement of $\ln F > \alpha_0^2/\beta_0$ to prevent φ from being imaginary is fulfilled because (B.2) has minimum α_0^2/β_0 at the forbidden point φ_c, which can easily be checked from Fig. B.1. We see that the discussions of the sign problem of F_ϕ above are consistent with the sign in (B.6) .

B.0.2 Brans-Dicke-Bergmann-Wagoner theory

Another example is the Brans-Dicke-Bergmann-Wagoner (BDBW) theory with $F = \phi$ in the action (9.1), given by

$$S = \int d^4x \frac{\sqrt{-g}}{16\pi G}\left(\phi R - \frac{\omega(\phi)}{\phi} g^{\mu\nu}\partial_\mu\phi\partial_\nu\phi - U(\phi)\right) + S_m[\psi_m, g^{\mu\nu}]. \tag{B.7}$$

It can be found that the sign of $d\varphi/d\phi$ can be completely determined through since the sign of $F_\phi = 1$ is unique. In this specific case, we have

$$\phi = A^{-2} > 0, \tag{B.8}$$

since $F(\phi) = A^{-2}$ is simply ϕ, leading to

$$\ln\phi = -2\alpha_0\varphi - \beta_0\varphi^2, \tag{B.9}$$

and

$$\frac{d\ln A}{d\varphi} = -\frac{1}{2\phi}\frac{d\phi}{d\varphi}. \tag{B.10}$$

From the inequality (B.8), we have

$$\frac{d\ln A}{d\varphi}\frac{d\varphi}{d\phi} = -\frac{1}{2\phi} < 0, \tag{B.11}$$

where $d\varphi/d\phi$ can be either positive or negative as stated above. The valid value of φ can determine the sign in (9.5) in contrast to the case in Sec. B.0.1. In particular, for $\varphi > \varphi_c$, the sign of the redefinition (9.2) is positive (cf. Fig. B.1), namely

$$\frac{d\varphi}{d\phi} = \frac{\sqrt{3+2\omega}}{2\phi}, \tag{B.12}$$

thus requiring $d\ln A/d\varphi$ to be negative. Similarly, the redefinition of the scalar fields leads to

$$\frac{d\varphi}{d\phi} = -\frac{\sqrt{3+2\omega}}{2\phi} \tag{B.13}$$

for $\varphi < \varphi_c$.

In the limit of the BD theory, ω in (B.7) is constant, denoted as $\omega(\phi) = \omega_{\rm BD}$. Consequently, equation (B.10) reads

$$\frac{d\ln A}{d\varphi} = \alpha_0 + \beta_0\varphi = \mp\frac{1}{\sqrt{3+2\omega_{\rm BD}}} \tag{B.14}$$

where the minus (plus) case corresponds to the branch of $\varphi > \varphi_c$ ($\varphi < \varphi_c$). Since the right-hand side of (B.14) is constant, we have two possibilities: (i) $\beta_0 = 0$, or (ii) φ is almost constant. Due to the negativity of considered β_0, we specify ourselves to the second scenario.

It is interesting to note that $\omega_{\rm BD} \to \infty$ leads to the critical value $\varphi = \varphi_c$ since $d\ln A/d\varphi = 0$. Even though this case is consistent with those in the literature and in turn reproduces the results in GR in the sense that all its predictions become indistinguishable from GR in the *Jordan frame* [470], it cannot be transformed to the *Einstein frame* due to the violation of the derivative constraints and α-constraint. Therefore, the case of the infinite $\omega_{\rm BD}$ is improper to be discussed in the *Einstein frame*, which shows the *inequivalence* between the two frames.

We again note that the critical value of φ_c is so generic that the results of all the simulations should obey the criterion $\varphi \neq \varphi_c$. For instance, it has been concentrated on the BDBW theory to investigate the dynamical scalarization of the neutron star binaries in ST in [557]. The critical value for the scalar field in their setting is $\varphi_c = 0$, and the results therein do all satisfy this criterion, i.e., no crossing the line of $\varphi = 0$.

The potential V in the Einstein frame is connected to the Jordan-frame one U through $U = 4VA^{-4} = 4m^2\varphi^2\phi^2$, which thus can be expressed as

$$U(\phi) = 4m^2\beta_0^{-2}\left(2\alpha_0^2 - \beta_0\ln\phi \mp 2\alpha_0\sqrt{\alpha_0^2 - \beta_0\ln\phi}\right)\phi^2, \tag{B.15}$$

or

$$U(\varphi) = 4m^2\varphi^2\exp\left(-4\alpha_0\varphi - 2\beta_0\varphi^2\right), \tag{B.16}$$

by substituting in Eq. (B.9)

$$\varphi = \varphi_c \pm \frac{\sqrt{\alpha_0^2 - \beta_0\ln\phi}}{\beta_0}. \tag{B.17}$$

The Jordan-frame potential should however be unique, and either '+' or '-' can represent the theory. Determination on the sign depends on the branches of the scalar field in the Einstein frame, i.e., the sign chosen in (B.17). For the case of the action (9.1) in Sec. B.0.1, we cannot consider only the positive $d\varphi/d\phi$ (cf. Eq. (9.2)) therefore, which effectively chooses one from the two candidates without a clear reason.

In addition, the undetermined signs in (B.17) can be eliminated by considering the function of $(\varphi - \varphi_c)^2$. Hence, the solution space has an $\mathbb{Z}_2$ symmetry with respect to φ_c. In other

words, the model in the Jordan frame, which is responsible for the given model in the Einstein frame, remains the same under the transformation $\varphi - \varphi_c \longleftrightarrow -(\varphi - \varphi_c)$. We can shift φ to $\bar{\varphi} = \varphi - \varphi_c$, resulting in that the existence of the $\mathbb{Z}_2$ symmetry is characterized by an even potential $U(\bar{\varphi})$ of $\bar{\varphi}$. The potential (B.16), which can be rewritten as

$$U(\bar{\varphi}) = 4m^2(\bar{\varphi} + \varphi_c)^2 \exp\Big[-2\beta_0\big(\bar{\varphi}^2 - \varphi_c^2\big)\Big], \tag{B.18}$$

is not a even function of $\bar{\varphi}$ apparently. As a result, the one to one correspondence between models in both frames holds strictly. In general, it is hard to have the same symmetry of $\mathbb{Z}_2$ at φ_c for $U(\varphi)$. Particularly, the direct effect of the $\mathbb{Z}_2$ symmetry at φ_c for the potential is that the model in the Einstein frame is associated with a unique model in the Jordan frame.

Appendix C

Gravitational-wave bursts from accretion-induced descalarization in massless scalar-tensor theory

C.1 Numerical setup

Adopting the spherically-symmetric spacetime, perfect fluid, and the piecewise polytropic approximation of EOS APR4 as done in Chap. 8 only with the scalar mass now vanishing, i.e., $m_\varphi = 0$ eV. In Fig. C.1, we plot equilibria with (blue curve) and without (red curve) scalar hair for $\alpha_0 = 10^{-3}$, $\beta_0 = -5$, and $m_\varphi = 10^{-14}$ eV. The parameters are chosen in a way so that that the phase transition to a non-scalarize neutron star is possible, i.e., the maximal mass for the scalarized branch ($2.086 M_\odot$) is less than that for the GR branch ($2.168 M_\odot$).

Here we apply slightly different accretions from those utilised in Chap. 8, and are defined as:

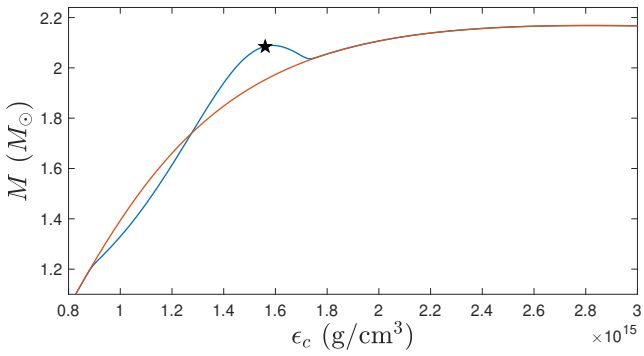

Figure C.1: Scalarized (blue) and unscalarized (red; also present in GR) hydrostatic equilibria for $\alpha_0 = 10^{-3}$, and $\beta_0 = -5$ for the APR4 EOS. The maximum mass of the GR star is $2.168 M_\odot$, while the scalarized configuration can only support masses up to $2.086 M_\odot$. The black star represents the initial state for the simulation.

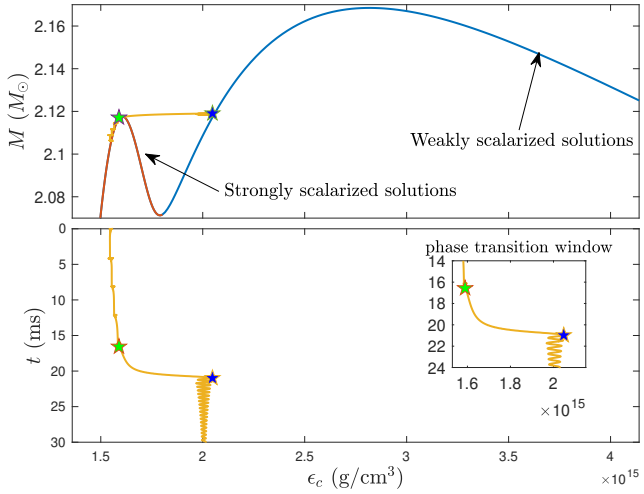

Figure C.2: Evolutionary track of a near-critical scalarized star under Type I accretion: gravitational mass M as a function of central energy density ϵ (top panel), and the temporal dependence of the central energy density (bottom panel). The green and blue stars mark the onset and the termination of descalarization, respectively.

- *Type I* — Superposing a Gaussian bulk at the outermost layer of the star every 4 ms, which is centred at $0.9R_\star$ with width of 1 km, and halts when a total (baryon) mass of $0.01M_\odot$ has been added (after 12.03 ms). Here $R_\star$ is the radius of the star. In this case, the averaged accretion rate is $\dot{M}_a \simeq 0.83M_\odot \mathrm{s}^{-1}$, and the descalarization lasts ~ 2.75 ms.

- *Type II* — Introducing a Gaussian bulk out of but close to the surface of the neutron star every 4 ms, which is centred at $1.2R_\star$ with width of 1 km, and terminates when a total (baryon) mass of $0.01M_\odot$ has been added (after 12.01 ms). We find again $\dot{M}_a \simeq 0.83M_\odot \mathrm{s}^{-1}$, but the descalarization lasts ~ 3.72 ms.

The accretion rates of both types are marginally slower than the numerical result of $\lesssim 1M_\odot \mathrm{s}^{-1}$ over the first few ms of merger simulations (cf. Fig. 7 of [177]).

In the massless theory, where the dispersion driven by m_φ is turned off, $2\alpha_0 D/L$ actually represents the strain of the scalar-induced GW, which can be estimated by the relation

$$\Delta h \approx 4.8 \times 10^{-22} \left(\frac{\alpha_0}{10^{-3}}\right) \left(\frac{E_{\mathrm{GW}}^{(\mathrm{scalar})}}{10^{-3} M_\odot}\right)^{1/2} \left(\frac{\tau}{5\ \mathrm{ms}}\right)^{1/2} \left(\frac{100\ \mathrm{kpc}}{Y}\right) \tag{C.1}$$

for the distance between the source and the detector Y, the emitted energy $E^{(\mathrm{scalar})}$, and the descalarization timescale τ.

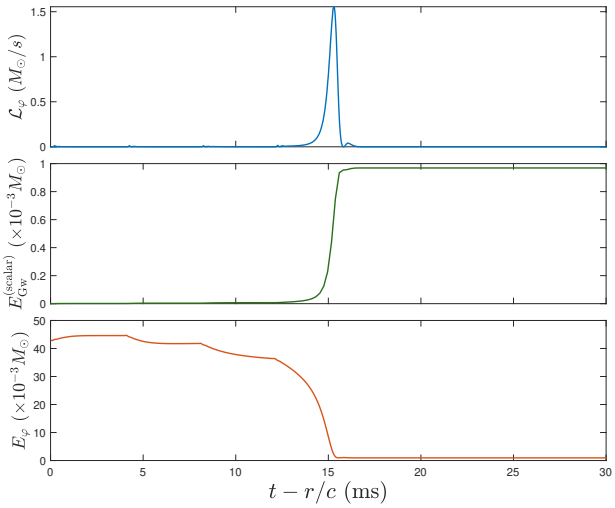

Figure C.3: Evolution of scalar energy under Type I accretion: scalar luminosity [Eq. (8.8)] (top panel), energy emitted via scalar sector [Eq. (8.9)] extracted at $r = 10^4$ km (middle panel), and scalar energy [Eq. (8.8)] integrated from the centre to the outer boundary of the grid, $r_{\rm out}/c = 166.78$ ms (bottom panel), all as functions of retarded time.

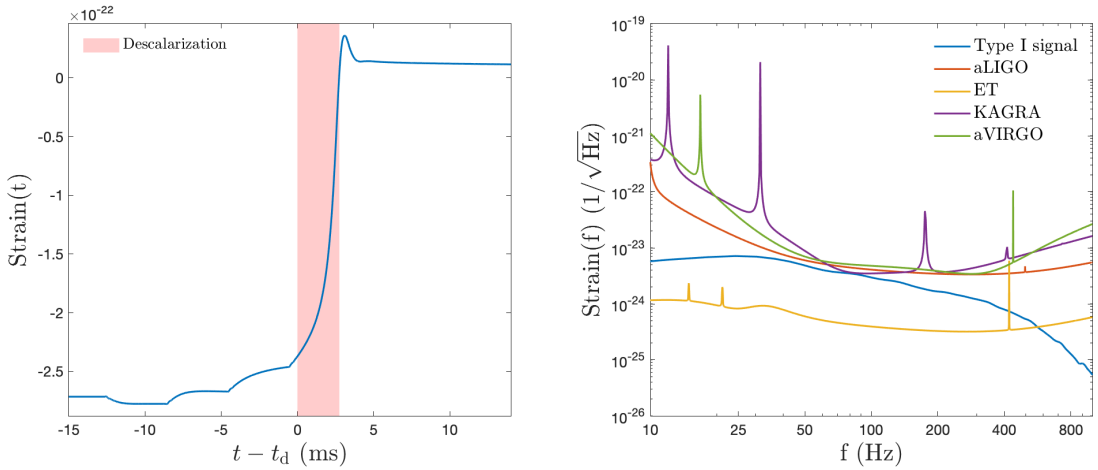

Figure C.4: Strain of the scalar-induced GW mode [Eq. (6.32)] for Type I accretion, extracted at $r = 100$ kpc in the time (left panel) and frequency (right panel) domains. The x-axis of left panel shows the time relative to the onset of descalarization, $t_{\rm d}$.

C.2 Results

In Fig. C.2, we plot the evolutionary track of a particular scalarized model with gravitational mass of $\sim 2.082 M_\odot$ undergoing accretion in the Type I manner. The scalarized star undergoes a phase transition, and heads to the GR branch, on the timescales described above. Due to numerical truncation errors, the code cannot make a complete riddance of the scalar field, thus the final state will not exactly lie on the GR branch. Nonetheless, the amplitude of φ for the debris is $\lesssim 10^{-2}$ times the profile right before the descalarization, and have been checked to be monotonically decreasing with increasing resolution. The onset and offset of the phase transition to the scalar-free state are chosen as the moments when the last bulk has been accreted and when the final state is formed, respectively. After the descalarization, the model oscillates about a certain, stable state as shown in the inset in the bottom panels. The timescale of the scalar-peeling process is found to be $\lesssim 5$ ms.

Fig. C.3 shows the flux of the scalar radiation at $r = 10^4$ km (top panel) and the associated energy loss (middle panel) as functions of time. At this distance, the asymptotic behaviour of the scalar field has already saturated. The difference in the former two quantities from those at $r = 1.5 \times 10^4$ km, for example, is $\sim 10^{-3}$ times the peak values. A drop of the kinetic, scalar energy to zero is observed after the descalarization (bottom panel). The difference between the decrease of E_φ and the emitted energy $E_{\rm GW}^{\rm (scalar)}$ indicates that most of the scalar kinetic energy transforms into gravitational binding energy since the stellar radius shrinks from 11.75 km to 10.65 km between the initial and the final states, while the (gravitational) mass increases by $\approx 0.015 M_\odot$.

The scalar GW strain is plotted in Fig. C.4 in the time (left panel) and frequency (right panel) domains. The rapid increase in the amplitude of the strain results from the descalarization over timescales of ~ 5 ms (shaded area), as described above. In order to avoid spectral leakage and spurious oscillations when processing the time domain strain to get the frequency domain expression, we windowed the temporal signal in Tukey's fashion before fast Fourier transforming (see Sec. 4 of [558] for a discussion). We use the signal of the first 120 ms for the left panel of Fig. C.4, where we see that the scalar-led GW sourced by the accretion-driven descalarization at a distance of 100 kpc may be detectable with several future ground-based apparatus for the particular parameters of the coupling function, though we note that the strain plotted here is for the optimally oriented signal (6.32). With the inclusion of the next generation Einstein Telescope, the signal may be observed even out to several Mpc.

The ratio of the coupling strength of matter to scalar field and metric fields is

$$\left[\frac{d\ln A}{d\varphi}(\varphi_0)\right]^2 = \alpha_0^2 \tag{C.2}$$

when $\varphi_0 = 0$, which regulates the efficiency of the transformation from the energy leakage

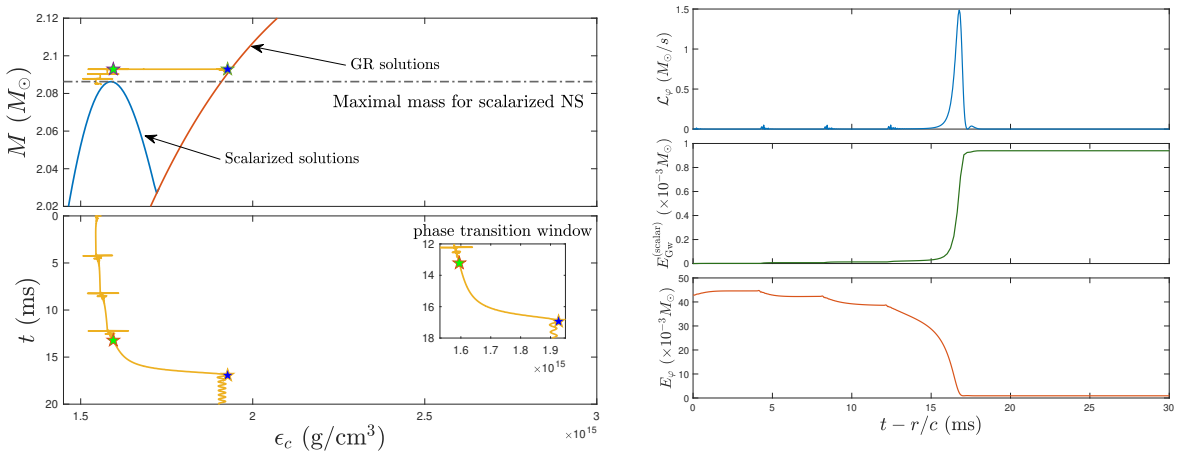

Figure C.5: *left panel*: Evolutionary track of a near-critical scalarized star under Type II accretion. *right panel*: Evolution of scalar energy under Type II accretion.

via the scalar sector to the energy mediated via scalar-GW strain (cf. Sec. 6.2 of [420]). From the definition of scalar energy Eq. (8.8), we can therefore estimate the generated scalar strain by implementing the flux formula (see, e.g., Eq. (17) in [559] for the GR version),

$$\alpha_0^2 \mathcal{L}_\varphi = \frac{(\dot{h}L)^2}{4}, \tag{C.3}$$

along with the assumption that $\mathcal{L}_\varphi \approx E_\varphi/\tau$ and $\dot{h} \approx \Delta h/\tau$, where τ denotes the timescale of descalarization. Matching these formulae we find

$$\Delta h \approx 4.8 \times 10^{-22} \left(\frac{\alpha_0}{10^{-3}}\right) \left(\frac{E_{\rm GW}^{\rm (scalar)}}{10^{-3} M_\odot}\right)^{1/2} \left(\frac{\tau}{5\ {\rm ms}}\right)^{1/2} \left(\frac{100\ {\rm kpc}}{L}\right), \tag{C.4}$$

which gives the same order of magnitude as the numerical results (left panels in Fig. C.4). We note the above two equations do not depend on β_0 since the contribution of β_0 is linear to φ_0, which we assume vanishes.

In Fig. C.5, we plot the evolution track of the star undergoing Type II accretion (top panel), and the scalar emission during the descalarization (bottom panel); the GW strain caused by the emanating scalar field is presented in Fig. C.6. We see that the process is both qualitatively and quantitatively similar to that of Type I accretion, which indicates that for the two distinct types of accretion we get practically the same results thus strengthening the confidence that the process is physical.

In addition, we plot in Fig. C.7 the evolution of the quantity

$$D = r\varphi \tag{C.5}$$

during the accretion-induced descalarization of the star with $M = 2.082 M_\odot$ for two mutations

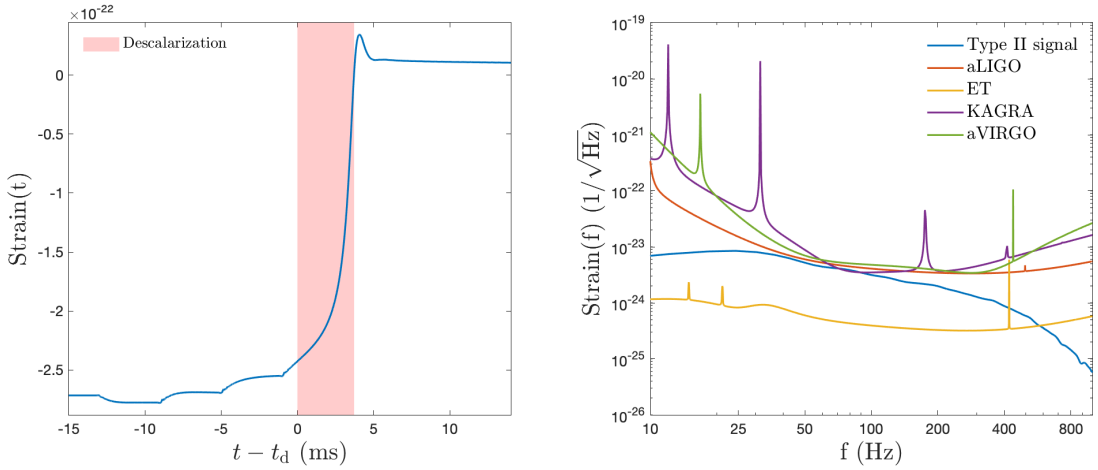

Figure C.6: Strain of the scalar-induced GW mode [Eq. (6.32)] for Type II accretion, extracted at $r = 100$ kpc in the time (left panel) and frequency (right panel) domains.

in the $\beta_0 = -5$ class of STT other than the case considered in Chap. 8, which are defined by $\alpha_0 = 10^{-3}, m_\varphi = 0$ eV, and $\alpha_0 = 0, m_\varphi = 10^{-14}$ eV. We note that the equilibria with the chosen mass $2.086 M_\odot$ for these sets of parameters are similar to that for $\alpha_0 = 10^{-3}, m_\varphi = 10^{-14}$ eV. In particular, the central density ϵ_c and the central value of φ for models with α_0 less than 10^{-3} and m_φ less than 10^{-14} eV have only a variance of $\lesssim 0.3\%$ and $\lesssim 0.9\%$, respectively, when compared to the case of $\alpha_0 = 10^{-3}, m_\varphi = 10^{-14}$ eV. The influences of α_0 and m_φ on the results are also minor in the considered range of parameters, viz. $\alpha_0 \leq 10^{-3}$ and $m_\varphi \leq 10^{-14}$ eV; only the onset of the phase transition is accelerated or delaed slightly. The tail decline in the scalar charge for the massive cases is due to dispersion (blue and yellow lines), which is absent in the massless theory (red line). We also observe that the time of the onset of the descalarizaion is more sensitive to α_0, as can be seen in the inset.

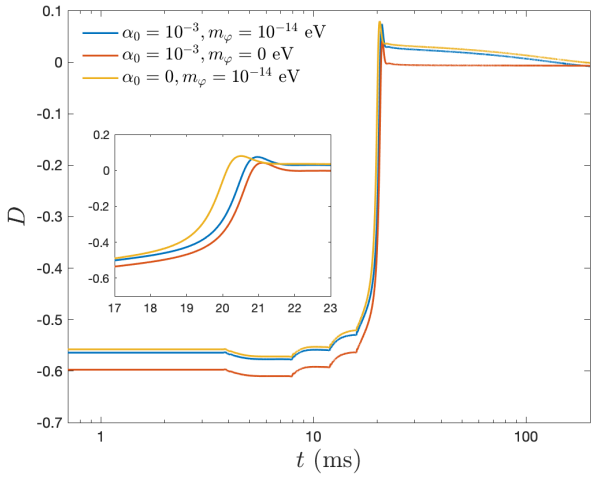

Figure C.7: Evolution of the scalar charge under Type II accretion for three STTs: $\alpha_0 = 10^{-3}, m_\varphi = 10^{-14}$ eV (blue line), $\alpha_0 = 10^{-3}, m_\varphi = 0$ eV (red line), and $\alpha_0 = 0, m_\varphi = 10^{-14}$ eV (yellow line). We have taken $\beta_0 = -5$ for all cases. The inset shows the magnification of the signal around the offset of the descalarization.

Bibliography

[1] Hao-Jui Kuan, Christian J. Krüger, Arthur G. Suvorov, and Kostas D. Kokkotas. Constraining equation of state groups from g-mode asteroseismology. *MNRAS*, April 2022.

[2] Hao-Jui Kuan, Arthur G. Suvorov, and Kostas D. Kokkotas. General-relativistic treatment of tidal g-mode resonances in coalescing binaries of neutron stars - I. Theoretical framework and crust breaking. *Mon. Not. Roy. Astron. Soc.*, 506(2):2985–2998, 2021.

[3] Hao-Jui Kuan, Arthur G. Suvorov, and Kostas D. Kokkotas. General-relativistic treatment of tidal g-mode resonances in coalescing binaries of neutron stars - II. As triggers for precursor flares of short gamma-ray bursts. *Mon. Not. Roy. Astron. Soc.*, 508(2):1732–1744, 2021.

[4] Hao-Jui Kuan and Kostas D. Kokkotas. f -mode imprints on gravitational waves from coalescing binaries involving aligned spinning neutron stars. *Phys. Rev. D*, 106(6):064052, September 2022.

[5] Hao-Jui Kuan, Jasbir Singh, Daniela D. Doneva, Stoytcho S. Yazadjiev, and Kostas D. Kokkotas. Nonlinear evolution and nonuniqueness of scalarized neutron stars. *Phys. Rev. D*, 104(12):124013, 2021.

[6] Hao-Jui Kuan, Arthur G. Suvorov, Daniela D. Doneva, and Stoytcho S. Yazadjiev. Gravitational Waves from Accretion-Induced Descalarization in Massive Scalar-Tensor Theory. *Phys. Rev. Lett.*, 129(12):121104, September 2022.

[7] Chao-Qiang Geng, Hao-Jui Kuan, and Ling-Wei Luo. Viable constraint on scalar field in scalar-tensor theory. *Class. Quant. Grav.*, 37(11):115001, 2020.

[8] Chao-Qiang Geng, Hao-Jui Kuan, and Ling-Wei Luo. Inverse-chirp imprint of gravitational wave signals in scalar tensor theory. *Eur. Phys. J. C*, 80(8):780, 2020.

[9] Da Huang, Chao-Qiang Geng, and Hao-Jui Kuan. Scalar gravitational wave signals from core collapse in massive scalar-tensor gravity with triple-scalar interactions. *Class. Quant. Grav.*, 38(24):245006, 2021.

[10] Hao-Jui Kuan, Daniela D. Doneva, and Stoytcho S. Yazadjiev. Dynamical Formation of Scalarized Black Holes and Neutron Stars through Stellar Core Collapse. *Phys. Rev. Lett.*, 127(16):161103, 2021.

[11] B. P. Abbott et al. Observation of Gravitational Waves from a Binary Black Hole Merger. *Phys. Rev. Lett.*, 116(6):061102, 2016.

[12] B. P. Abbott et al. GW170817: Observation of Gravitational Waves from a Binary Neutron Star Inspiral. *Phys. Rev. Lett.*, 119(16):161101, 2017.

[13] Guillaume Faye, Sylvain Marsat, Luc Blanchet, and Bala R. Iyer. The third and a half post-Newtonian gravitational wave quadrupole mode for quasi-circular inspiralling compact binaries. *Class. Quant. Grav.*, 29:175004, 2012.

[14] Tanguy Marchand, Quentin Henry, François Larrouturou, Sylvain Marsat, Guillaume Faye, and Luc Blanchet. The mass quadrupole moment of compact binary systems at the fourth post-Newtonian order. *Class. Quant. Grav.*, 37(21):215006, 2020.

[15] François Larrouturou, Quentin Henry, Luc Blanchet, and Guillaume Faye. The Quadrupole Moment of Compact Binaries to the Fourth post-Newtonian Order: I. Non-Locality in Time and Infra-Red Divergencies. *arXiv e-prints*, page arXiv:2110.02240, October 2021.

[16] François Larrouturou, Luc Blanchet, Quentin Henry, and Guillaume Faye. The Quadrupole Moment of Compact Binaries to the Fourth post-Newtonian Order: II. Dimensional Regularization and Renormalization. *arXiv e-prints*, page arXiv:2110.02243, October 2021.

[17] Quentin Henry, Guillaume Faye, and Luc Blanchet. Tidal effects in the gravitational-wave phase evolution of compact binary systems to next-to-next-to-leading post-Newtonian order. *Phys. Rev. D*, 102(4):044033, 2020.

[18] Quentin Henry, Guillaume Faye, and Luc Blanchet. Hamiltonian for tidal interactions in compact binary systems to next-to-next-to-leading post-Newtonian order. *Phys. Rev. D*, 102(12):124074, 2020.

[19] Curt Cutler and Eanna E. Flanagan. Gravitational waves from merging compact binaries: How accurately can one extract the binary's parameters from the inspiral wave form? *Phys. Rev. D*, 49:2658–2697, 1994.

[20] Kostas Kokkotas, Andrzej Królak, and George Tsegas. Statistical analysis of the estimators of the parameters of the gravitational-wave signal from a coalescing binary. *Classical and Quantum Gravity*, 11(7):1901–1918, July 1994.

[21] Thibault Damour, Alessandro Nagar, and Loic Villain. Measurability of the tidal polarizability of neutron stars in late-inspiral gravitational-wave signals. *Phys. Rev. D*, 85:123007, 2012.

[22] B. P. Abbott et al. GW170817: Measurements of neutron star radii and equation of state. *Phys. Rev. Lett.*, 121(16):161101, 2018.

[23] B. P. Abbott et al. Gravitational Waves and Gamma-rays from a Binary Neutron Star Merger: GW170817 and GRB 170817A. *Astrophys. J. Lett.*, 848(2):L13, 2017.

[24] B. P. Abbott et al. Multi-messenger Observations of a Binary Neutron Star Merger. *Astrophys. J. Lett.*, 848(2):L12, 2017.

[25] A. S. Pozanenko, M. V. Barkov, P. Yu. Minaev, A. A. Volnova, E. D. Mazaeva, A. S. Moskvitin, M. A. Krugov, V. A. Samodurov, V. M. Loznikov, and M. Lyutikov. GRB 170817A Associated with GW170817: Multi-frequency Observations and Modeling of Prompt Gamma-Ray Emission. *ApJ*, 852(2):L30, January 2018.

[26] M. Soares-Santos et al. The Electromagnetic Counterpart of the Binary Neutron Star Merger LIGO/Virgo GW170817. I. Discovery of the Optical Counterpart Using the Dark Energy Camera. *Astrophys. J. Lett.*, 848(2):L16, 2017.

[27] V. Savchenko et al. INTEGRAL Detection of the First Prompt Gamma-Ray Signal Coincident with the Gravitational-wave Event GW170817. *Astrophys. J. Lett.*, 848(2):L15, 2017.

[28] A. Goldstein et al. An Ordinary Short Gamma-Ray Burst with Extraordinary Implications: Fermi-GBM Detection of GRB 170817A. *Astrophys. J. Lett.*, 848(2):L14, 2017.

[29] D. A. Coulter et al. Swope Supernova Survey 2017a (SSS17a), the Optical Counterpart to a Gravitational Wave Source. *Science*, 358:1556, 2017.

[30] B. P. Abbott et al. GW190425: Observation of a Compact Binary Coalescence with Total Mass $\sim 3.4 M_{\odot}$. *Astrophys. J. Lett.*, 892(1):L3, 2020.

[31] Nicholas Farrow, Xing-Jiang Zhu, and Eric Thrane. The mass distribution of Galactic double neutron stars. *Astrophys. J.*, 876(1):18, 2019.

[32] Jianwei Zhang, Yiyan Yang, Chengmin Zhang, Wuming Yang, Di Li, Shaolan Bi, and Xianfei Zhang. The mass distribution of Galactic double neutron stars: constraints on the gravitational-wave sources like GW170817. *Mon. Not. Roy. Astron. Soc.*, 488(4):5020–5028, 2019.

[33] R. Abbott et al. Observation of Gravitational Waves from Two Neutron Star-Black Hole Coalescences. *Astrophys. J. Lett.*, 915(1):L5, 2021.

[34] E. Troja, S. Rosswog, and N. Gehrels. Precursors of Short Gamma-ray Bursts. *Astrophys. J.*, 723(2):1711–1717, November 2010.

[35] Pavel Minaev and Alexei Pozanenko. Precursors of Short Gamma-Ray Bursts in the SPI-ACS/INTEGRAL Experiment. *Astron. Lett.*, 43(1):1–20, 2017.

[36] Pavel Minaev, Alexei Pozanenko, and Sergei Molkov. Precursors of short gamma-ray bursts detected by the INTEGRAL observatory. *Int. J. Mod. Phys. D*, 27(10):1844013, 2018.

[37] Shu-Qing Zhong, Zi-Gao Dai, Ji-Gui Cheng, Lin Lan, and Hai-Ming Zhang. Precursors in Short Gamma-Ray Bursts as a Possible Probe of Progenitors. *Astrophys. J.*, 884(1):25, October 2019.

[38] Jie-Shuang Wang, Zong-Kai Peng, Jin-Hang Zou, Bin-Bin Zhang, and Bing Zhang. Stringent Search for Precursor Emission in Short GRBs from Fermi/GBM data and Physical Implications. *Astrophys. J. Lett.*, 902(2):L42, 2020.

[39] David Tsang, Jocelyn S. Read, Tanja Hinderer, Anthony L. Piro, and Ruxandra Bondarescu. Resonant Shattering of Neutron Star Crusts. *Phys. Rev. Lett.*, 108:011102, 2012.

[40] David Tsang. Shattering Flares During Close Encounters of Neutron Stars. *Astrophys. J.*, 777:103, 2013.

[41] Arthur G. Suvorov and Kostas D. Kokkotas. Precursor flares of short gamma-ray bursts from crust yielding due to tidal resonances in coalescing binaries of rotating, magnetized neutron stars. *Phys. Rev. D*, 101(8):083002, 2020.

[42] Tomoki Wada, Masaru Shibata, and Kunihito Ioka. Analytic properties of the electromagnetic field of binary compact stars and electromagnetic precursors to gravitational waves. *PTEP*, 2020(10):103E01, 2020.

[43] Elias R. Most and Alexander A. Philippov. Electromagnetic precursors to gravitational wave events: Numerical simulations of flaring in pre-merger binary neutron star magnetospheres. *Astrophys. J. Lett.*, 893(1):L6, 2020.

[44] Federico Carrasco, Masaru Shibata, and Oscar Reula. Magnetospheres of black hole-neutron star binaries. *Phys. Rev. D*, 104(6):063004, 2021.

[45] C. J. Horowitz and Kai Kadau. The Breaking Strain of Neutron Star Crust and Gravitational Waves. *Phys. Rev. Lett.*, 102:191102, 2009.

[46] A. I. Chugunov and C. J. Horowitz. Breaking stress of neutron star crust. *Mon. Not. Roy. Astron. Soc.*, 407(1):L54–L58, September 2010.

[47] Kelsey Hoffman and Jeremy Heyl. Mechanical properties of non-accreting neutron star crusts. *Mon. Not. Roy. Astron. Soc.*, 426(3):2404–2412, November 2012.

[48] D. A. Baiko and A. A. Kozhberov. Anisotropic crystal structure of magnetized neutron star crust. *Mon. Not. Roy. Astron. Soc.*, 470(1):517–521, June 2017.

[49] D. A. Baiko and A. I. Chugunov. Breaking properties of neutron star crust. *Mon. Not. Roy. Astron. Soc.*, 480(4):5511–5516, 2018.

[50] P. N. McDermott, H. M. van Horn, and J. F. Scholl. Nonradial g-mode oscillations of warm neutron stars. *Astrophys. J.*, 268:837–848, May 1983.

[51] P. N. McDermott, C. J. Hansen, H. M. van Horn, and R. Buland. The nonradial oscillation spectra of neutron stars. *Astrophys. J. Lett.*, 297:L37–L40, October 1985.

[52] P. N. McDermott, H. M. van Horn, and C. J. Hansen. Nonradial Oscillations of Neutron Stars. *Astrophys. J.*, 325:725, February 1988.

[53] Lee Samuel Finn. G-modes in zero-temperature neutron stars. *Mon. Not. Roy. Astron. Soc.*, 227:265–293, July 1987.

[54] P. N. McDermott. Density Discontinuity G-Modes. *Mon. Not. Roy. Astron. Soc.*, 245:508, July 1990.

[55] E. M. Kantor and M. E. Gusakov. Composition temperature-dependent g-modes in superfluid neutron stars. *Mon. Not. Roy. Astron. Soc.*, 442:90, 2014.

[56] A. Passamonti, N. Andersson, and W. C. G. Ho. Buoyancy and g-modes in young superfluid neutron stars. *Mon. Not. Roy. Astron. Soc.*, 455(2):1489–1511, 2016.

[57] Hang Yu and Nevin N. Weinberg. Resonant tidal excitation of superfluid neutron stars in coalescing binaries. *Mon. Not. Roy. Astron. Soc.*, 464(3):2622–2637, 2017.

[58] Constantinos Constantinou, Sophia Han, Prashanth Jaikumar, and Madappa Prakash. g modes of neutron stars with hadron-to-quark crossover transitions. *Phys. Rev. D*, 104(12):123032, 2021.

[59] Prashanth Jaikumar, Alexandra Semposki, Madappa Prakash, and Constantinos Constantinou. g-mode oscillations in hybrid stars: A tale of two sounds. *Phys. Rev. D*, 103(12):123009, 2021.

[60] Hajime Sotani and Tomoya Takiwaki. Gravitational wave asteroseismology with protoneutron stars. *Phys. Rev. D*, 94(4):044043, 2016.

[61] Alejandro Torres-Forné, Pablo Cerdá-Durán, Martin Obergaulinger, Bernhard Müller, and José A. Font. Universal Relations for Gravitational-Wave Asteroseismology of Protoneutron Stars. *Phys. Rev. Lett.*, 123(5):051102, 2019.

[62] Marie-Anne Bizouard, Patricio Maturana-Russel, Alejandro Torres-Forné, Martin Obergaulinger, Pablo Cerdá-Durán, Nelson Christensen, José A. Font, and Renate Meyer. Inference of protoneutron star properties from gravitational-wave data in core-collapse supernovae. *Phys. Rev. D*, 103(6):063006, 2021.

[63] Hajime Sotani, Tomoya Takiwaki, and Hajime Togashi. Universal relation for supernova gravitational waves. *Phys. Rev. D*, 104(12):123009, 2021.

[64] Nicolas Yunes, Kent Yagi, and Frans Pretorius. Theoretical Physics Implications of the Binary Black-Hole Mergers GW150914 and GW151226. *Phys. Rev. D*, 94(8):084002, 2016.

[65] Andreas Bauswein, Nikolaos Stergioulas, and Hans-Thomas Janka. Exploring properties of high-density matter through remnants of neutron-star mergers. *Eur. Phys. J. A*, 52(3):56, 2016.

[66] Harry Ho-Yin Ng, Patrick Chi-Kit Cheong, Lap-Ming Lin, and Tjonnie Guang Feng Li. Gravitational-wave Asteroseismology with f-modes from Neutron Star Binaries at the Merger Phase. *Astrophys. J.*, 915(2):108, 2021.

[67] Praveen Manoharan, Christian J. Krüger, and Kostas D. Kokkotas. Universal relations for binary neutron star mergers with long-lived remnants. *Phys. Rev. D*, 104(2):023005, 2021.

[68] Jocelyn S. Read, Benjamin D. Lackey, Benjamin J. Owen, and John L. Friedman. Constraints on a phenomenologically parameterized neutron-star equation of state. *Phys. Rev. D*, 79:124032, 2009.

[69] Michael F. O'Boyle, Charalampos Markakis, Nikolaos Stergioulas, and Jocelyn S. Read. Parametrized equation of state for neutron star matter with continuous sound speed. *Phys. Rev. D*, 102(8):083027, 2020.

[70] Tod Strohmayer and Simin Mahmoodifar. A Non-radial Oscillation Mode in an Accreting Millisecond Pulsar? *Astrophys. J.*, 784:72, 2014.

[71] N. Andersson, D. I. Jones, and W. C. G. Ho. Implications of an r-mode in XTE J1751-305: Mass, radius and spin evolution. *Mon. Not. Roy. Astron. Soc.*, 442(2):1786–1793, 2014.

[72] Umin Lee. Excitation of a non-radial mode in a millisecond X-ray pulsar XTE J1751-305. *Mon. Not. Roy. Astron. Soc.*, 442(4):3037–3043, 2014.

[73] Geraint Pratten, Patricia Schmidt, and Natalie Williams. Impact of Dynamical Tides on the Reconstruction of the Neutron Star Equation of State. *arXiv e-prints*, page arXiv:2109.07566, September 2021.

[74] Natalie Williams, Geraint Pratten, and Patricia Schmidt. Prospects for distinguishing dynamical tides in inspiralling binary neutron stars with third generation gravitational-wave detectors. *arXiv e-prints*, page arXiv:2203.00623, March 2022.

[75] Tanja Hinderer. Tidal Love numbers of neutron stars. *Astrophys. J.*, 677:1216–1220, 2008.

[76] Eanna E. Flanagan and Tanja Hinderer. Constraining neutron star tidal Love numbers with gravitational wave detectors. *Phys. Rev. D*, 77:021502, 2008.

[77] Tanja Hinderer, Benjamin D. Lackey, Ryan N. Lang, and Jocelyn S. Read. Tidal deformability of neutron stars with realistic equations of state and their gravitational wave signatures in binary inspiral. *Phys. Rev. D*, 81:123016, 2010.

[78] Tanja Hinderer et al. Effects of neutron-star dynamic tides on gravitational waveforms within the effective-one-body approach. *Phys. Rev. Lett.*, 116(18):181101, 2016.

[79] Jan Steinhoff, Tanja Hinderer, Alessandra Buonanno, and Andrea Taracchini. Dynamical Tides in General Relativity: Effective Action and Effective-One-Body Hamiltonian. *Phys. Rev. D*, 94(10):104028, 2016.

[80] Patricia Schmidt and Tanja Hinderer. Frequency domain model of f-mode dynamic tides in gravitational waveforms from compact binary inspirals. *Phys. Rev. D*, 100(2):021501, 2019.

[81] Manuel Arca Sedda. Dissecting the properties of neutron star - black hole mergers originating in dense star clusters. *Commun. Phys.*, 3:43, 2020.

[82] Manuel Arca Sedda. Dynamical Formation of the GW190814 Merger. *Astrophys. J. Lett.*, 908(2):L38, 2021.

[83] Wenbin Lu, Paz Beniamini, and Clément Bonnerot. On the formation of GW190814. *Mon. Not. Roy. Astron. Soc.*, 500(2):1817–1832, 2020.

[84] R. A. Mardling. Tidal Capture in Star Clusters. In Piet Hut and Junichiro Makino, editors, *Dynamical Evolution of Star Clusters: Confrontation of Theory and Observations*, volume 174, page 273, January 1996.

[85] Erez Michaely, Dimitry Ginzburg, and Hagai B. Perets. Neutron star natal kicks: Collisions, μTDEs, faint SNe, GRBs and GW sources with preceding electromagnetic counterparts. *arXiv e-prints*, page arXiv:1610.00593, September 2016.

[86] Barton Zwiebach. Curvature Squared Terms and String Theories. *Phys. Lett. B*, 156:315–317, 1985.

[87] David J. Gross and John H. Sloan. The Quartic Effective Action for the Heterotic String. *Nucl. Phys. B*, 291:41–89, 1987.

[88] Valerio Faraoni and Salvatore Capozziello. *Beyond Einstein Gravity: A Survey of Gravitational Theories for Cosmology and Astrophysics*. Springer, Dordrecht, 2011.

[89] Thibault Damour and Gilles Esposito-Farese. Nonperturbative strong field effects in tensor - scalar theories of gravitation. *Phys. Rev. Lett.*, 70:2220–2223, 1993.

[90] Ulrich Sperhake, Christopher J. Moore, Roxana Rosca, Michalis Agathos, Davide Gerosa, and Christian D. Ott. Long-lived inverse chirp signals from core collapse in massive scalar-tensor gravity. *Phys. Rev. Lett.*, 119(20):201103, 2017.

[91] Hector O. Silva, Jeremy Sakstein, Leonardo Gualtieri, Thomas P. Sotiriou, and Emanuele Berti. Spontaneous scalarization of black holes and compact stars from a Gauss-Bonnet coupling. *Phys. Rev. Lett.*, 120(13):131104, 2018.

[92] Daniela D. Doneva, Lucas G. Collodel, Christian J. Krüger, and Stoytcho S. Yazadjiev. Spin-induced scalarization of Kerr black holes with a massive scalar field. *Eur. Phys. J. C*, 80(12):1205, 2020.

[93] Daniela D. Doneva and Stoytcho S. Yazadjiev. Dynamics of the nonrotating and rotating black hole scalarization. *Phys. Rev. D*, 103(6):064024, 2021.

[94] Daniela D. Doneva and Stoytcho S. Yazadjiev. Spontaneously scalarized black holes in dynamical Chern-Simons gravity: dynamics and equilibrium solutions. *Phys. Rev. D*, 103(8):083007, 2021.

[95] William E. East and Justin L. Ripley. Dynamics of Spontaneous Black Hole Scalarization and Mergers in Einstein-Scalar-Gauss-Bonnet Gravity. *Phys. Rev. Lett.*, 127(10):101102, 2021.

[96] Emanuele Berti et al. Testing General Relativity with Present and Future Astrophysical Observations. *Class. Quant. Grav.*, 32:243001, 2015.

[97] Philippe Brax, Anne-Christine Davis, Scott Melville, and Leong Khim Wong. Spin-orbit effects for compact binaries in scalar-tensor gravity. *JCAP.*, 2021(10):075, October 2021.

[98] Oliver Schön and Daniela D. Doneva. Tensor-multiscalar gravity: Equations of motion to 2.5 post-Newtonian order. *Phys. Rev. D*, 105(6):064034, 2022.

[99] Banafsheh Shiralilou, Tanja Hinderer, Samaya M. Nissanke, Néstor Ortiz, and Helvi Witek. Post-Newtonian gravitational and scalar waves in scalar-Gauss-Bonnet gravity. *Class. Quant. Grav.*, 39(3):035002, 2022.

[100] Laura Bernard, Luc Blanchet, and David Trestini. Gravitational waves in scalar-tensor theory to one-and-a-half post-Newtonian order. *arXiv e-prints*, page arXiv:2201.10924, January 2022.

[101] Kostas Glampedakis, George Pappas, Hector O. Silva, and Emanuele Berti. Post-Tolman-Oppenheimer-Volkoff formalism for relativistic stars. *Phys. Rev. D*, 92(2):024056, 2015.

[102] Valerio Faraoni and Shahn Nadeau. The (pseudo)issue of the conformal frame revisited. *Phys. Rev. D*, 75:023501, 2007.

[103] Laur Jarv, Piret Kuusk, and Margus Saal. Scalar-tensor cosmology at the general relativity limit: Jordan versus Einstein frame. *Phys. Rev. D*, 76:103506, 2007.

[104] S. Capozziello, P. Martin-Moruno, and C. Rubano. Physical non-equivalence of the Jordan and Einstein frames. *Phys. Lett. B*, 689:117–121, 2010.

[105] G. Antoniou, A. Bakopoulos, and P. Kanti. Evasion of No-Hair Theorems and Novel Black-Hole Solutions in Gauss-Bonnet Theories. *Phys. Rev. Lett.*, 120(13):131102, 2018.

[106] Daniela D. Doneva and Stoytcho S. Yazadjiev. New Gauss-Bonnet Black Holes with Curvature-Induced Scalarization in Extended Scalar-Tensor Theories. *Phys. Rev. Lett.*, 120(13):131103, 2018.

[107] Richard C. Tolman. Static Solutions of Einstein's Field Equations for Spheres of Fluid. *Physical Review*, 55(4):364–373, February 1939.

[108] J. R. Oppenheimer and G. M. Volkoff. On Massive Neutron Cores. *Physical Review*, 55(4):374–381, February 1939.

[109] H. T. Cromartie et al. Relativistic Shapiro delay measurements of an extremely massive millisecond pulsar. *Nature Astron.*, 4(1):72–76, 2019.

[110] L. Lindblom and S. L. Detweiler. The quadrupole oscillations of neutron stars. *Astrophy. J. Supp.*, 53:73–92, September 1983.

[111] Steven L. Detweiler and L. Lindblom. On the nonradial pulsations of general relativistic stellar models. *Astrophys. J.*, 292:12–15, 1985.

[112] C. J. Krüger, W. C. G. Ho, and N. Andersson. Seismology of adolescent neutron stars: Accounting for thermal effects and crust elasticity. *Phys. Rev. D*, 92(6):063009, 2015.

[113] N. Froeman, P. O. Froeman, N. Andersson, and A. Hoekback. Black hole normal modes: Phase integral treatment. *Phys. Rev. D*, 45:2609–2616, 1992.

[114] Nils Andersson, Kostas D. Kokkotas, and Bernard F. Schutz. A New numerical approach to the oscillation modes of relativistic stars. *Mon. Not. Roy. Astron. Soc.*, 274:1039, 1995.

[115] Carolyn Raithel, Feryal Özel, and Dimitrios Psaltis. Tidal deformability from GW170817 as a direct probe of the neutron star radius. *Astrophys. J. Lett.*, 857(2):L23, 2018.

[116] Soumi De, Daniel Finstad, James M. Lattimer, Duncan A. Brown, Edo Berger, and Christopher M. Biwer. Tidal Deformabilities and Radii of Neutron Stars from the Observation of GW170817. *Phys. Rev. Lett.*, 121(9):091102, 2018. [Erratum: Phys.Rev.Lett. 121, 259902 (2018)].

[117] S. K. Greif, K. Hebeler, J. M. Lattimer, C. J. Pethick, and A. Schwenk. Equation of state constraints from nuclear physics, neutron star masses, and future moment of inertia measurements. *Astrophys. J.*, 901(2):155, 2020.

[118] Nils Andersson and Kostas D. Kokkotas. Towards gravitational wave asteroseismology. *Mon. Not. Roy. Astron. Soc.*, 299:1059–1068, 1998.

[119] H. K. Lau, P. T. Leung, and L. M. Lin. Inferring physical parameters of compact stars from their f-mode gravitational wave signals. *Astrophys. J.*, 714:1234–1238, 2010.

[120] T. K. Chan, Y. H. Sham, P. T. Leung, and L. M. Lin. Multipolar universal relations between f-mode frequency and tidal deformability of compact stars. *Phys. Rev. D*, 90(12):124023, 2014.

[121] C. J. Krüger and K. D. Kokkotas. Fast Rotating Relativistic Stars: Spectra and Stability without Approximation. *Phys. Rev. Lett.*, 125(11):111106, 2020.

[122] Ernesto Benitez, Joseph Weller, Victor Guedes, Cecilia Chirenti, and M. Coleman Miller. Investigating the I-Love-Q and w-mode Universal Relations Using Piecewise Polytropes. *Phys. Rev. D*, 103(2):023007, 2021.

[123] Hajime Sotani and Bharat Kumar. Universal relations between the quasinormal modes of neutron star and tidal deformability. *Phys. Rev. D*, 104(12):123002, 2021.

[124] Dong Lai. Resonant oscillations and tidal heating in coalescing binary neutron stars. *Mon. Not. Roy. Astron. Soc.*, 270:611, 1994.

[125] Paul Coppin, Krijn D. de Vries, and Nick van Eijndhoven. Identification of gamma-ray burst precursors in Fermi-GBM bursts. *Phys. Rev. D*, 102(10):103014, 2020.

[126] Tod E. Strohmayer. Oscillations of Rotating Neutron Stars. *Astrophys. J.*, 372:573, May 1991.

[127] Andreas Reisenegger and Peter Goldreich. A New Class of g-Modes in Neutron Stars. *Astrophys. J.*, 395:240, August 1992.

[128] Keith H. Lockitch, Nils Andersson, and John L. Friedman. The Rotational modes of relativistic stars. 1. Analytic results. *Phys. Rev. D*, 63:024019, 2001.

[129] P. Haensel, K. P. Levenfish, and D. G. Yakovlev. Adiabatic index of dense matter and damping of neutron star pulsations. *Astron. Astrophys.*, 394:213–218, 2002.

[130] J. Hoyos, A. Reisenegger, and J. A. Valdivia. Magnetic Field Evolution in Neutron Stars: One-Dimensional Multi-Fluid Model. *Astron. Astrophys.*, 487:789, 2008.

[131] Jaime H. Hoyos, Andreas Reisenegger, and Juan A. Valdivia. Asymptotic, non-linear solutions for ambipolar diffusion in one dimension. *MNRAS*, 408(3):1730–1741, November 2010.

[132] Andreas Reisenegger. Chemical equilibrium and stable stratification of a multicomponent fluid: Thermodynamics and application to neutron stars. *Astrophys. J.*, 550:860–862, 2001.

[133] L. S. Finn. G-modes of non-radially pulsating relativistic stars - The slow-motion formalism. *Mon. Not. Roy. Astron. Soc.*, 222:393–416, September 1986.

[134] Richard Price and Kip S. Thorne. Non-Radial Pulsation of General-Relativistic Stellar Models. II. Properties of the Gravitational Waves. *Astrophys. J.*, 155:163, January 1969.

[135] Nils Andersson and Kostas D. Kokkotas. Pulsation modes for increasingly relativistic polytropes. *Mon. Not. Roy. Astron. Soc.*, 297:493, 1998.

[136] Nils Andersson and Kostas D. Kokkotas. Gravitational waves and pulsating stars: What can we learn from future observations? *Phys. Rev. Lett.*, 77:4134–4137, 1996.

[137] Sebastian H. Völkel, Christian J. Krüger, and Kostas D. Kokkotas. Bayesian Inverse Problem of Rotating Neutron Stars. *Phys. Rev. D*, 103(8):083008, 2021.

[138] K. D. Kokkotas, T. A. Apostolatos, and N. Andersson. The Inverse problem for pulsating neutron stars: A 'Fingerprint analysis' for the supranuclear equation of state. *Mon. Not. Roy. Astron. Soc.*, 320:307–315, 2001.

[139] L. K. Tsui and P. T. Leung. Universality in quasi-normal modes of neutron stars. *Mon. Not. Roy. Astron. Soc.*, 357:1029–1037, 2005.

[140] Wenrui Xu and Dong Lai. Resonant Tidal Excitation of Oscillation Modes in Merging Binary Neutron Stars: Inertial-Gravity Modes. *Phys. Rev. D*, 96(8):083005, 2017.

[141] Andrei M. Beloborodov and Xinyu Li. Magnetar heating. *Astrophys. J.*, 833(2):261, 2016.

[142] Albino Perego, Sebastiano Bernuzzi, and David Radice. Thermodynamics conditions of matter in neutron star mergers. *Eur. Phys. J. A*, 55(8):124, 2019.

[143] Roland Oechslin, H. T. Janka, and A. Marek. Relativistic neutron star merger simulations with non-zero temperature equations of state. 1. Variation of binary parameters and equation of state. *Astron. Astrophys.*, 467:395, 2007.

[144] Wolfgang Kastaun, Riccardo Ciolfi, Andrea Endrizzi, and Bruno Giacomazzo. Structure of Stable Binary Neutron Star Merger Remnants: Role of Initial Spin. *Phys. Rev. D*, 96(4):043019, 2017.

[145] A. Y. Potekhin, D. G. Yakovlev, G. Chabrier, and Oleg Y. Gnedin. Thermal structure and cooling of superfluid magnetic neutron stars. *Astrophys. J.*, 594:404–418, 2003.

[146] Giovanni Camelio, Tim Dietrich, Stephan Rosswog, and Brynmor Haskell. Axisymmetric models for neutron star merger remnants with realistic thermal and rotational profiles. *Phys. Rev. D*, 103(6):063014, 2021.

[147] A. Passamonti, N. Andersson, and P. Pnigouras. Dynamical tides in neutron stars: The impact of the crust. *Mon. Not. Roy. Astron. Soc.*, 504(1):1273–1293, 2021.

[148] N. Andersson and P. Pnigouras. The g-mode spectrum of reactive neutron star cores. *Mon. Not. Roy. Astron. Soc.*, 489(3):4043–4048, 2019.

[149] Yotam Sherf. Tidal-heating and viscous dissipation correspondence in black holes and viscous compact objects. *Phys. Rev. D*, 103(10):104003, 2021.

[150] Nils Andersson, G. L. Comer, and K. Glampedakis. How viscous is a superfluid neutron star core? *Nucl. Phys. A*, 763:212–229, 2005.

[151] E. E. Kolomeitsev and D. N. Voskresensky. Viscosity of neutron star matter and r-modes in rotating pulsars. *Phys. Rev. C*, 91(2):025805, 2015.

[152] Phil Arras and Nevin N. Weinberg. Urca reactions during neutron star inspiral. *Mon. Not. Roy. Astron. Soc.*, 486(1):1424–1436, 2019.

[153] Wynn C. G. Ho and Dong Lai. Resonant tidal excitations of rotating neutron stars in coalescing binaries. *Mon. Not. Roy. Astron. Soc.*, 308:153, 1999.

[154] Dong Lai and Yanqin Wu. Resonant Tidal Excitations of Inertial Modes in Coalescing Neutron Star Binaries. *Phys. Rev. D*, 74:024007, 2006.

[155] A. Akmal, V. R. Pandharipande, and D. G. Ravenhall. The Equation of state of nucleon matter and neutron star structure. *Phys. Rev. C*, 58:1804–1828, 1998.

[156] H. Müther, M. Prakash, and T. L. Ainsworth. The nuclear symmetry energy in relativistic Brueckner-Hartree-Fock calculations. *Physics Letters B*, 199(4):469–474, December 1987.

[157] Horst Mueller and Brian D. Serot. Relativistic mean field theory and the high density nuclear equation of state. *Nucl. Phys. A*, 606:508–537, 1996.

[158] Robert B. Wiringa, V. Fiks, and A. Fabrocini. Equation of state for dense nucleon matter. *Phys. Rev. C*, 38:1010–1037, 1988.

[159] L. Engvik, M. Hjorth-Jensen, E. Osnes, G. Bao, and E. Ostgaard. Asymmetric nuclear matter and neutron star properties. *Phys. Rev. Lett.*, 73:2650–2653, 1994.

[160] F. Douchin and P. Haensel. A unified equation of state of dense matter and neutron star structure. *Astron. Astrophys.*, 380:151, 2001.

[161] B. Friedman and V. R. Pandharipande. Hot and cold, nuclear and neutron matter. *Nucl. Phys. A*, 361:502–520, 1981.

[162] M. Baldo, I. Bombaci, and G. F. Burgio. Microscopic nuclear equation of state with three-body forces and neutron star structure. *Astron. Astrophys.*, 328:274–282, 1997.

[163] B. K. Agrawal, S. Shlomo, and V. Kim Au. Determination of the parameters of a Skyrme type effective interaction using the simulated annealing approach. *Phys. Rev. C*, 72:014310, 2005.

[164] Benjamin D. Lackey, Mohit Nayyar, and Benjamin J. Owen. Observational constraints on hyperons in neutron stars. *Phys. Rev. D*, 73:024021, 2006.

[165] N. K. Glendenning. Neutron Stars Are Giant Hypernuclei? *Astrophys. J.*, 293:470–493, 1985.

[166] M. Prakash, T. L. Ainsworth, and J. M. Lattimer. Equation of state and the maximum mass of neutron stars. *Phys. Rev. Lett.*, 61:2518–2521, 1988.

[167] M. Prakash, J. R. Cooke, and J. M. Lattimer. Quark - hadron phase transition in protoneutron stars. *Phys. Rev. D*, 52:661–665, 1995.

[168] Mark Alford, Matt Braby, M. W. Paris, and Sanjay Reddy. Hybrid stars that masquerade as neutron stars. *Astrophys. J.*, 629:969–978, 2005.

[169] Christian D. Ott, Adam Burrows, Luc Dessart, and Eli Livne. A New Mechanism for Gravitational Wave Emission in Core-Collapse Supernovae. *Phys. Rev. Lett.*, 96:201102, 2006.

[170] I. Kowalska-Leszczynska, T. Regimbau, T. Bulik, M. Dominik, and K. Belczynski. Effect of metallicity on the gravitational-wave signal from the cosmological population of compact binary coalescences. *A&A*, 574:A58, February 2015.

[171] S. Woosley, Tuguldur Sukhbold, and H. T. Janka. The Birth Function for Black Holes and Neutron Stars in Close Binaries. *Astrophys. J.*, 896(1):56, 2020.

[172] M. Coleman Miller, Cecilia Chirenti, and Frederick K. Lamb. Constraining the equation of state of high-density cold matter using nuclear and astronomical measurements. *Astrophys. J.*, 888:12, 2019.

[173] G. Raaijmakers et al. Constraining the dense matter equation of state with joint analysis of NICER and LIGO/Virgo measurements. *Astrophys. J. Lett.*, 893(1):L21, 2020.

[174] G. Raaijmakers, S. K. Greif, K. Hebeler, T. Hinderer, S. Nissanke, A. Schwenk, T. E. Riley, A. L. Watts, J. M. Lattimer, and W. C. G. Ho. Constraints on the Dense Matter Equation of State and Neutron Star Properties from NICER's Mass-Radius Estimate of PSR J0740+6620 and Multimessenger Observations. *Astrophys. J. Lett.*, 918(2):L29, 2021.

[175] Kenta Kiuchi, Pablo Cerdá-Durán, Koutarou Kyutoku, Yuichiro Sekiguchi, and Masaru Shibata. Efficient magnetic-field amplification due to the Kelvin-Helmholtz instability in binary neutron star mergers. *Phys. Rev. D*, 92(12):124034, 2015.

[176] Matthew D. Duez, Yuk Tung Liu, Stuart L. Shapiro, and Branson C. Stephens. General relativistic hydrodynamics with viscosity: Contraction, catastrophic collapse, and disk formation in hypermassive neutron stars. *Phys. Rev. D*, 69:104030, 2004.

[177] Sho Fujibayashi, Kenta Kiuchi, Nobuya Nishimura, Yuichiro Sekiguchi, and Masaru Shibata. Mass Ejection from the Remnant of a Binary Neutron Star Merger: Viscous-Radiation Hydrodynamics Study. *Astrophys. J.*, 860(1):64, 2018.

[178] Lee Lindblom. Determining the Nuclear Equation of State from Neutron-Star Masses and Radii. *ApJ*, 398:569, October 1992.

[179] L. R. Weih, E. R. Most, and L. Rezzolla. Optimal Neutron-star Mass Ranges to Constrain the Equation of State of Nuclear Matter with Electromagnetic and Gravitational-wave Observations. *Astrophys. J.*, 881(1):73, 2019.

[180] P. C. Peters and J. Mathews. Gravitational Radiation from Point Masses in a Keplerian Orbit. *Physical Review*, 131(1):435–440, July 1963.

[181] Geraint Pratten, Patricia Schmidt, and Tanja Hinderer. Gravitational-Wave Asteroseismology with Fundamental Modes from Compact Binary Inspirals. *Nature Commun.*, 11(1):2553, 2020.

[182] Jan Steinhoff, Tanja Hinderer, Tim Dietrich, and Francois Foucart. Spin effects on neutron star fundamental-mode dynamical tides: Phenomenology and comparison to numerical simulations. *Phys. Rev. Res.*, 3(3):033129, 2021.

[183] Kent Yagi and Nicolas Yunes. I-Love-Q Relations in Neutron Stars and their Applications to Astrophysics, Gravitational Waves and Fundamental Physics. *Phys. Rev. D*, 88(2):023009, 2013.

[184] Andrzej Królak, Kostas D. Kokkotas, and Gerhard Schäfer. Estimation of the post-Newtonian parameters in the gravitational-wave emission of a coalescing binary. *Phys. Rev. D*, 52(4):2089–2111, August 1995.

[185] B. P. Abbott et al. Properties of the binary neutron star merger gw170817. *Physical Review X*, 9(1):011001, January 2019.

[186] Collin D. Capano, Ingo Tews, Stephanie M. Brown, Ben Margalit, Soumi De, Sumit Kumar, Duncan A. Brown, Badri Krishnan, and Sanjay Reddy. Stringent constraints on neutron-star radii from multimessenger observations and nuclear theory. *Nature Astron.*, 4(6):625–632, 2020.

[187] Philippe Landry, Reed Essick, and Katerina Chatziioannou. Nonparametric constraints on neutron star matter with existing and upcoming gravitational wave and pulsar observations. *Phys. Rev. D*, 101(12):123007, 2020.

[188] Tim Dietrich, Michael W. Coughlin, Peter T. H. Pang, Mattia Bulla, Jack Heinzel, Lina Issa, Ingo Tews, and Sarah Antier. Multimessenger constraints on the neutron-star equation of state and the Hubble constant. *Science*, 370(6523):1450–1453, 2020.

[189] Peter T. H. Pang, Ingo Tews, Michael W. Coughlin, Mattia Bulla, Chris Van Den Broeck, and Tim Dietrich. Nuclear Physics Multimessenger Astrophysics Constraints on the Neutron Star Equation of State: Adding NICER's PSR J0740+6620 Measurement. *Astrophys. J.*, 922(1):14, 2021.

[190] Eric D. Van Oeveren and John L. Friedman. Upper limit set by causality on the tidal deformability of a neutron star. *Phys. Rev. D*, 95(8):083014, 2017.

[191] Ch. C. Moustakidis, T. Gaitanos, Ch. Margaritis, and G. A. Lalazissis. Bounds on the speed of sound in dense matter, and neutron star structure. *Phys. Rev. C*, 95(4):045801, 2017. [Erratum: Phys.Rev.C 95, 059904 (2017)].

[192] Na Zhang, Dehua Wen, and Houyuan Chen. Imprint of the speed of sound in nuclear matter on global properties of neutron stars. *Phys. Rev. C*, 99(3):035803, March 2019.

[193] A. Kanakis-Pegios, P. S. Koliogiannis, and Ch. C. Moustakidis. Speed of sound constraints from tidal deformability of neutron stars. *Phys. Rev. C*, 102(5):055801, 2020.

[194] Ingo Tews, Peter T. H. Pang, Tim Dietrich, Michael W. Coughlin, Sarah Antier, Mattia Bulla, Jack Heinzel, and Lina Issa. On the Nature of GW190814 and Its Impact on the Understanding of Supranuclear Matter. *Astrophys. J. Lett.*, 908(1):L1, 2021.

[195] Ingo Tews, Joseph Carlson, Stefano Gandolfi, and Sanjay Reddy. Constraining the speed of sound inside neutron stars with chiral effective field theory interactions and observations. *Astrophys. J.*, 860(2):149, 2018.

[196] Denis A. Leahy, Sharon M. Morsink, and Yi Chou. Constraints on the Mass and Radius of the Neutron Star XTE J1807-294. *Astrophys. J.*, 742(1):17, November 2011.

[197] Cecilia Chirenti, M. Coleman Miller, Tod Strohmayer, and Jordan Camp. Searching for hypermassive neutron stars with short gamma-ray bursts. *Astrophys. J. Lett.*, 884(1):L16, 2019.

[198] David Radice, Albino Perego, Francesco Zappa, and Sebastiano Bernuzzi. GW170817: Joint Constraint on the Neutron Star Equation of State from Multimessenger Observations. *Astrophys. J. Lett.*, 852(2):L29, 2018.

[199] Kostas D. Kokkotas and Gerhard Schaefer. Tidal and tidal resonant effects in coalescing binaries. *Mon. Not. Roy. Astron. Soc.*, 275:301, 1995.

[200] Michelle Vick and Dong Lai. Tidal Effects in Eccentric Coalescing Neutron Star Binaries. *Phys. Rev. D*, 100(6):063001, 2019.

[201] Greg Ushomirsky, Curt Cutler, and Lars Bildsten. Deformations of accreting neutron star crusts and gravitational wave emission. *Mon. Not. Roy. Astron. Soc.*, 319:902, 2000.

[202] Benjamin J. Owen. Maximum elastic deformations of compact stars with exotic equations of state. *Phys. Rev. Lett.*, 95:211101, 2005.

[203] Christopher S. Kochanek. Coalescing Binary Neutron Stars. *Astrophys. J.*, 398:234, October 1992.

[204] A. J. Penner, N. Andersson, D. I. Jones, L Samuelsson, and I. Hawke. Crustal failure during binary inspiral. *Astrophys. J. Lett.*, 749:L36, 2012.

[205] O. Blaes, R. Blandford, P. Goldreich, and P. Madau. Neutron Starquake Models for Gamma-Ray Bursts. *Astrophys. J.*, 343:839, August 1989.

[206] Christopher Thompson and Robert C. Duncan. The Soft gamma repeaters as very strongly magnetized neutron stars - 1. Radiative mechanism for outbursts. *Mon. Not. Roy. Astron. Soc.*, 275:255–300, 1995.

[207] H. C. Spruit, F. Daigne, and G. Drenkhahn. Large scale magnetic fields and their dissipation in grb fireballs. *Astron. Astrophys.*, 369:694, 2001.

[208] Chryssa Kouveliotou, Charles A. Meegan, Gerald J. Fishman, Narayana P. Bhat, Michael S. Briggs, Thomas M. Koshut, William S. Paciesas, and Geoffrey N. Pendleton. Identification of Two Classes of Gamma-Ray Bursts. *Astrophys. J. Lett.*, 413:L101, August 1993.

[209] B. Paczynski. Gamma-ray bursters at cosmological distances. *Astrophys. J. Lett.*, 308:L43–L46, September 1986.

[210] Ramesh Narayan, Bohdan Paczynski, and Tsvi Piran. Gamma-ray bursts as the death throes of massive binary stars. *Astrophys. J. Lett.*, 395:L83–L86, 1992.

[211] Krzysztof Belczynski, Rosalba Perna, Tomasz Bulik, Vassiliki Kalogera, Natalia Ivanova, and Donald Q. Lamb. A study of compact object mergers as short gamma-ray burst progenitors. *Astrophys. J.*, 648:1110–1116, 2006.

[212] Bruno Giacomazzo, Rosalba Perna, Luciano Rezzolla, Eleonora Troja, and Davide Lazzati. Compact Binary Progenitors of Short Gamma-Ray Bursts. *Astrophys. J. Lett.*, 762:L18, 2013.

[213] M. Gullón, J. A. Pons, J. A. Miralles, D. Viganò, N. Rea, and R. Perna. Population synthesis of isolated neutron stars with magneto-rotational evolution - II. From radio-pulsars to magnetars. *Mon. Not. Roy. Astron. Soc.*, 454(1):615–625, 2015.

[214] Lars Bildsten and Curt Cutler. Tidal Interactions of Inspiraling Compact Binaries. *Astrophys. J.*, 400:175, November 1992.

[215] Pantelis Pnigouras. Gravitational-wave-driven tidal secular instability in neutron star binaries. *Phys. Rev. D*, 100(6):063016, 2019.

[216] Anthony L. Piro and Lars Bildsten. Neutron star crustal interface waves. *Astrophys. J.*, 619:1054–1063, 2005.

[217] B. L. Schumaker and K. S. Thorne. Torsional oscillations of neutron stars. *Mon. Not. Roy. Astron. Soc.*, 203:457–489, May 1983.

[218] H. Sotani, K. D. Kokkotas, and N. Stergioulas. Torsional Oscillations of Relativistic Stars with Dipole Magnetic Fields. *Mon. Not. Roy. Astron. Soc.*, 375:261–277, 2007.

[219] M. Vavoulidis, K. D. Kokkotas, and A. Stavridis. Crustal Oscillations of Slowly Rotating Relativistic Stars. *Mon. Not. Roy. Astron. Soc.*, 384:1711, 2008.

[220] Hajime Sotani. Empirical formula of crustal torsional oscillations. *Phys. Rev. D*, 93:044059, 2016.

[221] S. K. Lander and K. N. Gourgouliatos. Magnetic-field evolution in a plastically-failing neutron-star crust. *Mon. Not. Roy. Astron. Soc.*, 486(3):4130–4143, 2019.

[222] S. Nasiri and Y. Sobouti. Global modes of oscillation of magnetized stars. *Astron. Astrophys.*, 217(1-2):127–136, June 1989.

[223] S. Yoshida and Y. Eriguchi. A numerical study of normal modes of rotating neutron star models by the cowling approximation. *Astrophys. J.*, 515:414, 1999.

[224] Erich Gaertig and Kostas D. Kokkotas. Relativistic g-modes in rapidly rotating neutron stars. *Phys. Rev. D*, 80:064026, 2009.

[225] J. M. Lattimer and M. Prakash. Neutron star structure and the equation of state. *Astrophys. J.*, 550:426, 2001.

[226] Yixiao Zhou and Fan Zhang. Equation of State Dependence of Nonlinear Mode-tide Coupling in Coalescing Binary Neutron Stars. *Astrophys. J.*, 849:114, 2017.

[227] Duncan Neill, William G. Newton, and David Tsang. Resonant Shattering Flares as Multimessenger Probes of the Nuclear Symmetry Energy. *Mon. Not. Roy. Astron. Soc.*, 504(1):1129–1143, 2021.

[228] Alpha Mastrano, Arthur George Suvorov, and Andrew Melatos. Neutron star deformation due to poloidal-toroidal magnetic fields of arbitrary multipole order: a new analytic approach. *Mon. Not. Roy. Astron. Soc.*, 447:3475, 2015.

[229] A. Bauswein, H. Th. Janka, and R. Oechslin. Testing Approximations of Thermal Effects in Neutron Star Merger Simulations. *Phys. Rev. D*, 82:084043, 2010.

[230] Robert B. Wiringa, V. G. J. Stoks, and R. Schiavilla. An Accurate nucleon-nucleon potential with charge independence breaking. *Phys. Rev. C*, 51:38–51, 1995.

[231] Robert C. Duncan and Christopher Thompson. Formation of Very Strongly Magnetized Neutron Stars: Implications for Gamma-Ray Bursts. *Astrophys. J. Lett.*, 392:L9, June 1992.

[232] S. Chandrasekhar and E. Fermi. Problems of Gravitational Stability in the Presence of a Magnetic Field. *Astrophys. J.*, 118:116, July 1953.

[233] Dong Lai. Matter in strong magnetic fields. *Rev. Mod. Phys.*, 73:629–662, Aug 2001.

[234] James M. Lattimer and Maddapa Prakash. Neutron Star Observations: Prognosis for Equation of State Constraints. *Phys. Rept.*, 442:109–165, 2007.

[235] Andreas Reisenegger. Stable magnetic equilibria and their evolution in the upper main sequence, white dwarfs, and neutron stars. *Astron. Astrophys.*, 499:557, 2009.

[236] T. Akgün, A. Reisenegger, A. Mastrano, and P. Marchant. Stability of magnetic fields in non-barotropic stars: an analytic treatment. *Mon. Not. Roy. Astron. Soc.*, 433(3):2445–2466, August 2013.

[237] R. Ciolfi, V. Ferrari, L. Gualtieri, and J. A. Pons. Relativistic models of magnetars: the twisted-torus magnetic field configuration. *Mon. Not. Roy. Astron. Soc.*, 397:913, 2009.

[238] A. Mastrano, A. Melatos, A. Reisenegger, and T. Akgün. Gravitational wave emission from a magnetically deformed non-barotropic neutron star. *Mon. Not. Roy. Astron. Soc.*, 417(3):2288–2299, November 2011.

[239] Kostas Glampedakis and Paul D. Lasky. The freedom to choose neutron star magnetic field equilibria: Table 1. *Mon. Not. Roy. Astron. Soc.*, 463(3):2542–2552, December 2016.

[240] S. Chandrasekhar. Axisymmetric Magnetic Fields and Fluid Motions. *Astrophys. J.*, 124:232, July 1956.

[241] J. Braithwaite. Axisymmetric magnetic fields in stars: relative strengths of poloidal and toroidal components. *Mon. Not. Roy. Astron. Soc.*, 397:763, 2009.

[242] I. Wasserman and S. L. Shapiro. Masses, radii, and magnetic fields of pulsating X-ray sources : is the "standard" model self-consistent ? *Astrophys. J.*, 265:1036–1046, February 1983.

[243] Steven Weinberg. *Gravitation and Cosmology: Principles and Applications of the General Theory of Relativity.* 1972.

[244] D. Papadopoulos and F. P. Esposito. Relativistic hydromagnetic wave propagation and instability in an anisotropic universe. *Astrophys. J.*, 257:10–16, June 1982.

[245] John L. Friedman. Generic instability of rotating relativistic stars. *Commun. Math. Phys.*, 62(3):247–278, 1978.

[246] S. K. Lander. Magnetic Fields in Superconducting Neutron Stars. *Phys. Rev. Lett.*, 110(7):071101, February 2013.

[247] A. G. Suvorov. Ultra-compact X-ray binaries as dual-line gravitational-wave sources. *Mon. Not. Roy. Astron. Soc.*, 503(4):5495–5503, 2021.

[248] Vanessa Graber, Nils Andersson, Kostas Glampedakis, and Samuel K. Lander. Magnetic field evolution in superconducting neutron stars. *Mon. Not. Roy. Astron. Soc.*, 453(1):671–681, October 2015.

[249] P. Hut. Tidal evolution in close binary systems. *Astron. Astrophys.*, 99:126–140, June 1981.

[250] Jean-Paul Zahn. Tidal dissipation in binary systems. *EAS Publ. Ser.*, 29:67, 2008.

[251] Adam Pound. Second-order gravitational self-force. *Phys. Rev. Lett.*, 109:051101, 2012.

[252] Donato Bini, Thibault Damour, and Guillaume Faye. Effective action approach to higher-order relativistic tidal interactions in binary systems and their effective one body description. *Phys. Rev. D*, 85:124034, 2012.

[253] M. E. Alexander. Tidal resonances in binary star systems. *Mon. Not. Roy. Astron. Soc.*, 227:843–861, August 1987.

[254] Thibault Damour, Piotr Jaranowski, and Gerhard Schaefer. Dynamical invariants for general relativistic two-body systems at the third postNewtonian approximation. *Phys. Rev. D*, 62:044024, 2000.

[255] A. Buonanno and T. Damour. Effective one-body approach to general relativistic two-body dynamics. *Phys. Rev. D*, 59:084006, 1999.

[256] G. Schaefer. Reduced Hamiltonian formalism for general-relativistic adiabatic fluids and applications. *Astronomische Nachrichten*, 311(4):213–217, May 1990.

[257] Philippe Landry and Eric Poisson. Tidal deformation of a slowly rotating material body: External metric. *Physical Review D*, 91(10):104018, 2015.

[258] Eric Poisson and Jean Doucot. Gravitomagnetic tidal currents in rotating neutron stars. *Phys. Rev. D*, 95(4):044023, 2017.

[259] Eric Poisson. Gravitomagnetic tidal resonance in neutron-star binary inspirals. *Phys. Rev. D*, 101(10):104028, 2020.

[260] Justin E. Vines and Eanna E. Flanagan. Post-1-Newtonian quadrupole tidal interactions in binary systems. *Phys. Rev. D*, 88:024046, 2013.

[261] V. Ferrari, L. Gualtieri, and A. Maselli. Tidal interaction in compact binaries: a post-Newtonian affine framework. *Phys. Rev. D*, 85:044045, 2012.

[262] W. H. Press and S. A. Teukolsky. On formation of close binaries by two-body tidal capture. *Astrophys. J.*, 213:183–192, April 1977.

[263] J. P. Zahn. Reprint of 1977A&A....57..383Z. Tidal friction in close binary stars. *Astron. Astrophys.*, 500:121–132, May 1977.

[264] Bart Willems. Excitation of oscillation modes by tides in close binaries: constraints on stellar and orbital parameters. *Mon. Not. Roy. Astron. Soc.*, 346:968, 2003.

[265] J. Fuller, D. W. Kurtz, G. Handler, and S. Rappaport. Tidally trapped pulsations in binary stars. *Mon. Not. Roy. Astron. Soc.*, 498(4):5730–5744, November 2020.

[266] J. L. Friedman and B. F. Schutz. On the stability of relativistic systems. *Astrophys. J.*, 200:204–220, August 1975.

[267] Steven L. Detweiler and J. R. Ipser. Variational principle and a stability-criterion for nonradial modes of pulsation of stellar models in general relativity. *Astrophys. J.*, 185:685–707, 1973.

[268] Dong Lai, Frederic A. Rasio, and Stuart L. Shapiro. Hydrodynamic Instability and Coalescence of Close Binary Systems. *Astrophys. J. Lett.*, 406:L63, April 1993.

[269] Dong Lai, Frederic A. Rasio, and Stuart L. Shapiro. Equilibrium, stability and orbital evolution of close binary systems. *Astrophys. J.*, 423:344, 1994.

[270] Dong Lai, Frederic A. Rasio, and Stuart L. Shapiro. Hydrodynamic instability and coalescence of binary neutron stars. *Astrophys. J.*, 420:811–829, 1994.

[271] Kip S. Thorne and Alfonso Campolattaro. Non-Radial Pulsation of General-Relativistic Stellar Models. I. Analytic Analysis for L ¿= 2. *Astrophys. J.*, 149:591, September 1967.

[272] Wasaburo Unno, Yoji Osaki, Hiroyasu Ando, H. Saio, and H. Shibahashi. *Nonradial oscillations of stars*. 1989.

[273] S. L. Bi, Y. Liao, and J. X. Wang. Influence of turbulent magnetic fields on mode frequencies. *Astron. Astrophys.*, 397:1069–1074, January 2003.

[274] Marlene Herbrik and Kostas D. Kokkotas. Stability analysis of magnetized neutron stars - a semi-analytic approach. *Mon. Not. Roy. Astron. Soc.*, 466(2):1330–1347, April 2017.

[275] James B. Hartle. Slowly Rotating Relativistic Stars. I. Equations of Structure. *Astrophys. J.*, 150:1005, December 1967.

[276] Shijun Yoshida and Umin Lee. Rotational modes of nonisentropic stars and the gravitational radiation driven instability. *Astrophys. J. Suppl.*, 129:353, 2000.

[277] A. Passamonti, B. Haskell, N. Andersson, D. I. Jones, and I. Hawke. Oscillations of rapidly rotating stratified neutron stars. *Mon. Not. Roy. Astron. Soc.*, 394:730, 2009.

[278] Daniela D. Doneva, Erich Gaertig, Kostas D. Kokkotas, and Christian Krüger. Gravitational wave asteroseismology of fast rotating neutron stars with realistic equations of state. *Phys. Rev. D*, 88(4):044052, 2013.

[279] B. Carter and H. Quintana. Foundations of general relativistic high-pressure elasticity theory. *Proc. R. Soc. Lond. A*, 331:57–83, 1999.

[280] B. Carter and H. Quintana. Stationary elastic rotational deformation of a relativistic neutron star model. *Astrophys. J.*, 202:511–522, December 1975.

[281] Chongming Xu, Xuejun Wu, and Michael Soffel. General relativistic theory of elastic deformable astronomical bodies. *Phys. Rev. D*, 63:043002, 2001. [Erratum: Phys.Rev.D 63, 109901 (2001)].

[282] Lev Davidovich Landau and E. M. Lifshitz. *The classical theory of fields*. 1975.

[283] Nathan K. Johnson-McDaniel and Benjamin J. Owen. Maximum elastic deformations of relativistic stars. *Phys. Rev. D*, 88:044004, 2013.

[284] N. Andersson and W. C. G. Ho. Using gravitational-wave data to constrain dynamical tides in neutron star binaries. *Phys. Rev. D*, 97(2):023016, 2018.

[285] Ehud Nakar. Short-Hard Gamma-Ray Bursts. *Phys. Rept.*, 442:166–236, 2007.

[286] Omer Bromberg, Ehud Nakar, Tsvi Piran, and Re'em Sari. Short versus Long and Collapsars versus Non-collapsars: A Quantitative Classification of Gamma-Ray Bursts. *Astrophys. J.*, 764(2):179, February 2013.

[287] Edo Berger. Short-Duration Gamma-Ray Bursts. *Ann. Rev. Astron. Astrophys.*, 52:43–105, 2014.

[288] W. S. Paciesas et al. The Fourth batse gamma-ray burst catalog (revised). *Astrophys. J. Suppl.*, 122:465–495, 1999.

[289] Christian K. Jespersen, Johann B. Severin, Charles L. Steinhardt, Jonas Vinther, Johan P. U. Fynbo, Jonatan Selsing, and Darach Watson. An Unambiguous Separation of Gamma-Ray Bursts into Two Classes from Prompt Emission Alone. *Astrophys. J. Lett.*, 896(2):L20, 2020.

[290] D. Burlon, G. Ghirlanda, G. Ghisellini, D. Lazzati, L. Nava, M. Nardini, and A. Celotti. Precursors in Swift Gamma Ray Bursts with redshift. *Astrophys. J. Lett.*, 685:L19, 2008.

[291] Bing Zhang. The delay time of gravitational wave — gamma-ray burst associations. *Front. Phys. (Beijing)*, 14(6):64402, 2019.

[292] Huan Yang, William E. East, Vasileios Paschalidis, Frans Pretorius, and Raissa F. P. Mendes. Evolution of Highly Eccentric Binary Neutron Stars Including Tidal Effects. *Phys. Rev. D*, 98(4):044007, 2018.

[293] Jose Nijaid Arredondo and Nicholas Loutrel. Neutron stars in the effective fly-by framework: f-mode resummation. *Class. Quant. Grav.*, 38(16):165001, 2021.

[294] Wataru Ogawaguchi and Yasufumi Kojima. Evolution of close neutron star binaries. *Prog. Theor. Phys.*, 96:901–916, 1996.

[295] Masaru Shibata. Effects of tidal resonances in coalescing compact binary systems. *Prog. Theor. Phys.*, 91:871–884, 1994.

[296] Nevin N. Weinberg, Phil Arras, and Joshua Burkart. An instability due to the nonlinear coupling of p-modes to g-modes: Implications for coalescing neutron star binaries. *Astrophys. J.*, 769:121, 2013.

[297] Reed Essick, Salvatore Vitale, and Nevin N. Weinberg. Impact of the tidal p-g instability on the gravitational wave signal from coalescing binary neutron stars. *Phys. Rev. D*, 94(10):103012, 2016.

[298] B. P. Abbott et al. Constraining the p-Mode-g-Mode Tidal Instability with GW170817. *Phys. Rev. Lett.*, 122(6):061104, 2019.

[299] Steven Reyes and Duncan A. Brown. Constraints on Nonlinear Tides due to p–g Mode Coupling from the Neutron Star Merger GW170817. *Astrophys. J.*, 894(1):41, 2020.

[300] Curt Cutler and Lee Lindblom. The Effect of Viscosity on Neutron Star Oscillations. *ApJ*, 314:234, March 1987.

[301] Dong Lai. Secular instability of g modes in rotating neutron stars. *Mon. Not. Roy. Astron. Soc.*, 307:1001–1007, 1999.

[302] Konstantinos N. Gourgouliatos and Samuel K. Lander. Axisymmetric magneto-plastic evolution of neutron-star crusts. *Mon. Not. Roy. Astron. Soc.*, 506(3):3578–3587, 2021.

[303] Kip S. Thorne. Nonradial Pulsation of General-Relativistic Stellar Models. III. Analytic and Numerical Results for Neutron Stars. *Astrophys. J.*, 158:1, October 1969.

[304] James B. Hartle. Slowly-Rotating Relativistic Stars.IV. Rotational Energy and Moment of Inertia for Stars in Differential Rotation. *Astrophys. J.*, 161:111, July 1970.

[305] I. A. Morrison, Thomas W. Baumgarte, S. L. Shapiro, and V. R. Pandharipande. The Moment of inertia of the binary pulsar J0737-3039A: Constraining the nuclear equation of state. *Astrophys. J. Lett.*, 617:L135–L138, 2004.

[306] R. Belvedere, K. Boshkayev, Jorge A. Rueda, and R. Ruffini. Uniformly rotating neutron stars in the global and local charge neutrality cases. *Nucl. Phys. A*, 921:33–59, 2014.

[307] Feryal Özel and Paulo Freire. Masses, Radii, and the Equation of State of Neutron Stars. *Ann. Rev. Astron. Astrophys.*, 54:401–440, 2016.

[308] D. R. Lorimer. Binary and Millisecond Pulsars. *Living Rev. Rel.*, 11:8, 2008.

[309] Bülent Kiziltan, Athanasios Kottas, Maria De Yoreo, and Stephen E. Thorsett. The Neutron Star Mass Distribution. *Astrophys. J.*, 778:66, 2013.

[310] Thomas M. Koshut, Chryssa Kouveliotou, William S. Paciesas, Jan van Paradijs, Geoffrey N. Pendleton, Michael S. Briggs, Gerald J. Fishman, and Charles A. Meegan. Gamma-Ray Burst Precursor Activity as Observed with BATSE. *Astrophys. J.*, 452:145, October 1995.

[311] Marc Favata. Systematic parameter errors in inspiraling neutron star binaries. *Phys. Rev. Lett.*, 112:101101, 2014.

[312] Taylor Binnington and Eric Poisson. Relativistic theory of tidal Love numbers. *Phys. Rev. D*, 80:084018, 2009.

[313] Tim Dietrich, Maximiliano Ujevic, Wolfgang Tichy, Sebastiano Bernuzzi, and Bernd Bruegmann. Gravitational waves and mass ejecta from binary neutron star mergers: Effect of the mass-ratio. *Phys. Rev. D*, 95(2):024029, 2017.

[314] A. Rowlinson, P. T. O'Brien, B. D. Metzger, N. R. Tanvir, and A. J. Levan. Signatures of magnetar central engines in short GRB lightcurves. *Mon. Not. Roy. Astron. Soc.*, 430:1061, 2013.

[315] B. P. Gompertz, P. T. O'Brien, and G. A. Wynn. Magnetar powered GRBs: Explaining the extended emission and X-ray plateau of short GRB light curves. *Mon. Not. Roy. Astron. Soc.*, 438(1):240–250, 2014.

[316] Wei-Hong Gao. Short-living supermassive magnetar model for the early X-ray flares following short GRBs. *Chin. J. Astron. Astrophys.*, 6:513–516, 2006.

[317] Riccardo Ciolfi, Wolfgang Kastaun, Jay Vijay Kalinani, and Bruno Giacomazzo. First 100 ms of a long-lived magnetized neutron star formed in a binary neutron star merger. *Phys. Rev. D*, 100(2):023005, 2019.

[318] Joshua A. Faber, Philippe Grandclement, Frederic A. Rasio, and Keisuke Taniguchi. Measuring neutron star radii with gravitational wave detectors. *Phys. Rev. Lett.*, 89:231102, 2002.

[319] Andreas Bauswein and Nikolaos Stergioulas. Spectral classification of gravitational-wave emission and equation of state constraints in binary neutron star mergers. *J. Phys. G*, 46(11):113002, 2019.

[320] Michele Vallisneri. Prospects for gravitational wave observations of neutron star tidal disruption in neutron star / black hole binaries. *Phys. Rev. Lett.*, 84:3519, 2000.

[321] V. Ferrari, L. Gualtieri, and F. Pannarale. Neutron star tidal disruption in mixed binaries: the imprint of the equation of state. *Phys. Rev. D*, 81:064026, 2010.

[322] Thomas W. Baumgarte and Stuart L. Shapiro. Numerical relativity and compact binaries. *Phys. Rept.*, 376:41–131, 2003.

[323] Kostas D. Kokkotas. High frequency sources of gravitational waves. *Nucl. Phys. B Proc. Suppl.*, 138:433–435, 2005.

[324] C. J. Moore, R. H. Cole, and C. P. L. Berry. Gravitational-wave sensitivity curves. *Class. Quant. Grav.*, 32(1):015014, 2015.

[325] Kai Schmitz. New Sensitivity Curves for Gravitational-Wave Signals from Cosmological Phase Transitions. *JHEP*, 01:097, 2021.

[326] Burkhard Zink, Paul D. Lasky, and Kostas D. Kokkotas. Are gravitational waves from giant magnetar flares observable? *Phys. Rev. D*, 85:024030, 2012.

[327] William E. East, Vasileios Paschalidis, Frans Pretorius, and Antonios Tsokaros. Binary neutron star mergers: Effects of spin and post-merger dynamics. *Phys. Rev. D*, 100(12):124042, December 2019.

[328] L. Jens Papenfort, Elias R. Most, Samuel Tootle, and Luciano Rezzolla. Impact of extreme spins and mass ratios on the post-merger observables of high-mass binary neutron stars. *arXiv e-prints*, page arXiv:2201.03632, January 2022.

[329] Eemeli Annala, Tyler Gorda, Aleksi Kurkela, and Aleksi Vuorinen. Gravitational-Wave Constraints on the Neutron-Star-Matter Equation of State. *Phys. Rev. Lett.*, 120(17):172703, April 2018.

[330] Bhaskar Biswas, Rana Nandi, Prasanta Char, Sukanta Bose, and Nikolaos Stergioulas. GW190814: on the properties of the secondary component of the binary. *MNRAS*, 505(2):1600–1606, August 2021.

[331] A. Kanakis-Pegios, P. S. Koliogiannis, and Ch. C. Moustakidis. Thermal effects on tidal deformability in the last orbits of an inspiraling binary neutron star system. *arXiv e-prints*, page arXiv:2202.01820, February 2022.

[332] E. Fonseca, H. T. Cromartie, T. T. Pennucci, P. S. Ray, A. Yu. Kirichenko, S. M. Ransom, P. B. Demorest, I. H. Stairs, Z. Arzoumanian, L. Guillemot, A. Parthasarathy, M. Kerr, I. Cognard, P. T. Baker, H. Blumer, P. R. Brook, M. DeCesar, T. Dolch, F. A. Dong, E. C. Ferrara, W. Fiore, N. Garver-Daniels, D. C. Good, R. Jennings, M. L. Jones, V. M. Kaspi, M. T. Lam, D. R. Lorimer, J. Luo, A. McEwen, J. W. McKee, M. A. McLaughlin, N. McMann, B. W. Meyers, A. Naidu, C. Ng, D. J. Nice, N. Pol, H. A. Radovan, B. Shapiro-Albert, C. M. Tan, S. P. Tendulkar, J. K. Swiggum, H. M. Wahl, and W. W. Zhu. Refined Mass and Geometric Measurements of the High-mass PSR J0740+6620. *ApJ*, 915(1):L12, July 2021.

[333] J. G. Martinez, K. Stovall, P. C. C. Freire, J. S. Deneva, F. A. Jenet, M. A. McLaughlin, M. Bagchi, S. D. Bates, and A. Ridolfi. Pulsar J0453+1559: A Double Neutron Star System with a Large Mass Asymmetry. *ApJ*, 812(2):143, October 2015.

[334] Paul D. Lasky and Kostas Glampedakis. Observationally constraining gravitational wave emission from short gamma-ray burst remnants. *MNRAS*, 458(2):1660–1670, May 2016.

[335] Daniela D. Doneva, Kostas D. Kokkotas, and Pantelis Pnigouras. Gravitational wave afterglow in binary neutron star mergers. *Phys. Rev. D*, 92(10):104040, November 2015.

[336] Riccardo Ciolfi. The key role of magnetic fields in binary neutron star mergers. *General Relativity and Gravitation*, 52(6):59, June 2020.

[337] A. Rowlinson, P. T. O'Brien, B. D. Metzger, N. R. Tanvir, and A. J. Levan. Signatures of magnetar central engines in short GRB light curves. *MNRAS*, 430(2):1061–1087, April 2013.

[338] Arthur G. Suvorov and Kostas D. Kokkotas. Evidence for magnetar precession in X-ray afterglows of gamma-ray bursts. *Astrophys. J. Lett.*, 892(2):L34, 2020.

[339] A. G. Suvorov and K. D. Kokkotas. Precessing magnetars as central engines in short gamma-ray bursts. *MNRAS*, 502(2):2482–2494, April 2021.

[340] Ph. Podsiadlowski, N. Langer, A. J. T. Poelarends, S. Rappaport, A. Heger, and E. Pfahl. The Effects of Binary Evolution on the Dynamics of Core Collapse and Neutron Star Kicks. *ApJ*, 612(2):1044–1051, September 2004.

[341] Anthony L. Piro. Magnetic Interactions in Coalescing Neutron Star Binaries. *ApJ*, 755(1):80, August 2012.

[342] Dong Lai. DC Circuit Powered by Orbital Motion: Magnetic Interactions in Compact Object Binaries and Exoplanetary Systems. *ApJ*, 757(1):L3, September 2012.

[343] A. Passamonti and N. Andersson. Towards real neutron star seismology: accounting for elasticity and superfluidity. *MNRAS*, 419(1):638–655, January 2012.

[344] S. Yoshida and U. Lee. Nonradial oscillations of neutron stars with a solid crust. Analysis in the relativistic Cowling approximation. *A&A*, 395:201–208, November 2002.

[345] Cosmin Stachie, Tito Dal Canton, Nelson Christensen, Marie-Anne Bizouard, Michael Briggs, Eric Burns, Jordan Camp, and Michael Coughlin. Searches for Modulated {}-Ray Precursors to Compact Binary Mergers in Fermi-GBM Data. *arXiv e-prints*, page arXiv:2112.04555, December 2021.

[346] M. Burgay, N. D'Amico, A. Possenti, R. N. Manchester, A. G. Lyne, B. C. Joshi, M. A. McLaughlin, M. Kramer, J. M. Sarkissian, F. Camilo, V. Kalogera, C. Kim, and D. R. Lorimer. An increased estimate of the merger rate of double neutron stars from observations of a highly relativistic system. *Nature*, 426(6966):531–533, December 2003.

[347] Alan G. Wiseman. Coalescing binary systems of compact objects to (post)5/2 Newtonian order. 2. Higher order wave forms and radiation recoil. *Phys. Rev. D*, 46:1517–1539, 1992.

[348] Eric Poisson and Clifford M. Will. Gravitational waves from inspiraling compact binaries: Parameter estimation using second postNewtonian wave forms. *Phys. Rev. D*, 52:848–855, 1995.

[349] Justin Vines, Eanna E. Flanagan, and Tanja Hinderer. Post-1-Newtonian tidal effects in the gravitational waveform from binary inspirals. *Phys. Rev. D*, 83:084051, 2011.

[350] Andreas Guerra Chaves and Tanja Hinderer. Probing the equation of state of neutron star matter with gravitational waves from binary inspirals in light of GW170817: a brief review. *J. Phys. G*, 46(12):123002, 2019.

[351] Tim Dietrich, Sebastiano Bernuzzi, and Wolfgang Tichy. Closed-form tidal approximants for binary neutron star gravitational waveforms constructed from high-resolution numerical relativity simulations. *Phys. Rev. D*, 96(12):121501, 2017.

[352] Luc Blanchet, Thibault Damour, Bala R. Iyer, Clifford M. Will, and Alan G. Wiseman. Gravitational radiation damping of compact binary systems to second postNewtonian order. *Phys. Rev. Lett.*, 74:3515–3518, 1995.

[353] K. G. Arun, Alessandra Buonanno, Guillaume Faye, and Evan Ochsner. Higher-order spin effects in the amplitude and phase of gravitational waveforms emitted by inspiraling compact binaries: Ready-to-use gravitational waveforms. *Phys. Rev. D*, 79:104023, 2009. [Erratum: Phys.Rev.D 84, 049901 (2011)].

[354] Tim Dietrich et al. Matter imprints in waveform models for neutron star binaries: Tidal and self-spin effects. *Phys. Rev. D*, 99(2):024029, 2019.

[355] William G. Laarakkers and Eric Poisson. Quadrupole moments of rotating neutron stars. *Astrophys. J.*, 512:282–287, 1999.

[356] Eric Poisson. Gravitational waves from inspiraling compact binaries: The Quadrupole moment term. *Phys. Rev. D*, 57:5287–5290, 1998.

[357] Michele Levi and Jan Steinhoff. Equivalence of ADM Hamiltonian and Effective Field Theory approaches at next-to-next-to-leading order spin1-spin2 coupling of binary inspirals. *JCAP*, 12:003, 2014.

[358] Michalis Agathos, Jeroen Meidam, Walter Del Pozzo, Tjonnie G. F. Li, Marco Tompitak, John Veitch, Salvatore Vitale, and Chris Van Den Broeck. Constraining the neutron star equation of state with gravitational wave signals from coalescing binary neutron stars. *Phys. Rev. D*, 92(2):023012, 2015.

[359] Antonios Tsokaros, Milton Ruiz, Vasileios Paschalidis, Stuart L. Shapiro, and Kōji Uryū. Effect of spin on the inspiral of binary neutron stars. *Phys. Rev. D*, 100(2):024061, 2019.

[360] Reetika Dudi, Tim Dietrich, Alireza Rashti, Bernd Bruegmann, Jan Steinhoff, and Wolfgang Tichy. High-accuracy simulations of highly spinning binary neutron star systems. *arXiv eprint = 2108.10429*, 8 2021.

[361] Ian Harry and Tanja Hinderer. Observing and measuring the neutron-star equation-of-state in spinning binary neutron star systems. *Class. Quant. Grav.*, 35(14):145010, 2018.

[362] Thomas E. Riley et al. A NICER View of the Massive Pulsar PSR J0740+6620 Informed by Radio Timing and XMM-Newton Spectroscopy. *Astrophys. J. Lett.*, 918(2):L27, 2021.

[363] Margherita Fasano, Tiziano Abdelsalhin, Andrea Maselli, and Valeria Ferrari. Constraining the Neutron Star Equation of State Using Multiband Independent Measurements of Radii and Tidal Deformabilities. *Phys. Rev. Lett.*, 123(14):141101, 2019.

[364] Curt Cutler et al. The Last three minutes: issues in gravitational wave measurements of coalescing compact binaries. *Phys. Rev. Lett.*, 70:2984–2987, 1993.

[365] Nai-Bo Zhang and Bao-An Li. GW190814's Secondary Component with Mass 2.50-2.67 M $_\odot$ as a Superfast Pulsar. *Astrophys. J.*, 902(1):38, 2020.

[366] Elias R. Most, L. Jens Papenfort, Lukas R. Weih, and Luciano Rezzolla. A lower bound on the maximum mass if the secondary in GW190814 was once a rapidly spinning neutron star. *Mon. Not. Roy. Astron. Soc.*, 499(1):L82–L86, 2020.

[367] Serge Droz, Daniel J. Knapp, Eric Poisson, and Benjamin J. Owen. Gravitational waves from inspiraling compact binaries: Validity of the stationary phase approximation to the Fourier transform. *Phys. Rev. D*, 59:124016, 1999.

[368] Luca Baiotti, Thibault Damour, Bruno Giacomazzo, Alessandro Nagar, and Luciano Rezzolla. Accurate numerical simulations of inspiralling binary neutron stars and their comparison with effective-one-body analytical models. *Phys. Rev. D*, 84:024017, 2011.

[369] Luc Blanchet. Gravitational Radiation from Post-Newtonian Sources and Inspiralling Compact Binaries. *Living Rev. Rel.*, 17:2, 2014.

[370] Thibault Damour and Alessandro Nagar. An Improved analytical description of inspiralling and coalescing black-hole binaries. *Phys. Rev. D*, 79:081503, 2009.

[371] Thibault Damour, Alessandro Nagar, and Sebastiano Bernuzzi. Improved effective-one-body description of coalescing nonspinning black-hole binaries and its numerical-relativity completion. *Phys. Rev. D*, 87(8):084035, 2013.

[372] Kyohei Kawaguchi, Kenta Kiuchi, Koutarou Kyutoku, Yuichiro Sekiguchi, Masaru Shibata, and Keisuke Taniguchi. Frequency-domain gravitational waveform models for inspiraling binary neutron stars. *Phys. Rev. D*, 97(4):044044, 2018.

[373] Tim Dietrich, Anuradha Samajdar, Sebastian Khan, Nathan K. Johnson-McDaniel, Reetika Dudi, and Wolfgang Tichy. Improving the NRTidal model for binary neutron star systems. *Phys. Rev. D*, 100(4):044003, 2019.

[374] Michael Boyle, Duncan A. Brown, Lawrence E. Kidder, Abdul H. Mroue, Harald P. Pfeiffer, Mark A. Scheel, Gregory B. Cook, and Saul A. Teukolsky. High-accuracy comparison of numerical relativity simulations with post-Newtonian expansions. *Phys. Rev. D*, 76:124038, 2007.

[375] Kenta Hotokezaka, Koutarou Kyutoku, Hirotada Okawa, and Masaru Shibata. Exploring tidal effects of coalescing binary neutron stars in numerical relativity. II. Long-term simulations. *Phys. Rev. D*, 91(6):064060, 2015.

[376] Sebastiano Bernuzzi, Alessandro Nagar, Tim Dietrich, and Thibault Damour. Modeling the Dynamics of Tidally Interacting Binary Neutron Stars up to the Merger. *Phys. Rev. Lett.*, 114(16):161103, 2015.

[377] Thibault Damour and Alessandro Nagar. Effective One Body description of tidal effects in inspiralling compact binaries. *Phys. Rev. D*, 81:084016, 2010.

[378] Donato Bini, Thibault Damour, and Guillaume Faye. Effective action approach to higher-order relativistic tidal interactions in binary systems and their effective one body description. *Phys. Rev. D*, 85:124034, 2012.

[379] Benjamin D. Lackey, Sebastiano Bernuzzi, Chad R. Galley, Jeroen Meidam, and Chris Van Den Broeck. Effective-one-body waveforms for binary neutron stars using surrogate models. *Phys. Rev. D*, 95(10):104036, 2017.

[380] Lawrence E. Kidder, Clifford M. Will, and Alan G. Wiseman. Spin effects in the inspiral of coalescing compact binaries. *Phys. Rev. D*, 47(10):R4183–R4187, 1993.

[381] Theocharis A. Apostolatos, Curt Cutler, Gerald J. Sussman, and Kip S. Thorne. Spin-induced orbital precession and its modulation of the gravitational waveforms from merging binaries. *Phys. Rev. D*, 49(12):6274–6297, June 1994.

[382] Andrea Maselli, Leonardo Gualtieri, Francesco Pannarale, and Valeria Ferrari. On the validity of the adiabatic approximation in compact binary inspirals. *Phys. Rev. D*, 86:044032, 2012.

[383] Leslie Wade, Jolien D. E. Creighton, Evan Ochsner, Benjamin D. Lackey, Benjamin F. Farr, Tyson B. Littenberg, and Vivien Raymond. Systematic and statistical errors in a bayesian approach to the estimation of the neutron-star equation of state using advanced gravitational wave detectors. *Phys. Rev. D*, 89(10):103012, 2014.

[384] Gerhard Schaefer. The Gravitational Quadrupole Radiation Reaction Force and the Canonical Formalism of Adm. *Annals Phys.*, 161:81–100, 1985.

[385] Tim Dietrich, Tanja Hinderer, and Anuradha Samajdar. Interpreting Binary Neutron Star Mergers: Describing the Binary Neutron Star Dynamics, Modelling Gravitational Waveforms, and Analyzing Detections. *Gen. Rel. Grav.*, 53(3):27, 2021.

[386] Benjamin D. Lackey, Michael Pürrer, Andrea Taracchini, and Sylvain Marsat. Surrogate model for an aligned-spin effective one body waveform model of binary neutron star inspirals using Gaussian process regression. *Phys. Rev. D*, 100(2):024002, 2019.

[387] Sizheng Ma, Hang Yu, and Yanbei Chen. Detecting resonant tidal excitations of Rossby modes in coalescing neutron-star binaries with third-generation gravitational-wave detectors. *Phys. Rev. D*, 103(6):063020, 2021.

[388] James M. Lattimer and Bernard F. Schutz. Constraining the equation of state with moment of inertia measurements. *Astrophys. J.*, 629:979–984, 2005.

[389] Tianqi Zhao and James M. Lattimer. Tidal Deformabilities and Neutron Star Mergers. *Phys. Rev. D*, 98(6):063020, 2018.

[390] Christian J. Krüger and Kostas D. Kokkotas. Dynamics of fast rotating neutron stars: An approach in the Hilbert gauge. *Phys. Rev. D*, 102(6):064026, September 2020.

[391] Christian J. Krüger, Kostas D. Kokkotas, Praveen Manoharan, and Sebastian H. Völkel. Fast Rotating Neutron Stars: Oscillations and Instabilities. *Frontiers in Astronomy and Space Sciences*, 8:166, September 2021.

[392] Mark Hannam, Duncan A. Brown, Stephen Fairhurst, Chris L. Fryer, and Ian W. Harry. When can gravitational-wave observations distinguish between black holes and neutron stars? *Astrophys. J. Lett.*, 766:L14, 2013.

[393] Paolo Pani, Leonardo Gualtieri, Andrea Maselli, and Valeria Ferrari. Tidal deformations of a spinning compact object. *Phys. Rev. D*, 92(2):024010, 2015.

[394] Lee Samuel Finn and David F. Chernoff. Observing binary inspiral in gravitational radiation: One interferometer. *Phys. Rev. D*, 47:2198–2219, 1993.

[395] R. Abbott et al. GW190814: Gravitational Waves from the Coalescence of a 23 Solar Mass Black Hole with a 2.6 Solar Mass Compact Object. *Astrophys. J. Lett.*, 896(2):L44, 2020.

[396] Ka-Wai Lo and Lap-Ming Lin. The spin parameter of uniformly rotating compact stars. *Astrophys. J.*, 728:12, 2011.

[397] Tetsuro Yamamoto, Masaru Shibata, and Keisuke Taniguchi. Simulating coalescing compact binaries by a new code (SACRA). *Phys. Rev. D*, 78(6):064054, September 2008.

[398] Elias R. Most, L. Jens Papenfort, Antonios Tsokaros, and Luciano Rezzolla. Impact of high spins on the ejection of mass in GW170817. *Astrophys. J.*, 884:40, 2019.

[399] Milton Ruiz, Antonios Tsokaros, Vasileios Paschalidis, and Stuart L. Shapiro. Effects of spin on magnetized binary neutron star mergers and jet launching. *Phys. Rev. D*, 99(8):084032, 2019.

[400] Tim Dietrich and Maximiliano Ujevic. Modeling dynamical ejecta from binary neutron star mergers and implications for electromagnetic counterparts. *Class. Quant. Grav.*, 34(10):105014, 2017.

[401] Kent Yagi and Nicolas Yunes. I-Love-Q. *Science*, 341:365–368, 2013.

[402] Francesco Zappa, Sebastiano Bernuzzi, David Radice, Albino Perego, and Tim Dietrich. Gravitational-wave luminosity of binary neutron stars mergers. *Phys. Rev. Lett.*, 120(11):111101, 2018.

[403] Thibault Damour and Alessandro Nagar. Relativistic tidal properties of neutron stars. *Phys. Rev. D*, 80:084035, 2009.

[404] Eric Poisson. Gravitomagnetic Love tensor of a slowly rotating body: post-Newtonian theory. *Phys. Rev. D*, 102(6):064059, 2020.

[405] Pawan Kumar Gupta, Jan Steinhoff, and Tanja Hinderer. Relativistic effective action of dynamical gravitomagnetic tides for slowly rotating neutron stars. *Phys. Rev. Res.*, 3(1):013147, 2021.

[406] Eric Poisson and Cyann Buisson. Tidal driving of inertial modes of Maclaurin spheroids. *Phys. Rev. D*, 102(10):104005, 2020.

[407] Gonçalo Castro, Leonardo Gualtieri, Andrea Maselli, and Paolo Pani. Impact and detectability of spin-tidal couplings in neutron star inspirals. *arXiv e-prints*, page arXiv:2204.12510, April 2022.

[408] Thibault Damour and Gilles Esposito-Farese. Tensor - scalar gravity and binary pulsar experiments. *Phys. Rev. D*, 54:1474–1491, 1996.

[409] Ivan Zh. Stefanov, Stoytcho S. Yazadjiev, and Michail D. Todorov. Phases of 4D scalar-tensor black holes coupled to Born-Infeld nonlinear electrodynamics. *Mod. Phys. Lett. A*, 23:2915–2931, 2008.

[410] Daniela D. Doneva, Stoytcho S. Yazadjiev, Kostas D. Kokkotas, and Ivan Zh. Stefanov. Quasi-normal modes, bifurcations and non-uniqueness of charged scalar-tensor black holes. *Phys. Rev. D*, 82:064030, 2010.

[411] Vitor Cardoso, Isabella P. Carucci, Paolo Pani, and Thomas P. Sotiriou. Black holes with surrounding matter in scalar-tensor theories. *Phys. Rev. Lett.*, 111:111101, 2013.

[412] K. Lazaridis, N. Wex, A. Jessner, M. Kramer, B. W. Stappers, G. H. Janssen, G. Desvignes, M. B. Purver, I. Cognard, G. Theureau, A. G. Lyne, C. A. Jordan, and J. A. Zensus. Generic tests of the existence of the gravitational dipole radiation and the variation of the gravitational constant. *Mon. Not. Roy. Astron. Soc.*, 400(2):805–814, December 2009.

[413] John Antoniadis et al. A Massive Pulsar in a Compact Relativistic Binary. *Science*, 340:6131, 2013.

[414] Paulo C. C. Freire, Norbert Wex, Gilles Esposito-Farese, Joris P. W. Verbiest, Matthew Bailes, Bryan A. Jacoby, Michael Kramer, Ingrid H. Stairs, John Antoniadis, and Gemma H. Janssen. The relativistic pulsar-white dwarf binary PSR J1738+0333 II. The most stringent test of scalar-tensor gravity. *Mon. Not. Roy. Astron. Soc.*, 423:3328, 2012.

[415] Lijing Shao, Noah Sennett, Alessandra Buonanno, Michael Kramer, and Norbert Wex. Constraining nonperturbative strong-field effects in scalar-tensor gravity by combining pulsar timing and laser-interferometer gravitational-wave detectors. *Phys. Rev. X*, 7(4):041025, 2017.

[416] D. Popchev. Master thesis, 2015.

[417] Fethi M. Ramazanoğlu and Frans Pretorius. Spontaneous Scalarization with Massive Fields. *Phys. Rev. D*, 93(6):064005, 2016.

[418] Stoytcho S. Yazadjiev, Daniela D. Doneva, and Dimitar Popchev. Slowly rotating neutron stars in scalar-tensor theories with a massive scalar field. *Phys. Rev. D*, 93(8):084038, 2016.

[419] Roxana Rosca-Mead, Christopher J. Moore, Ulrich Sperhake, Michalis Agathos, and Davide Gerosa. Structure of neutron stars in massive scalar-tensor gravity. *Symmetry*, 12(9):1384, 2020.

[420] Thibault Damour and Gilles Esposito-Farese. Tensor multiscalar theories of gravitation. *Class. Quant. Grav.*, 9:2093–2176, 1992.

[421] Michael Horbatsch, Hector O. Silva, Davide Gerosa, Paolo Pani, Emanuele Berti, Leonardo Gualtieri, and Ulrich Sperhake. Tensor-multi-scalar theories: relativistic stars and 3 + 1 decomposition. *Class. Quant. Grav.*, 32(20):204001, 2015.

[422] Stoytcho S. Yazadjiev and Daniela D. Doneva. Dark compact objects in massive tensor-multi-scalar theories of gravity. *Phys. Rev. D*, 99(8):084011, 2019.

[423] Daniela D. Doneva and Stoytcho S. Yazadjiev. Mixed configurations of tensor-multiscalar solitons and neutron stars. *Phys. Rev. D*, 101(2):024009, 2020.

[424] Daniela D. Doneva and Stoytcho S. Yazadjiev. Topological neutron stars in tensor-multi-scalar theories of gravity. *Phys. Rev. D*, 101(6):064072, 2020.

[425] S. Gottlober, H. J. Schmidt, and Alexei A. Starobinsky. Sixth Order Gravity and Conformal Transformations. *Class. Quant. Grav.*, 7:893, 1990.

[426] Lucas G. Collodel, Daniela D. Doneva, and Stoytcho S. Yazadjiev. Rotating tensor-multiscalar solitons. *Phys. Rev. D*, 101(4):044021, 2020.

[427] Daniela D. Doneva, Stoytcho S. Yazadjiev, and Kostas D. Kokkotas. Stability of topological neutron stars. *Phys. Rev. D*, 102(4):044043, 2020.

[428] Daniela D. Doneva and Stoytcho S. Yazadjiev. Nontopological spontaneously scalarized neutron stars in tensor-multiscalar theories of gravity. *Phys. Rev. D*, 101(10):104010, 2020.

[429] Hajime Sotani. Scalar gravitational waves from relativistic stars in scalar-tensor gravity. *Phys. Rev. D*, 89(6):064031, 2014.

[430] Raissa F. P. Mendes and Néstor Ortiz. New class of quasinormal modes of neutron stars in scalar-tensor gravity. *Phys. Rev. Lett.*, 120(20):201104, 2018.

[431] H. Th. Janka, Th. Zwerger, and R. Moenchmeyer. Does artificial viscosity destroy prompt type-II supernova explosions? *Astron. Astrophys.*, 268(1):360–368, February 1993.

[432] T. Zwerger and E. Mueller. Dynamics and gravitational wave signature of axisymmetric rotational core collapse. *Astron. Astrophys.*, 320:209–227, 1997.

[433] Harald Dimmelmeier, Jose A. Font, and Ewald Muller. Relativistic simulations of rotational core collapse. 2. Collapse dynamics and gravitational radiation. *Astron. Astrophys.*, 393:523–542, 2002.

[434] Evan O'Connor and Christian D. Ott. A New Open-Source Code for Spherically-Symmetric Stellar Collapse to Neutron Stars and Black Holes. *Class. Quant. Grav.*, 27:114103, 2010.

[435] Davide Gerosa, Ulrich Sperhake, and Christian D. Ott. Numerical simulations of stellar collapse in scalar-tensor theories of gravity. *Class. Quant. Grav.*, 33(13):135002, 2016.

[436] Jocelyn S. Read, Benjamin D. Lackey, Benjamin J. Owen, and John L. Friedman. Constraints on a phenomenologically parameterized neutron-star equation of state. *Phys. Rev. D*, 79:124032, 2009.

[437] Johannes Ruoff. The Numerical Evolution of Neutron Star Oscillations. Master's thesis, -, October 2000.

[438] Francesc Banyuls, José A. Font, José M. Ibáñez, José M. Martí, and Juan A. Miralles. Numerical $\{3 + 1\}$ General Relativistic Hydrodynamics: A Local Characteristic Approach. *Astrophys. J.*, 476(1):221–231, February 1997.

[439] Jose A. Font. Numerical hydrodynamics in general relativity. *Living Rev. Rel.*, 3:2, 2000.

[440] Evan O'Connor. An Open-Source Neutrino Radiation Hydrodynamics Code for Core-Collapse Supernovae. *Astrophys. J. Suppl.*, 219(2):24, 2015.

[441] Patrick Chi-Kit Cheong and Tjonnie Guang Feng Li. Numerical studies on core collapse supernova in self-interacting massive scalar-tensor gravity. *Phys. Rev. D*, 100(2):024027, 2019.

[442] Roxana Rosca-Mead, Christopher J. Moore, Michalis Agathos, and Ulrich Sperhake. Inverse-chirp signals and spontaneous scalarisation with self-interacting potentials in stellar collapse. *Class. Quant. Grav.*, 36(13):134003, 2019.

[443] A. O. Barvinsky and G. A. Vilkovisky. The Generalized Schwinger-Dewitt Technique in Gauge Theories and Quantum Gravity. *Phys. Rept.*, 119:1–74, 1985.

[444] Michael S. Ruf and Christian F. Steinwachs. One-loop divergences for $f(R)$ gravity. *Phys. Rev. D*, 97(4):044049, 2018.

[445] Justin Alsing, Emanuele Berti, Clifford M. Will, and Helmut Zaglauer. Gravitational radiation from compact binary systems in the massive Brans-Dicke theory of gravity. *Phys. Rev. D*, 85:064041, 2012.

[446] M. Kramer et al. Strong-Field Gravity Tests with the Double Pulsar. *Phys. Rev. X*, 11(4):041050, 2021.

[447] Junjie Zhao, Paulo C. C. Freire, Michael Kramer, Lijing Shao, and Norbert Wex. Closing a spontaneous-scalarization window with binary pulsars. *arXiv e-prints*, page arXiv:2201.03771, January 2022.

[448] B. P. Abbott et al. Tests of general relativity with GW150914. *Phys. Rev. Lett.*, 116(22):221101, 2016. [Erratum: Phys.Rev.Lett. 121, 129902 (2018)].

[449] Carlos A. R. Herdeiro and Eugen Radu. Asymptotically flat black holes with scalar hair: a review. *Int. J. Mod. Phys. D*, 24(09):1542014, 2015.

[450] Daniela D. Doneva and Stoytcho S. Yazadjiev. Beyond the spontaneous scalarization: New fully nonlinear mechanism for the formation of scalarized black holes and its dynamical development. *Phys. Rev. D*, 105(4):L041502, 2022.

[451] Hajime Sotani and Kostas D. Kokkotas. Maximum mass limit of neutron stars in scalar-tensor gravity. *Phys. Rev. D*, 95(4):044032, 2017.

[452] Burkhard Kampfer. On the Possibility of Stable Quark and Pion Condensed Stars. *J. Phys. A*, 14:L471–L475, 1981.

[453] Norman K. Glendenning and Christiane Kettner. Nonidentical neutron star twins. *Astron. Astrophys.*, 353:L9, 2000.

[454] K. Schertler, C. Greiner, J. Schaffner-Bielich, and M. H. Thoma. Quark phases in neutron stars and a 'third family' of compact stars as a signature for phase transitions. *Nucl. Phys. A*, 677:463–490, 2000.

[455] Jurgen Schaffner-Bielich, Matthias Hanauske, Horst Stoecker, and Walter Greiner. Phase transition to hyperon matter in neutron stars. *Phys. Rev. Lett.*, 89:171101, 2002.

[456] Jerome Novak and Jose M. Ibanez. Gravitational waves from the collapse and bounce of a stellar core in tensor scalar gravity. *Astrophys. J.*, 533:392–405, 2000.

[457] Jerome Novak. Spherical neutron star collapse in tensor - scalar theory of gravity. *Phys. Rev. D*, 57:4789–4801, 1998.

[458] Roxana Rosca-Mead, Ulrich Sperhake, Christopher J. Moore, Michalis Agathos, Davide Gerosa, and Christian D. Ott. Core collapse in massive scalar-tensor gravity. *Phys. Rev. D*, 102(4):044010, 2020.

[459] Raissa F. P. Mendes, Néstor Ortiz, and Nikolaos Stergioulas. Nonlinear dynamics of oscillating neutron stars in scalar-tensor gravity. *Phys. Rev. D*, 104(10):104036, 2021.

[460] Katerina Chatziioannou and Sophia Han. Studying strong phase transitions in neutron stars with gravitational waves. *Phys. Rev. D*, 101(4):044019, 2020.

[461] Bing Zhang and Peter Meszaros. Gamma-ray burst afterglow with continuous energy injection: Signature of a highly magnetized millisecond pulsar. *Astrophys. J. Lett.*, 552:L35–L38, 2001.

[462] Sebastiano Bernuzzi. Neutron Star Merger Remnants. *Gen. Rel. Grav.*, 52(11):108, 2020.

[463] Nikhil Sarin, Paul D. Lasky, and Gregory Ashton. Gravitational waves or deconfined quarks: what causes the premature collapse of neutron stars born in short gamma-ray bursts? *Phys. Rev. D*, 101(6):063021, 2020.

[464] Elias R. Most, L. Jens Papenfort, Veronica Dexheimer, Matthias Hanauske, Stefan Schramm, Horst Stöcker, and Luciano Rezzolla. Signatures of quark-hadron phase transitions in general-relativistic neutron-star mergers. *Phys. Rev. Lett.*, 122(6):061101, 2019.

[465] Andreas Bauswein, Niels-Uwe F. Bastian, David B. Blaschke, Katerina Chatziioannou, James A. Clark, Tobias Fischer, and Micaela Oertel. Identifying a first-order phase transition in neutron star mergers through gravitational waves. *Phys. Rev. Lett.*, 122(6):061102, 2019.

[466] Lukas R. Weih, Matthias Hanauske, and Luciano Rezzolla. Postmerger Gravitational-Wave Signatures of Phase Transitions in Binary Mergers. *Phys. Rev. Lett.*, 124(17):171103, 2020.

[467] Steven L. Liebling, Carlos Palenzuela, and Luis Lehner. Effects of High Density Phase Transitions on Neutron Star Dynamics. *Class. Quant. Grav.*, 38(11):115007, 2021.

[468] Elias R. Most, L. Jens Papenfort, Veronica Dexheimer, Matthias Hanauske, Horst Stoecker, and Luciano Rezzolla. On the deconfinement phase transition in neutron-star mergers. *Eur. Phys. J. A*, 56(2):59, 2020.

[469] Sebastian Blacker, Niels-Uwe F. Bastian, Andreas Bauswein, David B. Blaschke, Tobias Fischer, Micaela Oertel, Theodoros Soultanis, and Stefan Typel. Constraining the onset density of the hadron-quark phase transition with gravitational-wave observations. *Phys. Rev. D*, 102(12):123023, 2020.

[470] Clifford M. Will. The Confrontation between General Relativity and Experiment. *Living Rev. Rel.*, 17:4, 2014.

[471] Anthony L. Piro and Christian D. Ott. Supernova Fallback onto Magnetars and Propeller-powered Supernovae. *Astrophys. J.*, 736(2):108, 2011.

[472] Wataru Ishizaki, Kunihito Ioka, and Kenta Kiuchi. Fallback Accretion Model for the Years-to-decades X-Ray Counterpart to GW170817. *Astrophys. J. Lett.*, 916(2):L13, 2021.

[473] E. P. J. van den Heuvel and O. Bitzaraki. The magnetic field strength versus orbital period relation for binary radio pulsars with low-mass companions: evidence for neutron-star formation by accretion-induced collapse? *Astron. Astrophys.*, 297:L41, May 1995.

[474] Dhruv Desai, Brian D. Metzger, and Francois Foucart. Imprints of r-process heating on fall-back accretion: distinguishing black hole-neutron star from double neutron star mergers. *Mon. Not. Roy. Astron. Soc.*, 485(3):4404–4412, 2019.

[475] F. K. Lamb, C. J. Pethick, and D. Pines. A Model for Compact X-Ray Sources: Accretion by Rotating Magnetic Stars. *ApJ*, 184:271–290, August 1973.

[476] Marek Szczepanczyk et al. Detecting and reconstructing gravitational waves from the next galactic core-collapse supernova in the advanced detector era. *Phys. Rev. D*, 104(10):102002, 2021.

[477] Madappa Prakash, Ignazio Bombaci, Manju Prakash, Paul J. Ellis, James M. Lattimer, and Roland Knorren. Composition and structure of protoneutron stars. *Phys. Rept.*, 280:1–77, 1997.

[478] K. Glampedakis, N. Andersson, and L. Samuelsson. Magnetohydrodynamics of superfluid and superconducting neutron star cores. *Mon. Not. Roy. Astron. Soc.*, 410:805, 2011.

[479] Masaru Shibata, Keisuke Taniguchi, Hirotada Okawa, and Alessandra Buonanno. Coalescence of binary neutron stars in a scalar-tensor theory of gravity. *Phys. Rev. D*, 89(8):084005, 2014.

[480] Enrico Barausse, Carlos Palenzuela, Marcelo Ponce, and Luis Lehner. Neutron-star mergers in scalar-tensor theories of gravity. *Phys. Rev. D*, 87:081506, 2013.

[481] Marcelo Ponce, Carlos Palenzuela, Enrico Barausse, and Luis Lehner. Electromagnetic outflows in a class of scalar-tensor theories: Binary neutron star coalescence. *Phys. Rev. D*, 91(8):084038, 2015.

[482] Laura Sagunski, Jun Zhang, Matthew C. Johnson, Luis Lehner, Mairi Sakellariadou, Steven L. Liebling, Carlos Palenzuela, and David Neilsen. Neutron star mergers as a probe of modifications of general relativity with finite-range scalar forces. *Phys. Rev. D*, 97(6):064016, 2018.

[483] Shu-Jin Hou, Tong Liu, Ren-Xin Xu, Hui-Jun Mu, Cui-Ying Song, Da-Bin Lin, and Wei-Min Gu. The x-ray light curve in grb 170714a: Evidence for a quark star? *Astrophys. J.*, 854(2):104, 2018.

[484] T. J. Galama, P. M. Vreeswijk, J. van Paradijs, C. Kouveliotou, T. Augusteijn, H. Böhnhardt, J. P. Brewer, V. Doublier, J. F. Gonzalez, B. Leibundgut, C. Lidman, O. R. Hainaut, F. Patat, J. Heise, J. in't Zand, K. Hurley, P. J. Groot, R. G. Strom, P. A. Mazzali, K. Iwamoto, K. Nomoto, H. Umeda, T. Nakamura, T. R. Young, T. Suzuki, T. Shigeyama, T. Koshut, M. Kippen, C. Robinson, P. de Wildt, R. A. M. J. Wijers,

N. Tanvir, J. Greiner, E. Pian, E. Palazzi, F. Frontera, N. Masetti, L. Nicastro, M. Feroci, E. Costa, L. Piro, B. A. Peterson, C. Tinney, B. Boyle, R. Cannon, R. Stathakis, E. Sadler, M. C. Begam, and P. Ianna. An unusual supernova in the error box of the γ-ray burst of 25 April 1998. *Nature*, 395(6703):670–672, October 1998.

[485] David Reitze et al. Cosmic Explorer: The U.S. Contribution to Gravitational-Wave Astronomy beyond LIGO. *Bull. Am. Astron. Soc.*, 51(7):035, 2019.

[486] M. Punturo et al. The Einstein Telescope: A third-generation gravitational wave observatory. *Class. Quant. Grav.*, 27:194002, 2010.

[487] Michele Maggiore et al. Science Case for the Einstein Telescope. *JCAP*, 03:050, 2020.

[488] S. Hild et al. Sensitivity Studies for Third-Generation Gravitational Wave Observatories. *Class. Quant. Grav.*, 28:094013, 2011.

[489] I. Sagert, T. Fischer, M. Hempel, G. Pagliara, J. Schaffner-Bielich, A. Mezzacappa, F. K. Thielemann, and M. Liebendorfer. Signals of the QCD phase transition in core-collapse supernovae. *Phys. Rev. Lett.*, 102:081101, 2009.

[490] Bo Qin, Xiang-Ping Wu, Ming-Chung Chu, and Li-Zhi Fang. The collapse of neutron stars in high mass binaries as the energy source for the gamma-ray bursts. *Astrophys. J. Lett.*, 494:L57, 1998.

[491] Rosalba Perna, Hiromichi Tagawa, Zoltan Haiman, and Imre Bartos. Accretion-Induced Collapse of Neutron Stars in the Disks of Active Galactic Nuclei. *Astrophys. J.*, 915(1):10, 2021.

[492] Dimitrios Psaltis. Probes and Tests of Strong-Field Gravity with Observations in the Electromagnetic Spectrum. *Living Rev. Rel.*, 11:9, 2008.

[493] C. P. Burgess. Quantum gravity in everyday life: General relativity as an effective field theory. *Living Rev. Rel.*, 7:5–56, 2004.

[494] David N. Spergel. The dark side of cosmology: Dark matter and dark energy. *Science*, 347:1100–1102, 2015.

[495] Pascual Jordan. The present state of Dirac's cosmological hypothesis. *Z. Phys.*, 157:112–121, 1959.

[496] M. Fierz. On the physical interpretation of P.Jordan's extended theory of gravitation. *Helv. Phys. Acta*, 29:128–134, 1956.

[497] C. Brans and R. H. Dicke. Mach's principle and a relativistic theory of gravitation. *Phys. Rev.*, 124:925–935, 1961.

[498] Marcelo Salgado. The Cauchy problem of scalar tensor theories of gravity. *Class. Quant. Grav.*, 23:4719–4742, 2006.

[499] Marcelo Salgado, David Martinez-del Rio, Miguel Alcubierre, and Dario Nunez. Hyperbolicity of scalar-tensor theories of gravity. *Phys. Rev. D*, 77:104010, 2008.

[500] Takeshi Chiba, Tomohiro Harada, and Ken-ichi Nakao. Gravitational physics in scalar tensor theories: Tests of strong field gravity. *Prog. Theor. Phys. Suppl.*, 128:335–372, 1997.

[501] Y. Fujii and K. Maeda. *The scalar-tensor theory of gravitation.* Cambridge Monographs on Mathematical Physics. Cambridge University Press, 7 2007.

[502] Valerio Faraoni. *Cosmology in scalar tensor gravity.* 2004.

[503] Thomas P. Sotiriou. Gravity and Scalar Fields. *Lect. Notes Phys.*, 892:3–24, 2015.

[504] I. I. Shapiro. A century of relativity. *Rev. Mod. Phys.*, 71:S41–S53, 1999.

[505] James G. Williams, Slava G. Turyshev, and Dale H. Boggs. Lunar laser ranging tests of the equivalence principle with the earth and moon. *Int. J. Mod. Phys. D*, 18:1129–1175, 2009.

[506] S. S. Shapiro, J. L. Davis, D. E. Lebach, and J. S. Gregory. Measurement of the Solar Gravitational Deflection of Radio Waves using Geodetic Very-Long-Baseline Interferometry Data, 1979-1999. *Phys. Rev. Lett.*, 92:121101, 2004.

[507] B. Bertotti, L. Iess, and P. Tortora. A test of general relativity using radio links with the Cassini spacecraft. *Nature*, 425:374–376, 2003.

[508] Giulia Ventagli, Antoine Lehébel, and Thomas P. Sotiriou. Onset of spontaneous scalarization in generalized scalar-tensor theories. *Phys. Rev. D*, 102(2):024050, 2020.

[509] Marcelo Salgado, Daniel Sudarsky, and Ulises Nucamendi. On spontaneous scalarization. *Phys. Rev. D*, 58:124003, 1998.

[510] Norbert Wex. Testing Relativistic Gravity with Radio Pulsars. *arXiv e-prints*, page arXiv:1402.5594, February 2014.

[511] Soichiro Morisaki and Teruaki Suyama. Spontaneous scalarization with an extremely massive field and heavy neutron stars. *Phys. Rev. D*, 96(8):084026, 2017.

[512] B. P. Abbott et al. Tests of General Relativity with GW170817. *Phys. Rev. Lett.*, 123(1):011102, 2019.

[513] B. P. Abbott et al. Tests of General Relativity with the Binary Black Hole Signals from the LIGO-Virgo Catalog GWTC-1. *Phys. Rev. D*, 100(10):104036, 2019.

[514] Nikolas Andreou, Nicola Franchini, Giulia Ventagli, and Thomas P. Sotiriou. Spontaneous scalarization in generalised scalar-tensor theory. *Phys. Rev. D*, 99(12):124022, 2019. [Erratum: Phys.Rev.D 101, 109903 (2020)].

[515] Jerome Novak. Neutron star transition to strong scalar field state in tensor scalar gravity. *Phys. Rev. D*, 58:064019, 1998.

[516] Peter G. Bergmann. Comments on the scalar tensor theory. *Int. J. Theor. Phys.*, 1:25–36, 1968.

[517] Robert V. Wagoner. Scalar tensor theory and gravitational waves. *Phys. Rev. D*, 1:3209–3216, 1970.

[518] Thibault Damour. Binary Systems as Test-beds of Gravity Theories. In *6th SIGRAV Graduate School in Contemporary Relativity and Gravitational Physics: A Century from Einstein Relativity: Probing Gravity Theories in Binary Systems*, 4 2007.

[519] R. H. Dicke. Mach's principle and invariance under transformation of units. *Phys. Rev.*, 125:2163–2167, 1962.

[520] Evan O'Connor and Christian D. Ott. Black Hole Formation in Failing Core-Collapse Supernovae. *Astrophys. J.*, 730:70, 2011.

[521] Drew Clausen, Anthony L. Piro, and Christian D. Ott. The Black Hole Formation Probability. *Astrophys. J.*, 799(2):190, 2015.

[522] Tuguldur Sukhbold, T. Ertl, S. E. Woosley, Justin M. Brown, and H. T. Janka. Core-Collapse Supernovae from 9 to 120 Solar Masses Based on Neutrino-powered Explosions. *Astrophys. J.*, 821(1):38, 2016.

[523] H. A. Bethe. Supernova mechanisms. *Rev. Mod. Phys.*, 62:801–866, 1990.

[524] Adam Burrows, Eli Livne, Luc Dessart, Christian Ott, and Jeremiah Murphy. A new mechanism for core-collapse supernova explosions. *Astrophys. J.*, 640:878–890, 2006.

[525] A. Harada, H. Nagakura, W. Iwakami, and S. Yamada. A Parametric Study of the Acoustic Mechanism for Core-Collapse Supernovae. *Astrophys. J.*, 839(1):28, 2017.

[526] H. Thomas Janka. Conditions for shock revival by neutrino heating in core collapse supernovae. *Astron. Astrophys.*, 368:527, 2001.

[527] Ondrej Pejcha and Todd A. Thompson. The Physics of the Neutrino Mechanism of Core-Collapse Supernovae. *Astrophys. J.*, 746:106, 2012.

[528] Sean M. Couch. The mechanism(s) of core-collapse supernovae. *Philosophical Transactions of the Royal Society of London Series A*, 375(2105):20160271, September 2017.

[529] Jose A. Font, Mark A. Miller, Wai-Mo Suen, and Malcolm Tobias. Three-dimensional numerical general relativistic hydrodynamics. 1. Formulations, methods, and code tests. *Phys. Rev. D*, 61:044011, 2000.

[530] Jose A. Font. Numerical Hydrodynamics and Magnetohydrodynamics in General Relativity. *Living Rev. Rel.*, 11:7, 2008.

[531] S. E. Woosley and Alexander Heger. Nucleosynthesis and Remnants in Massive Stars of Solar Metallicity. *Phys. Rept.*, 442:269–283, 2007.

[532] Željko Ivezić, Andrew J. Connelly, Jacob T. VanderPlas, and Alexander Gray. *Statistics, Data Mining, and Machine Learning in Astronomy.* 2014.

[533] Keith Riles. Recent searches for continuous gravitational waves. *Mod. Phys. Lett. A*, 32(39):1730035, 2017.

[534] Harald Dimmelmeier, Christian D. Ott, Hans-Thomas Janka, Andreas Marek, and Ewald Mueller. Generic Gravitational Wave Signals from the Collapse of Rotating Stellar Cores. *Phys. Rev. Lett.*, 98:251101, 2007.

[535] Harald Dimmelmeier, Christian D. Ott, Andreas Marek, and H. Thomas Janka. The Gravitational Wave Burst Signal from Core Collapse of Rotating Stars. *Phys. Rev. D*, 78:064056, 2008.

[536] Jose Luis Blázquez-Salcedo, Fech Scen Khoo, and Jutta Kunz. Ultra-long-lived quasi-normal modes of neutron stars in massive scalar-tensor gravity. *EPL*, 130(5):50002, 2020.

[537] Jose Luis Blázquez-Salcedo, Fech Scen Khoo, Jutta Kunz, and Vincent Preut. Polar Quasinormal Modes of Neutron Stars in Massive Scalar-Tensor Theories. *Front. in Phys.*, 9:741427, 2021.

[538] Daniela D. Doneva and Stoytcho S. Yazadjiev. Neutron star solutions with curvature induced scalarization in the extended Gauss-Bonnet scalar-tensor theories. *JCAP*, 04:011, 2018.

[539] Alexandru Dima, Enrico Barausse, Nicola Franchini, and Thomas P. Sotiriou. Spin-induced black hole spontaneous scalarization. *Phys. Rev. Lett.*, 125(23):231101, 2020.

[540] Daniela D. Doneva, Lucas G. Collodel, Christian J. Krüger, and Stoytcho S. Yazadjiev. Black hole scalarization induced by the spin: 2+1 time evolution. *Phys. Rev. D*, 102(10):104027, 2020.

[541] Pedro V. P. Cunha, Carlos A. R. Herdeiro, and Eugen Radu. Spontaneously Scalarized Kerr Black Holes in Extended Scalar-Tensor-Gauss-Bonnet Gravity. *Phys. Rev. Lett.*, 123(1):011101, 2019.

[542] Lucas G. Collodel, Burkhard Kleihaus, Jutta Kunz, and Emanuele Berti. Spinning and excited black holes in Einstein-scalar-Gauss-Bonnet theory. *Class. Quant. Grav.*, 37(7):075018, 2020.

[543] Carlos A. R. Herdeiro, Eugen Radu, Hector O. Silva, Thomas P. Sotiriou, and Nicolás Yunes. Spin-induced scalarized black holes. *Phys. Rev. Lett.*, 126(1):011103, 2021.

[544] Emanuele Berti, Lucas G. Collodel, Burkhard Kleihaus, and Jutta Kunz. Spin-induced black-hole scalarization in Einstein-scalar-Gauss-Bonnet theory. *Phys. Rev. Lett.*, 126(1):011104, 2021.

[545] Justin L. Ripley and Frans Pretorius. Dynamics of a $\mathbb{Z}_2$ symmetric EdGB gravity in spherical symmetry. *Class. Quant. Grav.*, 37(15):155003, 2020.

[546] Hector O. Silva, Helvi Witek, Matthew Elley, and Nicolás Yunes. Dynamical Descalarization in Binary Black Hole Mergers. *Phys. Rev. Lett.*, 127(3):031101, 2021.

[547] Robert Benkel, Thomas P. Sotiriou, and Helvi Witek. Dynamical scalar hair formation around a Schwarzschild black hole. *Phys. Rev. D*, 94(12):121503, 2016.

[548] Justin L. Ripley and Frans Pretorius. Scalarized Black Hole dynamics in Einstein dilaton Gauss-Bonnet Gravity. *Phys. Rev. D*, 101(4):044015, 2020.

[549] Daniela D. Doneva, Stella Kiorpelidi, Petya G. Nedkova, Eleftherios Papantonopoulos, and Stoytcho S. Yazadjiev. Charged Gauss-Bonnet black holes with curvature induced scalarization in the extended scalar-tensor theories. *Phys. Rev. D*, 98(10):104056, 2018.

[550] Justin L. Ripley and Frans Pretorius. Hyperbolicity in Spherical Gravitational Collapse in a Horndeski Theory. *Phys. Rev. D*, 99(8):084014, 2019.

[551] S. B. Popov and R. Turolla. Initial spin periods of neutron stars in supernova remnants. *Astrophys. Space Sci.*, 341:457–464, 2012.

[552] Aristeidis Noutsos, Dominic Schnitzeler, Evan Keane, Michael Kramer, and Simon Johnston. Pulsar Spin-Velocity Alignment: Kinematic Ages, Birth Periods and Braking Indices. *Mon. Not. Roy. Astron. Soc.*, 430:2281, 2013.

[553] H. Shen, H. Toki, K. Oyamatsu, and K. Sumiyoshi. Relativistic Equation of State for Core-Collapse Supernova Simulations. *Astrophys. J. Suppl.*, 197:20, 2011.

[554] James M. Lattimer and F. Douglas Swesty. A Generalized equation of state for hot, dense matter. *Nucl. Phys. A*, 535:331–376, 1991.

[555] David Radice, Viktoriya Morozova, Adam Burrows, David Vartanyan, and Hiroki Nagakura. Characterizing the Gravitational Wave Signal from Core-Collapse Supernovae. *Astrophys. J. Lett.*, 876(1):L9, 2019.

[556] Ernazar Abdikamalov, Giulia Pagliaroli, and David Radice. Gravitational Waves from Core-Collapse Supernovae. *arXiv e-prints*, page arXiv:2010.04356, October 2020.

[557] Carlos Palenzuela, Enrico Barausse, Marcelo Ponce, and Luis Lehner. Dynamical scalarization of neutron stars in scalar-tensor gravity theories. *Phys. Rev. D*, 89(4):044024, 2014.

[558] Benjamin P Abbott et al. A guide to LIGO-Virgo detector noise and extraction of transient gravitational-wave signals. *Class. Quant. Grav.*, 37(5):055002, 2020.

[559] Nils Andersson. A superfluid perspective on neutron star dynamics. *Universe*, 7(1):17, 2021.